Universidade de Aveiro Departamento de Química
2016

Patrícia Manuela Ribeiro Pereira

Fotossensibilizadores conjugados com galactose para terapia fotodinâmica do cancro

Galactose-conjugated photosensitizers for targeted cancer photodynamic therapy

Universidade de Aveiro Departamento de Química
2016

Patrícia Manuela Ribeiro Pereira

Fotossensibilizadores conjugados com galactose para terapia fotodinâmica do cancro

Galactose-conjugated photosensitizers for targeted cancer photodynamic therapy

Tese apresentada à Universidade de Aveiro para cumprimento dos requisitos necessários à obtenção do grau de Doutor em Química, realizada sob a orientação científica do Professor Doutor João Paulo Costa Tomé, Professor Associado do Departamento de Engenharia Química do Instituto Superior Técnico da Universidade de Lisboa e co-orientação da Doutora Rosa Cristina Simões Fernandes, Investigadora Auxiliar do Instituto da Imagem Biomédica e Ciências da Vida - Faculdade de Medicina da Universidade de Coimbra.

Apoio financeiro do POPH-QREN.

Apoio financeiro da FCT e do FSE no âmbito do III Quadro Comunitário de Apoio.

Para os meus pais
Pelo amor incondicional, pelas sábias palavras
Por nunca me terem deixado desistir!

"… eu peço que vocês vão contra a corrente; sim, nisto peço que se rebelem: que se rebelem contra esta cultura do provisório ... Eu tenho confiança em vocês, jovens, ... Tenham a coragem de "ir contra a corrente". E tenham também a coragem de ser felizes!"

Papa Francisco

o júri

presidente

Prof. Doutor Anibal Manuel de Oliveira Duarte
Professor Catedrático do Departamento de Eletrónica, Telecomunicações e Informática da Universidade de Aveiro

Prof. Doutor Charles Michael Drain
Professor Catedrático of Department of Chemistry and Biochemistry of Hunter College of the City University of New York

Prof. Doutora Maria Matilde Soares Duarte Marques
Professora Catedrática do Departamento de Engenharia Química do Instituto Superior Técnico Universidade de Lisboa

Prof. Doutor Rudolf Josef Schneider
Head of Division of BAM Federal Institute for Materials Research and Testing, Berlin,
Professor Associado com Agregação of Technische Universität Berlin

Prof. Doutora Maria da Graça de Pinho Morgado da Silva Neves
Professora Associada com Agregação do Departamento de Química da Universidade de Aveiro

Prof. Doutor João Paulo Costa Tomé
Professor Associado do Departamento de Engenharia Química do Instituto Superior Técnico Universidade de Lisboa

Doutora Rosa Cristina Simões Fernandes
Investigadora Auxiliar da Faculdade de Medicina da Universidade de Coimbra

Doutor Henrique Manuel Paixão dos Santos Girão
Investigador Auxiliar da Faculdade de Medicina da Universidade de Coimbra

agradecimentos

Este trabalho é muito mais do que uma tese – representa uma etapa fascinante da minha vida em que contei com o apoio de várias pessoas para as quais quero deixar aqui algumas palavras:

Aos meus orientadores, Doutor João Tomé e Doutora Rosa Fernandes, quero agradecer por me terem aberto as portas no desafiante mundo de investigação em Terapia Fotodinâmica. Um agradecimento especial pela partilha das suas experiências e de conhecimento científico, pela partilha de entusiasmos e desalentos, pelos conselhos, pela paciência e pela confiança que sempre depositaram em mim. Os ensinamentos do Dr. João e da Dra. Rosa marcarão inevitavelmente a minha atitude não só na ciência mas também na vida.
À Dra. Sandrina Silva, quero agradecer a amizade, os momentos de discussão científica e a ajuda na síntese de alguns dos compostos usados neste trabalho.
À Dra. Célia Gomes desejo expressar a minha gratidão pela disponibilidade e ajuda nos estudos com modelos animais.
Ao Dr. José Ramalho, um muito obrigado pela produção e fornecimento dos lentivirus.
Ao Dr. Henrique Girão agradeço todo o apoio científico que me concedeu durante a realização deste trabalho, o seu contagiante bom humor e incentivo constante.

I would like to thank Professor Charles Michael Drain for providing me with the lab facilities, guidance and support during my stay in his research group. To all the people in the group of Professor Drain, for their good work and friendship. Not forgetting the others, I particularly would like to thank Dinesh and Waqar for their help in the synthesis of some molecules used in this work.

A todos os meus amigos nos laboratórios de Aveiro e Coimbra. Um muito obrigado pela pronta ajuda no trabalho laboratorial e pelas palavras de apoio.
À Andreia Gonçalves, a minha “irmã da ciência” quero agradecer a amizade e todo o apoio que me deu ao longo destes anos. Ao Leandro Lourenço agradeço toda a sua ajuda e todas as palavras de calma e de motivação.

agradecimentos

Aos meus amigos de sempre, aos da academia e todos os que chegaram depois, agradeço a amizade que temos e por acreditarem em mim em todos os momentos. Em especial ao Márcio, ao Jean e à Carla América agradeço o valor que me dão e a preocupação que têm comigo. To Junior and Ana for being more than friends during my stay in NYC. Thank you for being like family and for making my stay less “hard”. "I see friends shaking hands... saying how do you do... They're really saying... I love you.../And I think to myself... what a wonderful world".

Aos meus pais, à minha mana Lili e ao meu mano Carlitos pelo orgulho que têm em mim, por serem o meu porto seguro e por me apoiaram incondicionalmente qualquer que seja o meu rumo.
À minha madrinha Helena pelo seu sorriso contagiante e pelo apoio que sempre me deu. À minha restante família pela amizade e interesse que sempre demonstraram.

Finalmente, ao David por encher a minha vida de amor, por saber como lidar com o meu stress e por tornar tudo menos complicado.

À Universidade de Aveiro, muito em especial ao Departamento de Química.
À Faculdade de Medicina da Universidade de Coimbra, muito em especial ao IBILI.
À Fundação para a Ciência e Tecnologia, a bolsa de investigação.

palavras-chave

Terapia Fotodinâmica, Cancro, Porfirinas, Ftalocianinas, Clorinas, Galactose, Galectina-1, GLUT1

resumo

A Terapia Fotodinâmica (do inglês *Photodynamic Therapy*, PDT) tem sido aplicada com bastante sucesso no tratamento de doenças oncológicas. Esta terapia baseia-se na utilização conjunta de luz e de um agente fotossensibilizador (do inglês photosensitizer, PS) para gerar reações citotóxicas no tecido tumoral. A vasta gama dos PSs usados na clínica para o tratamento de cancro apresenta baixas solubilidade em meios fisiológicos e seletividade para as células tumorais. Este projeto surge de uma colaboração entre químicos e bioquímicos e tem como objetivo principal o desenvolvimento de novos PSs conjugados com moléculas de galactose para serem reconhecidos por proteínas com afinidade por galactose sobrexpressas nas células tumorais. Numa primeira fase foram avaliadas as propriedades foto-químicas e –físicas dos novos conjugados. Na presença de características reveladoras de um potencial terapêutico, o seu potencial em PDT foi avaliado em diferentes modelos biológicos.

No primeiro capítulo desta dissertação faz-se uma introdução ao uso da PDT no tratamento de doenças oncológicas e ao potencial em PDT de PSs conjugados com galactose. No segundo capítulo, descreve-se a síntese de PSs ligados a unidades dendríticas de galactose ou a galactose através de conjugação ao carbono-3 deste açúcar. No terceiro capítulo, foram realizados estudos *in vitro* com as linhas celulares do cancro da bexiga HT-1376 e UM-UC-3 (células em monocamada), para avaliar o potencial fotodinâmico de uma ftalocianina conjugada com unidades dendríticas de galactose (**$PcGal_{16}$**). As proteínas galectina-1 e GLUT1 demonstraram estar envolvidas no uptake da **$PcGal_{16}$** pelas células tumorais. Posteriormente, no quarto capítulo, foi demonstrado que as vias de endocitose mediadas por clatrina e cavéolas são importantes na internalização da **$PcGal_{16}$**. Estudos ao nível celular revelaram que a foto-toxicidade em células HT-1376 resistentes à PDT pode ser aumentada por alteração das vias endocíticas. O potencial biológico *in vitro* e *in vivo* de uma porfirina conjugada com unidades dendríticas de galactose (**$PorGal_8$**) é descrito no quinto capítulo deste trabalho. O *uptake* e a foto-toxicidade da **$PorGal_8$** são superiores na linha tumoral UM-UC-3 que contém níveis elevados da proteína galectina-1. Os estudos *in vivo*, utilizando as células UM-UC-3 para indução do tumor, comprovaram o efeito terapêutico da **$PorGal_8$** após PDT. No sexto capítulo, aborda-se um tratamento repetido de PDT com uma clorina conjugada com unidades dendríticas de galactose (**$ChlGal_8$**), como uma abordagem terapêutica promissora em células HT-1376 resistentes à terapia. No sétimo capítulo, descreve-se o potencial anticancerígeno de uma porfirina conjugada com galactose através do carbono-3 (**Por-C3-Gal_4**) em células de cancro de cólon HCT-116, de cancro da mama MCF-7, de cancro da bexiga UM-UC-3 e de cancro cervical HeLa, tanto em monocamadas como em esferoides.

keywords

Photodynamic Therapy, Cancer, Porphyrins, Phthalocyanines, Chlorins, Galactose, Galectin-1, GLUT1

abstract

The combination of a photosensitizing molecule (Photosensitizer, PS) and light to induce toxicity by Reactive Oxygen Species (ROS) production is very attractive in the treatment of cancer by Photodynamic Therapy (PDT). Unfortunately, the PSs used in clinic for the treatment of cancer have low cancer selectivity and poor water solubility. The success of new PDT agents in cancer treatment requires a strong collaboration between chemists for the synthesis of the porphyrinoid molecule and conjugation with a cancer-targeting motif, physicists for the development of appropriate light irradiation devices, biochemists for understanding cellular responses, and clinicians for the clinical studies. In this study, we have combined the knowledge of chemists and biochemists to develop new PSs by conjugating them with specific galactose motifs to be used in the treatment of cancer by PDT. These new galactose-PSs were designed for a specific target such as a galactose-binding protein overexpressed in cancer cells, and their photophysical properties evaluated. We have tested the photo-chemical and –physical properties of the new PSs and their photodynamic potential in different biological models.

Chapter I of this dissertation presents a brief introduction to the use of PDT in the treatment of cancer and the potential of galactose-PSs in PDT. Chapter II reports the synthesis of water-soluble porphyrinoids attached to dendritic units of galactose or to galactose through carbon-3. In Chapter III, HT-1376 and UM-UC-3 bladder cancer cells growing as monolayers were used to determine the uptake and photodynamic potential of a phthalocyanine conjugated with galactodendritic units (**$PcGal_{16}$**). The galactose-binding proteins galectin-1 and GLUT1 demonstrated to be involved in the uptake and further phototoxicity of **$PcGal_{16}$** by bladder cancer cells. The role of caveolae- and clathrin-mediated endocytosis in the internalization of **$PcGal_{16}$** by bladder cancer cells is reported in Chapter IV. Cellular studies revealed that interfering with endocytic pathways led to increased phototoxicity in HT-1376 cancer cells resistant to PDT. Chapter V describes the *in vitro* and *in vivo* photodynamic properties of a porphyrin conjugated with dendritic units of galactose (**$PorGal_8$**). **$PorGal_8$** uptake and PDT-induced cytotoxicity were higher in UM-UC-3 compared to HT-1376 bladder cancer cells. These differences were correlated with the levels of galectin-1 protein expression and cytoskeleton alterations. **$PorGal_8$** accumulated in UM-UC-3 xenograft tumors and induced tumor ablation after PDT. Chapter VI discussed the potential of a repeated PDT treatment to increase *in vitro* and *in vivo* phototoxicity with a galactodendritic chlorin (**$ChlGal_8$**) in HT-1376 cells resistant to PDT. Chapter VII reports the potential of a porphyrin conjugated with C3-galactose (**Por-C3-Gal_4**) in monolayers and spheroid cultures of HCT-116 colon cancer cells, MCF-7 breast cancer cells, UM-UC-3 bladder cancer cells and HeLa cervical cancer cells.

Table of contents

List of abbreviations

ALA	5-aminolevulinic acid
Apaf-1	apoptosis activating factor-1
ATP	adenosine-triphosphate
Bcl-2	B-cell lymphoma 2
CAM	chorioallantoic membrane
Chl	chlorin
$ChlF_{20}$	perfluorophenylchlorin
DAPI	4′,6-Diamidino-2-phenylindole
DFFA	DNA fragmentation factor alpha
DHE	dihydroethidium
E-cadherin/FL	full-length E-cadherin
EGFR	epidermal growth factor receptor
ELISA	enzyme-Linked Immunosorbent Assay
F_2BMet	5,10,15,20-tetrakis(2,6-difluoro-3-*N*-methylsulfamoylphenyl) bacteriochlorin
FDA	food and drug administration
GLUT1	glucose transporter 1
HIF1α	hypoxia-inducible factor-1α
HSA	human serum albumin
K_a	affinity constant
K_D	dissociation constant
LDH	lactate dehydrogenase
LED	light emitting diode
MAL	methyl aminolevulinate
MCT 1	monocarboxylate transporter 1
MitoPY1	mitochondria peroxy yellow 1
MTT	3-[4,5-dimethylthiazol-2-yl]-2,5-diphenyl-tetrazolium bromide

2-NBDG	2-deoxy-2-[(7-nitro-2,1,3-benzoxadiazol-4-yl)amino]-D-glucose
n	number of binding sites
NMR	nuclear magnetic resonance
NPe6	N-aspartylchlorin e_6
$^1O_2$	singlet oxygen
$^3O_2$	triplet oxygen
OPD	optical penetration depth
PDT	photodynamic therapy
pO_2	partial pressure of oxygen
Pc	phthalocyanine
Por	porphyrin
PS	photosensitizer
ROS	reactive oxygen species
siRNA	small interfering RNA
TBR	tumor-to-background ratio
TNFR1	tumor necrosis factor receptor 1
TPP	5,10,15,20-tetraphenylporphyrin
TUNEL	terminal deoxynucleotidyl transferase dUTP nick end labeling
VEGF	vascular endothelial growth factor

Introduction

CHAPTER I

Chapter I Introduction

1.1 General overview

Photodynamic Therapy will never be the right or only answer for every type of cancers, but it has a great potential…

"Photodynamic Therapy: A Light at the End of the Tunnel for Cancer Patients"

Ellen Blum Barish, Roswell Park Cancer Institute, The Better World Report, 2010

Cancer is the term used to describe malignant diseases in which abnormal cells divide without control and are able to invade the tissues and the organs of the body. In 2012, an estimated 14.1 million new cases of cancer occurred worldwide and 8.2 million people died from cancer. Cancer is an important public health problem and its incidence is likely to increase in the future due to worldwide population ageing.

Redox regulation, with increasing generation of reactive oxygen species (ROS) and upregulated antioxidant capacity in adaptation to intrinsic oxidative stress, has long been observed in cancer cells, especially those in advanced disease stages [1]. This is a biochemical property that can confer drug resistance to cancer cells. Redox modulation by pharmacological agents could have significant therapeutic benefits since it could contribute to intracellular ROS increase and/or protective antioxidant systems depletion, which abrogates such drug-resistant mechanisms and leads to the induction of cancer cell death and tissue destruction [2, 3]. It has been shown that agents counteracting such adaptive mechanisms by an additive or synergistic effect become more effective against these cancer cells [1, 2].

Photodynamic therapy (PDT) is an oxidative stress-based therapy which makes use of the production of ROS to induce toxicity, by combining light at specific wavelength, molecular oxygen and a photosensitizer (PS) [4]. PDT is a two-step therapy, involving the administration of the PS and *in situ* irradiation with light at appropriate wavelength [5]. The phototoxicity induced by PDT is a result of several direct and indirect mechanisms including toxicity at the cancer cellular level, alterations in the intrinsic anti-tumor immune activity, increase in leukocyte function, alteration in the tumor vessels leading to tumor ischemia and

amplification of proinflamatory cytokines [6, 7]. Currently available PSs exhibit accumulation in the cancer cells, but their uptake by the non-cancerous cells cannot be completely avoided. PDT has shown significant advances in recent years, not only on the optimization of light delivery systems but also on the synthesis of new PSs [8]. The precise light irradiation of the tumor tissue using flexible fiber optic devices promotes a therapeutic selectivity. Selective therapeutic effect can be enhanced if selectivity in the PS accumulation in cancer cells can be achieved. Their cellular uptake and subcellular localization are controlled by PS intrinsic properties such as lipophilicity, type and number of groups and/or charges and degree of asymmetry [9-11]. Concerning cancer cellular uptake, PS internalization is also influenced by diffusion or endocytosis processes [12] or membrane pumps (*e.g.* the adenosine-triphosphate (ATP)-binding cassette transporter ABCG2) [13]. PS subcellular localization is considered one of the most important parameters for predicting the PDT outcome.

One way of generating molecular-targeted PSs with practical application in PDT is to conjugate a porphyrinoid (porphyrin, chlorin or phthalocyanine) with a carbohydrate, since they are able to bind to proteins called lectins, found on surface of the cancer cells [14, 15]. Galectins are a family of lectins, non-enzymatic proteins with altered expression in cancer cells. Galectins and certain other carbohydrate-binding proteins such as glucose transporters are found to be overexpressed on cancer cells [16, 17]. As a result, noteworthy research has been devoted to develop porphyrinoids conjugated with galactose molecules [15, 18-42] able to bind galectins (mainly galectin-1) or even the glucose transporter GLUT1 overexpressed in cancer cells. Galactose units, in addition to providing interaction of the conjugate with galactose-binding proteins, have the potential to provide amphiphilicity or even water solubility to the conjugate. Galactose-conjugates are envisaged to tackle the obstacles of first or second generation PS agents.

This Chapter deals with the use of the oxidative stress-based therapy PDT in the treatment of cancer. The role of three components in PDT – PS, light and molecular oxygen – is highlighted. The mechanism of action of PDT, the steps involved in the photodynamic efficiency of a new PS (ranging from its photophysical/photochemical properties to its uptake by cancer cells and induction of cell death) and the different *in vitro* and *in vivo* biological models available for the evaluation of a new PS in oncology are discussed in this chapter.

Finally, promising results in cancer PDT with porphyrinoids conjugated with galactose and dendritic units of galactose are described.

1.1.1 Publication

This chapter comprises the following publication:

Patrícia M. R. Pereira, João P. C. Tomé, Rosa Fernandes, "Molecular Targeted Photodynamic Therapy for Cancer", in Handbook of Porphyrin Science, Karl M Kadish, Kevin M Smith, Roger Guilard, Eds., World Scientific, **2016**, *in press*.

1.2 Photodynamic Therapy: Brief history

Perhaps the best way to start is the beginning… A detailed description of the PDT history is too complex to be encompassed here. Nevertheless, some key findings are important to understand the urgent necessity for new and effective PSs.

The idea of combining light and a chemical compound has ancient beginnings. Scientific records of the therapeutic effect of sunlight activation of psoralens (extracted from plants) date back to approximately 3,000 years ago when this early photochemotherapy was used for repigmentation of vitiligo [43, 44]. The most important discoveries in the history of PDT are described in the following topics, focusing those who encouraged the medical applications of PDT in the oncologic field. A timeline starting with the ancient developments and leading into the more recent milestones in the evolution of PDT in oncology is presented in Figure 1.1.

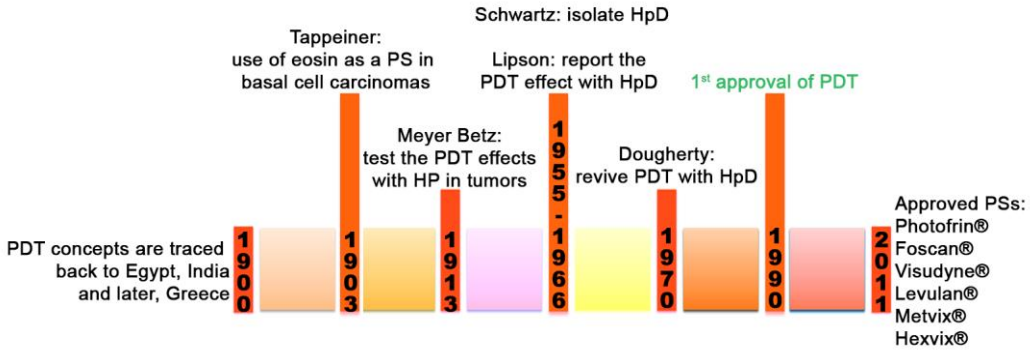

Figure 1.1 Timeline showing selected milestones in the historical development of photodynamic therapy in oncology. PDT-photodynamic therapy, PS = photosensitizer, HP = Hematoporphyrin, HpD =Hematoporphyrin Derivative.

The first application of PDT in cancer treatment was described by von Tappeiner and Jesionek in 1903 [45], who applied eosin to basal cell carcinomas prior to illumination. Porphyrins (Pors), the most explored class of drugs in PDT, were initially investigated by Meyer-Betz in 1913 [46]. In these investigations, the PDT effects with Hematoporphyrin in rat tumors are reported. Meyer-Hertz also performed a heroic self-experiment: he injected himself with Hematoporphyrin and irradiated a small area at his forearm. Consequently, exposure to direct sunlight led to phototoxic reactions with swelling and burning sensation. Modern time

of PDT applications was stimulated after Schwartz [47] and Lipson´s findings in which the acid treatment of Hematoporphyrin yielded a mixture of Pors and other chemical species, termed Hematoporphyrin Derivative. Hematoporphyrin Derivative after red light activation demonstrated better PDT effect than Hematoporphyrin [44]. Although the chemical characterization of Hematoporphyrin Derivative was not completely clear, in 1975 Dougherty [48] reported that the combination of this drug and red light results in mammary tumor eradication. This exciting result encouraged the first clinical experiments with Hematoporphyrin Derivative to treat patients with bladder cancer and skin tumors [49, 50]. PDT researches were demonstrating successful results (despite some gaps, mostly in PS chemistry) and in the late 1980s, Quadra Logic Technologies Photo Therapeutics (Vancouver, British Columbia, Canada) and Lederle Laboratories (American Cyanamid, Pearl River, NY) formed a partnership to achieve approvals for the clinical use of PDT [44]. The first PDT approval occurred in 1993 in Canada using Photofrin®, a more purified and better characterized version of Hematoporphyrin Derivative, for the treatment of bladder cancer [51]. The first Food and Drug Administration approval of PDT in the United States was also obtained with Photofrin®, in 1995, for palliation of obstructive esophageal cancer [51]. The favourable results obtained with Photofrin® and the PDT approvals generated curiosity in the scientific community, as a brief search on Web of Science for the keyword "photodynamic" for the period 1900-2010. The number of papers increased from 128 in the first half of the century (1900-1955) to more than 10,000 in the second half (1955-2010). Additionally, in the last 14 years (2000-2016) they have been published more than 25,000 papers. The new recent time of clinical PDT is stimulating organic chemists to develop synthetic pathways that make possible the production of potential PSs.

1.3 Photodynamic Therapy: Components and mechanism of action

Photosensitization reactions have been successfully applied in a wide variety of medical areas. However the photophysical and photochemical mechanisms by which an activated PS (by light) induces biological response are challenges in photobiological and photochemical research areas…

1.3.1 Photosensitizer

PSs are naturally occurring substances or synthetic derivatives (containing a chromophore in their structure) which are therapeutically inert until irradiated by light [52]. An "ideal" PS for cancer PDT should exhibit the following chemical, physical and biological properties [53-55]: (1) readily available in pure form with known chemical composition; (2) have low dark toxicity and exhibit high phototoxicity, which is frequently mediated by the production of singlet oxygen ($^1O_2$); (3) photostable and soluble in aqueous media; (4) high molar absorption coefficient in the 600-900 nm range of the electromagnetic spectrum; (5) selective to the cancer cells and (6) limited skin phototoxicity. Porphyrinoid compounds, such as porphyrins (Pors), chlorins (Chls), bacteriochlorins, phthalocyanines (Pcs), and related structures (Figure 1.2) are the most appropriate PSs for PDT [53, 56, 57]. Porphyrins have a chemical structure composed of four modified pyrrole subunits, interconnected *via* methane carbon atoms. Such types of free base macrocycles (*i.e.* a porphyrins without metal-ions in their cavity) have an absorption spectrum characterized by five bands, the strongest known as Soret band (around 400 nm) and four smaller absorption bands (Q-bands) at wavelengths in the red region. Their low water solubility, poor absorption in the red region of the electromagnetic spectrum and low selectivity to the cancer cells result in unwanted side effects in cancer PDT. Chlorins (dihydroporphyrins) are porphyrinoids which have one of the pyrrole subunits reduced. Compared to porphyrins, the intensity of the lowest energy absorption band (near 650 nm) is increased in Chls. Phthalocyanines consist of a ring of four isoindole units linked by imine nitrogen atoms, where the pyrrole groups are fused with benzene rings. Due to their chemical structure, Pcs absorb strongly in the red region of the electromagnetic spectrum, with a maximum at around 670 nm.

Normally, PSs are in a low energy level named the ground-state (^{1}PS). To initiate the photodynamic effect, a PS is irradiated with light at a specific wavelength promoting its excitation from the stable ^{1}PS to the excited-singlet-state energy level ($^1PS^*$). The photo-excited $^1PS^*$ is extremely unstable with a half-life generally less than 1 µs. To obtain the photodynamic effect, $^1PS^*$ must undergo intersystem crossing to a longer-lived electronically different excited state, the excited-triplet-state ($^3PS^*$) [8, 52, 58].

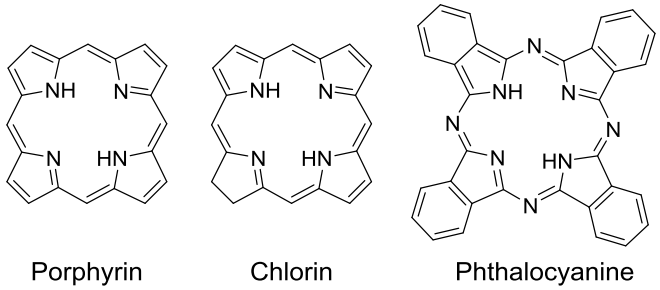

Figure 1.2 Basic chemical structures of the porphyrinoids porphyrin, chlorin and phthalocyanine.

At this stage, the excited PS returns to its ground-state by type I (electron transfer) and type II (energy transfer) photochemical reactions [59]. These two competing mechanisms are instantaneous and can occur simultaneously [60]. The occurrence of the two mechanisms is mainly dependent on the PS, oxygen content, the abundance of the biological substrate and the microenvironment where the PS is localized, as well as the binding affinity of the PS to the substrate [60-63]. In the type I reaction, the $^{3}PS^{*}$ interacts with a biological substrate forming free radicals able to react with subcellular components such as nucleic acids, proteins, peptides and plasma membrane [60]. In the type II reaction, $^{1}O_{2}$ is formed as a result of energy transfer from the $^{3}PS^{*}$ to the triplet-ground-state of molecular oxygen ($^{3}O_{2}$). The role of $^{1}O_{2}$ in the cytotoxicity induced by a PS after PDT was introduced in 1976 by Dougherty and coworkers [64]. The type II photochemical reaction is considered to be the major path of phototoxicity (Figure 1.3), in that $^{1}O_{2}$ exhibits high chemical reactivity and irreversible destruction of cancer cells [65]. Although $^{1}O_{2}$ is generally accepted as the main damaging species in PDT, ROS formation from the type I mechanism may amplify PDT response under hypoxic conditions [63, 66].

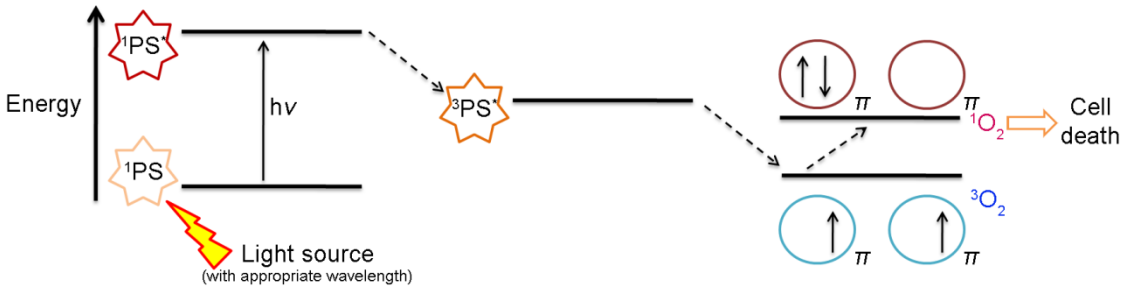

Figure 1.3 Modified Jablonski diagram showing Type II photochemical reaction in photodynamic therapy. PS = photosensitizer, $^{3}O_{2}$ = molecular oxygen, $^{1}O_{2}$ = singlet oxygen. Adapted from Ref. [53].

ROS generated during type I and type II photochemical reactions are characterized by high reactivity and short lifetimes [67-69]. Therefore, the phototoxic effect should be limited to the local and proximal irradiated area containing the PS. The lifetime of $^1O_2$ has been estimated to be inferior to 0.04 milliseconds, which limits its diffusion distance to approximately 20 nm from its point of origin within a cell [69-71]. Contrary to this idea, Skovsen *et al.* have demonstrated that in experiments performed in a single nerve cell from the hippocampus of Wistar rats, $^1O_2$ generated by the PS 5,10,15,20-tetrakis(*N*-methyl-4-pyridyl)-21H,23H-porphyrin (TMPyP) can be quite long-lived in a cell and able to diffuse across the cell membrane into the extracellular environment [67]. It should be noted that factors such as the location of $^1O_2$ formation and the nature of the surrounding medium influence both the distance over which $^1O_2$ can diffuse and the probability with which it undergoes biomolecular reactions [10, 68]. In a heterogeneous biological sample, the lifetime of $^1O_2$ is highly dependent on the presence of dissolved solutes that can quench $^1O_2$ (*e.g.* proteins) and on the solvent covering the cells [68, 70]. For example, an increase in $^1O_2$ lifetime has been described when cells were exposed to deuterium oxide (D_2O) instead of water (H_2O) [72].

The standard method used to perform quantitative time-resolved detection of $^1O_2$ is based on its specific phosphorescence at 1270 nm. However, the phosphorescence quantum yield in a biological sample is strongly reduced due to the presence of quenchers [67]. Sodium azide (NaN_3) and carotenoids are well-known quenchers of $^1O_2$ and they can also be used to qualitatively infer if these reactive species are generated during a specific PDT treatment [41, 73]. However, quenching is affected by the concentration of quencher and the intracellular location of the species, and such quenchers can be unspecific. The probes (*e.g.* 1,3-diphenylisobenzofuran, DPBF, and 2',7'-dichlorodihydrofluorescein, DCFDA) which exhibit spectral changes in the presence of $^1O_2$, have been also used for qualitative determination of $^1O_2$ production by a certain PS [41, 74-76]. However, these probes are often unspecific and the results obtained do not always correlate with the photocytotoxic effects. Other techniques have been developed to detect the formation of $^1O_2$, for example: by observation of oxygen quenching of triplet-excited single molecules, by time-resolved experiments of $^1O_2$ luminescence *in vivo*, by novel luminescent $^1O_2$ probes and the time-resolved detection of $^1O_2$ in a transmission microscope [68, 70].

The aggregation of the PSs can also influence their production of ROS and mechanism of action. Aggregation can be easily identified by changes in the electronic absorption spectrum of the PS and it can be affected by PS concentration, temperature, interaction with molecules and ionic strength [77-82]. The aggregation of PSs can be reduced by controlling the ionic strength, stabilizing the most active groups of the PS or by conjugating the PS with one or more biomolecules. Nuñez *et al*. reported that the photodynamic activity of the PS methylene blue against *Candida albicans* is improved when the assays are performed in aqueous urea solution [82]. Urea stabilizes the monomeric species of methylene blue by a direct (water replacement) or indirect mechanism (decrease in solvation entropy of water/urea mixtures) [83]. Lourenço *et al*. have compared the photoactivity of a Pc conjugated with α-, β- and γ-cyclodextrins [78]. Interestingly, the Pc conjugated with α- and γ-cyclodextrins demonstrated higher water solubility, $^1O_2$ production and photoactivity against bladder cancer cells when compared with Pc conjugated with β-cyclodextrin.

1.3.2 Tissue oxygenation

The content of oxygen plays an important role in PDT effect induced by type II photochemical reaction. An inadequate supply of oxygen to cancer tissues limits photodynamic effectiveness in hypoxic tumors [84-86]. In addition, an increase in hypoxia can be observed during PDT due to fast depletion of oxygen supply. As a result, the PDT effect can be impaired by the secretion of angiogenic factors which lead to the formation and growth of new blood vessels (Figure 1.4) [84]. It is well established that hypoxic tumors are less susceptible to PDT [87] and that the development of hypoxia after PDT favors the treatment response[88]. However, the consequences of hypoxia induced during PDT are less straight forward. Krzykawska-Serda *et al*. have described that the level of hypoxia generated after PDT is an important factor in the phototoxic induced by 5,10,15,20-tetrakis(2,6-difluoro-3-*N*-methylsulfamoylphenyl)bacteriochlorin (F_2BMet) [89]. When PDT was performed with a PS-to-light interval of 15 min (cancer vascular-targeted PDT), there was induction of chronic and/or extreme hypoxia which resulted in long-term tumor responses. On the other hand, when PDT was performed with a PS-to-light interval of 72 hours (cancer cell-targeted PDT) there

was mild and transient hypoxia associated with tumor re-growths. Lee See *et al*. [86] described a 50% decrease in the photodynamic effect when partial pressure of oxygen (pO_2) was reduced from 180 to about 50 mmHg, while Moan and Sommer [85] detected a 50% reduction in cell photosensitivity at a pO_2 of 7.6 mmHg, with full PDT effect at about 40 mmHg. Further studies performed by Henderson and Fingar demonstrated that lowering pO_2 levels below 40 mmHg resulted in a decrease of cellular photo-inactivation [84].

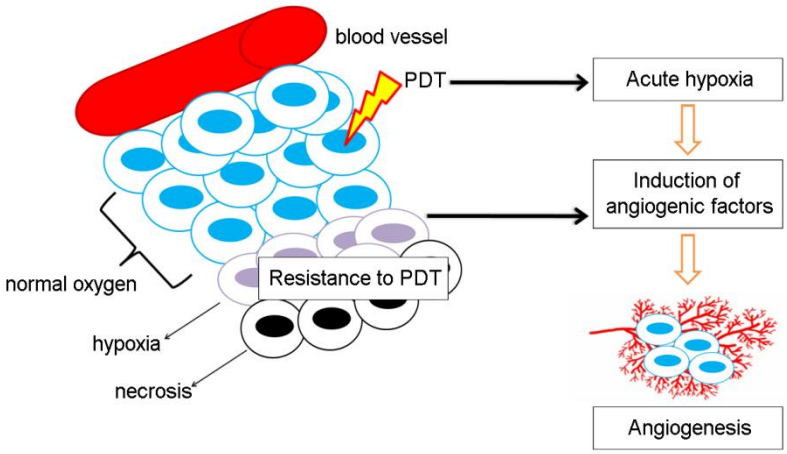

Figure 1.4 Hypoxia in solid tumors and acute hypoxia induced after PDT.

Several preclinical and clinical studies have also demonstrated changes in blood flow during and immediately after PDT [90-94], which can alter the rate of oxygen transported to the tissue. The changes on blood flow during PDT are due to the cancer vascular effects mediated by this therapy, such as damage to tumor vasculature [6, 92], vasoconstriction [93], vasodilatation induced by edema [93], or by decrease or increase in the production of vasoactive substances [94, 95], such as nitric oxide. Wang *et al*. reported that a blood flow decrease was mediated by a decrease of nitric oxide production during PDT with 5-aminolevulinic acid (ALA) [94]. Nitric oxide is used by endothelium of blood vessels to induce relaxation in the surrounding smooth muscle, signaling vasodilatation and blood flow increase. On the other hand, a decrease in nitric oxide may result in vasoconstriction and decreased blood flow. Thus, a decrease in tissue oxygen levels during PDT may reduce the production of nitric oxide, since its biosynthesis requires molecular oxygen [95].

Approaches that can locally produce oxygen have been proposed for PDT treatment of hypoxic tumors. Chen *et al*. have developed an interesting strategy based on a nanoparticle composed of a PS and catalase, functionalized with a ligand that recognizes an integrin overexpressed in cancer cells [96]. In this approach, intracellular hydrogen peroxide (H_2O_2) is catalyzed by catalase to generate O_2 when it penetrates into the shell, which leads to the release of the PS. Upon irradiation, the released PS generates ROS inducing cell death.

1.3.3 Light source and light delivery

Light sources used in PDT comprised of laser (diode laser, metal vapor-pumped dye laser, argon laser and argon-pumped dye laser, solid state laser, *etc.*) and non-laser sources/lamps (metal halide lamps, xenon arc lamps, quartz halogen lamps, phosphor-coated sodium lamp, fluorescent lamps, *etc.*) [97, 98]. Light emitting diodes (LEDs) and femtosecond solid state lasers are other sources of light with potential to be used in PDT. LEDs are less expensive when compared with all the other sources described so far and they can be engineered in arrays to irradiate large areas. However, the power output is a limiting factor in their use for PDT. For example, Ambulight is a magnetic LED lighting system for the treatment of non-melanoma skin cancer. Femtosecond lasers have been proposed for two-photon PDT, however they have technical limitations [97, 98]. Lasers and non-lasers have been both used as light sources in PDT and the superiority of one source over the other one has not been demonstrated. Noncoherent light sources and conventional arc lamps are more suitable, because they are less expensive and may be used with various PSs since they produce a wide spectrum of light. The LumaCare irradiation system is an example of a compact portable irradiation source, equipped with interchangeable fiber-optics and optical filters, capable of producing light between 350 to 800 nm. The conjunction of a LumaCare system with filters or interchangeable fiber-optic probes allows the emission of light at restricted wavelengths. Although noncoherent light sources are preferred in PDT studies, they have the disadvantage of significant thermal effect. The choice of light source for PDT is dependent on the absorption properties of the PS used, the optical characteristics of the tissue and the light dose [98]. Additionally, the type of light source used in PDT is highly dependent on the

location of the tumor (Figure 1.5): surface illumination for treating superficial tumors, intraoperative cavitary illumination for brain tumors, bronchoscopic for pulmonary diseases, endoscopic for gastroenterology and transurethral for urologic diseases [51, 98].

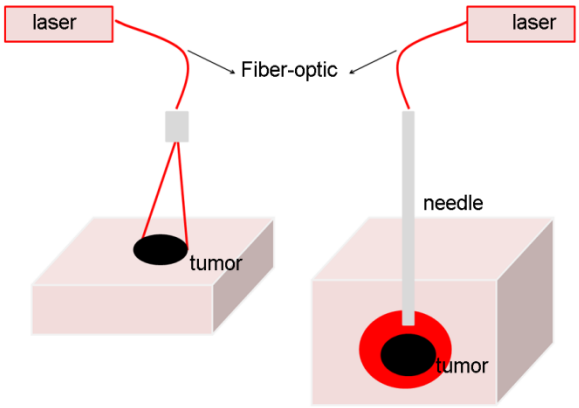

Figure 1.5 Representation for light delivery during surface and interstitial photodynamic therapy. Adapted from Ref. [99].

The time interval between PS administration and irradiation can highly influence the effectiveness of PDT. For example, benzoporphyrin derivative monoacid ring A (Verteporfin) induces microvascular damage when irradiation is performed at 15 minutes post-injection of the PS and damage to both microvasculature and cancer cells occur at later time points (3 hours post-injection) [100, 101]. Chen *et al*. have demonstrated that targeting both cellular and tumor vascular compartments by combining a long drug-light interval PDT with a short drug-light interval is more effective than each individual or combinative PDT treatments [100].

As the therapeutic efficiency of PDT is highly dependent on the levels of oxygen in the tissue, the light delivery method should be optimized to improve oxygen maintenance during the treatment. Xiao *et al*. have demonstrated in a preclinical study that continuous light delivery is less effective than computer-switched fractionated light delivery with seven interstitial fibers in PDT of solid tumors (rat prostate carcinomas) [102]. The rationale of the experimental design is that in the light-off period of a fractionated light delivery protocol there is reoxigenation of the tumor, improving phototoxicity. However, in these protocols it is

difficult to define the most appropriate light-off and light-on periods for each type of tumor. Preclinical studies have shown that PDT response is enhanced when a light-fractionated approach (two light fractions separated by a dark interval of several hours) is used with ALA-PDT in the treatment of superficial basal cell carcinoma [103-105]. Additionally, it was also demonstrated that this increase in PDT effect is higher when a low-dose light fraction is followed by a high-dose light fraction, separated by a dark interval of 2 hours [105]. Based on these preclinical studies, further clinical studies were performed, comparing the traditional non-fractionated ALA-PDT (single irradiation of 75 J/cm^2) with fractionated treatment (20 and 80 J/cm^2, with a dark interval of 2 hours) [106, 107]. Long-term follow-up demonstrated higher efficacy of ALA-PDT with a two-fold irradiation protocol, compared to ALA-PDT with single irradiation in the treatment of superficial basal cell carcinoma.

Photosensitizers containing absorption bands in the range between 600 to 900 nm have particular interest for PDT. A tissue generally contains chromophores which are able to absorb light used during a PDT treatment, reducing its absorption by the administrated PS. Hemoglobin (λ_{max} at 420 nm) and bilirubin (λ_{max} at 460 nm) are examples of these endogenous chromophores. Water molecules are also able to absorb light at wavelengths higher than 1000 nm. Another fact is that at wavelengths higher than 900 nm, the photons have reduced energy to induce a photochemical reaction. As a result, PDT is usually performed at wavelengths higher than 600 nm where the penetration of light through the tissues is higher. Briefly, the absolute penetration of a light in a certain tissue depends on both the characteristics of the light and the optical properties of the tissue [108, 109]. The optical penetration depth (OPD, *i.e.* the depth at which the intensity of the propagating light is reduced 37% of its initial value at the air/tissue interface) [110] is reduced in optically dense tissues (0.8 mm and 0.9 mm in the brain and liver tissues, respectively) and 4 mm at 633 nm in the bladder tissue [109]. Additionally, PDT is most effective when light delivery is homogeneous and in tumors that can be reached directly by light or light delivery devices such as optic fibers.

1.4 Photosensitizing agents used in oncology

Clinical PDT is a two-stage and a dual selective process with the first stage corresponding to the administration of the PS. After a certain period of time the PS is preferentially retained in tumor (first time selective). The tumor is illuminated with light at a specific wavelength, a process which constitutes the second and final stage in the therapy…

In the clinic, a typical PDT session involves two crucial steps: the administration of the PS and the local irradiation of the target tissue where the PS is accumulated (Figure 1.6). The session begins with the administration of the PS (intravenous in most of the tumors or topical in skin lesions). Next, there is a period of time for systemic PS (intravenous injection) to be retained preferentially in the cancer cells, or for topical PS to be absorbed by the skin. If the PS is also accumulated in normal tissues during the initial post-administration period, its clearance from those tissues should occur before irradiation.

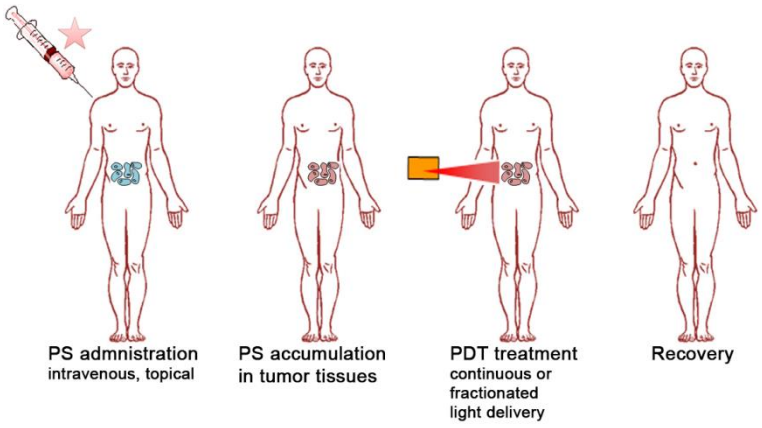

Figure 1.6 The crucial steps in clinical cancer PDT. Adapted from Ref. [5].

The preferential accumulation of the PS in the tumor tissue, compared to certain normal tissues, can be favored by the large tumor interstitial compartment with increased levels of collagen and leaky vasculature, reduced lymphatic drainage and/or higher proliferative rates of cancer cells. The irradiation of the target tissue at early times post-administration can result in tumor vascular effects (preferential for highly vascularized tumors) [111] and PDT treatment at later times post-administration would favor a phototoxic effect at the cancer cellular level

(Figure 1.7) [101]. There is a strong clinical interest in combining different doses of PS and light, as well as different intervals between PS administration and light exposure, in order to promote vascular and selective tumor destruction or even immunomodulatory effects [53]. Fluorescent monitoring and prediction of the outcome of PDT for cancer can be accomplished if a fluorescent PS is used [112]. Unfortunately, the use of fluorescent PSs for both detection of disease and treatment outcome (named theranostics) is underused. The dosages of both PS and light should be adjusted for each treatment [58]. Excellent response rates are obtained when using low PS drug dose and high light fluences (more light photons). On the other hand, combination of high PS dose with high light fluence may eventually lead to normal tissue damage, since normal cells are also able to accumulate PS. The use of high light fluence is normally associated with necrotic pathways, while low light fluence allows for apoptosis, reduced inflammation and immune response.

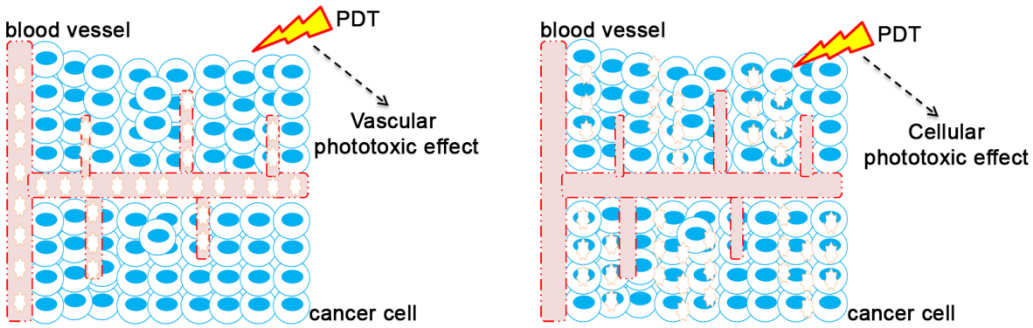

Figure 1.7 Phototoxicity induced in cancer vasculature (left) and cancer cells (right) after PDT.

Currently, several compounds have been identified as PSs, but a few of those have reached an advanced stage and entered human clinical trials or have been approved by the US Food and Drug Administration (FDA). PSs currently on the market for the treatment of cancer are briefly described in Table 1.1. Some PSs have also been clinically approved in specific countries but they are not licensed to be administrated in other ones [53, 54]. There are other PSs such as the methyl ester of ALA (methyl aminolevulinate, MAL, Metvix, or Metvixia) and benzoporphyrin derivative monoacid ring A (Visudyne) used in non-oncologic treatments. Metvix was approved by the FDA in 2004 for treatment of actinic keratosis [113, 114]. Visudyne was approved in 1999 by the FDA for the wet form of age-related macular degeneration in ophthalmology [53].

Table 1.1 Properties of some PSs approved for PDT treatment in oncology.

Compound	Trademark	λ_{max} (nm); ε_{max} (M^{-1} cm^{-1})	Country/	Year approved
Porfirmer sodium	Photofrin	632; 1,170	US	1990s
5-Aminolevulinic acid (ALA)	Levulan	632; 5,000	US	2000
Tetrakis(*m*-hydroxyphenyl) chlorin	Foscan	652; 35,000	Europe	2003
N-Aspartylchlorin e_6 (NPe6; LS-11)	*Laserphyrin*	664; 40,000	Japan	2003
Aluminum phthalocyaninetetrasulfonate (AlPcS4)	*Photosens*	676; 20,000	Russia	2001

1.4.1 Porfimer Sodium (Photofrin)

Photofrin was the first PS to be approved by FDA and to be commercially available, having the most clinical experience [115, 116]. The success of PDT with this PS is dependent on its complex chemical structure composed of a mixture of various oligomers of hematoporphyrin. This PS is clinically approved for the treatment of early and late-stage lung cancers, esophageal cancer, bladder cancer, early stage cervical cancer, and malignant and nonmalignant skin diseases.

Photofrin is a long-acting PS which is retained in the skin for six to eight weeks post-administration which causes photosensitivity in patients receiving PDT. Severe burns can be produced after an unintentional exposure of skin to sunlight or strong artificial light after PDT treatment. The time interval between Photofrin administration and irradiation (50-500 J/cm^2) is usually 48 hours. In addition to being a mixture of porphyrin oligomers, it has low water solubility, reduced selectivity to the cancer cells and low molecular absorption coefficient at 632 nm. Photogem [117] and Photosan-3 [118] are other types of hematoporphyrin derivatives which have been approved for clinical applications in Russia/Brazil and the EU, respectively.

1.4.2 5-Aminolevulinic Acid (ALA, Levulan)

ALA (commercial name Levulan) acts as a prodrug, since it is enzymatically converted to the potent PS protoporphyrin IX *via* the heme biosynthetic pathway [119, 120]. ALA can be administered topically or intravenously and it is the PS of choice in the treatment of superficial lesions in the skin [119, 121] and oral cavity [122]. Additionally, this PS is also used in the

treatment of stomach and oesophageal malignancies and epithelial dysplasia [123]. The advantages of ALA-esters when compared with ALA have allowed the approval of these molecules. ALA-esters contain a lipophilic chain attached to ALA which improves their tissue penetration and diffusion through the stratum corneum. The metabolism of ALA-esters also results in the formation of high intracellular levels of protoporphyrin IX. Hexaminolevulinate is the *n*-hexyl ester of ALA (HAL, commercial name Cysview) ant it was approved by FDA in 2010 for the diagnosis of bladder cancer. HAL is converted into protoporphyrin IX more efficiently than Levulan [124]. The application of HAL for the treatment of cervical intraepithelial neoplasia and genital erosive lichen planus is under clinical trials.

1.4.3 Tetrakis(*m*-hydroxyphenyl)chlorin (Foscan)

Tetrakis(*m*-hydroxyphenyl) chlorin (commercial name Foscan) is a synthetic PS containing a mixture of four atropoisomers. This PS was approved in Europe (2003) for the treatment of neck and scalp cancer, and it was successfully used for the treatment of breast, prostate and pancreatic cancers [125, 126]. Foscan has higher absorption in the red region when compared with Photofrin, which allows a low fluence rate PDT light (10 J/cm^2) protocol. Additionally, the time of treatment with this PS is generally measured in seconds. After administration of Foscan, the patient should stay in a dark room for 24 hours since the PS can cause severe burns. The treatment with this PS is generally performed with the patients under anesthesia, since it is quite painful.

1.4.4 *N*-Aspartylchlorin e_6 (NPe6, Talaporfin, LS-11, Laserphyrin)

N-Aspartylchlorin e_6, NPe6 (commercial name Laserphyrin) is a chemically pure hydrophilic chlorin PS which can be activated with light at 664 nm, and was approved for the treatment of fibrosarcoma, brain, liver and oral cancers. In 2003, Laserphyrin was approved in Japan for the treatment of lung cancer [116]. This PS does not cause the dark toxicity observed with Foscan. Contrary to Photofrin or Foscan, PS administration and light irradiation can be performed on the same day.

1.4.5 Aluminum PhthalocyanineTetrasulfonate (AlPcS4, Photosens)

Aluminum phthalocyaninetetrasulfonate, AlPcS4 (commercial name Photosens), is a specific phthalocyanine derivative which can be activated with light at 676 nm. This PS has been approved in Russia for the treatment of stomach, skin, lip, oral and breast cancers [53]. However, like Photofrin, Photosens produces high skin photosensitivity for several weeks post-administration.

1.5 Cellular steps involved in the efficiency of a photosensitizer

Because of short lifetime and limited migration of $^1O_2$ from the site of its formation, sites of damage are closely related to the localization of the PS…

When a biological system is treated with a PS, a number of steps must take place before the irradiation step. The different biological models used to determine the effectiveness of a PS are described in the next section. In this section the steps occurring from PS administration until induction of phototoxicity are described. The PS must be specifically accumulated in the target tissue, internalized into the cancer cell, accumulated in subcellular compartments and then photo-activated to trigger oxidative stress-induced cell death (Figure 1.8). All of these steps have a great effect on the effectiveness of the therapy. However, predicting them all is a difficult task. In fact, studies have demonstrated that some hydrophilic PSs induce damage in tumor vasculature and block the supply of molecular oxygen and essential nutrients, compromising cancer cells in an indirect way [127-129]. This effect is due to the binding of hydrophilic PSs to serum albumin protein (a protein that mediates PS accumulation in vascular stroma) or to vascular structures/components (*e.g.* collagen). Other studies have demonstrated that hydrophobic PSs have a direct mechanism of action in the cancer cells. These PSs are transported inside the body by association with low density proteins, being targeted and accumulated in cancer intracellular sites [128, 130]. The studies at the *in vivo* biological level are rather complex and quite far from the molecular scale, since the *in vivo* PS intracellular localization is influenced by several factors, namely formation of complexes of systemically

injected PS with blood proteins. The reports available on the *in vivo* subcellular localization and cell death pathway of a certain PS are much more fragmentary than those for *in vitro* studies based on cultured cells. Herein, the steps involved in the efficiency of a PS based on *in vitro* cancer biological considerations at the molecular and cellular levels are discussed.

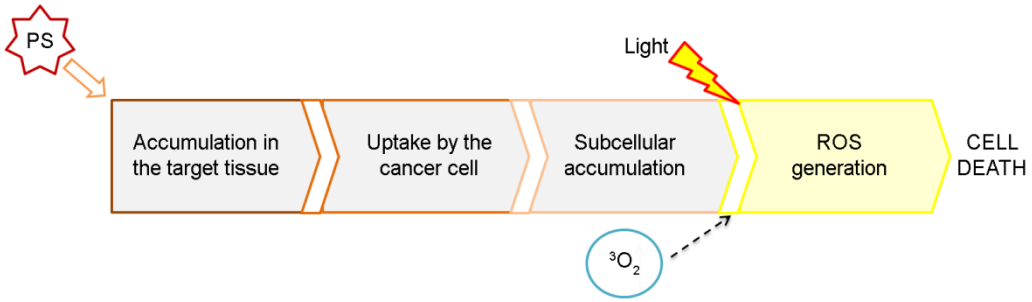

Figure 1.8 Proposed steps that should occur before induction of cell death by PDT.

1.5.1 PSs targeting cancer cells, uptake and subcellular localization

Once the PS targets cancer cells by either a passive or active mechanism [131], it should be accumulated inside these cells. The mechanisms of PSs cellular uptake and subcellular localization are highly dependent on the degree of lipophilicity, type and number of neutral and charged peripheral groups and degree of asymmetry in the molecular structure of the PS [9-11, 132]. The cancer cellular uptake of the PSs can occur by diffusion (few cases) or endocytosis [9, 133]. The intracellular uptake of PSs is also regulated by the ATP-binding cassette transporter ABCG2, which belongs to the family of multi-drug resistant proteins involved in the protection of cells from exogenous and endogenous toxins through the efflux system [13, 134]. The ABCG2 membrane pump mediates the porphyrins efflux from cancer cells, which influence their uptake and further phototoxicity.

Lipophilic compounds (characterized by high *n*-octanol/water partition coefficients) are able to bind and penetrate trough biological membranes [9]. On the other hand, hydrophilic PSs (containing polar or charged side chains) are too polar to cross biological membranes by diffusion and they are usually internalized by endocytosis [133]. The endocytosis of PSs can occur by caveolae and/or clathrin-dependent mechanisms [135, 136]. Unfortunately, scarce

information is available concerning the influence of the endocytic pathways on the uptake, subcellular localization and further phototoxicity of PSs.

The subcellular localization of the PS within subcellular compartments is one of the most important factors in terms of the PDT outcome, even for PSs with preferential localization at the plasma membrane [12, 137]. Cationic PSs have a higher accumulation in the mitochondria than in the cytoplasm due to electrostatic interaction with mitochondria negative electrochemical transmembrane potential [60, 138]. However, cationic PSs are also able to form complexes with nucleic acids which can result on the induction of genotoxicity and mutagenicity after PDT [139]. In fact, none of the cationic PSs have been clinically approved. Non-cationic PSs such as pheophorbide a (a product of chlorophyll degradation) and a diaryl brominated porphyrin were shown to accumulate in the mitochondria [140, 141]. Anionic PSs and compounds containing weak base amines tend to be accumulated in lysosomes after their cancer cellular uptake by endocytosis [142-144]. The simultaneous administration of PSs with different intracellular localization has demonstrated to be a promising strategy to improve PDT efficiency when compared with conventional PDT treatments where a single PS is used [145, 146]. Kessel and Reiners have elegantly shown an enhancement in the photokilling of cells by using the chlorin NPe6 and Verteporfin into separately targeted lysosomes and mitochondria, respectively [146]. Interestingly, the approach was less effective when the sequence of PSs administration was reversed [146]. The PS can also be coupled with specific targeting moieties which allow their accumulation in specific organelles. For example, conjugation of PSs with monoclonal antibodies targeting epidermal growth factor receptors promotes their accumulation in the mitochondria [147]. Zhang *et al*. have developed a PS with specific accumulation in mitochondria by targeting the 18 kDa mitochondrial translocator protein [148]. An intracellular redistribution after light irradiation, has also been demonstrated in the case of PSs, with initial accumulation at membrane-delimited subcellular compartments [149, 150]. Membrane damage induced by ROS after PDT promotes the release of the PS from its initial organelle targets, which can influence the cell death response. Therefore, different irradiation protocols, namely continuous and fractionated irradiation, have been explored.

1.5.2 Mechanisms of cell death

Activation of PSs with light at specific wavelengths (in the absorption spectrum of the photosensitizers) can evoke photochemical reactions with production of ROS, leading to cytodamage by oxidizing and degrading cell components [151]. If cell repair mechanisms fail, damaged cells undergo cell death by apoptosis, necrosis or by autophagy [65, 152-156].

Due to the limited lifetime of ROS generated after PDT, it is envisaged that the subcellular localization of the PS determines the targets of the primary damage. Considerable effort has been expended to design and develop PS that are able to target mitochondria and to identify the key molecular effectors regulating the cross-talk between apoptosis and necrosis/autophagy is an area deserving intense attention in cancer therapy. Due to the polarization and the presence of specific lipids and proteins in the inner and outer membranes of mitochondria, many PSs accumulate in this organelle, either as a consequence of their charge in the case of positively charged molecules, or their hydrophobicity, in the case of negatively charged molecules. The localization is influenced by the prevailing charge on porphyrinoid side chains, in which cationic or anionic characteristics show a tendency for mitochondrial and lysosomal distribution, respectively [157, 158]. It is well-established that PSs localized in mitochondria are able to induce apoptosis very rapidly. However, lysosomal localized PSs can elicit either a necrotic or an apoptotic response. In the plasma membrane, a target for various PSs, apoptosis and necrosis can be initiated. When PSs localize in the endoplasmic reticulum, an autophagic cell death response can be induced [159].

Moreover, most of the evidence of subcellular localization of PS is extrapolated from *in vitro* studies. Due to the existence of numerous cellular targets, it has been difficult to ascertain the key events in PDT-induced cell death. *In vivo* and *in vitro* results may differ because pharmacokinetics or effectiveness of the PS are affected by factors such as lipophilicity, serum binding, clearance [160, 161] and degree of stromal binding [162, 163]. Novel and more sensitive molecular and biochemical assays have provided important insights into cellular events occurring during and after photoactivation. The fact that cancer cells can die after PDT, through a number of different mechanisms [158, 164, 165], is an important hint

in the choice and design of anticancer PDT. Therefore, in order to combat a particular cancer it is important to know the level and mode of cell death.

A. Apoptotic cell death in PDT

Apoptosis is a complex, multi-step, multipathway process of cell death characterized by morphological hallmarks, such as: changes in the surface of plasma membrane, with appearance of blebs and consequent formation of the so-called apoptotic bodies, cell shrinkage, nuclear fragmentation, chromatin condensation and aggregation [165]. Two major apoptotic pathways have been characterized: the death receptor-mediated or extrinsic pathway and the mitochondria-mediated apoptosis or intrinsic pathway [166]. As regards the extrinsic apoptotic pathway, it is activated by death receptors, such as tumor necrosis factor receptor 1 (TNFR1) or Fas/CD95. The intrinsic pathway requires the permeabilization of the outer mitochondrial membrane leading to the release of cytochrome c into the cytosol. After development of the mitochondrial transition pore, released cytochrome c binds apoptosis activating factor-1 (Apaf-1) which, in the presence of dATP, recruits and activates the initiator caspase-9 and the effector caspase cascade. Evidence suggests that in both two pathways occurs the activation of a family intracellular cysteine aspartyl proteases (caspases 8 and 9) leading to activation of executioner caspases, such as caspase-3, -6 and -7 [167, 168], which can then activate other effector molecules to digest cellular contents. In addition, the binding of BH3-only members of the B-cell lymphoma 2 (Bcl-2) family to and inhibiting the action of pro-survival proteins can promote an apoptotic response to PDT. Several studies reported changes in expression of members of Bcl-2 family proteins after PDT in various cancer cell lines and tumors. Kessel and Castelli reported that three different photosensitizers [tin etiopurpurin, 9-capronyloxy-tetrakis-porphyrin and tetrakis(*m*-hydroxyphenyl)chlorin] induced selective photodamage in Bcl-2, without affecting other proapoptotic proteins such as Bax [169]. Xue *et al*. also reported that the anti-apoptotic Bcl-2 decreased in a dose dependent manner after PDT with phthalocyanine 4 (Pc4, a silicon phthalocyanine bearing a dimethylaminopropylsiloxy ligand on the central silicon), indicating that this protein is highly sensitive to PDT and PDT damage to Bcl-2 contributed to its efficient induction of apoptosis [170]. Mfouo-Tynga *et al*. used a zinc phthalocyanine (ZnPcSmix) in PDT to determine the

induced cell death pathways in a breast cancer cell line (MCF-7). ZnPcSmix was found to localize in mitochondria and was efficient at inducing cytodamage after PDT, leading preferentially to apoptosis, as revealed by nuclear fragmentation, oligonucleosomal degradation and increased expression of Bcl-2, DNA fragmentation factor alpha (DFFA1) and caspase 2 (CASP2) genes [171]. Release of cytochrome c from mytochondria has been described to occur in PDT-induced apoptosis. PDT using several PSs (Pc4 and hypericin) resulted in release of cytochrome c to the cytosol [172, 173], with loss of the mitochondrial membrane potential.

B. Necrotic cell death in PDT

Necrosis has been described as a less orderly cell death event than is apoptosis. It is caused by external stimuli to the cell or tissue, such as infection, toxins or trauma [151, 174, 175]. Necrosis is characterized morphologically by cytoplasm swelling, destruction of organelles and loss of cell membrane integrity accompanied by an uncontrolled release of cellular contents into the extracellular space and consequent inflammation [176].

Photodynamic therapy mediated by phthalocyanine- and chlorin-based PSs has shown to induce cell death by necrosis *in vitro* and *in vivo* studies. After photoactivation, liposomal aluminum chloro-phthalocyanine was shown to induce 90% necrotic cell death on oral cancer and tumoral vascular shutdown [177]. A Chl-based photosensititizer, TMMC, was found to accumulate in cytoplasm and nuclear membranes and, after PDT, an evident increase in necrotic cell death, as well as reduction of growth of Eca-109 tumors in nude mice were observed [178].

Two critical factors in determining cellular necrosis following PDT are PS accumulation in cell and conditions of PDT. Nagata *et al*. reported that using an amphiphilic iminochlorin aspartic acid derivative ATX-S10(Na)and human malignant melanoma cells, higher phototoxicity is obtained with higher dye and/or laser doses [179]. Lysosomes were the primary site of ATXS10(Na) accumulation and after PDT, cells showed changes in mitochondrial transmembrane potential. When induced less than 70% cytotoxicity, most of the dead cells were apoptotic. However, when cytotoxicity was higher (99%), most of the dead cells were necrotic. Thus, it is possible that PDT directly damaged lysosomes, leading to

inactivation of enzymes and other factors such as the caspases, executing apoptosis and releasing a large number of proteases into cytosol, thereby inducing necrosis of target cells [179]. Other studies revealed that after irradiation, Zn(II) phthalocyanines (pyridinium Zn(II), tetrasulfonated Zn(II) and tetradiethanolamine Zn(II) phthalocyanines) can undergo relocalization to different organelles within the cell in a charge dependent manner and that the secondary sites are more important in producing cell killing during PDT compared to primary sites of PSs localization [180].

C. Autophagic cell death in PDT

Autophagy is morphologically characterized by large-scale autophagic vacuolization of the cytoplasm. During the process of autophagy, a double-membrane known as an autophagosome surrounds the targeted cytoplasmic constituents, creating a vesicle that separates its content from the rest of the cell. The autophagosome fuses with a lysosome (forming the autophagolysosome) and the contents are degraded and recycled. Autophagy is generally thought as a survival mechanism when cells are exposed to stress. However, in some cases, it appears to promote cell death. Autophagic cell death is a process that is associated with autophagosomes and autolysosomes [181]. Many autophagy-related genes (*Atg*) and proteins that have been identified in autophagosomal assemblage and molecular degradation [151]are damaged by PDT induced ROS [182, 183]. PDT with phthalocyanines that localize in the endoplasmic reticulum and mitochondria affects mammalian target of rapamycin (mTor; a cell growth regulator that takes part in the autophagic signaling pathway) and Beclin-1 (a pro-autophagic protein) function [184].

Depending on the oxidative damage, PDT may induce autophagy [185] that can work as cytoprotective or cell death mechanism [158, 186]. Although autophagy and apoptosis may occur independently, it is possible that there exist molecular switches between these two cell death pathways. In agreement with this hypothesis, there is a study showing that PDT with a porphycene PS in mouse leukemia L1210 cells induces a rapid wave of autophagy, presumed to represent the recycling of some damaged organelles, followed by apoptosis [187]. Attempts at extensive recycling of damaged organelles by autophagy seem to be associated with apoptosis. However, PDT efficacy is not affected when cancer cells cannot undergo apoptosis

through Bax knockdown with shRNA or pharmacological inactivation of Bcl-2 function. Loss of cell viability was associated with a highly-vacuolated morphology consistent with autophagic cell death [187].

1.6 Biological models used to determine the efficiency of a photosensitizer

The most suitable in vitro and in vivo biological models should be used to evaluate the PDT efficacy of a new PS.

1.6.1 *In vitro* models

In vitro models, including conventional two-dimensional monolayer cell culture systems, have been extensively used to determine the efficacy of a PS [77, 188, 189]. However, monolayer cultures are too simple to replicate the several heterogeneous treatment effects found *in vivo*. Three-dimensional spheroid cultures characterized by cells in suspension growing in clumps have advantages when compared with monolayer cultures, since they mimic cell-cell and cell-matrix interactions (Figure 1.9) [190]. However, studies with spheroids are less easy to perform and not all cell lines are able to aggregate and form spheroids. When compared with *in vivo* biological models, these cultures do not mimic vascularization and tumor heterogeneity [191]. Nevertheless, properties found in tumors such as oxygen, pH and nutrient gradients are present in spheroids. As PDT is an oxygen-dependent therapy, the oxygen gradients found in spheroids (a decrease in oxygen partial pressure from the periphery towards the center of spheroid) make them an interesting approach for research in the field of PDT.

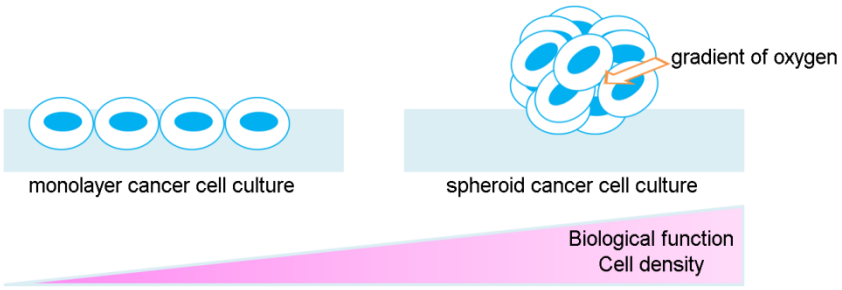

Figure 1.9 Monolayer and spheroid cancer cell cultures *in vitro* biological models for cancer PDT studies.

Bigelow *et al*. have demonstrated that in spheroids, the well-oxygenated cells in the outer layer are more sensitive to PDT than cells in the inner layers [192]. Interestingly, the surviving cells are able to form a new generation of spheroids with high sensitivity to repeated PDT. Yang *et al*. have developed an *in vitro* three-dimensional model in a microfluid culture system with human breast cancer cells and primary adipose-derived stromal cells to mimic tumor heterogeneity [193]. In addition, the system allowed real-time imaging of tissue development, light penetration for PDT and dynamic flow of the medium and PS.

1.6.2 *In vivo* models

The choice of the most appropriate *in vivo* biological model for PDT studies requires knowledge about its biological features. Before evaluating anticancer efficacy of a new PS using *in vivo* models, the properties of the PS should be assayed *in vitro*. Additionally, the pharmacological properties of the PS can be determined *a priori* by administration of the PS (through different routes) to non-tumor bearing mice. In addition, the photodynamic efficacy of a certain PS can be determined using *in vivo* models such as chorioallantoic membrane (CAM) [194, 195], subcutaneous syngeneic mouse and rat tumors [129, 196, 197], human xenograft tumors [112],orthotopic syngeneic mouse and rat tumors and orthotopic xenografts [198, 199], autochthonous tumors [200-203], and genetically-engineered mouse models (Figure 1.10) [204, 205].

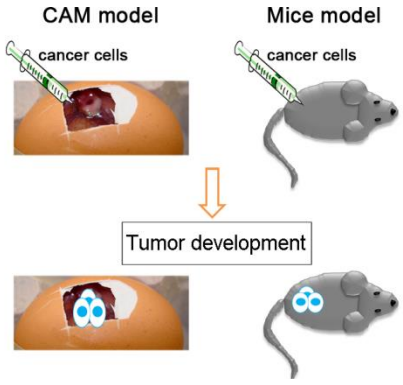

Figure 1.10 Chorioallantoic membrane (CAM) and mice *in vivo* biological models for cancer PDT studies.

The CAM model is based on a fertilized chicken egg in which CAM is exposed by cutting a window through the eggshell. A suspension of cancer cells can be applied onto the surface of the membrane and under specific conditions they are able to turn into "tumors" developing their own blood supply by angiogenesis. The process of angiogenesis in this model occurs in a similar fashion to real tumors in mice, making it a suitable approach for the study of vascular damage in cancer with PDT [194, 195]. The PS can be administered into the blood vessels or it can be topically applied to the xenografted tumors on the CAM and then tumors can easily be irradiated with light. This model allows *in vivo* real-time microscopy to follow changes on blood flow in normal and tumor vessels.

The most common *in vivo* approach used in PDT experiments is based on subcutaneous tumors in laboratory mice. The syngeneic mouse tumor approach is often used because the mice have intact immune systems, allowing the study of the effect of PDT on the anti-tumor immune response. There are several mouse tumor cell lines available for the induction of subcutaneous syngeneic models which differ in the type of tissue or organ that originated the tumor and also on the syngeneic inbred mouse strain that the tumors belong to. In addition to murine tumor cell lines, there are also rat tumor cell lines, but they are less common. In some situations, the cells can be injected with an extracellular matrix, named Matrigel. Nevertheless, it is necessary to point out that the use of Matrigel alters the response of the developed tumors to PDT [129]. The administration of PS in subcutaneous mouse tumors is normally performed intravenously in the tail vein. The injection of PS into the abdominal cavity (intraperitoneal) [196] or directly into the tumor (intratumoral) [197] is less frequent. After PDT, a circumscribed black eschar can be observed if tissue response to damage elicits a cancer vascular response. When PDT effects are induced at the cancer cellular level, tumor volume shrinkage is generally observed. The use of syngeneic mouse models on the photodynamic evaluation of new PSs is limited by the number of available tumor types and the rapid growth of the tumor. Additionally, PSs action can have different features in murine tumors when compared to those derived from humans.

Human xenograft tumors can be obtained by engraftment of human tumor cells into athymic nude mice or into severe combined immunodeficient mice that are T- and B-cell deficient. The mechanism of action of a certain PS in this model is more closed to solid human

tumors, when compared with subcutaneous syngeneic mouse and rat tumors. In the human xenograft tumor model, several tumor types are available, since patient explants and cell-line derived models have been reported for all major histological samples of tumors. Additionally, therapeutic or genetic manipulation can be performed *ex vivo* on cells before xenotransplantation. For example, mouse xenograft models bearing luciferase-expressing cancer cells have been established to monitor PDT efficacy with non-invasive bioluminescence imaging [206]. Several human cancer cell lines grown as xenograft tumors in a subcutaneous location, in either nude or severe combined immunodeficient mice, have been subjected to PDT [207, 208]. The disadvantages associated with this model are the facts that blood supply and neovascularization are provided by the host mice and the tumors are developed in murine stroma in an artificial tissue compartment (subcutaneous site).

Considering the disadvantages of human xenograft tumors, orthotopic models have been developed by injecting the cancer cells into the tissue of the organ of origin. The blood vessels developed to supply the tumor and the propensity to spontaneously metastasize are very different in orthotopic models [198, 199]. Chen *et al*. have compared the PDT efficacy of Verteporfin in orthotopic (in the prostate) and subcutaneous tumor models [199]. They showed that the uptake of the PS is highly different in the two models. The uptake was higher in the orthotopic model than in the subcutaneous one at 15 minutes post-injection, and it became similar in the two models at 3 hours after administration. Light irradiation performed 15 minutes after PS injection led to similar cancer vascular phototoxicity in the two models. When PDT was performed at 3 hours after injection of Verteporfin, there was induction of necrosis which was higher in the orthotopic when compared with subcutaneous model. A disadvantage of orthotopic models is the need for a surgical procedure in some organs, which can be technically difficult. Additionally, it is necessary to have a suitable light source to perform PDT in specific organs.

Autochthonous tumors have been developed in laboratory for PDT studies by using specific chemical carcinogens, viruses and physical carcinogenic stimuli (*e.g.* UV radiation) [200-203]. These models include mice, rats and hamsters treated topically, intraperitoneally or orally with polycyclic aromatic hydrocarbons or reactive organic chemicals alone or in combination with known tumor promoters.

Genetically-engineered mouse models of cancer have been constructed to more closely mimic the development of human disease and have also been used in PDT studies [204, 205]. These models include transgenic, knockout, and knocking mouse models [209] and, in some of them, an additional application of a carcinogen needs to be used to initiate tumor development.

1.7 Molecular targeted photosensitizers

PSs are the key element in PDT. None of the existing PS can be seen as an ideal one.

A selective phototoxicity is highly dependent on the specific accumulation of the PS in the target tissue if compared to normal cells. The majority of the PSs have low selectivity to the tumor tissue, with ratios of 2-5:1 in tumors *vs.* normal tissues, resulting in undesired phototoxic side effects [210]. In order to achieve maximum concentration of the PS in the cancer cells, it can be conjugated with a biomolecule with selectivity for structural features overexpressed in cancer cells [211]. Additionally, it is important to define the most appropriate time interval between the administration of the PS and the start of light irradiation, so that the concentration ratio between tumor and normal tissues is maximized [60]. The fluorescent properties of the PSs can be used to monitor its accumulation in the tumor [210].

PSs have been conjugated with sugars [14, 15, 41, 76, 78, 212, 213], serum albumins [189, 214], low density lipoproteins [215, 216] and epidermal growth factor [131, 217], since tumors exhibit higher glycolysis rates, higher serum albumin turnover, and overexpress low density lipoproteins and epidermal growth factor receptors when compared to normal cells. In addition, PSs have been also conjugated with antibodies, antibody fragments, peptide ligands, proteins and non-protein ligands (*e.g.* folic acid) [189, 218-222]. Another strategy is PSs with pH-dependent distributions, which induce high photodynamic activity in response to acidic pH of cancer cells [77, 223]. As glutathione levels are higher in cancer cells than in normal cells, glutathione-activated PSs have been also proposed [224].

1.7.1 Galactose binding proteins as targets of galactose-conjugated photosensitizers

Lectins are proteins able to bind carbohydrates attached to proteins and lipids (glycoconjugates) present on cell surface and extracellular matrix. Amongst lectins, galectins (Figure 1.11) are well-known by their ability to recognize β-galactose as well as by their consensus amino-acid sequences [225]. Therefore, the biocompatibility of galactose and their specific recognition by galectins have led to the development of promising galactose-conjugated porphyrinoids as potential molecular targeted PSs [14, 15, 226].

Galectins are small soluble proteins (molecular weight 14-35 kDa) with carbohydrate-recognition domains (CRDs), which are responsible for the specific and individual binding of each galectin to carbohydrates [227]. To date, 15 galectins have been identified in mammals. Galectins are divided into three main family members, prototypical galectins, tandem-repeat-type galectins and chimaera-type galectin-3 (Figure 1.11) [228]. Prototypical galectins have one CRD (galectin-1, -2, -5, -7, -10, -11, -13, -14 and -15), tandem-repeat-type galectins contain two homologous CRDs in a single polypeptide chain connected by a linker (galectin-4, -6, -8, -9 and -12), and galectin-3 has a non lectin *N*-terminal region (composed of unusual tandem repeats of proline- and glycine-rich short stretches) connected to a CRD.

Considering the carbohydrate-binding activities of galectins, they can be bivalent or multivalent. Prototypical galectins (one-CRD) exist as monomers (galectin-5, -7 and -10) or homodimers (galectin-1, -2, -11, -13, -14 and -15), tandem-repeat-type galectins (two-CRD) are inherently bivalent (contain two distinct CRDs in tandem connected by a linker). Therefore, the binding of galectins with multivalent carbohydrates results on the formation of ordered arrays (galectin-glycan lattices) [229, 230].

Galectins exhibit dual localization, being found in both the intracellular (nucleus and cytoplasm) and the extracellular (cell surface and medium) compartments [228]. Intracellularly, galectins are involved in fundamental processes [231] such as pre-mRNA (precursor messenger ribonucleic acid) splicing and the regulation of intracellular signalling pathways (*e.g.* mitosis, apoptosis and cell-cycle progression) after binding intracellular ligands (Figure 1.12).

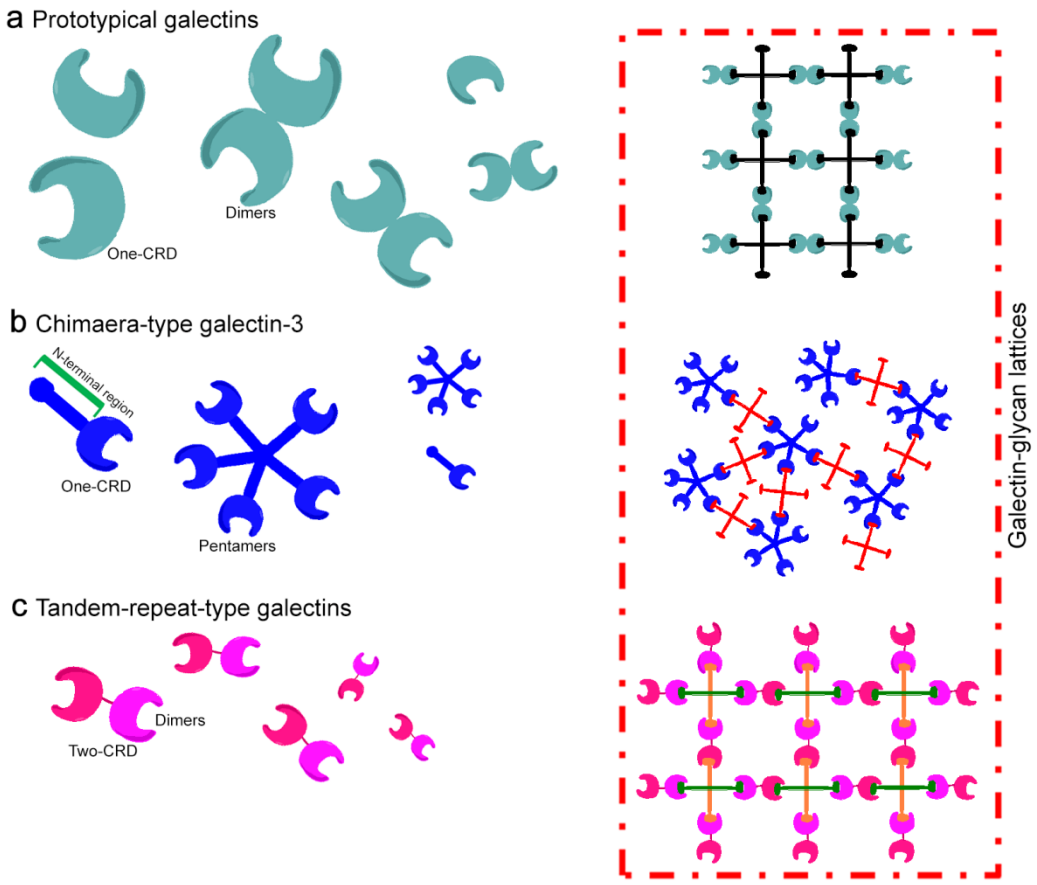

Figure 1.11 Three main family members of galectin (a: prototypical galectins, b: chimaera-type galectin-3 and c: tandem-repeat-type galectins) and the lattices formed by galectins after binding multivalent glycoconjugates. CRD = Carbohydrate recognition domain. Adapted from Ref. [228].

Interestingly, these proteins do not have a classical signal sequence, which is necessary for protein secretion through the classical secretory pathway (endoplasmic reticulum/Golgi pathway). Nevertheless, under specific conditions, they are secreted by the cells (involving an unusual mechanism of externalization) and these galectins can exert functions outside cells [228, 232, 233]. Extracellularly, the function of galectins includes the binding to carbohydrates on and around cells, and carbohydrate-mediated endocytosis (in a carbohydrate-dependent manner). Additionally, galectins are also involved in cell-cell adhesion and cell-matrix-adhesion biological processes.

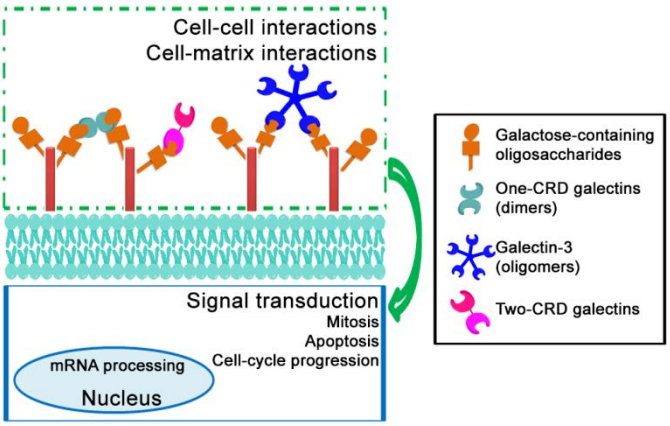

Figure 1.12 The biological functions of galectins outside cells (interaction with cell-surface glycoconjugates, cell-cell and cell-matrix interaction) and inside cells (intracellular functions in regulating metabolism). Adapted from Ref. [228].

Some galectins are widely distributed in different tissues, while others exhibit high tissue-specific patterns of distribution. The expression of galectins is modulated during the development of tissues and organisms and it is altered under several pathological and physiological conditions [234]. Of particular interest is the altered expression of galectins in cancer cells when compared with their normal counterparts [235-238]. Studies have indicated that altered expression of galectins is correlated with the progression and aggressiveness of the tumor, implying the influence of these proteins during tumor development [239].

Depending on the cell type, cell differentiation state, cell metastatic potential, cell oncogene expression, and cell anatomical growth site [240], the expression of galectins can be upregulated or downregulated in cancer cells. The expression of galectin-1 and galectin-3 is heightened in several tumors including melanomas, astrocytomas, bladder, osteosarcoma and ovarian tumors and their expression is normally correlated with the aggressiveness of the disease and the metastatic potential [238, 241, 242]. Additionally, these galectins have important roles in tumor progression [17, 243]. In the fight against cancer using PDT, both galectin-1 and galectin-3 are interesting molecular targets for the development on new PSs.

Galectin-1 was the first protein discovered in the family of galectins and it is classified as S-type lectin [244, 245], since it requires reducing conditions to maintain its activities (S stands for sulphydryl or thiol). The crystal structure of this protein is composed by a six-

stranded and a five-stranded β-sheet in an antiparallel arrangement [246]. In solution, galectin-1 is able to form homodimers and there is evidence for the extracellular and intracellular presence of this protein [228, 231, 233]. The overexpression of galectin-1 has been described for several tumor types [247] and it has been associated with low prognosis and high metastatic potential [238]. The galectin-1 expressed by cancer cells is involved in tumor growth, tumor progression and metastasis, as a result of its participation in a variety of biological processes. Galectin protein regulates cell migration, cell adhesion and angiogenesis, and suppresses the anti-tumor immune response [238, 248]. The protein galectin-1 is also an interesting target for anti-angiogenic therapy [249, 250] due to its overexpression on tumor vasculature.

Galectin-3 is a 31 kDa protein and it is the only member of the galectin family with an extended *N*-terminal region containing a tandem repeats of short amino-acid segments connected to a C-terminal CRD. The crystal structure of this protein is similar to the galectin-1 [251]. Unlike galectin-1, galectin-3 can exist in monomeric form in solution [252]. Besides being a cytosolic protein, galectin-3 is able to cross the intracellular and plasma membranes to reach the nucleus [253] and mitochondria or to get externalized. Galectin-3 is overexpressed in a variety of human cancer cells and the expression level correlates with the stage of tumor progression, invasiveness and metastatic potential [238].

1.7.2 Conjugation of Porphyrins, Chlorins and Phthalocyanines with galactose and dendritic units of galactose

The conjugation of galactose targeting moieties with a porphyrinoid is a valuable way to achieve a high local concentration of PSs in tumor tissues, due to the overexpression of galactose-binding proteins (*i.e.* galectin-1 and galectin-3) in cancer tissues [254]. Another advantage of galactose-conjugation is the possibility of tuning the PS macrocycle amphiphilicity [255]. The exact interaction mechanism of galactose-PS conjugates with cancer cells is still unknown. However, it is expected that the specific (non-covalent) binding of carbohydrates with galectins [19, 24, 254, 256] increases the accumulation of the conjugate around cancer cells. As PSs conjugated with carbohydrates are too large to be accumulated

inside cancer cells by sugar transporters, it is envisaged that their uptake is mediated by diffusion or endocytosis.

Amongst galactosylated porphyrinoid derivatives, *meso*-substitued aryl porphyrins (Figure 1.13) have received great attention. Most of these *meso*-substituted porphyrins have symmetrical phenyl groups at the *meso*-positions (*i.e.* position-5, 10, 15 and 20) of the macrocycle. In these porphyrins, the carbohydrate substituents have been introduced at *ortho*-, *meta*- or *para*-positions of the phenyl groups. The *meso*-substituted galactosylated porphyrins are mainly obtained by total synthesis strategies (starting from pyrroles) and using procedures already described for porphyrin conjugated with glucose units. In this context, the protected or unprotected sugar can be used in the synthesis of *meso*-galactose-conjugated PSs. The use of protected sugars enhances the reproducibility of the reaction yields and it is helpful in the isolation and characterization of the products by chromatography and nuclear magnetic resonance (NMR) spectroscopy, respectively. In general, deprotection can be easily and selectively achieved by removing the protecting groups in the presence of other functional groups, leading to the desired galactose-porphyrins with the sugar moiety bearing free hydroxyl groups [76].

Most biological studies using galactose-conjugated PSs involve conjugates containing unprotected sugars to allow sugar interaction with CRD present at galactose-binding proteins. Nevertheless Vedachalam *et al*. have reported that conjugates containing galactose residues protected by isopropylidene groups have improved metabolic stability and facilitated cancer cells internalization [20]. It was suggested that the isopropylidene groups in these conjugates are cleaved in the acidic medium within cancer cells, being accumulated intracellularly in the lysosomes of cancer cells and able to induce caspase-dependent apoptotic pathway after PDT. The ability of porphyrin conjugated with protected galactose moieties to enter cancer cells was not observed by Chen *et al*. in studies with acetal-protected porphyrin conjugates [212].

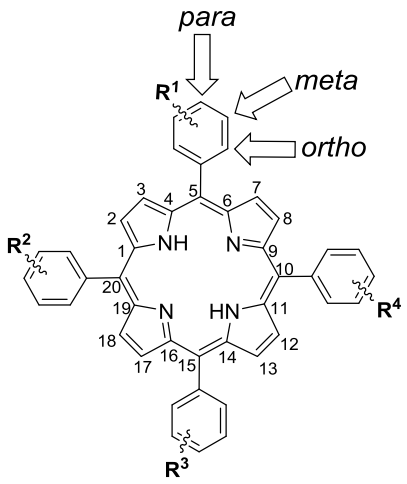

Figure 1.13 Chemical structure of *meso*-substituted aryl porphyrins.

Additionally, Mori *et al*. reported that acetal-protected galactose-conjugated Pc induced dark toxicity in human fibrosarcoma cells [257]. In some cases, deprotection of galactose sugar is not enough to achieve solubility in aqueous solution and *in vitro* studies are performed with the compounds prepared in liposomal suspensions [27]. Gomes *et al*. have reported that liposomal suspensions of Chl conjugated with one glucose or fructose molecule have no cancer cell selectivity, exhibiting phototoxicity in both cervical cancer cells and keratinocytes [27]. In spite of the similar intracellular distribution pattern of liposomal suspensions of galactose-Chl conjugate in both cancer and non-cancerous cell lines, the conjugate was able to induce selective phototoxicity in cancer cells. Choi *et al*. have also reported difficulties on the removal of the isopropylidene protecting groups of Pcs conjugated with galactose molecules [29]. Therefore, *in vitro* assays in colon adenocarcinoma cells were performed using conjugates in Cremophor EL emulsions. Lee *et al.* have also reported the use of Cremophor EL emulsions to perform *in vitro* studies in human hepatocellular carcinoma cells with Pcs containing one or two acetal-protected galactose substituent(s) [25].

Laville *et al*. have described the synthesis of galactosylated porphyrins containing diethylene glycol as linker [132]. *In vitro* studies in human retinoblastoma cells Y79 (a cell line containing β-galactose receptors) [258] demonstrated that lipophilic galactose-porphyrins have low accumulation inside cancer cells. In contrast, amphiphilic galactosylated porphyrins have high uptake. Additional studies in a melanoma cell line (B16) overexpressing β-galactose

receptors and in an adenocarcinoma colon cell line (HT29), which do not express these receptors in high levels, demonstrated that the uptake of galactose-conjugated porphyrins was independent on the cell line. Nevertheless, a decrease on the uptake of the compounds was detected when the cells were pre-incubated with glucose or glycosylated albumin suggesting that glucose-binding receptors can also contribute for the uptake of the galactosylated porphyrins. In fact, other studies have demonstrated that depending on the cell line, the uptake of a galactodendritic Pc is dependent on both galactose-binding protein (galectin-1) and GLUT1 [41]. The involvement of glucose-binding receptors on the uptake of galactose-PSs can be explained by the fact that galactose is a C4 epimer of glucose and the hydroxyl groups in C1, C3 and C4 positions of galactose are involved in hydrogen bonds with GLUT1 [259].

Most studies with galactose-PSs are related to their synthesis and photobiological properties (uptake, toxicity in darkness and after PDT). Only a few studies have been performed to assess the interaction of galactose-PSs with galactose-binding proteins. Li *et al*. have studied the ability of benzochlorin-galactose conjugates to bind galectin-1 protein [24]. Enzyme-linked immunosorbent assays (ELISA) have indicated that benzochlorin-galactose exhibits higher ability to bind galectin-1 when compared with benzochlorin-glucose conjugate or the non-conjugated benzochlorin. The interaction of the non-conjugated benzochlorin with galectin-1 was explained by hydrophobic interactions between the well-conserved hydrophobic core of the protein [260] and the porphyrinoid macrocycle. In fact, D´Auria *et al*. have demonstrated by spectrometric assays that non-galactose-conjugated porphyrinoids are able to bind galectin-1 protein [256]. Additionally, molecular modeling studies have demonstrated that the Chl macrocycle does not interfere in the binding of galactose with the galactose binding site of galectin-1, since it is far from this site in the protein [19].

Another interesting characteristic of galactose-PSs is that they prevent the efflux of the PS by the ABCG2 membrane pump [261]. Zheng *et al*. have tested the *in vitro* efficacy of galactose-PSs using murine radiation-induced fibrosarcoma and colon carcinoma cell lines, which express both galectin-1 and galectin-3 in similar levels and ABCG2 in different levels [261]. The uptake of non-conjugated PS was low in murine radiation-induced fibrosarcoma cells containing high levels of ABCG2, suggesting that the non-conjugated PS is a substrate for the ABCG2 transporter [23, 261]. On the other hand, the galactose-conjugated PS was not

a substrate for ABCG2 transporter and its accumulation in cancer cells was not affected by the tyrosine kinase inhibitor imatinib mesylate (an inhibitor of the ATP-dependent transport of ABCG2) [23, 261]. Additionally, the conjugation of porphyrinoid with galactose also changed its localization from mitochondria to lysosomes [261]. *In vivo* studies revealed that in spite of the lower uptake of galactose-conjugated PS in tumors when compared with non-conjugated PS, the conjugate exhibited high photodynamic efficacy in the tumors. The reduced accumulation of the galactose-PS in the tumors was due to its predominant localization in the liver, probably due to clearance through galactose receptor system on hepatic cells. The ability of galactose-conjugated PSs to be accumulated in the liver has prompted their use as *in vivo* probes for diagnosis of liver cancer [22].

The uptake of galactose-PSs inside cancer cells is dependent not only on the presence of galactose-binding proteins on the cells, but also on the balance between hydrophobicity and hydrophylicity [18, 21, 26, 28]. Hao *et al*. have demonstrated that a hydrophobic galactose-tetrabenzoporphyrin has higher accumulation in carcinoma HEp2 cells than the corresponding galactose-tetraphenylporphyrin [26]. In addition, an increase in the number of galactose molecules conjugated with tetraphenylporphyrin led to a decrease on the uptake and different subcellular localization. The most hydrophobic porphyrin (tetraphenylporphyrin conjugated with one molecule of galactose) was accumulated mainly on the endoplasmatic reticulum and endosomes, while a porphyrin conjugated with four molecules of galactose was found in the lysosomes. The authors did not report the ability of the galactose-porphyrins to induce phototoxicity upon light irradiation. Nevertheless, it is envisaged that the different subcellular localization of the compounds will influence the phototoxicity [33, 132]. The role of hydrophobicity on the uptake of galactose-conjugates was not observed by Fujimoto *et al*[28]. In these studies, the amide-linked octa(galactose) derivative of tetraphenylporphyrin exhibited higher specificity for liver cancer cells (containing receptors for galactose residues) when compared with the corresponding octa(glucose) conjugate. It was envisaged that these hydrophilic PSs have remarkable saccharide specificity which masked the non-specific hydrophobic interactions of the PS core with cancer cells. Hirohara *et al*. have demonstrated that the insertion of zinc in the core of porphyrin macrocycle and the position of sugar conjugation affects the uptake of galactose-conjugated porphyrins, by altering the shape of the

conjugates in water [33]. The *meta*-substituted free base galactose-porphyrin showed lower uptake when compared with *para*-substituted free base compound and higher uptake than the corresponding zinc compound. Interestingly, deprotection of *para*-substituted zinc compound led to the precipitation of the conjugate in cancer cells.

The specificity of galactose-conjugated PSs for cancer cells has been studied by *in vitro* studies: (1) compare the efficiency of the conjugates with the correspondent non-conjugated PS, commercially available PS and other glycoconjugated PSs [21, 28, 31, 33-35, 38, 41, 132, 212]; (2) using both cancer and non-cancerous cell lines [27] and (3) were performed in cell lines containing high and low levels of galactose-binding proteins [41, 132, 261]. Additionally, the efficiency of the galactose-conjugates has been validated using *in vivo* biological models [35, 261-263]. Overall, galactose-conjugation improves the selectivity and photo-efficacy of the PS. It should be pointed out that *in vitro* efficacy of galactose-conjugated PSs is not always correlated with *in vivo* efficacy [35].

The galactose sugar has been covalently conjugated with porphyrinoids *via N*-, *S*-, *C*- and *O*- galactosylation (Figure 1.14) [14, 21, 28, 30, 36, 39, 132]. Carbon-carbon bonds are expected to be chemically and metabolically robust and they retain the angles and conformations found in the *O*-glycoside linkage [30]. Nevertheless, *C*-galactosylated compounds have not been studied for cancer PDT. *O*- and *S*-galactose-conjugated porphyrinoids have been compared in terms of enzymatic hydrolysis of the glycoside bond by glycosidases, metabolism upon incubation with cancer cells and solubility in water [21, 36, 132]. Mass spectrometry studies of cancer cellular extracts have indicated that *O*-galactose-conjugated porphyrins undergo metabolic degradation, probably due to the ability of endogenous glycosidases to cleave the glycoside bonds [132]. In addition to metabolic stability, anomerically tetragalactosylated *S*-galactose Pc exhibits higher water solubility when compared with *O*-galactose conjugate [36]. These differences in water solubility were not observed for the corresponding octagalactosylated conjugates, and these compounds exhibited higher water solubility when compared with the tetragalactosylated conjugates [36]. Interestingly, Iqbal *et al*. have reported that replacement of the oxygen with sulfur in the non-peripherally tetra-galactose-conjugated Pc resulted in a red shift in the absorption spectra of the conjugate [39]. The linker/spacer separating the sugar from the porphyrinoid macrocycle

has also a key role in photodynamic efficiency of galactose-conjugated porphyrinoid [40, 42, 76, 132]. Lafont *et al*. have compared the photodynamic efficiency of galactose-conjugated Pcs obtained by the classical galactosylation grafting or by click conjugation [40]. Interestingly, the triazole linkage formed by click conjugation had a negative effect on the uptake and further phototoxicity of the compounds in HT-29 human colon adenocarcinoma cells.

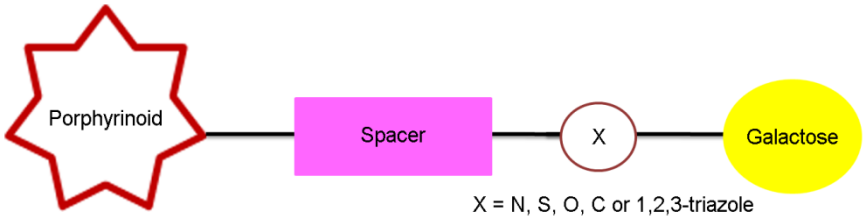

Figure 1.14 Representation of galactose-conjugated porphyrinoids. Adapted from Ref. 12.

The solubility of galactose-conjugated porphyrinoids has demonstrated to be higher than the corresponding non-conjugated PS [19]. Additionally, the solubility of the conjugates in aqueous solutions is highly dependent on the number, position and nature of the sugar substituents [36, 264]. Tetra-α-galactose substituted Pc exhibits less aggregation than tetra-α-glucose substituted Pc[36]. Additionally, octagalactosylated Pc containing galactose anomerically attached to the Pc ring in the β-position has a lower water solubility than Pc conjugated with eight galactose molecules through the carbon-6 of the sugar. Contrary to the results reported by Lyubimtsev *et al*. describing the different lipophilicity of gluco- and galactose-conjugates [36], Zheng *et al*. have reported that porphyrinoid conjugated with galactose or glucose moieties have similar lipophilicity [261]. Mori *et al*. have described that fluorine atoms on galactose-Pcs have a key role on phototoxicity, since these groups contribute to the amphiphilic character of the conjugate [257]. Fluorescence microscopy studies have demonstrated that the uptake of tetra-beta galactose-conjugated Pc (formulated with Cremophor EL) is negligible in adenocarcinoma cells due to their aggregation in the culture media [29]. On the other hand, tetra-alpha galactose-conjugated Pc and the mono-substituted conjugate demonstrated high fluorescence in the cytoplasm of cancer cells. The intracellular fluorescence intensity was higher for mono-conjugated than that for tetra-conjugated Pc. The differences in the uptake were correlated with different photoxicity of the

compounds and they were in accordance with other studies reporting the higher efficiency of unsymmetrical tetrapyrrolic PSs when compared with symmetrical analogues [32, 132]. Lv *et al*. have suggested that the *in vitro* reduced water solubility of galactose-conjugated Pcs did not limit their application as fluorescent markers *in vivo*[22], due to the disaggregation phenomenon of glycosylated PSs by the organs or tissues.

The conjugation of PSs with galactose molecules alters not only solubility and specificity of PS for cancer cells, but it also influences the fluorescence emission spectra of the conjugates [22]. The conjugation of zinc Pcs with galactose molecules induced red shifts on the emission spectra, which were dependent on the number of galactose substituents attached to the PS macrocycle.

It is envisaged that PSs containing dendritic units of galactose [76] have even higher water solubility and ability to interact with galactose binding proteins [18, 265], since these units would benefit from the ability of galectins to establish multivalent interactions with dendritic units of the sugar. Therefore, it is expected that a porphyrinoid conjugated with dendritic units of galactose will bind to a higher number of galactose-binding proteins overexpressed in cancer cells, when compared with the corresponding porphyrinoid conjugated with monomers of galactose (Figure 1.15). Such an enhancement in the binding of a conjugate with galactose-binding proteins will increase the amount of the porphyrinoid around the cancer cell. Pereira *et al*. have described that a Pc conjugated with eight dendritic units of galactose have an improved water solubility, a greater efficiency in the generation of $^1O_2$ as well as high accumulation and larger phototoxicity in bladder cancer cells overexpressing galactose-binding proteins [41]. Additionally, it was demonstrated that the uptake and phototoxicity of the conjugate was reduced after knockdown of these proteins *via* small interfering RNA (siRNA).

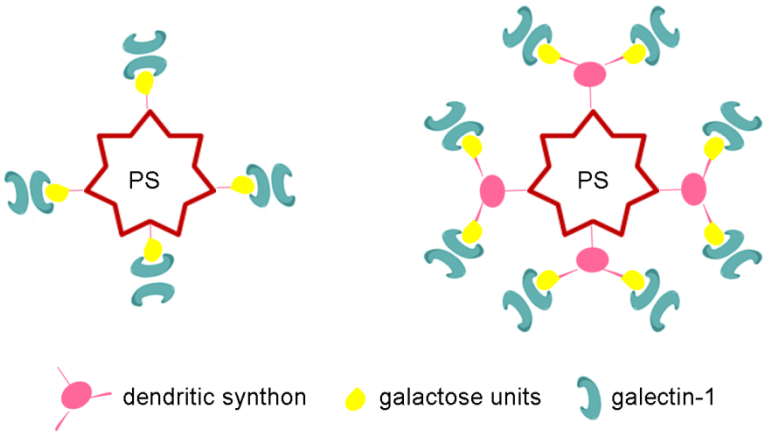

Figure 1.15 Representation of a PS conjugated with monomers of galactose (left) and dendritic units of galactose (right) and their possible interaction with the galactose-binding protein (galectin-1).

1.8 Hypothesis and thesis structure

PSs conjugated with galactose sugar have potential for the treatment of cancer by PDT. Cancer cells overexpress galectin-1, a galactose-binding protein that promotes the uptake of a galactose-PS. We hypothesize that galactodendritic-PSs (Chapter II) will have increased uptake by cancer cells. Dendritic units of galactose sugar will improve the uptake and further phototoxicity of a porphyrinoid (Chapters III-VI), due to their multivalent binding with galectin-1 protein in the surface of cancer cells. GLUT1 protein, a well-known glucose transporter overexpressed in cancer cells, can also have a role in the uptake of galactodendritic-PSs (Chapter III). Monolayers (Chapters III-VI) and spheroids (Chapter VII) of cancer cells containing different levels of GLUT1 and galectin-1 proteins are suitable *in vitro* biological models for studying phototoxicity of a galactose-PS, before *in vivo* validation (Chapters V and VI).

We hypothesize that after accumulation of a galactodendritic-PS around cancer cell membranes, its internalization occurs through endocytic mechanisms (Chapter IV). The knowledge about the endocytic mechanisms by which a galactose-PS is accumulated inside cancer cells can help in the design of more effective PSs. Additionally, the resistance of cancer cells to PDT can be overcome by interfering with PS endocytic pathway (Chapter IV).

The activation of an antioxidant response (Chapter III) or alterations in the cytoskeleton (Chapter V) after PDT, as well as the subcellular localization of PS before light irradiation (Chapter VI) can influence the phototoxicity of a galactodendritic-PS. We hypothesize that a repeated dose of light irradiation can decrease the resistance of cancer cells to PDT (Chapter VI).

The high affinity of compounds conjugated with galactose through carbon-3 to galectin-1 has been reported, however, this strategy has not been explored in the attachment of galactose to a porphyrinoid. We hypothesize that a porphyrin conjugated with galactose through carbon-3 will have increased uptake by cancer cells (Chapters II and VII).

1.9 Aims of the study

The objectives of this thesis were:

1. To synthesize new porphyrinoids with increased affinity for galactose-binding proteins overexpressed in cancer cells:

1.1 conjugate a porphyrin, phthalocyanine and chlorin with dendritic units of galactose;

1.2 conjugate a porphyrin with galactose through carbon-3.

2. To demonstrate the photodynamic efficacy of a new galactose-PS:

3.1 use cancer cells growing as monolayers and spheroids and containing different levels of galactose-binding proteins;

3.2 use *in vivo* biological models.

3. To improve the phototoxicity of a new galactose-PS in cancer cells resistant to therapy:

2.1 interfere with the endocytic pathway by which the PS is accumulated inside cancer cells;

2.2 use a repeated PDT protocol.

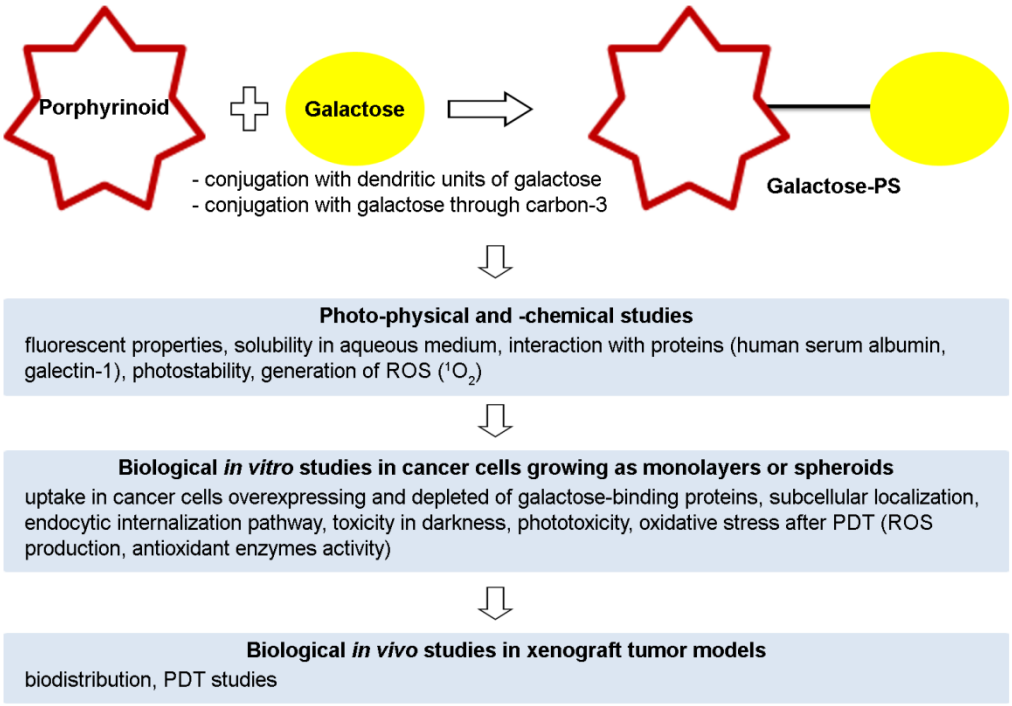

Figure 1.16 Schematic representation of this PhD project. Synthesis of porphyrinoids conjugated with galactose through carbon-3 or with dendritic units of galactose, which will be recognized by galactose-binding proteins overexpressed in cancer cells. Select the most promising galactose-PSs, accounting their photo–chemical and –physical characterization for *in vitro*, using monolayers and spheroids of cancer cell lines, and *in vivo* studies.

1.10 References

1. Trachootham D, Alexandre J, Huang P (2009) Targeting cancer cells by ROS-mediated mechanisms: a radical therapeutic approach? Nat Rev Drug Discov 8: 579-591.

2. Ganguly A, Basu S, Chakraborty P, Chatterjee S, Sarkar A, Chatterjee M, Choudhuri SK (2010) Targeting mitochondrial cell death pathway to overcome drug resistance with a newly developed iron chelate. PLoS One 5: e11253.

3. Engel RH, Evens AM (2006) Oxidative stress and apoptosis: a new treatment paradigm in cancer. Front Biosci 11: 300-312.

4. Manda G, Isvoranu G, Comanescu MV, Manea A, Butuner BD, Korkmaz KS (2015) The redox biology network in cancer pathophysiology and therapeutics. Redox Biol 5: 347-357.

5. Agostinis P, Berg K, Cengel KA, Foster TH, Girotti AW, Gollnick SO, Hahn SM, Hamblin MR, Juzeniene A, Kessel D, Korbelik M, Moan J, Mroz P, Nowis D, Piette J, Wilson BC, Golab J (2011) Photodynamic therapy of cancer: An update. CA Cancer J Clin 61: 250-281.

6. Henderson BW, Waldow SM, Mang TS, Potter WR, Malone PB, Dougherty TJ (1985) Tumor destruction and kinetics of tumor cell death in two experimental mouse tumors following photodynamic therapy. Cancer Res 45: 572-576.

7. Wachowska M, Muchowicz A, Golab J (2015) Targeting epigenetic processes in photodynamic therapy-induced anticancer immunity. Front Oncol 5: 176-185.

8. Yoon I, Li JZ, Shim YK (2013) Advance in photosensitizers and light delivery for photodynamic therapy. Clin Endosc 46: 7-23.

9. Ezzeddine R, Al-Banaw A, Tovmasyan A, Craik JD, Batinic-Haberle I, Benov LT (2013) Effect of molecular characteristics on cellular uptake, subcellular localization, and phototoxicity of Zn(II) N-Alkylpyridylporphyrins. J Biol Chem 288: 36579-36588.

10. Oliveira CS, Turchiello R, Kowaltowski AJ, Indig GL, Baptista MS (2011) Major determinants of photoinduced cell death: Subcellular localization versus photosensitization efficiency. Free Radical Bio Med 51: 824-833.

11. Pavani C, Uchoa AF, Oliveira CS, Iamamoto Y, Baptista MS (2009) Effect of zinc insertion and hydrophobicity on the membrane interactions and PDT activity of porphyrin photosensitizers. Photochem Photobiol Sci 8: 233-240.

12. Rosenkranz AA, Jans DA, Sobolev AS (2000) Targeted intracellular delivery of photosensitizers to enhance photodynamic efficiency. Immunol Cell Biol 78: 452-464.

13. Ishikawa T, Nakagawa H, Hagiya Y, Nonoguchi N, Miyatake S-I, Kuroiwa T (2010) Key role of human ABC transporter ABCG2 in photodynamic therapy and photodynamic diagnosis. Adv Phar Sc 2010: 1-13.

14. Singh S, Aggarwal A, Bhupathiraju NVSDK, Arianna G, Tiwari K, Drain CM (2015) Glycosylated porphyrins, phthalocyanines, and other porphyrinoids for diagnostics and therapeutics. Chem Rev 115: 10261-10306.

15. Moylan C, Scanlan EM, Senge MO (2015) Chemical synthesis and medicinal applications of glycoporphyrins. Curr Med Chem 22: 2238-2348.

16. Medina RA, Owen GI (2002) Glucose transporters: expression, regulation and cancer. Biol Res 35: 9-26.

17. Thijssen VL, Heusschen R, Caers J, Oen AWG (2015) Galectin expression in cancer diagnosis and prognosis: A systematic review. BBA -Rev Cancer 1855: 235-247.

18. Zorlu Y, Ermeydan MA, Dumoulin F, Ahsen V, Savoie H, Boyle RW (2009) Glycerol and galactose substituted zinc phthalocyanines. Synthesis and photodynamic activity. Photochem Photobiol Sci 8: 312-318.

19. Zheng G, Graham A, Shibata M, Missert JR, Oseroff AR, Dougherty TJ, Pandey RK (2001) Synthesis of beta-galactose-conjugated chlorins derived by enyne metathesis as galectin-specific photosensitizers for photodynamic therapy. J Org Chem 66: 8709-8716.

20. Vedachalam S, Choi B-H, Pasunooti KK, Ching KM, Lee K, Yoon HS, Liu X-W (2011) Glycosylated porphyrin derivatives and their photodynamic activity in cancer cells. Medchemcomm 2: 371-377.

21. Sylvain I, Zerrouki R, Granet R, Huang YM, Lagorce J-F, Guilloton M, Blais J-C, Krausz P (2002) Synthesis and biological evaluation of thioglycosylated porphyrins for an application in photodynamic therapy. Bioorg Med Chem 10: 57-69.

22. Lv F, Li Y, Cao B, Liu TJ (2013) Galactose substituted zinc phthalocyanines as near infrared fluorescence probes for liver cancer imaging. J Mater Sci-Mater M 24: 811-819.

23. Liu W, Baer MR, Bowman MJ, Pera P, Zheng X, Morgan J, Pandey RA, Oseroff AR (2007) The tyrosine kinase inhibitor imatinib mesylate enhances the efficacy of photodynamic therapy by inhibiting ABCG2. Clin Cancer Res 13: 2463-2470.

24. Li GL, Pandey SK, Graham A, Dobhal MP, Mehta R, Chen YH, Gryshuk A, Rittenhouse-Olson K, Oseroff A, Pandey RK (2004) Functionalization of OEP-based benzochlorins to develop carbohydrate-conjugated photosensitizers. Attempt to target β-galactoside-recognized proteins. J Org Chem 69: 158-172.

25. Lee PPS, Lo P-C, Chan EYM, Fong W-P, Ko W-H, Ng DKP (2005) Synthesis and in vitro photodynamic activity of novel galactose-containing phthalocyanines. Tetrahedron Lett 46: 1551-1554.

26. Hao E, Jensen TJ, Vicente MGH (2009) Synthesis of porphyrin-carbohydrate conjugates using "click" chemistry and their preliminary evaluation in human HEp2 cells. J Porphyrins Phthalocyanines 13: 51-59.

27. Gomes ATPC, Faustino MAF, Neves MGPMS, Ferreira VF, Juarranz A, Cavaleiro JAS, Sanz-Rodriguez F (2015) Photodynamic effect of glycochlorin conjugates in human cancer epithelial cells. Rsc Adv 5: 33496-33502.

28. Fujimoto K, Miyata T, Aoyama Y (2000) Saccharide-directed cell recognition and molecular delivery using macrocyclic saccharide clusters: Masking of hydrophobicity to enhance the saccharide specificity. J Am Chem Soc 122: 3558-3559.

29. Choi C-F, Huang J-D, Lo P-C, Fong W-P, Ng DKP (2008) Glycosylated zinc(II) phthalocyanines as efficient photosensitisers for photodynamic therapy. Synthesis, photophysical properties and in vitro photodynamic activity. Org Biomol Chem 6: 2173-2181.

30. Maillard P, Huel C, Momenteau M (1992) Synthesis of new *meso*-tetrakis (Glycosylated) Porphyrins. Tetrahedron Lett 33: 8081-8084.

31. Pasetto P, Chen X, Drain CM, Franck RW (2001) Synthesis of hydrolytically stable porphyrin *C*- and *S*-glycoconjugates in high yields. Chem Commun 81-82.

32. Laville I, Figueiredo T, Loock B, Pigaglio S, Maillard P, Grierson DS, Carrez D, Croisy A, Blais J (2003) Synthesis, cellular internalization and photodynamic activity of

glucoconjugated derivatives of tri and tetra(*meta*-hydroxyphenyl)chlorins. Bioorg Med Chem 11: 1643-1652.

33. Hirohara S, Obata M, Saito A, Ogata S-I, Ohtsuki C, Higashida S, Ogura S-I, Okura I, Sugai Y, Mikata Y, Tanihara M, Yano S (2004) Cellular uptake and photocytotoxicity of glycoconjugated porphyrins in HeLa cells. Photochem Photobiol 80: 301-308.

34. Obata M, Hirohara S, Sharyo K, Alitomo H, Kajiwara K, Ogata S-I, Tanihara M, Ohtsuki C, Yano S (2007) Sugar-dependent photodynamic effect of glycoconjugated porphyrins: A study on photocytotoxicity, photophysical properties and bindin behavior to bovine serum albumin (BSA). BBA -Gen Subjects 1770: 1204-1211.

35. Pandey SK, Zheng X, Morgan J, Missert JR, Liu T-H, Shibata M, Bellnier DA, Oseroff AR, Henderson BW, Dougherty TJ, Pandey RK (2007) Purpurinimide carbohydrate conjugates: Effect of the position of the carbohydrate moiety in photosensitizing efficacy. Mol Pharm 4: 448-464.

36. Lyubimtsev A, Iqbal Z, Crucius G, Syrbu S, Taraymovich ES, Ziegler T, Hanack M (2011) Aggregation behavior and UV-vis spectra of tetra- and octaglycosylated zinc phthalocyanines. J Porphyrins Phthalocyanines 15: 39-46.

37. Klyosov AA, Galectin-Targeted Drug Design, In: Glycobiology and Drug Design, American Chemical Society, 2012, Vol. 1102, pp. 25–66.

38. Daly R, Vaz G, Davies AM, Senge MO, Scanlan EM (2012) Synthesis and biological evaluation of a library of glycoporphyrin compounds. Chem Eur J 18: 14671-14679.

39. Iqbal Z, Masilela N, Nyokong T, Lyubimtsev A, Hanack M, Ziegler T (2012) Spectral, photophysical and photochemical properties of tetra- and octaglycosylated zinc phthalocyanines. Photochem Photobiol Sci 11: 679-686.

40. Lafont D, Zorlu Y, Savoie H, Albrieux F, Ahsen V, Boyle RW, Dumoulin F (2013) Monoglycoconjugated phthalocyanines: Effect of sugar and linkage on photodynamic activity. Photodiagnosis Photodyn Ther 10: 252-259.

41. Pereira PMR, Silva S, Cavaleiro JAS, Ribeiro CAF, Tomé JPC, Fernandes R (2014) Galactodendritic phthalocyanine targets carbohydrate-binding proteins enhancing Photodynamic Therapy. PLoS One 9: e95529.

42. Moylan C, Sweed AMK, Shaker YM, Scanlan EM, Senge MO (2015) Lead structures for applications in photodynamic therapy 7. Efficient synthesis of amphiphilic glycosylated lipid porphyrin derivatives: refining linker conjugation for potential PDT applications. Tetrahedron 71: 4145-4153.

43. Fitzpatrick TB, Pathak MA (1959) Historical aspects of methoxsalen and other furocoumarins. J Invest Dermatol 32: 229-231.

44. Moan J, Peng Q (2003) An outline of the hundred-year history of PDT. Anticancer Res 23: 3591-3600.

45. von Tappeiner H, Jesionek A (1903) Therapeutische versuche mit fluoreszierenden stoffen. Münchner Med Wochensch 50: 2042-2044.

46. Meyer-Betz B, F. (1913) Untersuchungen über die biologische (photodynamische) wirkung des hämatoporphyrins und andere derivate des blut- und gallenfarbstoffes. Dtsch Arch Klin Med 112: 476-503.

47. Schwartz S, Absolon K, Vermund H (1955) Some relationship of porphyrins, X-rays and tumors. University of Minnesota Bio-Medical Library 27: 1-37.

48. Dougherty TJ, Grindey GB, Fiel R, Weishaupt KR, Boyle DG (1975) Photoradiation therapy. II. Cure of animal tumors with hematoporphyrin and light. J Natl Cancer Inst 55: 115-121.

49. Dougherty TJ, Kaufman JE, Goldfarb A, Weishaupt KR, Boyle D, Mittleman A (1978) Photoradiation therapy for the treatment of malignant tumors. Cancer Res 38: 2628-2635.

50. Kelly JF, Snell ME (1976) Hematoporphyrin derivative: a possible aid in the diagnosis and therapy of carcinoma of the bladder. J Urol 115: 150-151.

51. Huang Z (2005) A review of progress in clinical photodynamic therapy. Technol Cancer Res Treat 4: 283-293.

52. Allison RR, Downie GH, Cuenca R, Hu X-H, Childs CJH, Sibata CH (2004) Photosensitizers in clinical PDT. Photodiagn Photodyn 1: 27-42.

53. Ormond AB, Freeman HS (2013) Dye sensitizers for photodynamic therapy. Materials 6: 817-840.

54. Debele TA, Peng S, Tsai H-C (2015) Drug carrier for photodynamic cancer therapy. Int J Mol Sci 16: 22094-22136.

55. Srivatsan A, Missert JR, Upadhyay SK, Pandey RK (2015) Porphyrin-based photosensitizers and the corresponding multifunctional nanoplatforms for cancer-imaging and phototherapy. J Porphyrins Phthalocyanines 19: 109-134.

56. Zimcik P.; Miletin MPT, In: Dyes and Pigments: New Research. Nova Science Publis hers, 2008, pp. 1–62.

57. Toganoh MF, H. In Handbook of Porphyrin Science with Applications to Chemistry, Physic s, Ma terials Science Engineering, Biology and Medicine, Kadish, K. M.; Smith, K. M.; Guilard, R.; Eds.; World Scientific Publishing: Singapore, 2010, Vol. 2, pp. 295–367.

58. Allison RR, Moghissi K (2013) Photodynamic Therapy (PDT): PDT mechanisms. Clin Endosc 46: 24-29.

59. Foote CS (1991) Definition of type-I and type-II photosensitized oxidation. Photochem Photobiol 54: 659-659.

60. Ochsner M (1997) Photophysical and photobiological processes in the photodynamic therapy of tumours. J Photochem Photobiol, B 39: 1-18.

61. Milanesio ME, Alvarez MG, Rivarola V, Silber JJ, Durantini EN (2005) Porphyrin-fullerene C_{60} dyads with high ability to form photoinduced charge-separated state as novel sensitizers for photodynamic therapy. Photochem Photobiol 81: 891-897.

62. Ding H, Yu H, Dong Y, Tian R, Huang G, Boothman DA, Sumer BD, Gao J (2011) Photoactivation switch from type II to type I reactions by electron-rich micelles for improved photodynamic therapy of cancer cells under hypoxia. J Control Release 156: 276-280.

63. Vakrat-Haglili Y, Weiner L, Brumfeld V, Brandis A, Salomon Y, McIlroy B, Wilson BC, Pawlak A, Rozanowska M, Sarna T, Scherz A (2005) The microenvironment effect on the generation of reactive oxygen species by Pd-bacteriopheophorbide. J Am Chem Soc 127: 6487-6497.

64. Weishaupt KR, Gomer CJ, Dougherty TJ (1976) Identification of singlet oxygen as cytotoxic agent in photo-inactivation of a murine tumor. Cancer Res 36: 2326-2329.

65. Dougherty TJ, Gomer CJ, Henderson BW, Jori G, Kessel D, Korbelik M, Moan J, Peng Q (1998) Photodynamic therapy. J Natl Cancer Inst 90: 889-905.

66. Silva EFF, Serpa C, Dabrowski JM, Monteiro CJP, Formosinho SJ, Stochel G, Urbanska K, Simões S, Pereira MM, Arnaut LG (2010) Mechanisms of singlet-oxygen and

superoxide-ion generation by porphyrins and bacteriochlorins and their implications in photodynamic therapy. Chem Eur J 16: 9273-9286.

67. Skovsen E, Snyder JW, Lambert JDC, Ogilby PR (2005) Lifetime and diffusion of singlet oxygen in a cell. J Phys Chem B 109: 8570-8573.

68. Snyder JW, Lambert JDC, Ogilby PR (2006) 5,10,15,20-tetrakis(*N*-methyl-4-pyridyl)-21*H*,23*H*-porphine (TMPyP) as a sensitizer for singlet oxygen imaging in cells: characterizing the irradiation-dependent behavior of TMPyP in a single cell. Photochem Photobiol 82: 177-184.

69. Snyder JW, Skovsen E, Lambert JDC, Ogilby PR (2005) Subcellular, time-resolved studies of singlet oxygen in single cells. J Am Chem Soc 127: 14558-14559.

70. Schweitzer C, Schmidt R (2003) Physical mechanisms of generation and deactivation of singlet oxygen. Chem Rev 103: 1685-1757.

71. Peng Q, Moan J, Nesland JM (1996) Correlation of subcellular and intratumoral photosensitizer localization with ultrastructural features after photodynamic therapy. Ultrastruct Pathol 20: 109-129.

72. Zebger I, Snyder JW, Andersen LK, Poulsen L, Gao Z, Lambert JDC, Kristiansen U, Ogilby PR (2004) Direct optical detection of singlet oxygen from a single cell. Photochem Photobiol 79: 319-322.

73. Bancirova M (2011) Sodium azide as a specific quencher of singlet oxygen during chemiluminescent detection by luminol and Cypridina luciferin analogues. Luminescence 26: 685-688.

74. Nagano T (2009) Bioimaging probes for reactive oxygen species and reactive nitrogen species. J Clin Biochem Nutr 45: 111-124.

75. Daghastanli NA, Itri R, Baptista MS (2008) Singlet oxygen reacts with 2 ',7 '-dichlorodihydrofluorescein and contributes to the formation of 2 ',7 '-dichlorofluorescein. Photochem Photobiol 84: 1238-1243.

76. Silva S, Pereira PMR, Silva P, Paz FAA, Faustino MAF, Cavaleiro JAS, Tomé JPC (2012) Porphyrin and phthalocyanine glycodendritic conjugates: synthesis, photophysical and photochemical properties. Chem Commun 48: 3608-3610.

77. Venkatramaiah N, Pereira PMR, Paz FAA, Ribeiro CAF, Fernandes R, Tomé JPC (2015) Dual functionality of phosphonic-acid-appended phthalocyanines: inhibitors of urokinase plasminogen activator and anticancer photodynamic agents. Chem Commun 51: 15550-15553.

78. Lourenço LMO, Pereira PMR, Maciel E, Válega M, Domingues FMJ, Domingues MRM, Neves MGPMS, Cavaleiro JAS, Fernandes R, Tomé JPC (2014) Amphiphilic phthalocyanine-cyclodextrin conjugates for cancer photodynamic therapy. Chem Commun 50: 8363-8366.

79. Severino D, Junqueira HC, Gugliotti M, Gabrielli DS, Baptista MS (2003) Influence of negatively charged interfaces on the ground and excited state properties of methylene blue. Photochem Photobiol 77: 459-468.

80. Fernández DA, Awruch J, Dicelio LE (1996) Photophysical and aggregation studies of *t*-butyl-substituted Zn phthalocyanines. Photochem Photobiol 63: 784-792.

81. de Oca MNM, Vara J, Milla L, Rivarola V, Ortiz CS (2013) Physicochemical properties and photodynamic activity of novel derivatives of triarylmethane and thiazine. Arch Pharm 346: 255-265.

82. Nuñez SC, Yoshimura TM, Ribeiro MS, Junqueira HC, Maciel C, Coutinho-Neto MD, Baptista MS (2015) Urea enhances the photodynamic efficiency of methylene blue. J Photochem Photobiol, B 150: 31-37.

83. Bennion BJ, Daggett V (2003) The molecular basis for the chemical denaturation of proteins by urea. PNAS 100: 5142-5147.

84. Henderson BW, Fingar VH (1987) Relationship of tumor hypoxia and response to photodynamic treatment in an experimental mouse tumor. Cancer Res 47: 3110-3114.

85. Moan J, Sommer S (1985) Oxygen dependence of the photosensitizing effect of hematoporphyrin derivative in NHIK 3025 cells. Cancer Res 45: 1608-1610.

86. Lee See K, Forbes IJ, Betts WH (1984) Oxygen dependency of photocytotoxicity with haematoporphyrin derivative. Photochem Photobiol 39: 631-634.

87. Kishimoto S, Bernardo M, Saito K, Koyasu S, Mitchell JB, Choyke PL, Krishna MC (2015) Evaluation of oxygen dependence on *in vitro* and *in vivo* cytotoxicity of photoimmunotherapy using IR-700-antibody conjugates. Free Radical Bio Med 85: 24-32.

88. Busch TM (2006) Local physiological changes during photodynamic therapy. Laser Surg Med 38: 494-499.

89. Krzykawska-Serda M, Dąbrowski JM, Arnaut LG, Szczygieł M, Urbańska K, Stochel G, Elas M (2014) The role of strong hypoxia in tumors after treatment in the outcome of bacteriochlorin-based photodynamic therapy. Free Radical Bio Med 73: 239-251.

90. Schacht V, Szeimies R-M, Abels C (2006) Photodynamic therapy with 5-aminolevulinic acid induces distinct microcirculatory effects following systemic or topical application. Photochem Photobiol Sci 5: 452-458.

91. Herman MA, Fromm D, Kessel D (1999) Tumor blood-flow changes following protoporphyrin IX-based photodynamic therapy in mice and humans. J Photochem Photobiol, B 52: 99-104.

92. Roberts DJH, Cairnduff F, Driver I, Dixon B, Brown SB (1994) Tumor vascular shutdown following photodynamic therapy based on Polyhematoporphyrin or 5-aminolevulinic acid. Int J Oncol 5: 763-768.

93. Palsson S, Gustafsson L, Bendsoe N, Thompson MS, Andersson-Engels S, Svanberg K (2003) Kinetics of the superficial perfusion and temperature in connection with photodynamic therapy of basal cell carcinomas using esterified and non-esterified 5-aminolaevulinic acid. Brit J Dermatol 148: 1179-1188.

94. Wang KK-H, Cottrell WJ, Mitra S, Oseroff AR, Foster TH (2009) Simulations of measured photobleaching kinetics in human basal cell carcinomas suggest blood flow reductions during ALA-PDT. Laser Surg Med 41: 686-696.

95. Fukumura D, Yuan F, Endo M, Jain RK (1997) Role of nitric oxide in tumor microcirculation - Blood flow, vascular permeability, and leukocyte-endothelial interactions. Am J Pathol 150: 713-725.

96. Chen H, Tian J, He W, Guo Z (2015) H_2O_2-activatable and O_2-evolving nanoparticles for highly efficient and selective photodynamic therapy against hypoxic tumor cells. J Am Chem Soc 137: 1539-1547.

97. Brancaleon L, Moseley H (2002) Laser and non-laser light sources for photodynamic therapy. Laser Med Sci 17: 173-186.

98. Mang TS (2004) Lasers and light sources for PDT: past, present and future. Photodiagnosis Photodyn Ther 1: 43-48.

99. Sunar U (2013) Monitoring photodynamic therapy of head and neck malignancies with optical spectroscopies. World J Clin Cases 1: 96-105.

100. Chen B, Pogue BW, Hoopes PJ, Hasan T (2005) Combining vascular and cellular targeting regimens enhances the efficacy of photodynamic therapy. Int J Radiat Oncol 61: 1216-1226.

101. Kurobane K, Tominaga A, Sato K, North JR, Namba Y, Oku N (2001) Photodynamic therapy targeted to tumor-induced angiogenic vessels. Cancer Lett 167: 49-56.

102. Xiao Z, Halls S, Dickey D, Tulip J, Moore RB (2007) Fractionated versus standard continuous light delivery in interstitial photodynamic therapy of dunning prostate carcinomas. Clin Cancer Res 13: 7496-7505.

103. Star WM, van't Veen AJ, Robinson DJ, Munte K, de Haas ERM, Sterenborg HJCM (2006) Topical 5-aminolevulinic acid mediated photodynamic therapy of superficial basal cell carcinoma using two light fractions with a two-hour interval: long-term follow-up. Acta Derm-Venereol 86: 412-417.

104. Robinson DJ, de Bruijn HS, Star WM, Sterenborg HJCM (2003) Dose and timing of the first light fraction in two-fold illumination schemes for topical ALA-mediated photodynamic therapy of hairless mouse skin. Photochem Photobiol 77: 319-323.

105. de Bruijn HS, van der Ploeg - van den Heuvel A, Sterenborg HJCM, Robinson DJ (2006) Fractionated illumination after topical application of 5-aminolevulinic acid on normal skin of hairless mice: the influence of the dark interval. J Photochem Photobiol, B 85: 184-190.

106. de Haas ERM, Kruijt B, Sterenborg HJCM, Neumann HAM, Robinson DJ (2006) Fractionated illumination significantly improves the response of superficial basal cell carcinoma to aminolevulinic acid photodynamic therapy. J Invest Dermatol 126: 2679-2686.

107. de Vijlder HC, Sterenborg HJCM, Neumann HAM, Robinson DJ, de Haas ERM (2012) Light fractionation significantly improves the response of superficial basal cell carcinoma to aminolaevulinic acid photodynamic therapy: Five-year follow-up of a randomized, prospective trial. Acta Derm-Venereol 92: 641-647.

108. Richards-Kortum R, Sevick-Muraca E (1996) Quantitative optical spectroscopy for tissue diagnosis. Annu Rev Phys Chem 47: 555-606.

109. Shackley DC, Whitehurst C, Moore JV, George NJ, Betts CD, Clarke NW (2000) Light penetration in bladder tissue: implications for the intravesical photodynamic therapy of bladder tumours. Brit J Urol 86: 638-643.

110. Profio AE, Doiron DR (1987) Transport of light in tissue in photodynamic therapy. Photochem Photobiol 46: 591-599.

111. Chen B, Roskams T, de Witte PAM (2002) Antivascular tumor eradication by hypericin-mediated photodynamic therapy. Photochem Photobiol 76: 509-513.

112. Allison RR, Sibata CH (2008) Photodiagnosis for cutaneous malignancy: a brief clinical and technical review. Photodiagnosis Photodyn Ther 5: 247-250.

113. Lee JW, Lee HI, Kim MN, Kim BJ, Chun Y-J, Kim D (2011) Topical photodynamic therapy with methyl aminolevulinate may be an alternative therapeutic option for the recalcitrant Malassezia folliculitis. Int J Dermatol 50: 488-490.

114. Ortiz-Policarpio B, Lui H (2009) Methyl aminolevulinate-PDT for actinic keratoses and superficial nonmelanoma skin cancers. Skin Therapy Lett 14: 1-3.

115. Pushpan SK, Venkatraman S, Anand VG, Sankar J, Parmeswaran D, Ganesan S, Chandrashekar TK (2002) Porphyrins in photodynamic therapy - a search for ideal photosensitizers. Curr Med Chem Anticancer Agents 2: 187-207.

116. Usuda J, Kato H, Okunaka T, Furukawa K, Tsutsui H, Yamada K, Suga Y, Honda H, Nagatsuka Y, Ohira T, Tsuboi M, Hirano T (2006) Photodynamic therapy (PDT) for lung cancers. J Thorac Oncol 1: 489-493.

117. Trindade FZ, Pavarina AC, Ribeiro APD, Bagnato VS, Vergani CE, Costa CAS (2012) Toxicity of photodynamic therapy with LED associated to Photogem®: an in vivo study. Laser Med Sci 27: 403-411.

118. Beneš J, Poučková P, Zeman J, Zadinová M, Sunka P, Lukeš P, Kolářová H (2011) Effects of tandem shock waves combined with photosan and cytostatics on the growth of tumours. Folia Biol 57: 255-260.

119. Kennedy JC, Pottier RH (1992) Endogenous Protoporphyrin IX, a clinically useful photosensitizer for photodynamic therapy. J Photochem Photobiol, B 14: 275-292.

120. Morton CA, Brown SB, Collins S, Ibbotson S, Jenkinson H, Kurwa H, Langmack K, McKenna K, Moseley H, Pearse AD, Stringer M, Taylor DK, Wong G, Rhodes LE (2002) Guidelines for topical photodynamic therapy: report of a workshop of the British Photodermatology Group. Brit J Dermatol 146: 552-567.

121. Rhodes LE, Tsoukas MM, Anderson RR, Kollias N (1997) Iontophoretic delivery of ALA provides a quantitative model for ALA pharmacokinetics and PpIX phototoxicity in human skin. J Invest Dermatol 108: 87-91.

122. Kübler A, Haase T, Rheinwald M, Barth T, Mühling J (1998) Treatment of oral leukoplakia by topical application of 5-aminolevulinic acid. Int J Oral Maxillofac Surg 27: 466-469.

123. Gossner L, May A, Sroka R, Stolte M, Hahn EG, Ell C (1999) Photodynamic destruction of high grade dysplasia and early carcinoma of the esophagus after the oral administration of 5-aminolevulinic acid. Cancer 86: 1921-1928.

124. Furre IE, Shahzidi S, Luksiene Z, Møller ATN, Borgen E, Morgan J, Tkacz-Stachowska K, Nesland JM, Peng Q (2005) Targeting PBR by hexaminolevulinate-mediated photodynamic therapy induces apoptosis through translocation of apoptosis-inducing factor in human leukemia cells. Cancer Res 65: 11051-11060.

125. Senge MO, Brandt JC (2011) Temoporfin (Foscan, 5,10,15,20-Tetra(*m*-hydroxyphenyl)chlorin)-a second-generation photosensitizer. Photochem Photobiol 87: 1240-1296.

126. Triesscheijn M, Ruevekamp M, Aalders M, Baas P, Stewart FA (2005) Outcome of mTHPC mediated photodynamic therapy is primarily determined by the vascular response. Photochem Photobiol 81: 1161-1167.

127. Hovhannisyan V, Guo HW, Hovhannisyan A, Ghukasyan V, Buryakina T, Chen YF, Dong CY (2014) Photo-induced processes in collagen-hypericin system revealed by fluorescence spectroscopy and multiphoton microscopy. Biomed Opt Express 5: 1355-1362.

128. Sharman WM, van Lier JE, Allen CM (2004) Targeted photodynamic therapy via receptor mediated delivery systems. Adv Drug Deliver Rev 56: 53-76.

129. Maas AL, Carter SL, Wileyto EP, Miller J, Yuan M, Yu G, Durham AC, Busch TM (2012) Tumor vascular microenvironment determines responsiveness to photodynamic therapy. Cancer Res 72: 2079-2088.

130. Jori G, Reddi E (1993) The role of lipoproteins in the delivery of tumor-targeting photosensitizers. Int J Biochem 25: 1369-1375.

131. Marchal S, Dolivet G, Lassalle H-P, Guillemin F, Bezdetnaya L (2015) Targeted photodynamic therapy in head and neck squamous cell carcinoma: heading into the future. Laser Med Sci 1-7.

132. Laville I, Pigaglio S, Blais JC, Doz F, Loock B, Maillard P, Grierson DS, Blais J (2006) Photodynamic efficiency of diethylene glycol-linked glycoconjugated porphyrins in human retinoblastoma cells. J Med Chem 49: 2558-2567.

133. Bonneau S, Vever-Bizet C (2008) Tetrapyrrole photosensitisers, determinants of subcellular localisation and mechanisms of photodynamic processes in therapeutic approaches. Expert Opin Ther Pat 18: 1011-1025.

134. Ishikawa T, Kajimoto Y, Inoue Y, Ikegami Y, Kuroiwa T (2015) Critical role of ABCG2 in ALA-photodynamic diagnosis and therapy of human brain tumor. Adv Cancer Res 125: 197-216.

135. Doherty GJ, McMahon HT (2009) Mechanisms of endocytosis. Annu Rev Biochem 78: 857-902.

136. Soriano J, Villanueva A, Stockert JC, Cañete M (2013) Vehiculization determines the endocytic internalization mechanism of Zn(II)-phthalocyanine. Histochem Cell Biol 139: 149-160.

137. Kim J, Santos OA, Park J-H (2014) Selective photosensitizer delivery into plasma membrane for effective photodynamic therapy. J Control Release 191: 98-104.

138. Jensen TJ, Vicente MGH, Luguya R, Norton J, Fronczek FR, Smith KM (2010) Effect of overall charge and charge distribution on cellular uptake, distribution and phototoxicity of cationic porphyrins in HEp2 cells. J Photochem Photobiol, B 100: 100-111.

139. Castano AP, Demidova TN, Hamblin MR (2005) Mechanisms in photodynamic therapy: Part 2. Cellular signaling, cell metabolism and modes of cell death. Photodiagnosis Photodyn Ther 2: 1-23.

140. Choi B-H, Ryoo I-G, Kang HC, Kwak M-K (2014) The sensitivity of cancer cells to Pheophorbide a-based photodynamic therapy is enhanced by *NRF2* silencing. PLoS One 9: e107158.

141. Laranjo M, Serra AC, Abrantes M, Pineiro M, Gonçalves AC, Casalta-Lopes J, Carvalho L, Sarmento-Ribeiro AB, Rocha-Gonsalves A, Botelho F (2013) 2-Bromo-5-hydroxyphenylporphyrins for photodynamic therapy: Photosensitization efficiency, subcellular localization and *in vivo* studies. Photodiagnosis Photodyn Ther 10: 51-61.

142. Andrzejak M, Santiago M, Kessel D (2011) Effects of endosomal photodamage on membrane recycling and endocytosis. Photochem Photobiol 87: 699-706.

143. Roberts WG, Berns MW (1989) In vitro Photosensitization I. Cellular uptake and subcellular-localization of mono-L-aspartyl chlorin e_6, chloro-aluminum sulfonated phthalocyanine, and Photofrin-II. Laser Surg Med 9: 90-101.

144. Zong D, Zielinska-Chomej K, Juntti T, Mörk B, Lewensohn R, Hååg P, Viktorsson K (2014) Harnessing the lysosome-dependent antitumor activity of phenothiazines in human small cell lung cancer. Cell Death Dis 5: e1111.

145. Acedo P, Stockert JC, Cañete M, Villanueva A (2014) Two combined photosensitizers: a goal for more effective photodynamic therapy of cancer. Cell Death Dis 5: e1122.

146. Kessel D, Reiners JJ (2014) Enhanced efficacy of photodynamic therapy via a sequential targeting protocol. Photochem Photobiol 90: 889-895.

147. Mitsunaga M, Ogawa M, Kosaka N, Rosenblum LT, Choyke PL, Kobayashi H (2011) Cancer cell-selective in vivo near infrared photoimmunotherapy targeting specific membrane molecules. Nat Med 17: 1685-1691.

148. Zhang S, Yang L, Ling X, Shao P, Wang X, Edwards WB, Bai M (2015) Tumor mitochondria-targeted photodynamic therapy with a translocator protein (TSPO)-specific photosensitizer. Acta Biomater 160-170.

149. Berg K, Madslien K, Bommer JC, Oftebro R, Winkelman JW, Moan J (1991) Light-induced relocalization of sulfonated *meso*-tetraphenylporphines in Nhik 3025 cells and effects of dose fractionation. Photochem Photobiol 53: 203-210.

150. Alvarez M, Villanueva A, Acedo P, Cañete M, Stockert JC (2011) Cell death causes relocalization of photosensitizing fluorescent probes. Acta Histochem 113: 363-368.

151. Mfouo-Tynga I, Abrahamse H (2015) Cell death pathways and phthalocyanine as an efficient agent for photodynamic cancer therapy. Int J Mol Sci 16: 10228-10241.

152. Gomer GJ, Ferrario A, Hayashi N, Rucker N, Szirth BC, Murphree AL (1988) Molecular, cellular, and tissue responses following photodynamic therapy. Laser Surg Med 8: 450-463.

153. Agarwal ML, Larkin HE, Zaidi SI, Mukhtar H, Oleinick NL (1993) Phospholipase activation triggers apoptosis in photosensitized mouse lymphoma cells. Cancer Res 53: 5897-5902.

154. Oleinick NL, Evans HH (1998) The photobiology of photodynamic therapy: cellular targets and mechanisms. Radiat Res 150: S146-S156.

155. Separovic D, Joseph N, Breen P, Bielawski J, Pierce JS, Buren EV, Bhatti G, Saad ZH, Bai A, Bielawska A (2011) Combining anticancer agents photodynamic therapy and LCL85 leads to distinct changes in the sphingolipid profile, autophagy, caspase-3 activation in the absence of cell death, and long-term sensitization. Biochem Biophys Res Commun 409: 372-377.

156. Garg AD, Maes H, Romano E, Agostinis P (2015) Autophagy, a major adaptation pathway shaping cancer cell death and anticancer immunity responses following photodynamic therapy. Photochem Photobiol Sci 14: 1410-1424.

157. Woodburn KW, Vardaxis NJ, Hill JS, Kaye AH, Phillips DR (1991) Subcellular-localization of porphyrins using confocal laser scanning microscopy. Photochem Photobiol 54: 725-732.

158. Mroz P, Yaroslavsky A, Kharkwal GB, Hamblin MR (2011) Cell death pathways in photodynamic therapy of cancer. Cancers 3: 2516-2539.

159. Moor ACE (2000) Signaling pathways in cell death and survival after photodynamic therapy. J Photochem Photobiol, B 57: 1-13.

160. Henderson BW, Bellnier DA, Greco WR, Sharma A, Pandey RK, Vaughan LA, Weishaupt KR, Dougherty TJ (1997) An *in vivo* quantitative structure-activity relationship for a congeneric series of pyropheophorbide derivatives as photosensitizers for photodynamic therapy. Cancer Res 57: 4000-4007.

161. Morgan J, Oseroff AR (2001) Mitochondria-based photodynamic anti-cancer therapy. Adv Drug Deliver Rev 49: 71-86.

162. Musser DA, Wagner JM, Datta-Gupta N (1982) The Interaction of tumor localizing porphyrins with collagen and elastin. Res Commun Chem Path 36: 251-259.

163. Musser DA, Wagner JM, Weber FJ, Datta-Gupta N (1980) The binding of tumor localizing porphyrins to a fibrin matrix and their effects following photoirradiation. Res Commun Chem Path 28: 505-525.

164. Nowis D, Makowski M, Stokłosa T, Legat M, Issat T, Gołąb J (2005) Direct tumor damage mechanisms of photodynamic therapy. Acta Biochim Pol 52: 339-352.

165. Pettigrew CA, Cotter TG (2009) Deregulation of cell death (apoptosis): implications for tumor development. Discov Med 8: 61-63.

166. Rustin P (2002) Mitochondria, from cell death to proliferation. Nat Genet 30: 352-353.

167. Perfettini J-L, Kroemer G (2003) Caspase activation is not death. Nat Immunol 4: 308-310.

168. Gougeon M-L, Kroemer G (2003) Charming to death: caspase-dependent or -independent? Cell Death Differ 10: 390-392.

169. Kessel D, Castelli M (2001) Evidence that Bcl-2 is the target of three photosensitizers that induce a rapid apoptotic response. Photochem Photobiol 74: 318-322.

170. Xue L-Y, Chiu S-M, Oleinick NL (2001) Photochemical destruction of the Bcl-2 oncoprotein during photodynamic therapy with the phthalocyanine photosensitizer Pc 4. Oncogene 20: 3420-3427.

171. Mfouo-Tynga I, Houreld NN, Abrahamse H (2014) Induced cell death pathway post photodynamic therapy using a metallophthalocyanine photosensitizer in breast cancer cells. Photomed Laser Surg 32: 205-211.

172. Chiu S-M, Oleinick NL (2001) Dissociation of mitochondrial depolarization from cytochrome c release during apoptosis induced by photodynamic therapy. Brit J Cancer 84: 1099-1106.

173. Vantieghem A, Xu Y, Declercq W, Vandenabeele P, Denecker G, Vandenheede JR, Merlevede W, de Witte PA, Agostinis P (2001) Different pathways mediate cytochrome c release after photodynamic therapy with hypericin. Photochem Photobiol 74: 133-142.

174. Kroemer G, Galluzzi L, Vandenabeele P, Abrams J, Alnemri ES, Baehrecke EH, Blagosklonny MV, El-Deiry WS, Golstein P, Green DR, Hengartner M, Knight RA, Kumar S, Lipton SA, Malorni W, Nunez G, Peter ME, Tschopp J, Yuan J, Piacentini M, Zhivotovsky B, Melino G (2009) Classification of cell death: recommendations of the Nomenclature Committee on Cell Death 2009. Cell Death Differ 16: 3-11.

175. Lemasters JJ (2005) Dying a thousand deaths: Redundant pathways from different organelles to apoptosis and necrosis. Gastroenterol J 129: 351-360.

176. Danial NN, Korsmeyer SJ (2004) Cell death: Critical control points. Cell 116: 205-219.

177. Longo JPF, Lozzi SP, Simioni AR, Morais PC, Tedesco AC, Azevedo RB (2009) Photodynamic therapy with aluminum-chloro-phtalocyanine induces necrosis and vascular damage in mice tongue tumors. J Photochem Photobiol, B 94: 143-146.

178. Zhang L-J, Bian J, Bao L-L, Chen H-F, Yan Y-J, Wang L, Chen Z-L (2014) Photosensitizing effectiveness of a novel chlorin-based photosensitizer for photodynamic therapy in vitro and in vivo. J Cancer Res Clin 140: 1527-1536.

179. Nagata S, Obana A, Gohto Y, Nakajima S (2003) Necrotic and apoptotic cell death of human malignant melanoma cells following photodynamic therapy using an Amphiphilic photosensitizer, ATX-S10(Na). Laser Surg Med 33: 64-70.

180. Wood SR, Holroyd JA, Brown SB (1997) The subcellular localization of Zn(II) phthalocyanines and their redistribution on exposure to light. Photochem Photobiol 65: 397-402.

181. Tsujimoto Y, Shimizu S (2005) Another way to die: autophagic programmed cell death. Cell Death Differ 12: 1528-1534.

182. Criollo A, Maiuri MC, Tasdemir E, Vitale I, Fiebig AA, Andrews D, Molgó J, Díaz J, Lavandero S, Harper F, Pierron G, di Stefano D, Rizzuto R, Szabadkai G, Kroemer G (2007) Regulation of autophagy by the inositol trisphosphate receptor. Cell Death Differ 14: 1029-1039.

183. Criollo A, Vicencio JM, Tasdemir E, Maiuri MC, Lavandero S, Kroemer G (2007) The inositol trisphosphate receptor in the control of autophagy. Autophagy 3: 350-353.

184. Xue L-Y, Chiu S-M, Azizuddin K, Joseph S, Oleinick NL (2007) The death of human cancer cells following photodynamic therapy: Apoptosis competence is necessary for Bcl-2 protection but not for induction of autophagy. Photochem Photobiol 83: 1016-1023.

185. Sasnauskiene A, Kadziauskas J, Vezelyte N, Jonusiene V, Kirveliene V (2009) Apoptosis, autophagy and cell cycle arrest following photodamage to mitochondrial interior. Apoptosis 14: 276-286.

186. Scherz-Shouval R, Elazar Z (2007) ROS, mitochondria and the regulation of autophagy. Trends Cell Biol 17: 422-427.

187. Kessel D, Arroyo AS (2007) Apoptotic and autophagic responses to Bcl-2 inhibition and photodamage. Photochem Photobiol Sci 6: 1290-1295.

188. Wang XB, Hu JM, Wang P, Zhang SL, Liu YC, Xiong WL, Liu QH (2015) Analysis of the in vivo and in vitro effects of photodynamic therapy on breast cancer by using a sensitizer, sinoporphyrin sodium. Theranostics 5: 772-786.

189. Pereira PMR, Carvalho JJ, Silva S, Cavaleiro JAS, Schneider RJ, Fernandes R, Tomé JPC (2014) Porphyrin conjugated with serum albumins and monoclonal antibodies boosts efficiency in targeted destruction of human bladder cancer cells. Org Biomol Chem 12: 1804-1811.

190. Madsen SJ, Sun C-H, Tromberg BJ, Cristini V, De Magalhães N, Hirschberg H (2006) Multicell tumor spheroids in photodynamic therapy. Laser Surg Med 38: 555-564.

191. Dubessy C, Merlin J-L, Marchal C, Guillemin F (2000) Spheroids in radiobiology and photodynamic therapy. Crit Rev Oncol Hematol 36: 179-192.

192. Bigelow CE, Mitra S, Knuechel R, Foster TH (2001) ALA- and ALA-hexylester-induced protoporphyrin IX fluorescence and distribution in multicell tumour spheroids. Brit J Cancer 85: 727-734.

193. Yang YM, Yang XC, Zou J, Jia C, Hu Y, Du HR, Wang HJ (2015) Evaluation of photodynamic therapy efficiency using an *in vitro* three-dimensional microfluidic breast cancer tissue model. Lab Chip 15: 735-744.

194. Xiang L, Xing D, Gu H, Yang D, Yang S, Zeng L, Chen WR (2007) Real-time optoacoustic monitoring of vascular damage during photodynamic therapy treatment of tumor. J Biomed Opt 12: 014001.

195. Hornung R, Hammer-Wilson MJ, Kimel S, Liaw L-H, Tadir Y, Berns MW (1999) Systemic application of photosensitizers in the chick chorioallantoic membrane (CAM) model: photodynamic response of CAM vessels and 5-aminolevulinic acid uptake kinetics by transplantable tumors. J Photochem Photobiol, B 49: 41-49.

196. Peng Q, Moan J, Kongshaug M, Evensen JF, Anholt H, Rimington C (1991) Sensitizer for photodynamic therapy of cancer - a comparison of the tissue distribution of Photofrin-II and Aluminum Phthalocyanine Tetrasulfonate in nude-mice bearing a human-malignant tumor. Int J Cancer 48: 258-264.

197. Gibson SL, van der Meid KR, Murant RS, Hilf R (1990) Increased efficacy of photodynamic therapy of R3230ac mammary adenocarcinoma by intratumoral injection of Photofrin-II. Brit J Cancer 61: 553-557.

198. Angell-Petersen E, Spetalen S, Madsen SJ, Sun C-H, Peng Q, Carper SW, Sioud M, Hirschberg H (2006) Influence of light fluence rate on the effects of photodynamic therapy in an orthotopic rat glioma model. J Neurosurg 104: 109-117.

199. Chen B, Pogue BW, Zhou XD, O'Hara JA, Solban N, Demidenko E, Hoopes PJ, Hasan T (2005) Effect of tumor host microenvironment on photodynamic therapy in a rat prostate tumor model. Clin Cancer Res 11: 720-727.

200. Ma G, Ikeda H, Inokuchi T, Sano K (1999) Effect of photodynamic therapy using 5-aminolevulinic acid on 4-nitroquinoline-1-oxide-induced premalignant and malignant lesions of mouse tongue. Oral Oncol 35: 120-124.

201. Hsu Y-C, Yang D-F, Chiang C-P, Lee J-W, Tseng M-K (2012) Successful treatment of 7,12-dimethylbenz(a)anthracene-induced hamster buccal pouch precancerous lesions by topical 5-aminolevulinic acid-mediated photodynamic therapy. Photodiagnosis Photodyn Ther 9: 310-318.

202. Ferreira I, Ferreira J, Vollet-Filho JD, Moriyama LT, Bagnato VS, Salvadori DMF, Rocha NS (2013) Photodynamic therapy for the treatment of induced mammary tumor in rats. Laser Med Sci 28: 571-577.

203. Boiy A, Roelandts R, de Witte PAM (2011) Photodynamic therapy using topically applied hypericin: Comparative effect with methyl-aminolevulinic acid on UV induced skin tumours. J Photochem Photobiol, B 102: 123-131.

204. Walt H, Nap M, Dorward AM, Leers MPG, Tennent BJ, Varga Z, Stallmach T, Björklund V, Beamer WG (2006) Early apoptotic responses in transgenic mouse mammary carcinoma for photodynamic therapy. Photodiagnosis Photodyn Ther 3: 227-233.

205. Dorward AM, Fancher KS, Duffy TM, Beamer WG, Walt H (2005) Early neoplastic and metastatic mammary tumours of transgenic mice detected by 5-aminolevulinic acid-stimulated protoporphyrin IX accumulation. Brit J Cancer 93: 1137-1143.

206. Shirasu N, Yamada H, Shibaguchi H, Kuroki M, Kuroki M (2014) Potent and specific antitumor effect of CEA-targeted photoimmunotherapy. Int J Cancer 135: 2697-2710.

207. Samkoe KS, Chen A, Rizvi I, O'Hara JA, Hoopes PJ, Pereira SP, Hasan T, Pogue BW (2010) Imaging tumor variation in response to photodynamic therapy in pancreatic cancer xenograft models. Int J Radiat Oncol 76: 251-259.

208. Koudinova NV, Pinthus JH, Brandis A, Brenner O, Bendel P, Ramon J, Eshhar Z, Scherz A, Salomon Y (2003) Photodynamic therapy with Pd-bacteriopheophorbide (TOOKAD): Successful *in vivo* treatment of human prostatic small cell carcinoma xenografts. Int J Cancer 104: 782-789.

209. Frese KK, Tuveson DA (2007) Maximizing mouse cancer models. Nat Rev Cancer 7: 654-658.

210. Josefsen LB, Boyle RW (2012) Unique diagnostic and therapeutic roles of porphyrins and phthalocyanines in photodynamic therapy, imaging and theranostics. Theranostics 2: 916-966.

211. Abrahamse H, Hamblin MR (2016) New photosensitizers for photodynamic therapy. Biochem J 473: 347-364.

212. Chen X, Hui L, Foster DA, Drain CM (2004) Efficient synthesis and photodynamic activity of porphyrin-saccharide conjugates: Targeting and incapacitating cancer cells. Biochemistry 43: 10918-10929.

213. Hirohara S, Nishida M, Sharyo K, Obata M, Ando T, Tanihara M (2010) Synthesis, photophysical properties and photocytotoxicity of mono-, di-, tri- and tetra-glucosylated fluorophenylporphyrins. Bioorg Med Chem 18: 1526-1535.

214. Xu DS, Chen X, Chen K, Peng Y, Li Y, Ke Y, Gan D (2014) Tetra-sulfonate phthalocyanine zinc-bovine serum albumin conjugate-mediated photodynamic therapy of human glioma. J Biomater Appl 29: 378-385.

215. Marotta DE, Cao W, Wileyto EP, Li H, Corbin I, Rickter E, Glickson JD, Chance B, Zheng G, Busch TM (2011) Evaluation of bacteriochlorophyll-reconstituted low-density lipoprotein nanoparticles for photodynamic therapy efficacy in vivo. Nanomedicine 6: 475-487.

216. Dozzo P, Koo M-S, Berger S, Forte TM, Kahl SB (2005) Synthesis, characterization, and plasma lipoprotein association of a nucleus-targeted boronated porphyrin. J Med Chem 48: 357-359.

217. Gijsens A, Missiaen L, Merlevede W, de Witte P (2000) Epidermal growth factor-mediated targeting of chlorin e6 selectively potentiates its photodynamic activity. Cancer Res 60: 2197-2202.

218. Serebrovskaya EO, Ryumina AP, Boulina ME, Shirmanova MV, Zagaynova EV, Bogdanova EA, Lukyanov SA, Lukyanov KA (2014) Phototoxic effects of lysosome-associated genetically encoded photosensitizer KillerRed. J Biomed Opt 19: 071403.

219. Obaid G, Chambrier I, Cook MJ, Russell DA (2015) Cancer targeting with biomolecules: a comparative study of photodynamic therapy efficacy using antibody or lectin conjugated phthalocyanine-PEG gold nanoparticles. Photochem Photobiol Sci 14: 737-747.

220. Gravier J, Schneider R, Frochot C, Bastogne T, Schmitt F, Didelon J, Guillemin F, Barberi-Heyob M (2008) Improvement of meta-tetra(hydroxyphenyl)chlorin-like photosensitizer selectivity with folate-based targeted delivery. Synthesis and in vivo delivery studies. J Med Chem 51: 3867-3877.

221. Li P-X, Mu J-H, Xiao H-L, Li D-H (2015) Antitumor effect of photodynamic therapy with a novel targeted photosensitizer on cervical carcinoma. Oncol Rep 33: 125-132.

222. Pereira PMR, Korsak B, Sarmento B, Schneider RJ, Fernandes R, Tomé JPC (2015) Antibodies armed with photosensitizers: from chemical synthesis to photobiological applications. Org Biomol Chem 13: 2518-2529.

223. Li X-S, Ke M-R, Huang W, Ye C-H, Huang J-D (2015) A pH-responsive layered double hydroxide (LDH)-phthalocyanine nanohybrid for efficient photodynamic therapy. Chem Eur J 21: 3310-3317.

224. Kolemen S, Isik M, Kim GM, Kim D, Geng H, Buyuktemiz M, Karatas T, Zhang X-F, Dede Y, Yoon J, Akkaya EU (2015) Intracellular modulation of excited-state dynamics in a chromophore dyad: Differential enhancement of photocytotoxicity targeting cancer cells. Angew Chem Int Edit 54: 5340-5344.

225. Gabius HJ (1997) Animal lectins. Eur J Biochem 243: 543-576.

226. Ernst B, Magnani JL (2009) From carbohydrate leads to glycomimetic drugs. Nat Rev Drug Discov 8: 661-677.

227. Hirabayashi J, Hashidate T, Arata Y, Nishi N, Nakamura T, Hirashima M, Urashima T, Oka T, Futai M, Muller WEG, Yagi F, Kasai K (2002) Oligosaccharide specificity of galectins: a search by frontal affinity chromatography. BBA -Gen Subjects 1572: 232-254.

228. Yang RY, Rabinovich GA, Liu FT (2008) Galectins: structure, function and therapeutic potential. Expert Rev Mol Med 10: e17.

229. Brewer CF (2002) Binding and cross-linking properties of galectins. BBA -Gen Subjects 1572: 255-262.

230. Sacchettini JC, Baum LG, Brewer CF (2001) Multivalent protein-carbohydrate interactions. A new paradigm for supermolecular assembly and signal transduction. Biochemistry 40: 3009-3015.

231. Vyakarnam A, Dagher SF, Wang JL, Patterson RJ (1997) Evidence for a role for galectin-1 in pre-mRNA splicing. Mol Cell Biol 17: 4730-4737.

232. Elola MT, Wolfenstein-Todel C, Troncoso MF, Vasta GR, Rabinovich GA (2007) Galectins: matricellular glycan-binding proteins linking cell adhesion, migration, and survival. Cell Mol Life Sci 64: 1679-1700.

233. He JL, Baum LG (2004) Presentation of galectin-1 by extracellular matrix triggers T cell death. J Biol Chem 279: 4705-4712.

234. Liu FT, Patterson RJ, Wang JL (2002) Intracellular functions of galectins. Biochim Biophys Acta 1572: 263-273.

235. Danguy A, Camby I, Kiss R (2002) Galectins and cancer. Biochim Biophys Acta 1572: 285-293.

236. van den Brule F, Califice S, Castronovo V (2004) Expression of galectins in cancer: a critical review. Glycoconj J 19: 537-542.

237. Oka N, Takenaka Y, Raz A (2004) Galectins and urological cancer. J Cell Biochem 91: 118-124.

238. Liu FT, Rabinovich GA (2005) Galectins as modulators of tumour progression. Nat Rev Cancer 5: 29-41.

239. Raz A, Lotan R (1987) Endogenous galactoside-binding lectins - a new class of functional tumor-cell surface molecules related to metastasis. Cancer Metastasis Rev 6: 433-452.

240. Gorelik E, Galili U, Raz A (2001) On the role of cell surface carbohydrates and their binding proteins (lectins) in tumor metastasis. Cancer Metastasis Rev 20: 245-277.

241. Andre S, Kojima S, Yamazaki N, Fink C, Kaltner H, Kayser K, Gabius HJ (1999) Galectins-1 and-3 and their ligands in tumor biology - Non-uniform properties in cell-surface presentation and modulation of adhesion to matrix glycoproteins for various tumor cell lines, in biodistribution of free and liposome-bound galectins and in their expression by breast and colorectal carcinomas with/without metastatic propensity. J Cancer Res Clin Oncol 125: 461-474.

242. Esmailiejah AA, Taheriazam A, Golbakhsh MR, Jamshidi M, Shakeri M, Yahaghi E, Moghtadaei M (2015) Analysis of serum levels and tissue expression of galectin-1 and galectin-3 as noninvasive biomarkers in osteosarcoma patients. Tumour Biol 1-7.

243. Fortuna-Costa A, Gomes AM, Kozlowski EO, Stelling MP, Pavão MSG (2014) Extracellular galectin-3 in tumor progression and metastasis. Front Oncol 4: 138-147.

244. Cooper DN (2002) Galectinomics: finding themes in complexity. Biochim Biophys Acta 1572: 209-231.

245. Cho MJ, Cummings RD (1997) Galectin-1: Oligomeric structure and interactions with polylactosamine. Trends Glycosci Glyc 9: 47-56.

246. Liao DI, Kapadia G, Ahmed H, Vasta GR, Herzberg O (1994) Structure of S-Lectin, a developmentally-regulated vertebrate beta-galactoside-binding protein. PNAS 91: 1428-1432.

247. Camby I, Le Mercier M, Lefranc F, Kiss R (2006) Galectin-1: a small protein with major functions. Glycobiology 16: 137R-157R.

248. Noda Y, Kishino M, Sato S, Hirose K, Sakai M, Fukuda Y, Murakami S, Toyosawa S (2016) Galectin-1 expression is associated with tumour immunity and prognosis in gingival squamous cell carcinoma. J Clin Pathol 1-8.

249. Van Mourik TR, Läppchen T, Rossin R, Van Beijnum JR, Macdonald JR, Mayo KH, Griffioen AW, Nicolay K, Grüll H (2015) Evaluation of ^{111}In-labeled Anginex as potential SPECT tracer for imaging of tumor angiogenesis. Anticancer Res 35: 5945-5954.

250. van Beijnum JR, Thijssen VL, Läppchen T, Wong TJ, Verel I, Engbersen M, Schulkens IA, Rossin R, Grüll H, Griffioen AW, Nowak-Sliwinska P (2016) A key role for galectin-1 in sprouting angiogenesis revealed by novel rationally designed antibodies. Int J Cancer 139: 824-835.

251. Seetharaman J, Kanigsberg A, Slaaby R, Leffler H, Barondes SH, Rini JM (1998) X-ray crystal structure of the human galectin-3 carbohydrate recognition domain at 2.1-A resolution. J Biol Chem 273: 13047-13052.

252. Birdsall B, Feeney J, Burdett ID, Bawumia S, Barboni EA, Hughes RC (2001) NMR solution studies of hamster galectin-3 and electron microscopic visualization of surface-adsorbed complexes: evidence for interactions between the N- and C-terminal domains. Biochemistry 40: 4859-4866.

253. Davidson PJ, Davis MJ, Patterson RJ, Ripoche MA, Poirier F, Wang JL (2002) Shuttling of galectin-3 between the nucleus and cytoplasm. Glycobiology 12: 329-337.

254. David A (2010) Carbohydrate-based biomedical copolymers for targeted delivery of anticancer drugs. Isr J Chem 50: 204-219.

255. Wojtyk JTC, Goyan R, Gudgin-Dickson E, Pottier R (2006) Exploiting tumour biology to develop novel drug delivery strategies for PDT. Med Laser Appl 21: 225-238.

256. D'Auria S, Petrova L, John C, Russev G, Varriale A, Bogoeva V (2009) Tumor-specific protein human galectin-1 interacts with anticancer agents. Mol Biosyst 5: 1331-1336.

257. Mori S, Yoshiyama H, Tokunaga E, Iida N, Hayashi M, Obata T, Tanaka M, Shibata N (2015) Design, synthesis, spectral investigations and biological activity of fluorinated

phthalocyanine conjugated with galactose and comparison to its non-fluorinated counterpart. J Fluorine Chem 174: 137-141.

258. Griegel S, Rajewsky MF, Ciesiolka T, Gabius HJ (1989) Endogenous sugar receptor (lectin) profiles of human retinoblastoma and retinoblast cell-lines analyzed by cytological markers, affinity-chromatography and neoglycoprotein - targeted photolysis. Anticancer Res 9: 723-730.

259. Barnett JE, Holman GD, Chalkley RA, Munday KA (1975) Evidence for two asymmetric conformational states in the human erythrocyte sugar-transport system. Biochem J 145: 417-429.

260. López-Lucendo MF, Solís D, André S, Hirabayashi J, Kasai K-I, Kaltner H, Gabius HJ, Romero A (2004) Growth-regulatory human galectin-1: Crystallographic characterisation of the structural changes induced by single-site mutations and their impact on the thermodynamics of ligand binding. J Mol Biol 343: 957-970.

261. Zheng X, Morgan J, Pandey SK, Chen Y, Tracy E, Baumann H, Missert JR, Batt C, Jackson J, Bellnier DA, Henderson BW, Pandey RK (2009) Conjugation of 2-(1'-hexyloxyethyl)-2-devinylpyropheophorbide-a (HPPH) to carbohydrates changes its subcellular distribution and enhances photodynamic activity in vivo. J Med Chem 52: 4306-4318.

262. Pandey SK, Sajjad M, Chen Y, Zheng X, Yao R, Missert JR, Batt C, Nabi HA, Oseroff AR, Pandey RK (2009) Comparative positron-emission tomography (PET) imaging and phototherapeutic potential of ^{124}I- labeled methyl- 3-(1'-iodobenzyloxyethyl)pyropheophorbide-α vs the corresponding glucose and galactose conjugates. J Med Chem 52: 445-455.

263. Morgan J, Jackson JD, Zheng X, Pandey SK, Pandey RK (2010) Substrate affinity of photosensitizers derived from chlorophyll-a: The ABCG2 transporter affects the phototoxic response of side population stem cell-like cancer cells to photodynamic therapy. Mol Pharm 7: 1789-1804.

264. Ballut S, Makky A, Chauvin B, Michel J-P, Kasselouri A, Maillard P, Rosilio V (2012) Tumor targeting in photodynamic therapy. From glycoconjugated photosensitizers to glycodendrimeric one. Concept, design and properties. Org Biomol Chem 10: 4485-4495.

265. Figueira F, Pereira PMR, Silva S, Cavaleiro JAS, Tomé JPC (2014) Porphyrins and phthalocyanines decorated with dendrimers: Synthesis and biomedical applications. Curr Org Synth 11: 110-126.

Synthesis of galactose-conjugated photosensitizers

CHAPTER II

Chapter II Synthesis of galactose-conjugated photosensitizers

2.1 General overview

Porphyrins are well-known first generation PSs and they are the main compounds used in clinical and pre-clinical settings for the treatment of cancer by PDT. Phthalocyanines (Pcs) and chlorins (Chls) are second generation PSs, having strong absorption in the wavelength range between 650 and 850 nm, where tissue light penetration is rather high. Unsubstituted Pors, Pcs and Chls are highly insoluble in aqueous solvents. The conjugation of PSs with galactose units increases their water solubility [1-9] and provides the possibility for specific interaction of the resulting galactose-conjugate with galactose-binding proteins overexpressed in cancer cells. In this work, the following compounds were developed (Figure 2.1)[1]:

PorGal$_8$: a porphyrin conjugated with four dendritic units of galactose (a total of four galactose sugars);

ChlGal$_8$: a chlorin conjugated with four dendritic units of galactose (a total of four galactose sugars);

PcGal$_{16}$: a phthalocyanine conjugated with eight dendritic units of galactose (a total of eight galactose sugars);

Por-C3-Gal$_4$: a porphyrin conjugated with four galactose sugars through carbon-3;

Por-C3-Gal$_4$: a porphyrin conjugated with four galactose sugars through carbon-1.

[1] The synthesis and characterization of **protected PcGal$_{16}$** were performed by Doctor Sandrina Silva, postdoc student, in the laboratory of Doctor João Tomé, Department of Chemistry – University of Aveiro, Aveiro, Portugal. **Por-C3-Gal$_4$** and **Por-C1-Gal$_4$** were synthesized and characterized by Doctor Dinesh Bhupathiraju (postdoc student) and Waqar Rizvi (PhD student) in the laboratory of Professor Charles Michael Drain, Department of Chemistry – Hunter College of CUNY, New York, United States.

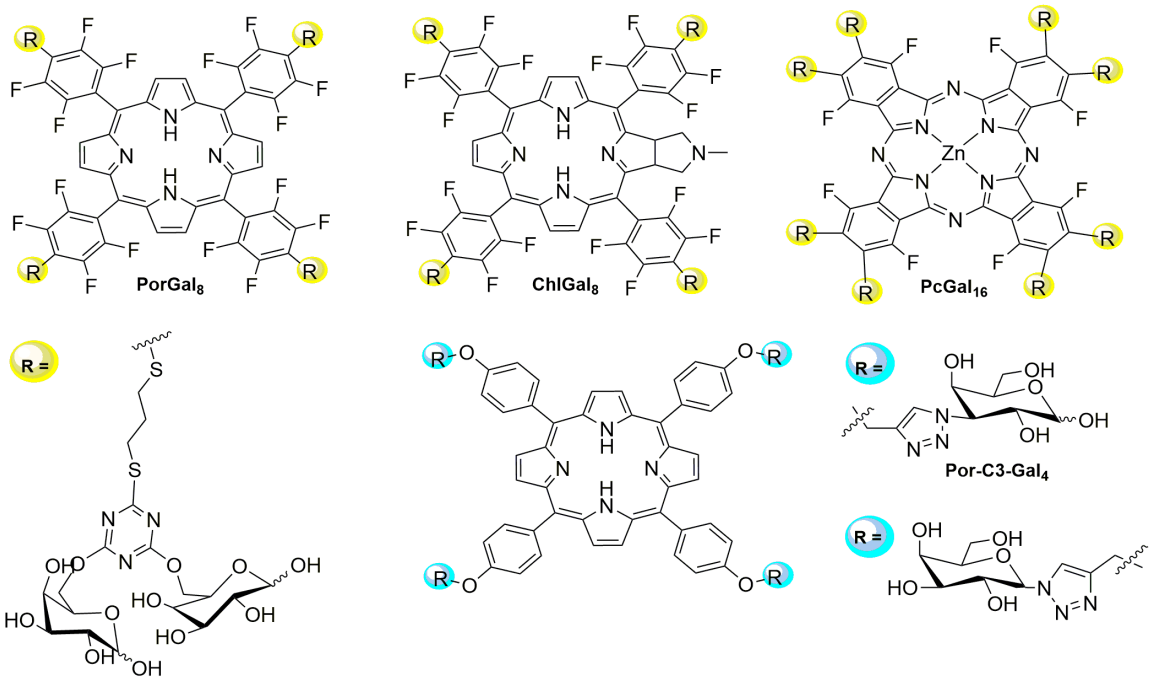

Figure 2.1 Chemical structures of **PorGal$_8$**, **ChlGal$_8$**, **PcGal$_{16}$**, **Por-C3-Gal$_4$** and **Por-C1-Gal$_4$**.

2.1.1 Methods

The following experimental protocols (please see Methods and Materials chapter IX) were used to obtain the data presented in this chapter:

- Synthesis of galactose-conjugates (9.1)

2.1.2 Publication

This chapter comprises the following publications:

Sandrina Silva, Patrícia M. R. Pereira, Maria A. F. Faustino, João P. C. Tomé, José A. S. Cavaleiro, "Porphyrin and phthalocyanine glycodendritic conjugates: synthesis, photophysical and photochemical properties", *Chem. Commun.*, **2012**, 48, 3608-3610.

Patrícia M.R. Pereira, N. V. S. Dinesh K. Bhupathiraju, Waqar Rizvi, Rosa Fernandes, João P.C. Tomé, Charles M. Drain, Comparative studies of porphyrin C3-galactose and porphyrin C1-galactose conjugates for enhanced photodynamic therapy, *under final preparation*.

2.2 Synthesis of galactodendritic porphyrin $PorGal_8$, chlorin $ChlGal_8$ and phthalocyanine $PcGal_{16}$

2.2.1 Rationale for the synthesis

The rationale for the synthesis of **$PorGal_8$, $ChlGal_8$** and **$PcGal_{16}$** was to improve the solubility and to increase the binding of porphyrinoids with galactose-binding proteins overexpressed in cancer cells. We have hypothesized that PSs coupled with galactodendritic units should be effective in targeting cancer cells, because galactose carbohydrates with a dendritic structure have increased affinity for galactose-binding proteins (namely galectin-1) [9-11].

2.2.2 Synthesis of galactodendritic unit 2

The selected dendritic framework was 2,4,6-trichloro-1,3,5-triazine (TCT) because of its well-known selective reactivity concerning substitution of the chlorine atoms at different temperatures. 1,2:3,4-di-*O*-isopropylidene-α-D-galactopyranose was chosen as the carbohydrate moiety. The synthesis of **galactodendritic unit 2** was carried out in two steps as depicted in Scheme 2.1. Di-nucleophilic substitution of TCT by the galactose moiety was carried out in dry toluene, in the presence of an excess of *N*,*N*-Diisopropylethylamine (DIPEA), providing **di-galactotriazine 1** in 92% yield. Reaction of **di-galactotriazine 1** with 1,3-dimercaptopropane provided the **galactodendritic unit 2** in 89% yield.

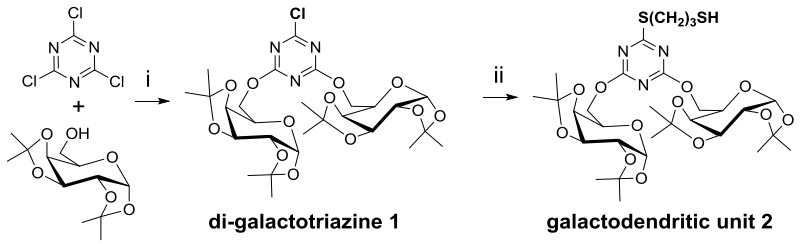

Scheme 2.1 General demonstration of the synthesis of **galactodendritic unit 2.** i)DIPEA, toluene, 48 h, 92%; ii) $HS(CH_2)_3SH$, DIPEA, toluene, 80 ºC, 48 h, 89%.

Di-galactotriazine 1 was easily identified by the resonances of carbohydrate units, and the double substitution was confirmed by two triazine carbon resonances at δ 171.9 and

172.6 ppm. ^{1}H and ^{13}C NMR of **galactodendritic unit 2** show, additionally, the resonance of the mercaptopropane chain.

2.2.3 Synthesis of galactodendritic porphyrinoids

The synthesis of **PorGal$_8$** was achieved by reacting the commercially available platform, 5,10,15,20-tetrakis(2,3,4,5,6-pentafluorophenyl)porphyrin (**TPPF$_{20}$**) with four equivalents of **galactodendritic unit 2** (Scheme 2.2).

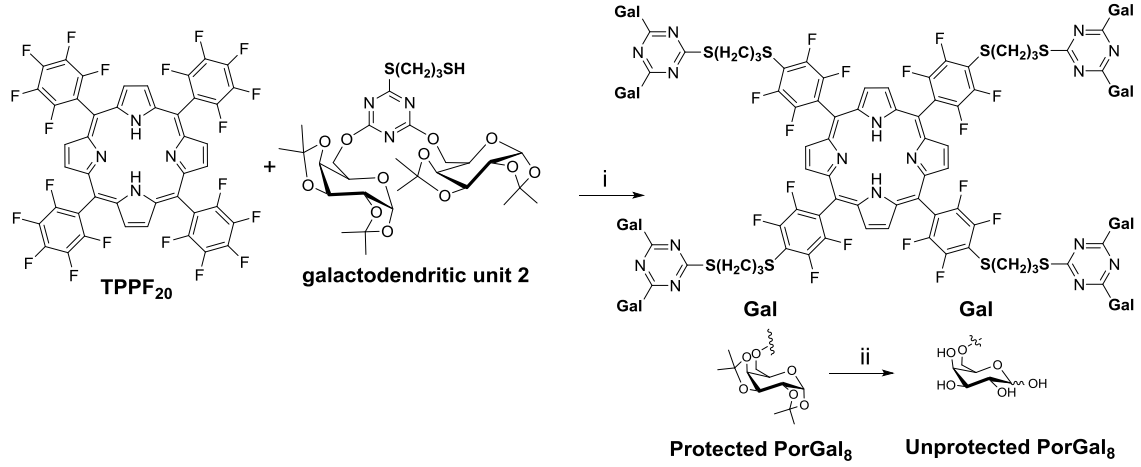

Scheme 2.2 General demonstration of the synthesis of **PorGal$_8$.** i)DIPEA, DMF, 50 ºC, N_2, 24 h, 78%; (ii) TFA/H_2O (9:1, v/v), 80%.

^{1}H, ^{19}F and ^{13}C NMR spectra of **protected PorGal$_8$** clearly illustrate the conjugation and the symmetry of **PorGal$_8$** structure. Accounting the ratio 1:1 between β-pyrrolic protons of Por and anomeric protons of carbohydrate, the tetra-substitution o the Por macrocycle is evident. The tetra-substitution of **TPPF$_{20}$** was further supported by ^{19}F NMR data, showing the absence of the signals corresponding to the Por *para* fluorine atoms. **PorGal$_8$** shows two quartet signals at δ -157.4 and δ -160.2 ppm, corresponding to the *meta* and *ortho* fluorine atoms. Hydrolysis of the isopropylidene protective groups with a mixture of TFA/H_2O (9:1, v:v) produced α/β mixtures of **unprotected PorGal$_8$**. Unprotection of the isopropylidene groups was confirmed by the complete disappearance of the corresponding ^{1}H and ^{13}C resonances. For the anomeric mixture of **unprotected PorGal$_8$**, ^{19}F NMR spectra show two multiplets between δ -158.0 to δ -158.1 and δ -162.7

to δ -162.8 ppm corresponding to *meta* and *ortho* fluorine atoms. Besides the NMR data, all structures were further confirmed by HRMS mass spectrometry.

The $ChlF_{20}$ was synthesized as previously described in the literature, by using 1,3-dipolar addition of $TPPF_{20}$ with azomethine ylides [12, 13], and it was used as a core platform to synthesize the new galactodendritic chlorin (**$ChlGal_8$**, Scheme 2.3). **$ChlGal_8$** was obtained in 70% yield by reacting $ChlF_{20}$ with four equivalents of the previously reported galactodendritic unit and it was characterized by ^{1}H, ^{19}F and ^{13}C NMR spectroscopy and mass spectrometry. The tetra-substitution of the *para* fluorine atoms in $ChlF_{20}$ by the galactodendritic unit was supported by ^{19}F NMR data, showing the absence of the signals corresponding to the Chl *para* fluorine atoms. Unprotection of the isopropylidene groups was confirmed by the complete disappearance of the corresponding ^{1}H resonances of the corresponding CH_3 groups of the isopropylidenes. Besides the NMR data, all structures were further confirmed by HRMS mass spectrometry.

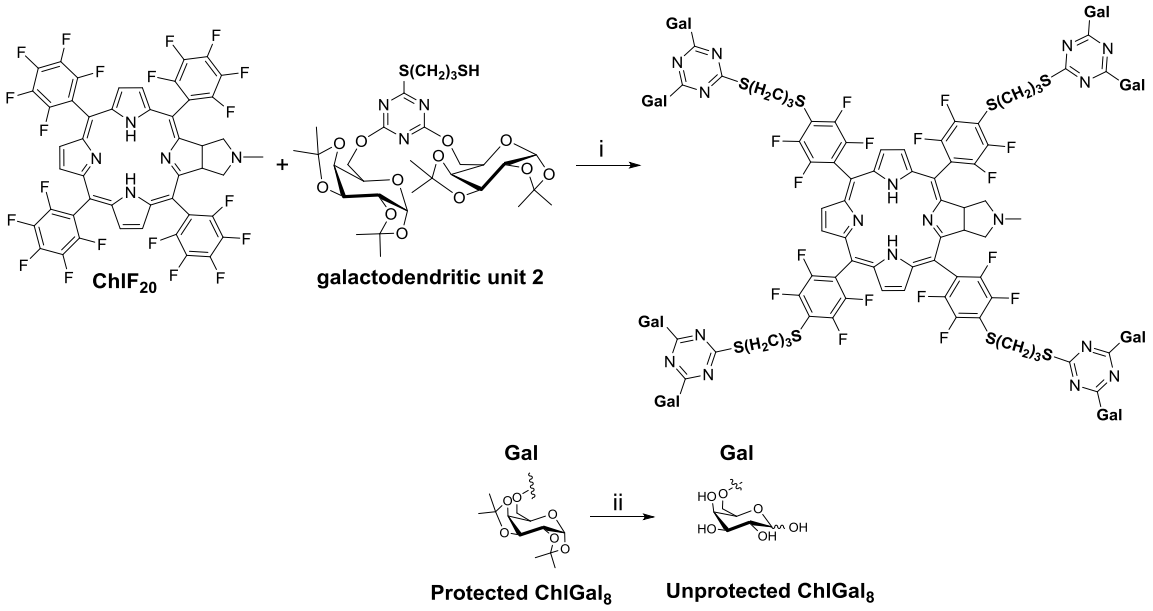

Scheme 2.3 General demonstration of the synthesis of **$ChlGal_4$ and $ChlGal_8$.** i)DIPEA, DMF, 40 ºC, N_2, 30 h, 70%; (ii) TFA/H_2O (9:1, v/v), 87% for **$ChlGal_8$** and 88% for **$ChlGal_4$**.

The synthesis and characterization of **$PcGal_{16}$** were performed by Doctor Sandrina Silva, postdoc student, in the laboratory of Doctor João Tomé, Department of Chemistry –

University of Aveiro, Aveiro, Portugal. Briefly, the synthesis of **$PcGal_{16}$** was achieved by reacting the commercially available platform, hexadecafluorophthalocyaninato zinc(II) (**$ZnPcF_{16}$**) with eight equivalents of **galactodendritic unit 2**. Deprotection was then performed as aforementioned for **$PorGal_8$** and **$ChlGal_8$**.

2.3 Synthesis of porphyrin Por-C3-Gal_4 and Por-C1-Gal_4

2.3.1 Rationale for the synthesis

The rationale for the synthesis of **Por-C3-Gal_4** was to improve the solubility and to increase the binding of porphyrinoids with galectin-1 protein overexpressed in cancer cells. We have hypothesized that the conjugation of a PS with galactose through carbon-3 will increase the affinity of the PS to galectin-1 [14]. To validate the specificity of **Por-C3-Gal_4** to galectin-1 protein, the same porphyrin was conjugated with galactose through carbon-1 **(Por-C1-Gal_4)**.

2.3.2 Synthesis of galactose porphyrinoids

Por-C3-Gal_4 and **Por-C1-Gal_4** were synthesized and characterized by Doctor Dinesh Bhupathiraju (postdoc student) and Waqar Rizvi (PhD student) in the laboratory of Professor Charles Michael Drain, Department of Chemistry – Hunter College of CUNY, New York, United States. Briefly, 3-azido-galactose-tetraacetate and a 5,10,15,20-Tetrakis(4'-propargyloxyphenyl)-2H-porphyrin (synthesized from commercially available 4'-propargyloxy benzaldehyde and pyrrole) four alkyne groups were synthesized as previously described in the literature [15, 16]. 1-azido-1-deoxy-β-D-galactopyranosidetetraacetate was purchase from commercially available source. Porphyrin was then reacted with 3-azido-galactose-tetraacetate or with the commercially available 1-azido-galactose-tetraacetate by copper catalysis (Scheme 2.4). **Por-C3-Gal_4** and **Por-C1-Gal_4** were obtained after deprotection of galactose-acetate groups using sodium methoxide in methanol. Zn demetalation on porphyrins were carried out using TFA at room temperature

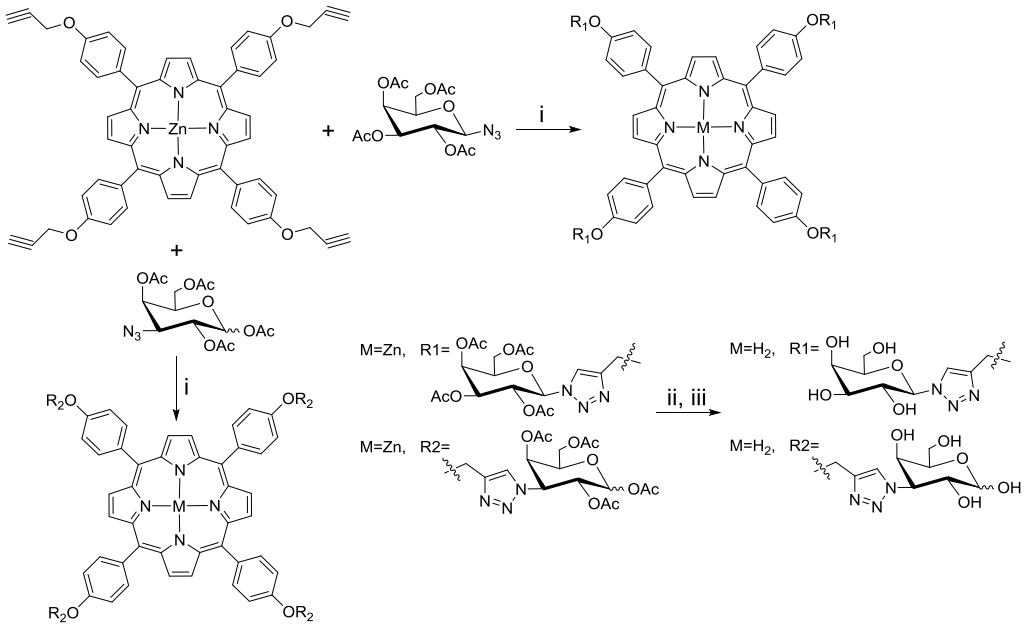

Scheme 2.4 General demonstration of the synthesis of **Por-C1-Gal$_4$** and **Por-C3-Gal$_4$.** i) $CuSO_4$, sodium ascorbate, Cu, THF/H_2O, reflux, 24 h, 90% for C1 galactose and 85% for C3 galactose. ii) NaOMe/MeOH, CH_2Cl_2/MeOH, overnight, r.t., 90% for C1 galactose and 89% for C3 galactose. iii) TFA, r.t. 6h, 86%.

2.4 References

1. Novakova V, Kobak RZU, Kucera R, Kopecky K, Miletin M, Krepsova V, Ivincova J, Zimcik P (2012) The effect of the number of carbohydrate moieties on the azaphthalocyanine properties. Dalton Trans 41: 10596-10604.

2. Lyubimtsev A, Iqbal Z, Crucius G, Syrbu S, Taraymovich ES, Ziegler T, Hanack M (2011) Aggregation behavior and UV-vis spectra of tetra- and octaglycosylated zinc phthalocyanines. J Porphyrins Phthalocyanines 15: 39-46.

3. Iqbal Z, Lyubimtsev A, Herrmann T, Hanack M, Ziegler T (2010) Synthesis of octaglycosylated Zinc(II) phthalocyanines. Synthesis-Stuttgart 3097-3104.

4. Zorlu Y, Dumoulin F, Bouchu D, Ahsen V, Lafont D (2010) Monoglycoconjugated water-soluble phthalocyanines. Design and synthesis of potential selectively targeting PDT photosensitisers. Tetrahedron Lett 51: 6615-6618.

5. Soares ARM, Tomé JPC, Neves MGPMS, Tomé AC, Cavaleiro JAS, Torres T (2009) Synthesis of water-soluble phthalocyanines bearing four or eight D-galactose units. Carbohydr Res 344: 507-510.

6. Choi CF, Huang JD, Lo PC, Fong WP, Ng DKP (2008) Glycosylated zinc(II) phthalocyanines as efficient photosensitisers for photodynamic therapy. Synthesis, photophysical properties and *in vitro* photodynamic activity. Org Biomol Chem 6: 2173-2181.

7. Ribeiro AO, Tomé JPC, Neves MGPMS, Tomé AC, Cavaleiro JAS, Iamamoto Y, Torres T (2006) [1,2,3,4-tetrakis(alpha/beta-D-galactopyranos-6-yl)-phthalocyaninato]zinc(II): a water-soluble phthalocyanine. Tetrahedron Lett 47: 9177-9180.

8. Soares ARM, Neves MGPMS, Tomé AC, Iglesias-de la Cruz MC, Zamarrón A, Carrasco E, González S, Cavaleiro JAS, Torres T, Guldi DM, Juarranz A (2012) Glycophthalocyanines as photosensitizers for triggering mitotic: catastrophe and apoptosis on cancer cells. Chem Res Toxicol 25: 940-951.

9. Silva S, Pereira PMR, Silva P, Paz FAA, Faustino MAF, Cavaleiro JAS, Tomé JPC (2012) Porphyrin and phthalocyanine glycodendritic conjugates: synthesis, photophysical and photochemical properties. Chem Commun 48: 3608-3610.

10. Liu F-T, Rabinovich GA (2005) Galectins as modulators of tumour progression. Nat Rev Cancer 5: 29-41.

11. Pereira PMR, Silva S, Cavaleiro JAS, Ribeiro CAF, Tomé JPC, Fernandes R (2014) Galactodendritic phthalocyanine targets carbohydrate-binding proteins enhancing Photodynamic Therapy. Plos One 9: e95529.

12. Silva AMG, Tomé AC, Neves MGPMS, Silva AMS, Cavaleiro JAS (2005) 1,3-dipolar cycloaddition reactions of porphyrins with azomethine ylides. J Org Chem 70: 2306-2314.

13. Silva AMG, Tomé AC, Neves MGPMS, Silva AMS, Cavaleiro JAS (1999) meso-tetraarylporphyrins as dipolarophiles in 1,3-dipolar cycloaddition reactions. Chem Commun 1767-1768.

14. van Hattum H, Branderhorst HM, Moret EE, Nilsson UJ, Leffler H, Pieters RJ (2013) Tuning the preference of thiodigalactoside- and lactosamine-based ligands to galectin-3 over galectin-1. J Med Chem 56: 1350-1354.

15. Lowary TL, Hindsgaul O (1994) Recognition of synthetic *O*-methyl, epimeric, and amino analogs of the acceptor α-L-Fuc *p*-(1→2)-β-D-Gal *p*-OR by the blood-group A and B gene-specified glycosyltransferases. Carbohydr Res 251: 33-67.

16. Chen H, Zeng J, Deng F, Luo X, Lei Z, Li H (2012) Synthesis and photophysical properties of porphyrin-containing polymers. J Polym Res 19: 9880-9889.

Galactodendritic phthalocyanine targets carbohydrate binding proteins enhancing photodynamic therapy

CHAPTER III

Chapter III Galactodendritic phthalocyanine targets carbohydrate binding proteins enhancing photodynamic therapy

3.1 General overview

The molecular mechanisms underlying PDT are not clearly understood. However, it has been described that the generation of ROS will trigger signalling pathways that ultimately destroy the targeted tissue. Cell death in PDT may occur by apoptotic and by non-apoptotic mechanisms (*e.g.* necrosis), or even by a combination of the two mechanisms [1]. Additionally, studies suggest that cell death pathway induced after PDT depends on the PS and its intracellular localization, the PDT dose and the cell metabolic potential (*e.g.* its intrinsic antioxidant capacity) [1]. To enhance the specific deliver/target of PSs in cancer cells, third generation PSs have been synthesized, by conjugating them with galactose sugar [2-12].

Due to their high ROS production and strong absorption in the wavelength range between 650 and 850 nm, where tissue light penetration is rather high, Pcs have been studied as PSs of excellence. Recently, we have reported the synthesis of a new Pc decorated with sixteen molecules of galactose (in a dendritic manner, **PcGal$_{16}$**, Figure SI3.1). **PcGal$_{16}$** demonstrated strong absorbance in the red spectral region (600-800 nm), fluorescence emission bands at 734 and 805 nm, solubility in a phosphate buffered saline (PBS) solution and interaction with human serum albumin (HSA)[12]. Additionally, **PcGal$_{16}$** demonstrated photostability and ability to generate ROS after photoactivation

It is envisaged that the galactose sugar around Pc macrocycle will interact with galectins overexpressed in cancer cells (*e.g.* galectin-1 and galectin-3 [13]). Besides galectins, galactose carbohydrates can bind to GLUT1 (a well-known glucose transporter [14]). The steriospecificity of GLUT1 (recognizing both D-glucose and D-galactose) has been reported [14]. Galactose is a C4 epimer of glucose that can bind the glucose-binding site of GLUT1.

The excellent photo-chemical and –physical properties of **PcGal$_{16}$** prompted us to validate its efficacy against two bladder cancer cell lines, HT-1376 and UM-UC-3 (Figure 3.1). In this section, we define the role of galactodendritic units in promoting the uptake of a Pc through interaction with GLUT1 and galectin-1. The photoactivation of **PcGal$_{16}$** induces

cell death by generating oxidative stress. Although PDT with **PcGal$_{16}$** induces an increase on the activity of antioxidant enzymes immediately after PDT, bladder cancer cells are unable to recover from the PDT-induced damage effects for at least 72 h after treatment. **PcGal$_{16}$** co-localization with galectin-1 and GLUT1 and/or generation of oxidative stress after **PcGal$_{16}$** photoactivation induces changes in the levels of these proteins. Knockdown of galectin-1 and GLUT1, *via* siRNA, in bladder cancer cells decreases intracellular uptake and phototoxicity of **PcGal$_{16}$**.

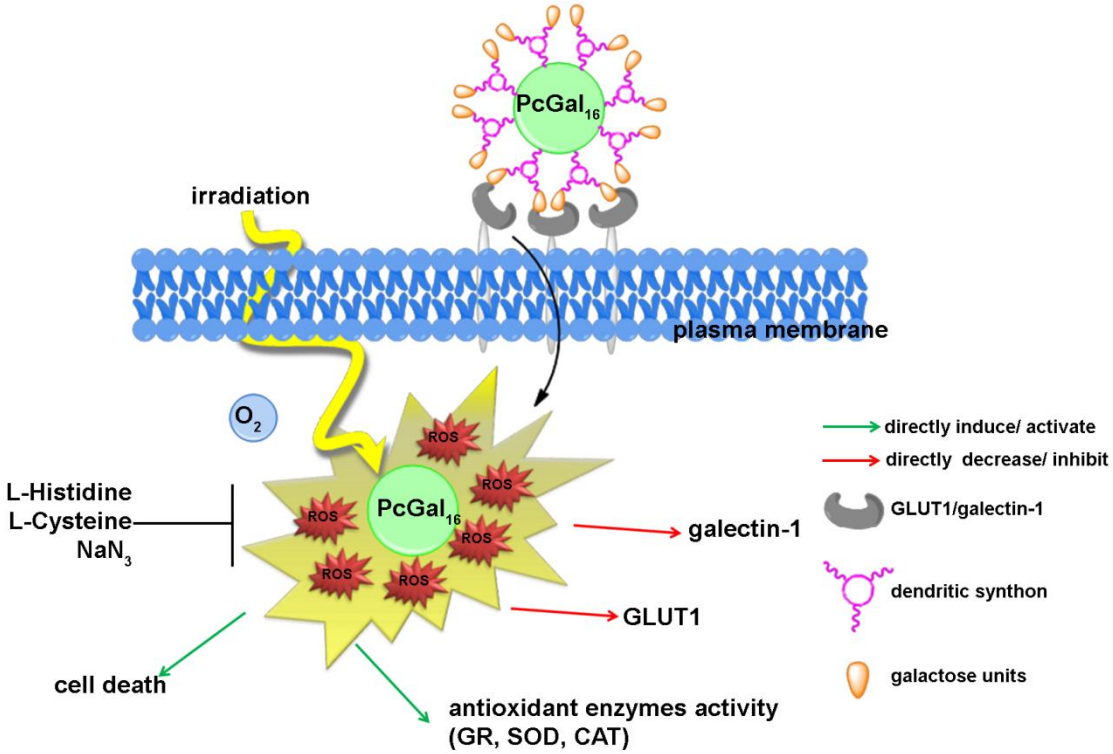

Figure 3.1 Hypothetic illustration of phototoxicity of PcGal$_{16}$ in human bladder cancer cells. The uptake of **PcGal$_{16}$** by bladder cancer cells is modulated by the presence of carbohydrate-binding proteins present at the cell surface (*i.e.* GLUT1 and galectin-1). **PcGal$_{16}$** is a nontoxic compound *per se*, and has high photocytotoxic efficiency against bladder cancer cell lines. Treatment with ROS quenchers demonstrated that cell death in bladder cancer cells is mediated by the production of ROS after PDT. Immediately after PDT with **PcGal$_{16}$** there is an increase on the activity of antioxidant enzymes (superoxide dismutase SOD, catalase CAT and glutathione reductase GR antioxidant enzymes). The photoactivated **PcGal$_{16}$** co-localizes with galectin-1 and GLUT1and reduces their levels.

3.1.1 Methods

The following experimental protocols (please see Methods and Materials chapter IX) were used to obtain the data presented in this chapter:

- Biological models – Culture of HT-1376 and UM-UC-3 bladder cancer cells (9.3.8A)
- Fluorescence spectroscopy and microscopy – uptake of **$PcGal_{16}$** (9.3.8C-E)
- PDT treatments – Photosensitizer **$PcGal_{16}$** (9.3.8F)
- Cell viability assays – MTT, Trypan blue and TUNEL assays (9.3.8G)
- Antioxidant enzyme activities (9.3.8H)
- Transfection assays – knockdown of galectin-1 and GLUT1 using siRNA (9.3.8I)
- Intracellular levels of Reactive Oxygen Species (9.3.8J)
- Redox quenching assays (9.3.8K)
- Western blotting assays – galectin-1, GLUT1, β-actin (9.3.8L)
- Immunocytochemistry assays – galectin-1, GLUT1 (9.3.8M)

3.1.2 Publication

This chapter comprises the following publication:

Patrícia M. R. Pereira, Sandrina Silva, José A. S. Cavaleiro, Carlos A. F. Ribeiro, João P. C. Tomé and Rosa Fernandes, Galactodendritic phthalocyanine targets carbohydrate-binding proteins enhancing photodynamic therapy, *PLOS ONE*, **2014**, 9, e95529.

3.2 $PcGal_{16}$ accumulates in cancer cells and is non-toxic in darkness

To study the cellular uptake of **$PcGal_{16}$**, HT-1376 and UM-UC-3 bladder cancer cells have been incubated with increasing concentrations (0.5, 2.5, 5 and 9 µM) of **$PcGal_{16}$** in PBS for up to 4 h. **$PcGal_{16}$** intracellular accumulation was determined by quantitative spectrofluorimetry and fluorescence microscopy. As shown in Figure 3.2, the uptake of **$PcGal_{16}$** was both concentration- and time- dependent, reaching a plateau in less than 2 h. Addition of 5 µM **$PcGal_{16}$** to HT-1376 and UM-UC-3 cells resulted in an intracellular concentration of 3531±126 and 2973±119 nmol **$PcGal_{16}$** per mg of protein, respectively, after 2 h of incubation (Figure 3.2A).

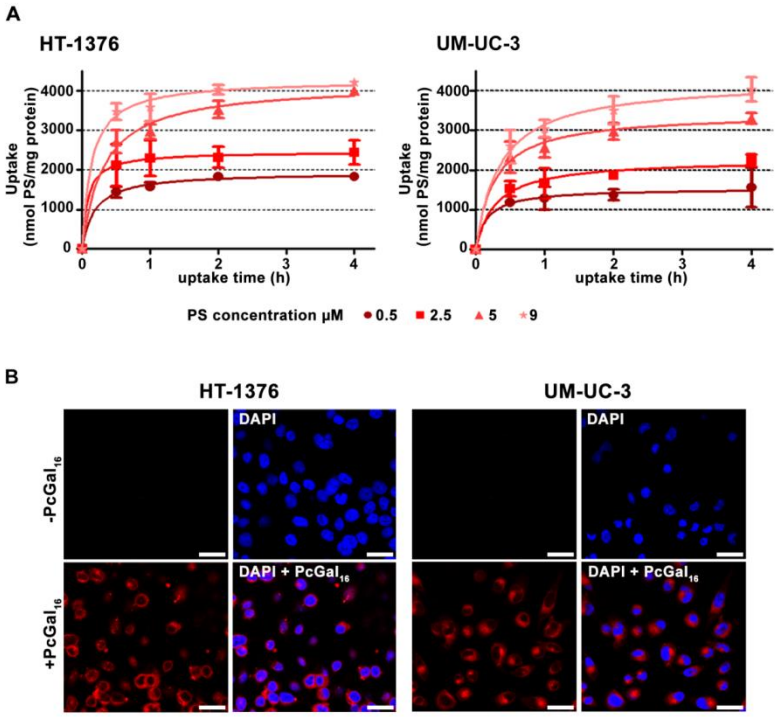

Figure 3.2 $PcGal_{16}$ accumulates in UM-UC-3 and HT-1376 human bladder cancer cells. Intracellular uptake of **$PcGal_{16}$** by HT-1376 and UM-UC-3 bladder cancer cells (A). The concentration of **$PcGal_{16}$** was determined by fluorescence spectroscopy and the results were normalized to protein quantity. Data are the mean ± S.D. of at least three independent experiments performed in triplicates. Representative fluorescence images (B) of bladder cancer cells incubated with **$PcGal_{16}$** (red) in darkness. Cell nucleus is stained with DAPI (blue). *Scale bars* 20 µm.

This spectrofluorimetric data was confirmed by confocal microscopy showing that cells treated with **PcGal$_{16}$** exhibit strong fluorescence, with occasional bright spots in the perinuclear region (Figure 3.2B). **PcF$_{16}$**, the non-conjugated Pc, was used as control (Figure SI3.1). No significant intracellular accumulation was observed when the cells were incubated with 0.5-9 µM **PcF$_{16}$** (data not shown), showing that the uptake of the **PcGal$_{16}$** by cancer cells is enhanced relatively to unconjugated **PcF$_{16}$**.

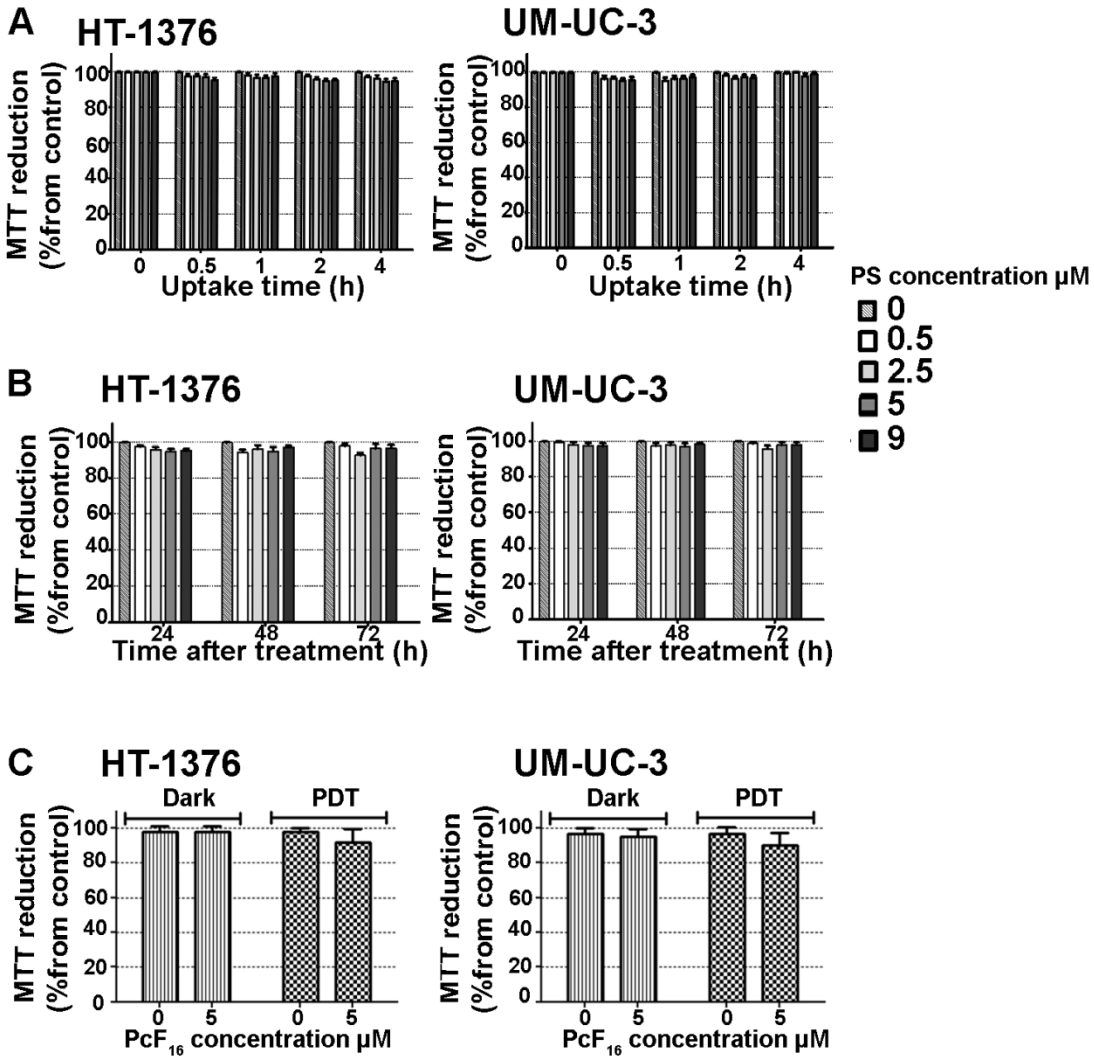

Figure 3.3 PcGal$_{16}$ is non-toxic in darkness, PcF16 is non-toxic in darkness and after PDT. Non-dark toxicity of various concentrations of **PcGal$_{16}$** in HT-1376 and UM-UC-3 cells (A). Non-dark toxicity was assessed using the MTT colorimetric assay 24, 48, and 72 h after treat HT-1376 and UM-UC-3 cells (B). Toxicity of PcF16 at 5 µM in darkness and after PDT (C) in HT-1376 and UM-UC-3 cells. The toxicity was assessed

using the MTT colorimetric assay 24 h after treat HT-1376 and UM-UC-3 cells. Data are the mean ± S.D. of at least three independent experiments performed in triplicates.

After confirmation of **PcGal$_{16}$** uptake by bladder cancer cells (Figure 3.2), its cytotoxic effect in darkness was assessed by the 3-[4,5-dimethylthiazol-2-yl]-2,5-diphenyl-tetrazolium bromide (MTT) colorimetric assay (Figure 3.3). No dark toxicity was observed in untreated cells (up to 4 h) in the presence of 0.45% v/v or less dimethyl sulfoxide (DMSO) in the incubation medium. Moreover, **PcGal$_{16}$** showed no significant cytotoxicity at concentrations up to 9 μM for at least 72 h after treatment (Figure 3.3).

3.3 PcGal$_{16}$ induces cytotoxicity after photodynamic activation

To test the effect of light irradiation (red light at 620-750 nm delivered at 2.5 mW/cm^2 for 40 min, *i.e.* 6 J/cm^2) after **PcGal$_{16}$** uptake on cell viability, MTT was performed 24 h after treatment (Figure 3.4). No cytotoxicity was observed in the untreated sham-irradiated cells (Figure 3.4A) or untreated irradiated cells in the presence of 0.45% (v/v) or less DMSO in PBS (data not shown). However, when HT-1376 and UM-UC-3 cells were incubated with **PcGal$_{16}$** and then irradiated, there was an increased phototoxicity in a concentration- and uptake time-dependent manner (Figure 3.4A). Data showed that **PcGal$_{16}$** exerted a higher phototoxicity on UM-UC-3 cells compared to HT-1376 cells (Figure 3.4A). Moreover, the percentage of cell death in treated cells compared to untreated cells was significantly influenced by the dose of light (Figure 3.4B). The phototoxicity was higher in cells irradiated at 6 J/cm^2 than in cells irradiated at 1.5 J/cm^2 (cells irradiated with light at 2.5 mW/cm^2 for 40 min or 10 min, respectively). On the other hand, irradiation of cells with light at 10 mW/cm^2 for 10 min (*i.e.* 6 J/cm^2) resulted in induction of cell death in untreated control cells. In subsequent experiments, we then performed cells irradiation with light at 2.5 mW/cm^2 for 40 min. Based on the uptake results (Figure 3.2) and MTT data before (Figure 3.3) and after **PcGal$_{16}$** photoactivation (Figure 3.4A,B), we estimate the lowest concentration of **PcGal$_{16}$** and the lowest dose of light necessary to achieve high phototoxicity for both bladder cancer cell lines. When cells were incubated with 5 μM **PcGal$_{16}$** for 2 h and then irradiated with light at 6

J/cm^2 (cells irradiated for 40 min with light at 2.5 mW/cm^2), we observed a significant increase in phototoxicity of HT-1376 and UM-UC-3 cells. The cells were also incubated with 5 µM of PcF_{16} during 2 h and then irradiated. As shown in Figure 3.3 and Figure 3.4, the phototoxicity was higher for **$PcGal_{16}$** than for non-conjugated **PcF_{16}**.

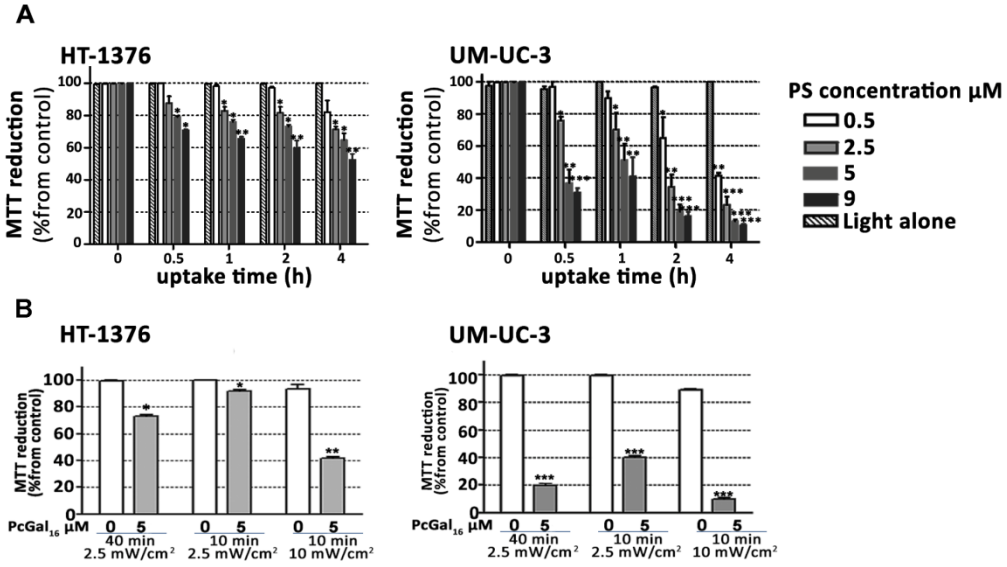

Figure 3.4 $PcGal_{16}$ produces toxicity after PDT. Photocytotoxic effects after **$PcGal_{16}$**-PDT in HT-1376 and UM-UC-3 cells evaluated 24 h after PDT using the MTT assay (A). The percentage of toxicity was calculated relatively to control cells (cells incubated with PBS and irradiated). Data are the mean ± S.D. of at least three independent experiments performed in triplicates. **P*< 0.05, ***P*< 0.01, ****P*< 0.001 significantly different from control cells. Irradiation dose-dependent cell death in response to PDT with **$PcGal_{16}$** (B). Cytotoxicity was assessed 24 h after treatment using the MTT assay. The percentage of cytotoxicity was calculated relatively to control cells (untreated cells). Data are the mean value ± S.D. of at least three independent experiments performed in triplicates. **P*< 0.05, ***P*< 0.01, ****P*< 0.001 significantly different from control cells.

Based on the critical role of ROS in causing cell death after PDT and considering the different PDT-induced phototoxicity observed in UM-UC-3 and HT-1376 cells, the intracellular production of ROS was evaluated immediately after PDT in the cells previously incubated with 5 µM **$PcGal_{16}$** for 2 h. The application of **$PcGal_{16}$** in combination with PDT led to a high significant augmentation of ROS in both bladder cancer cell lines compared with the control (Figure 3.5A,B). The ROS levels (DCF fluorescence fold increase per mg of

protein) in HT-1376 and UM-UC-3 cells were 50.52±12.77 and 74.88±11.49, respectively, when 5 µM H_2DCFDA was used for ROS detection (Figure 3.5B).

To assess the contribution of ROS in **PcGal$_{16}$**-mediated cell death, quenchers of ROS (histidine, sodium azide [15] and cysteine [16]) were added at non-toxic concentrations to the incubation medium when the cells were irradiated. Cell viability evaluated 24 h after treatment was dependent on the used scavenger and cell type (Figure 3.5C). For the cell line UM-UC-3, all quenchers at the employed concentration partially decrease the **PcGal$_{16}$**–PDT-induced phototoxicity. For the cell line HT-1376, none of the quenchers used in these experiments were able to reduce the phototoxicity induced by photoactivated **PcGal$_{16}$**.

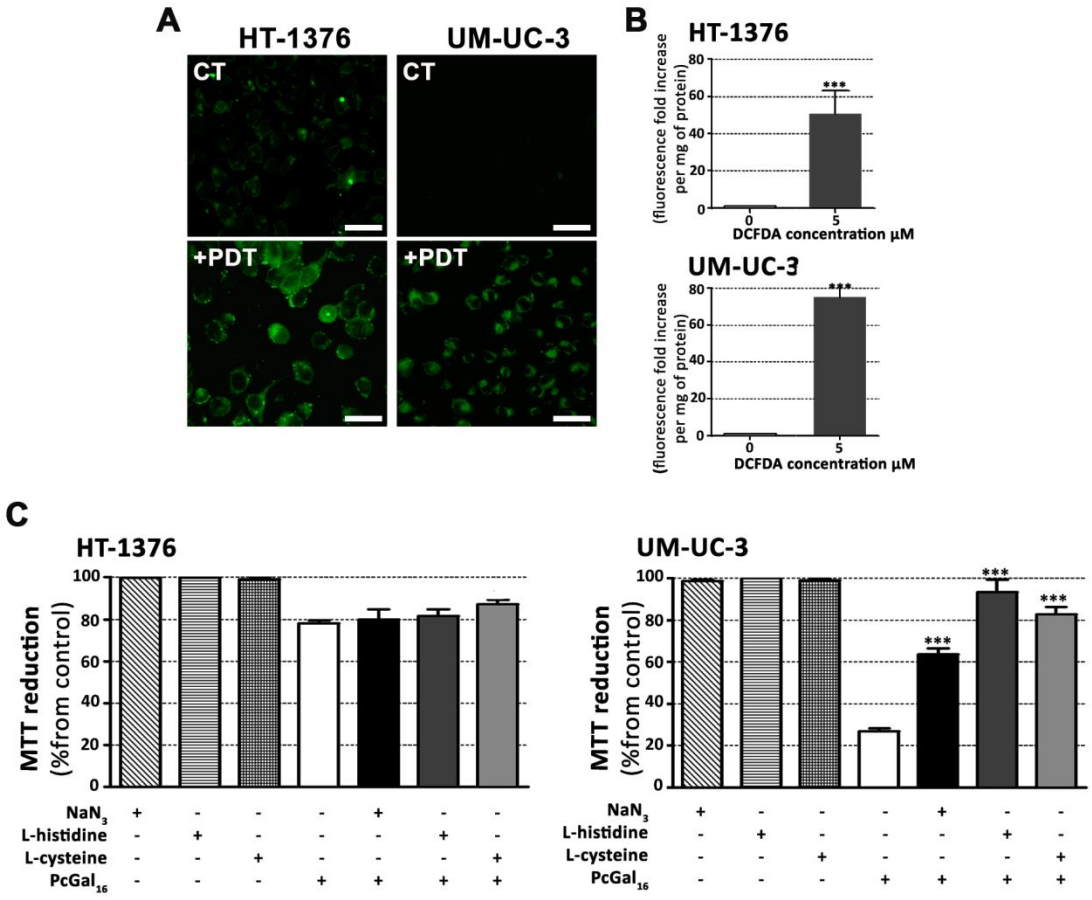

Figure 3.5 PcGal$_{16}$ generates ROS after PDT. Representative fluorescence images (A) and quantification (B) of DCF fluorescence increase (as a measure of ROS production) in HT-1376 and UM-UC-3 cells, after PDT with **PcGal$_{16}$**. *Scale bars* 20 µm. Data are the mean ± S.D. of at least three independent experiments performed in triplicates. *P< 0.05, ***P< 0.001 significantly different from control cells. Photocytotoxicity after PDT with

PcGal$_{16}$ in the presence of 50 nM of ROS quenchers (sodium azide, histidine and cysteine) in HT-1376 and UM-UC-3 cells (C). Cytotoxicity was assessed 24 h after treatment using the MTT assay. The percentage of cytotoxicity was calculated relatively to control cells (untreated cells). Data are the mean value ± S.D. of at least three independent experiments performed in triplicates. ****P*< 0.001 significantly different from MTT reduction (%) after **PcGal$_{16}$**-PDT.

To assess whether PDT has a long-term phototoxic effect, we evaluated cell viability for up to 72 h after PDT treatment. In both cell lines, the results obtained with the MTT colorimetric assay (cell metabolic activity) were correlated with the loss of cell membrane integrity (trypan blue staining) (Figure 3.6A,B). Overall, UM-UC-3 and HT-1376 bladder cancer cells were unable to recover from the PDT-induced damage effects 48 or 72 h after treatment, for **PcGal$_{16}$** concentrations above 5 µM.

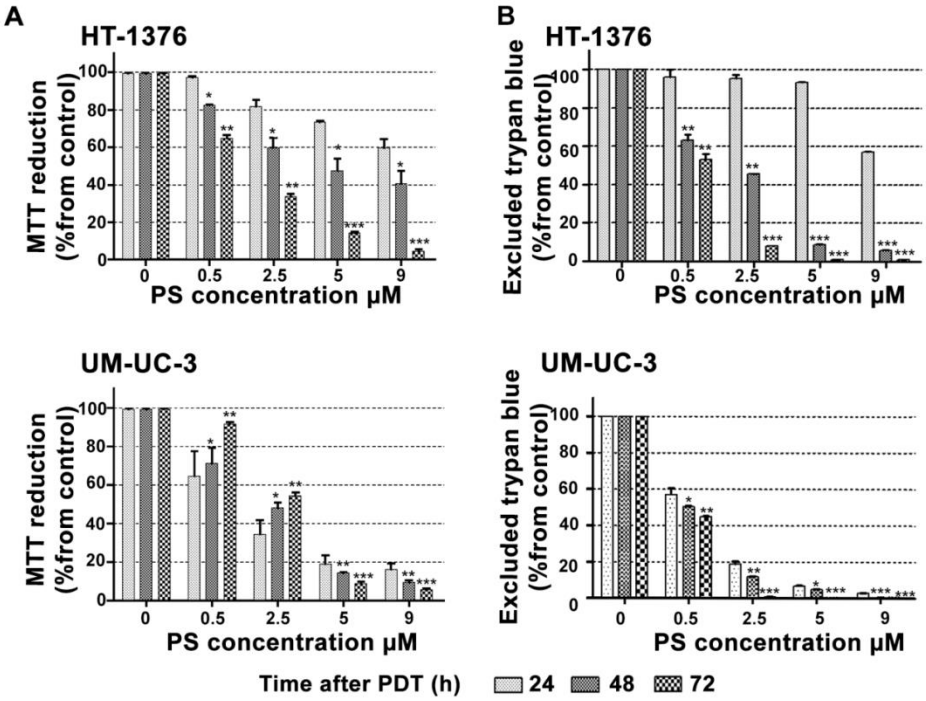

Figure 3.6 PDT with PcGal$_{16}$ has a long-term phototoxicity effect. Cytotoxicity was assessed 24, 48, and 72 h after **PcGal$_{16}$**-PDT using the MTT (A) and trypan blue staining (B) assays. The percentage of cytotoxicity was calculated relatively to control cells (cells incubated with PBS in darkness and then irradiated) at the respective uptake time. Data are the mean value ± S.D. of at least three independent experiments performed in triplicates. **P*< 0.05, ***P*< 0.01, ****P*< 0.001 significantly different from MTT reduction (%) or excluded trypan blue (%) at 24 h after PDT for the respective concentration.

TUNEL data revealed that there is an induction of cell death in a time-dependent manner in the cells irradiated after incubation with **PcGal$_{16}$** (Figure 3.7). Twenty-four hours after PDT with **PcGal$_{16}$**, the percentage of TUNEL positive cells in UM-UC-3 cell line was 1.8 higher than that of the HT-1376 cells, but after 72 h there was almost the same percentage of TUNEL-positive cells in both cell lines.

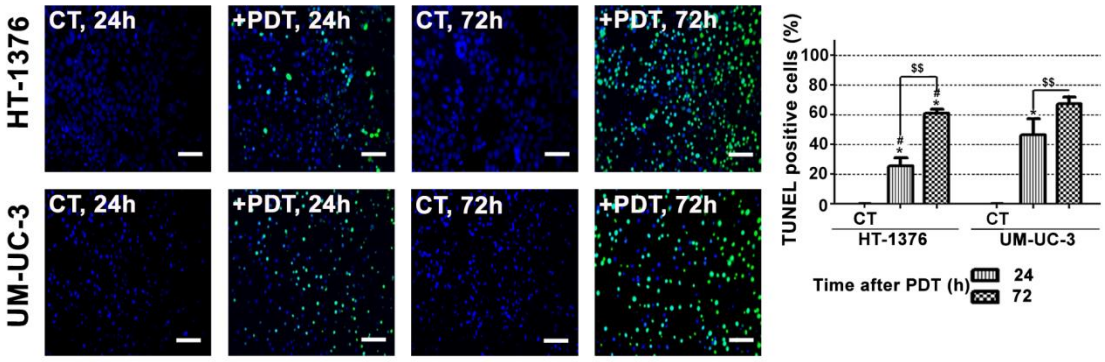

Figure 3.7 PDT with PcGal$_{16}$ has a long-term phototoxicity effect. Representative fluorescence images revealing cell death in HT-1376 and UM-UC-3 cells after PDT with **PcGal$_{16}$** by TUNEL staining 24 and 72 h after treatment. DAPI was used for nuclei staining (blue) and TUNEL staining was used to visualize dead cells (green). *Scale bars* 20 µm. Quantification of TUNEL-positive cells 24 and 72 h after PDT with **PcGal$_{16}$**. **P*< 0.05 significantly. different from control cells. $^{\$\$}$*P*< 0.01 significantly different from TUNEL-positive cells 24 h after PDT. $^{\#}$*P*< 0.05 significantly different from TUNEL-positive UM-UC-3 cells at the respective time after PDT.

Table 3.1 Values for photocytotoxic concentration (IC_{50}, µM) of photoactivated **PcGal$_{16}$** on human bladder cancer cell lines, HT-1376 and UM-UC-3.

	HT-1376 cell line			**UM-UC-3 cell line**		
Hours after PDT	24	48	72	24	48	72
IC_{50} (µM), $CI_{95\%}$	-	3.3 [0.6;10.7]	2.5 [2.2;2.9]	2.1 [0.9;5.0]	2.8 [2.4; 3.2]	2.6 [2.6;2.7]

IC_{50} is the incubation concentration that inhibits the proliferation of cultures in 50%, after cells´ incubation with **PcGal$_{16}$** and irradiation. IC_{50} values were calculated using the MTT dose response curves (24, 48, and 72 h after PDT), obtained for cells incubated with **PcGal$_{16}$** at various concentrations for 2 h.

$CI_{95\%}$: 95% Confidence interval.

The concentrations of **PcGal$_{16}$** necessary to inhibit the metabolic activity of UM-UC-3 and HT-1376 bladder cancer cells in 50% can be estimated from Figure 3.6. These values, named as "photocytotoxic concentrations" (IC_{50}) are reported in Table 3.1. Data show that 24 h after PDT, IC_{50} value is lower for UM-UC-3 when compared with HT-1376 cells and similar for these cell lines 72 h after PDT.

3.4 PcGal$_{16}$ induces antioxidant enzyme response after photodynamic therapy

Considering the different levels of ROS produced in the two bladder cancer cell lines after PDT with **PcGal$_{16}$**, we investigated (immediately after PDT) the involvement of specific antioxidant enzymes [17] in the detoxification of ROS and/or resulting toxic products. For that, the activities of the three major antioxidant enzymes, Superoxide dismutase (SOD), catalase (CAT), and glutathione peroxidase (GPox) were determined by spectroscopy [18]. SOD catalyses the dismutation of superoxide radical anions into hydrogen peroxide and molecular oxygen. Hydrogen peroxide is then removed by CAT when it is present at high concentrations or by GPox when present at low concentrations. Knowing about the indirect antioxidant function [17] of GR in the replenishment of gluthathione levels in reduced form (GSH) and of glutathione S-transferase (GST) in the elimination of reactive compounds through their conjugation with GSH, their activities were also determined.

In UM-UC-3 control cells, the activities of GR, SOD and CAT were 1.5-fold, 1.9-fold and 1.5-fold higher, respectively, than in HT-1376 control cells (Table 3.2). There was no significant difference in the activities of GST and GPox between the control cells of the two cell lines. After PDT with **PcGal$_{16}$**, there was a 1.3-fold, 3.1-fold and 1.5-fold increase in the activities of GR, SOD and CAT in UM-UC-3 cells. In HT-1376 cells, there was a 2.2-fold, 4.6-fold and 4.8-fold increase in GR, SOD and CAT activities and a 2-fold decrease in the activity of GST after PDT with **PcGal$_{16}$**. Treatment of HT-1376 resulted in a 2.3-fold increased of CAT activity as compared to UM-UC-3-treated cells. The ability of HT-1376 cells to produce an antioxidant adaptive response, activating the antioxidant enzymes GR, SOD and CAT can explain the higher resistance observed 24 h after PDT with **PcGal$_{16}$** as compared with UM-UC-3 cells.

Table 3.2 Values of activity (mU/mg of protein) of antioxidant enzymes superoxide dismutase (SOD), catalase (CAT), glutathione peroxidase (GPox), glutathione reductase (GR) and glutathione S-transferase (GST) determined after PDT.

Cell line	$PcGal_{16}$-PDT	Enzyme activity (mU/mg of protein)				
		GST	GPox	GR	SOD	CAT
UM-UC-3	-	44.0±1.4	232.4±23.6	252.3±13.9$^{\$}$	56.0±13.1$^{\$}$	36.31±1.3$^{\$}$
	+	39.7±2.7	243.6±12.0	316.1±11.3$^{\#}$	173.6±4.8$^{\#}$	52.89±2.7$^{\#}$
HT-1376	-	50.4±2.4	236.1±9.9	163.4±1.9	29.56±1.9	24.85±2.2
	+	24.6±0.5$^{\$,*}$	252.3±18.2	356.9±30.6$^{\$}$	134.7±4.3$^{\$,*}$	119.8±3.3$^{\$,*}$

$^{\$}P< 0.05$: significantly different from HT-1376 control cells;

$^{\#}P< 0.05$: significantly different from UM-UC-3 control cells;

$^{*}P< 0.05$: significantly different from UM-UC-3 treated cells.

3.5 Knockdown of galectin-1 and GLUT1 decreases the uptake and phototoxicity of $PcGal_{16}$

We investigated whether the presence of the dendritic galactose units around the core of Pc molecule could facilitate the interaction of this PS with specific domains in the plasma membrane of cancer cells. We hypothesized that domains enriched in carbohydrate-binding proteins [19] could facilitate the interaction with **$PcGal_{16}$**, enhancing somehow its cellular uptake, and therefore its photodynamic potential.

Galectin [13] and glucose transporters [14] are expressed in high levels in cancer cells and both have affinity for galactose molecules. Therefore, we have evaluated the protein levels of galectin-1 and GLUT 1 in UM-UC-3 and HT-1376 cells, by Western Blotting and immunofluorescence (Figure 3.8 and Figure 3.9).

The galectin-1 protein levels were higher in UM-UC-3 than in HT-1376 control cells (Figure 3.8A). To determine whether galectin-1 plays a role in the uptake of **$PcGal_{16}$** by cancer cells, siRNA was used to knockdown galectin-1 within UM-UC-3 bladder cancer cells. The treatment of UM-UC-3 cells with a pool of three target-specific siRNAs maximally suppressed galectin-1 by ≈50% at 24 h and 48 h post-transfection (Figure 3.8B), without

affecting the expression of the housekeeping protein β-actin. The transfected cells were then treated with **PcGal$_{16}$**48 h post-transfection. As shown in Figure 3.8C,D, transfected cells displayed a markedly decreased uptake and phototoxicity of **PcGal$_{16}$**.

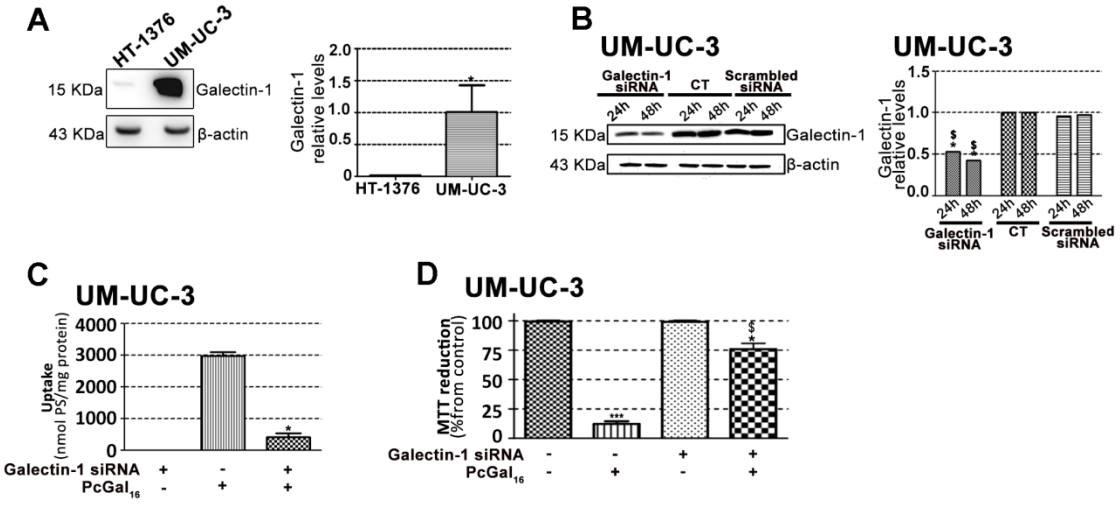

Figure 3.8 Knockdown of galectin-1 decreases the uptake and phototoxicity of PcGal$_{16}$. Western blotting analysis and quantification of galectin-1 protein levels in HT-1376 and UM-UC-3 cells (A). β-actin was blotted as loading control. Quantitative analysis of galectin-1 (normalized to β -actin) expressed as a ratio of the levels found in HT-1376 cells. **P* < 0.05 significantly different from HT-1376 cells. Knockdown of galectin-1 in UM-UC-3 bladder cancer cells as determined by Western blotting 24 and 48 h post-transfection (B). Quantitative analysis of galectin-1 (normalized to β-actin) expressed as a ratio of the levels found in non-transfected control cells. Data represents mean ± S.D. of five independent experiments. **P*< 0.05, $^{\$}$*P*< 0.05 significantly different from non-transfected control cells or cells treated with scrambled siRNA, respectively. Intracellular uptake of **PcGal$_{16}$** by UM-UC-3 bladder cancer cells transfected with galectin-1 siRNA (C). The cells were incubated with **PcGal$_{16}$** 48 h post-transfection with galectin-1 siRNA. Data are the mean ± S.D. of at least three independent experiments performed in triplicates. **P*< 0.05 significantly different from non-transfected control cells. Photocytotoxic effects after **PcGal$_{16}$**-PDT in UM-UC-3 cells transfected with galectin-1 siRNA (D). Phototoxicity was evaluated 72 h after PDT. Data are the mean ± S.D. of at least three independent experiments performed in triplicates. **P*< 0.05, ****P*< 0.001 significantly different from control cells. $^{\$}$*P*< 0.05, significantly different from PDT with **PcGal$_{16}$** in non-transfected cells.

The GLUT1 protein levels were higher in HT-1376 than in UM-UC-3 control cells (Figure 3.9A). Therefore, HT-1376 bladder cancer cells were also treated with a pool of three target-specific GLUT1 siRNAs. Application of GLUT1 siRNA suppressed GLUT1 by ≈50%

and ≈90% at 24 h and 48 h post-transfection, respectively (Figure 3.9B). Treatment of HT-1376 cells with **PcGal$_{16}$** twenty-four hours post-transfection, resulted in a substantial decrease in the uptake and phototoxicity (Figure 3.9C,D).

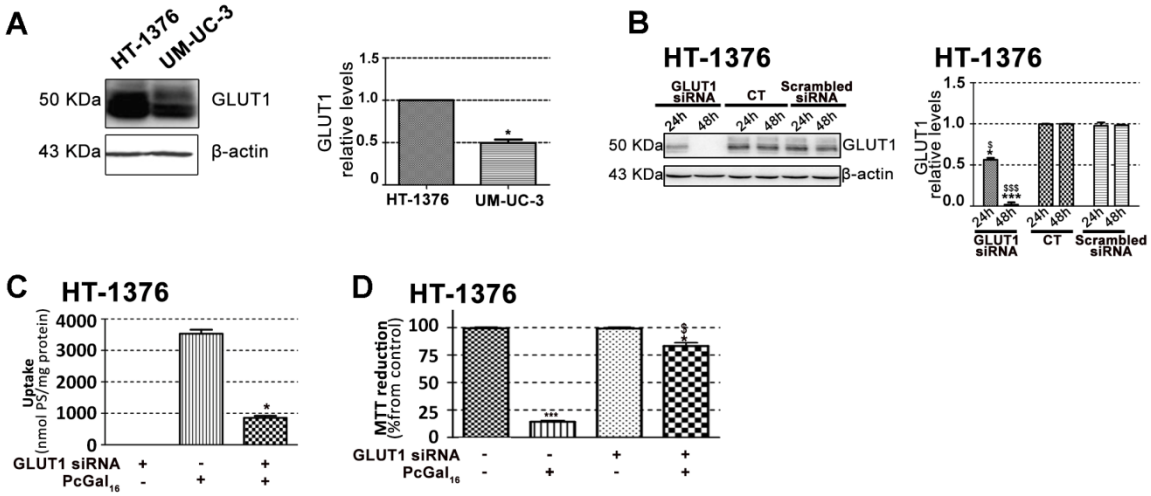

Figure 3.9 Knockdown of GLUT1 decreases de uptake and phototoxicity of PcGal$_{16}$. Western blotting analysis and quantification of GLUT1 protein levels in HT-1376 and UM-UC-3 cells (A). β-actin was blotted as loading control. Quantitative analysis of GLUT1 (normalized to β-actin) expressed as a ratio of the levels found in HT-1376 cells (A). **P*< 0.05 significantly different from HT-1376 cells. Knockdown of GLUT1 in HT-1376 bladder cancer cells as determined by Western blotting 24 and 48 h post-transfection (B). Quantitative analysis of GLUT1 (normalized to β-actin) expressed as a ratio of the levels found in non-transfected control cells. Data represents mean ± S.D. of five independent experiments. **P*< 0.05, ****P*< 0.001 significantly different from non-transfected control cells. $^{\$}$*P*< 0.05, $^{\$\$\$}$*P*< 0.001 significantly different from cells treated with scrambled siRNA. Intracellular uptake of **PcGal$_{16}$** by HT-1376 bladder cancer cells transfected with GLUT1 siRNA (C). The cells were incubated with **PcGal$_{16}$** 24 h post-transfection. Data are the mean ± S.D. of at least three independent experiments performed in triplicates. **P* < 0.05 significantly different from non-transfected control cells. Photocytotoxic effects after **PcGal$_{16}$**-PDT in UM-UC-3 cells transfected with GLUT1 siRNA (D). Phototoxicity was evaluated 72 h after PDT. Data are the mean ± S.D. of at least three independent experiments performed in triplicates. **P*< 0.05, ****P*< 0.001 significantly different from control cells. **P*< 0.05, significantly different from PDT with **PcGal$_{16}$** in non-transfected cells.

3.6 PcGal$_{16}$ decreases the galectin-1 and GLUT1 protein levels

To further explore the role of galectin-1 and GLUT1 in the photodynamic effect induced by **PcGal$_{16}$**, we determined the levels of these proteins before and after PDT. Both incubation of cancer cells with **PcGal$_{16}$** (*i.e.* incubation of cancer cells with **PcGal$_{16}$** in darkness) and PDT with **PcGal$_{16}$** induced a decrease in galectin-1 as observed by Western Blotting and immunofluorescence (Figure 3.10A-C). The decrease observed in galectin-1 was higher in UM-UC-3 cells as compared to HT-1376 cells and it was more evident after PDT. Using confocal fluorescence microscopy, we observed co-localization of **PcGal$_{16}$** with galectin-1 inside bladder cancer cells (Figure 3.10 C).

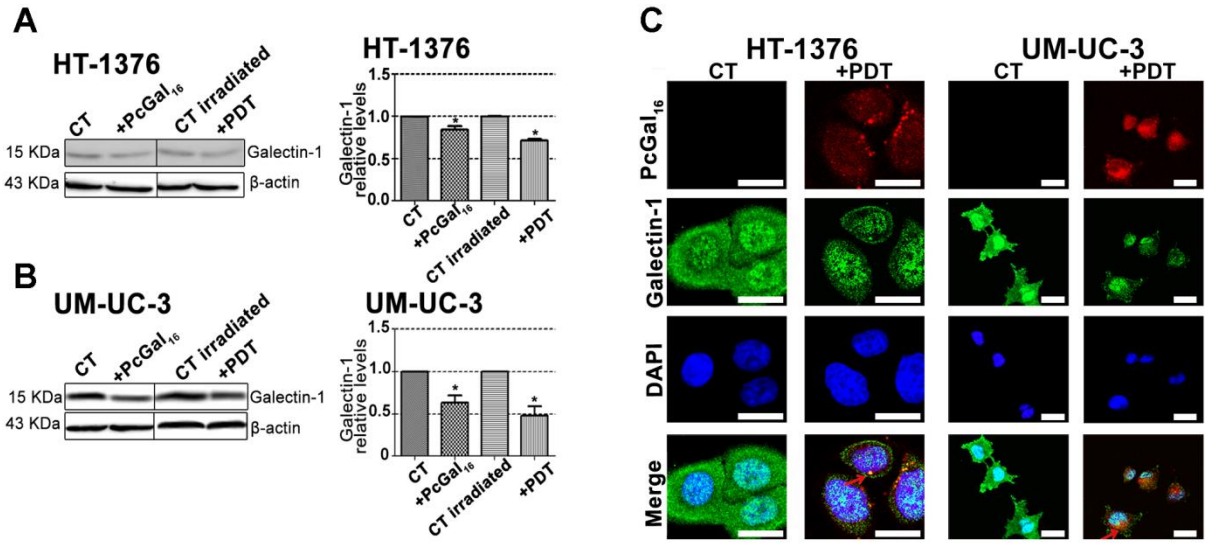

Figure 3.10 PcGal$_{16}$ reduces the levels of galectin-1 in UM-UC-3 and HT-1376 bladder cancer cells. Western blotting analysis and quantification of galectin-1 protein levels in HT-1376 cells (A) or UM-UC-3 cells (B) after uptake with **PcGal$_{16}$** in darkness and after PDT. β-actin was blotted as loading control. Quantitative analysis of galectin-1 (normalized to β-actin) expressed as a ratio of the levels found in untreated HT-1376 or UM-UC-3 cells (A, B). Data represents mean ± S.D. of five independent experiments. **P*<0.05 significantly different from untreated HT-1376 or UM-UC-3 cells. Representative fluorescence images (C) of galectin-1 protein (green) in cancer cells before and after incubation with **PcGal$_{16}$** (red), with DAPI staining the nucleus (blue). *Scale bars* 20 μm.

Similar to what was observed for galectin-1, there was also a decrease in GLUT1 (Figure 3.11A-C) both after **PcGal$_{16}$** uptake and after PDT treatment in HT-1376 cancer cells.

Furthermore, in these cancer cells it was higher after PDT than after **PcGal$_{16}$** uptake in darkness. In UM-UC-3 cells, **PcGal$_{16}$** was not able to reduce GLUT1 protein levels (Figure 3.11 B). In both bladder cancer cell lines there was co-localization of **PcGal$_{16}$** with GLUT1 (Figure 3.11 C). Overall, these findings clearly indicate show the critical involvement of the carbohydrate-binding proteins in the potential of **PcGal$_{16}$** as a therapeutic agent.

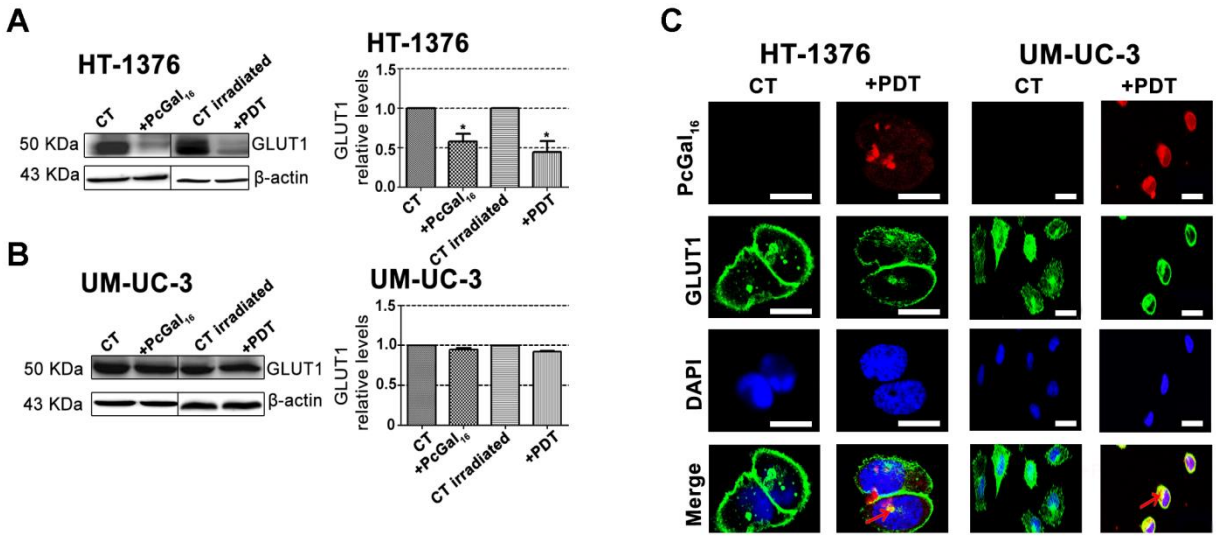

Figure 3.11 PcGal$_{16}$ reduces the levels of GLUT1 in UM-UC-3 and HT-1376 bladder cancer cells. Western blotting analysis and quantification of GLUT1 protein levels in HT-1376 cells (A) or UM-UC-3 cells(B) after uptake with **PcGal$_{16}$** in darkness and after PDT. β-actin was blotted as loading control. Quantitative analysis of GLUT1 (normalized to β-actin) expressed as a ratio of the levels found in untreated HT-1376 or UM-UC-3 cells (A, B). Data represents mean ± S.D. of five independent experiments. **P*<0.05 significantly different from untreated HT-1376 cells. Representative fluorescence images (**C**) of GLUT1 protein (green) in cancer cells before and after incubation with **PcGal$_{16}$** (red), with DAPI staining the nucleus (blue). *Scale bars* 20 µm.

3.7 Discussion

Third-generation PSs such as Pc coupled to carbohydrates are interesting for PDT, because they can be recognized by glycoprotein-based membrane proteins that are overexpressed in tumors [2]. Besides the enhancement of cellular recognition, the presence of dendritic galactose molecules improves Pc solubility and biocompatibility [12]. We have recently reported the synthesis of a new Pc with dendrimers of galactose sugar (**$PcGal_{16}$**) that has valuable spectroscopic and photochemical properties [12]. In this study, we showed that **$PcGal_{16}$** is a nontoxic compound *per se*, and has high photocytotoxic efficiency in two bladder cancer cell lines, which is paralleled with its high ability to produce ROS and to induce oxidative stress.

The high intracellular uptake of the glycoconjugated PS, **$PcGal_{16}$**, can be explained by the presence of carbohydrate cellular transporters or receptors present at the cell surface. Although the **$PcGal_{16}$** uptake was quite similar in the two bladder cancer cell lines, the expression of carbohydrate-binding proteins GLUT1 and galectin-1 is different amongst them. Besides its role in the import and export of glucose [14], the isoform of GLUT1 also transports D-galactose [14] having lower affinity for it than for D-glucose. Studies have been suggested that the hydroxyl groups in C1, C3 and C4 positions of D-galactose are hydrogen bond acceptors for GLUT1 sugar uptake site [20]. Like other galectins, galectin-1 has a CRD able to recognize and bind β-galactose [21]. Our assays demonstrated that galectin-1 and GLUT1 are both expressed by UM-UC-3 and HT-1376 cells. However, HT-1376 cells present higher GLUT1 levels compared with UM-UC-3 cells, and the contrary was observed for galectin-1. Although a similar **$PcGal_{16}$** uptake was observed in the two bladder cancer cell lines, both GLUT1 and galectin-1 may contribute for its specificity modulating the intracellular uptake. Knockdown of galectin-1 and GLUT1 in UM-UC-3 and HT-1376 cells, respectively, was associated with a marked decrease of **$PcGal_{16}$** uptake and phototoxicity. Together, these data demonstrated that galectin-1 and GLUT1 contribute for the efficacy of PDT mediated by **$PcGal_{16}$**.

Interestingly, although the similar uptake of **$PcGal_{16}$** by UM-UC-3 and HT-1376 cells, the phototoxicity induced 24 h after PDT was higher in UM-UC-3 cells than in HT-1376 cells.

Such lack of association between uptake and phototoxicity has been described [22, 23]. We investigated whether the higher phototoxicity observed in UM-UC-3 cells was due to higher production of ROS and/or higher oxidative damage compared with that in HT-1376 cells. As expected, the ability of **PcGal$_{16}$** to produce ROS was higher in UM-UC-3 than in HT-1376 cells.

In PDT, it has been described that ROS can be generated by two photochemical reactions [24, 25]. In type-II photochemical reactions, the excited PS in its triplet state can transfer its energy to molecular oxygen leading to the formation of $^1O_2$. Type-I photochemical reactions happen when an excited PS reacts with a biological substrate forming radicals and radical ions. Treatment with ROS quenchers demonstrated that in UM-UC-3 cells, $^1O_2$ should have a high effect since cell death was highly reduced with quenchers of $^1O_2$ (sodium azide and histidine). Further studies using more accurate techniques (*e.g.* electron spin resonance) are needed to gain insight into the contribution of specific ROS in **PcGal$_{16}$**-mediated cell death after PDT.

Interestingly, we observed that PDT with **PcGal$_{16}$** has a long-term phototoxic effect in both cancer cell lines. Cytotoxicity assays (MTT, trypan blue and TUNEL assays) performed 72 h after PDT demonstrated that UM-UC-3 cells were not able to recover. Moreover, in HT-1376 cells there was a marked induction of cell death occurring from 24 to 72 h after PDT with **PcGal$_{16}$**. The three distinct cytotoxic methods used in the present work are widely applied in the study of cell death: MTT (indicator of metabolic activity), trypan blue staining (indicator of membrane integrity loss occurring in necrosis or in late stages of apoptosis) and TUNEL assay (indicator of DNA fragmentation, a key factor of apoptosis). Cell death in PDT may occur by apoptosis or necrosis, or even by a combination of the two mechanisms [1]. A more specific and comprehensive study is needed to understand the specific cell death pathways induced after PDT with **PcGal$_{16}$** in the bladder cancer cells used in this study. The different cell death obtained 24 h after PDT in UM-UC-3 and HT-1376 cells can be partially explained by the different amount of ROS present in both cells lines after irradiation. In addition, the resistance exhibited by HT-1376 cells could be due to the presence of efficient protective mechanisms, at least in the first stages after photodynamic treatment. Cytoprotective mechanisms initiated by cancer cells after PDT are well-known [25]. The

increase of antioxidant molecules (*e.g.* gluthathione, vitamin C and vitamin E) [26] and the induction of genes encoding proteins involved in apoptosis or in the repair of lesions [27] are two of the well-known cytoprotective mechanisms induced after PDT. Another one is based on the equilibrium between photo-oxidative impairment of cells by ROS *vs.* elimination of ROS by the activity of cellular antioxidant enzymes. Recent studies have shown that PDT caused increased-antioxidant enzymes activity and expression [28]. Thus, PDT efficacy can be influenced by the antioxidant response of the enzymes SOD, the GSH system and CAT.

Our data demonstrated that after PDT with **PcGal$_{16}$** there was an increase in the activity of SOD, CAT and GR antioxidant enzymes in both cell lines, being higher in HT-1376 than in UM-UC-3 cells. This higher antioxidant defense of HT-1376 cells against ROS can explain the results obtained 24 h after treatment. However, it is hypothesized that this was not maintained for 72 h after PDT since for this time point there was a massive cell death. This not only suggests that in this cell line there is a temporal relationship between ROS levels and cell death, but shows that antioxidant enzymes activity is of greater importance in protecting HT-1376 cells for at least 24 h after PDT with **PcGal$_{16}$**. Regarding the activity of antioxidant enzymes, in HT-1376 cells it was also observed a decrease in the activity of GST, which is an enzyme implicated in cells defense against oxidation products. This enzyme has been described as protecting cells from DNA desintegration and drug toxicity [29]. GST isoforms are overexpressed in multidrug resistant tumors having an important role in tumors drug resistance by direct detoxification or inhibition of the MAP kinase pathway [29]. Thus, the higher cell death observed in HT-1376 cells 72 h after treatment can be also related with the activity of GST. A decrease in the activity of GST can be associated with DNA fragmentation and cell death 72 h after treatment.

Understanding the role of galactose moieties in the recognition of the PS by cancer cells may allow the investigation and development of more focused therapeutic strategies. Thus, we investigated whether **PcGal$_{16}$** could be directly recognized by specific carbohydrate-binding proteins present at the plasma membrane. Consistently, the photoactivated **PcGal$_{16}$** was shown to co-localize and reduce the levels of the plasma membrane proteins galectin-1 and GLUT1. Moreover, the immunofluorescence and Western Blotting studies demonstrated that, although its non-dark toxicity, **PcGal$_{16}$** decreases the levels of galectin-1 and GLUT1 proteins. A

plausible explanation for the decreased levels of the galactose binding proteins, galectin-1 and GLUT1, after incubation with **PcGal$_{16}$** can be the masking of the epitope, which can block antibody-epitope binding due to changes in protein conformation or, eventually, endocytosis of these proteins and subsequent degradation. Thus, the changes observed in the levels of galectin-1 and GLUT1 could be induced directly by the binding of **PcGal$_{16}$** to the carbohydrate-binding proteins and/or indirectly by the generation of ROS after PDT with **PcGal$_{16}$**.

Although significant progress has been made in research related with the role of galectins in cancer, the information underlying the molecular mechanisms that control the expression of these proteins in tumor cells is scarce. The interaction of PSs with galectins (namely galectin-1 and galectin-3) has been studied by spectroscopic studies [30] and molecular modeling analysis [2, 9]; however, they have not been validated by *in vitro* studies. As far as we know, there are no *in vitro* reports indicating whether PSs can modulate the expression of carbohydrate-binding proteins such as galectin-1 and GLUT1. Knowing that galectin-1 expression is correlated with cell metastatic potential [13, 31] and contributes to tumor progression and resistance after conventional cancer therapeutic modalities [13], the ability of **PcGal$_{16}$** to reduce the levels of galectin-1 after its uptake and/or photoactivation prompted us to envisage **PcGal$_{16}$** as a potential candidate for cancer treatment.

Knowing that the overexpression of GLUTs is involved in tumor glycolysis - one of the biochemical "hallmarks" of cancer - the efficiency of **PcGal$_{16}$** as an efficient anti-cancer PS is also evidenced by its ability to reduce GLUT1. GLUT1 is an attractive target to consider in the development of new PSs because it is lower expressed in normal-epithelial tissues or benign epithelial cell tumors when compared with human cancer cells [32]. The function of GLUT1 in the tumorogenesis process has been demonstrated by *in vitro* and *in vivo* studies, where the overexpression of GLUT1 antisense resulted in the inhibition of HL60 leukaemia cells proliferation and MKN-45 derived xenografs, respectively [33, 34]. Based on the results of the current study, we envisage **PcGal$_{16}$** as a promising therapeutic agent for the treatment of bladder cancer.

3.8 References

1. Almeida RD, Manadas BJ, Carvalho AP, Duarte CB (2004) Intracellular signaling mechanisms in photodynamic therapy. Biochim Biophys Acta 1704: 59-86.

2. Zheng G, Graham A, Shibata M, Missert JR, Oseroff AR, Dougherty TJ, Pandey RK (2001) Synthesis of beta-galactose-conjugated chlorins derived by enyne metathesis as galectin-specific photosensitizers for photodynamic therapy. J Org Chem 66: 8709-8716.

3. Daly R, Vaz G, Davies AM, Senge MO, Scanlan EM (2012) Synthesis and Biological Evaluation of a Library of Glycoporphyrin Compounds. Chemistry 18: 14671-14679.

4. Vedachalam S, Choi BH, Pasunooti KK, Ching KM, Lee K, Yoon HS, Liu X-W (2011) Glycosylated porphyrin derivatives and their photodynamic activity in cancer cells. Medchemcomm 2: 371-377.

5. Silva AMG, Tomé AC, Neves MGPMS, Cavaleiro JAS, Perrone D, Dondoni A (2005) Porphyrins in 1,3-dipolar cycloadditions with sugar azomethine ylides. Synthesis of pyrrolidinoporphyrin glycoconjugates. Synlett 857-859.

6. Choi C-F, Huang J-D, Lo P-C, Fong W-P, Ng DKP (2008) Glycosylated zinc(II) phthalocyanines as efficient photosensitisers for photodynamic therapy. Synthesis, photophysical properties and in vitro photodynamic activity. Org Biomol Chem 6: 2173-2181.

7. Iqbal Z, Hanack M, Ziegler T (2009) Synthesis of an octasubstituted galactose zinc(II) phthalocyanine. Tetrahedron Lett 50: 873-875.

8. Lee PPS, Lo P-C, Chan EYM, Fong W-P, Ko W-H, Ng DKP (2005) Synthesis and in vitro photodynamic activity of novel galactose-containing phthalocyanines. Tetrahedron Lett 46: 1551-1554.

9. Pandey SK, Zheng X, Morgan J, Missert JR, Liu TH, Shibata M, Bellnier DA, Oseroff AR, Henderson BW, Dougherty TJ, Pandey RK (2007) Purpurinimide carbohydrate conjugates: effect of the position of the carbohydrate moiety in photosensitizing efficacy. Mol Pharm 4: 448-464.

10. Singh S, Aggarwal A, Thompson S, Tomé JPC, Zhu XC, Samaroo D, Vinodu M, Gao RM, Drain CM (2010) Synthesis and photophysical properties of thioglycosylated chlorins,

isobacteriochlorins, and bacteriochlorins for bioimaging and diagnostics. Bioconjugate Chem 21: 2136-2146.

11. Fujimoto K, Miyata T, Aoyama Y (2000) Saccharide-directed cell recognition and molecular delivery using macrocyclic saccharide clusters: Masking of hydrophobicity to enhance the saccharide specificity. J Am Chem Soc 122: 3558-3559.

12. Silva S, Pereira PMR, Silva P, Paz FAA, Faustino MAF, Cavaleiro JAS, Tomé JPC (2012) Porphyrin and phthalocyanine glycodendritic conjugates: synthesis, photophysical and photochemical properties. Chem Commun 48: 3608-3610.

13. Cindolo L, Benvenuto G, Salvatore P, Pero R, Salvatore G, Mirone V, Prezioso D, Altieri V, Bruni CB, Chiariotti L (1999) Galectin-1 and galectin-3 expression in human bladder transitional-cell carcinomas. Int J Cancer 84: 39-43.

14. Carruthers A, DeZutter J, Ganguly A, Devaskar SU (2009) Will the original glucose transporter isoform please stand up! Am J Physiol Endocrinol Metab 297: E836-E848.

15. Bancirova M (2011) Sodium azide as a specific quencher of singlet oxygen during chemiluminescent detection by luminol and Cypridina luciferin analogues. Luminescence 26: 685-688.

16. Aruoma OI, Halliwell B, Hoey BM, Butler J (1989) The Antioxidant Action of N-Acetylcysteine - Its Reaction with Hydrogen-Peroxide, Hydroxyl Radical, Superoxide, and Hypochlorous Acid. Free Radical Bio Med 6: 593-597.

17. Sies H (1993) Strategies of antioxidant defense. Eur J Biochem 215: 213-219.

18. Weydert CJ, Cullen JJ (2010) Measurement of superoxide dismutase, catalase and glutathione peroxidase in cultured cells and tissue. Nat Protoc 5: 51-66.

19. Lotan R, Raz A (1988) Lectins in cancer cells. Ann N Y Acad Sci 551: 385-396; discussion 396-388.

20. Barnett JE, Holman GD, Chalkley RA, Munday KA (1975) Evidence for two asymmetric conformational states in the human erythrocyte sugar-transport system. Biochem J 145: 417-429.

21. Liu FT, Rabinovich GA (2005) Galectins as modulators of tumour progression. Nat Rev Cancer 5: 29-41.

22. Hirohara S, Obata M, Ogata S, Ohtsuki C, Higashida S, Ogura S, Okura I, Takenaka M, Ono H, Sugai Y, Mikata Y, Tanihara M, Yano S (2005) Cellular uptake and photocytotoxicity of glycoconjugated chlorins in HeLa cells. J Photochem Photobiol B 78: 7-15.

23. Laville I, Pigaglio S, Blais JC, Doz F, Loock B, Maillard P, Grierson DS, Blais J (2006) Photodynamic efficiency of diethylene glycol-linked glycoconjugated porphyrins in human retinoblastoma cells. J Med Chem 49: 2558-2567.

24. Plaetzer K, Krammer B, Berlanda J, Berr F, Kiesslich T (2009) Photophysics and photochemistry of photodynamic therapy: fundamental aspects. Lasers Med Sci 24: 259-268.

25. Buytaert E, Dewaele M, Agostinis P (2007) Molecular effectors of multiple cell death pathways initiated by photodynamic therapy. BBA -Rev Cancer 1776: 86-107.

26. Sattler UG, Mueller-Klieser W (2009) The anti-oxidant capacity of tumour glycolysis. Int J Radiat Biol 85: 963-971.

27. Oleinick NL, Morris RL, Belichenko I (2002) The role of apoptosis in response to photodynamic therapy: what, where, why, and how. Photochem Photobiol Sci 1: 1-21.

28. Saczko J, Kulbacka J, Chwilkowsa A, Pola A, Lugowski M, Marcinkowska A, Malarska A, Banas T (2007) Cytosolic superoxide dismutase activity after photodynamic therapy, intracellular distribution of Photofrin II and hypericin, and P-glycoprotein localization in human colon adenocarcinoma. Folia Histochem Cytobiol 45: 93-98.

29. Townsend DM, Tew KD (2003) The role of glutathione-S-transferase in anti-cancer drug resistance. Oncogene 22: 7369-7375.

30. Bogoeva V, Variale A, Constance J, D'Auria S (2010) Human galectin-3 interacts with two anticancer drugs. Febs J 277: 240-240.

31. Chiariotti L, Berlingieri MT, De Rosa P, Battaglia C, Berger N, Bruni CB, Fusco A (1992) Increased expression of the negative growth factor, galactoside-binding protein, gene in transformed thyroid cells and in human thyroid carcinomas. Oncogene 7: 2507-2511.

32. Younes M, Lechago LV, Somoano JR, Mosharaf M, Lechago J (1996) Wide expression of the human erythrocyte glucose transporter GLUT1 in human cancers. Cancer Res 56: 1164-1167.

33. Chan JY, Kong SK, Choy YM, Lee CY, Fung KP (1999) Inhibition of glucose transporter gene expression by antisense nucleic acids in HL-60 leukemia cells. Life Sci 65: 63-70.

34. Noguchi Y, Saito A, Miyagi Y, Yamanaka S, Marat D, Doi C, Yoshikawa T, Tsuburaya A, Ito T, Satoh S (2000) Suppression of facilitative glucose transporter 1 mRNA can suppress tumor growth. Cancer Lett 154: 175-182.

3.9 Supporting information

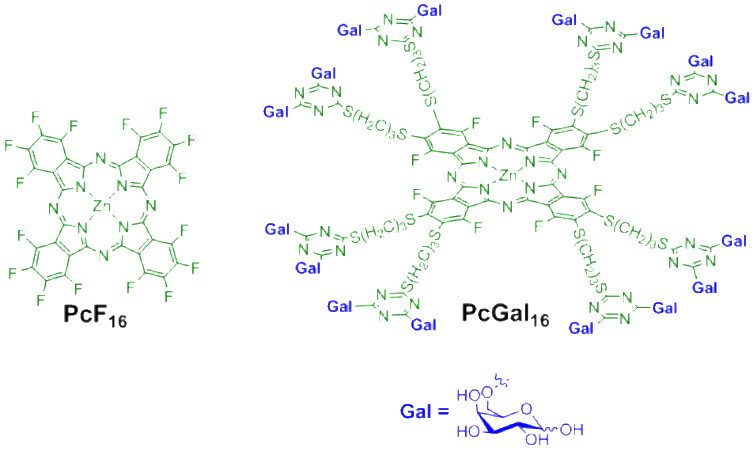

Figure SI3.1 Chemical structures of **PcF$_{16}$** and **PcGal$_{16}$**.

Role of clathrin- and caveolae-mediated pathways in galactodendritic conjugated phthalocyanine uptake by bladder cancer cells

CHAPTER IV

Chapter IV Role of clathrin- and caveolae-mediated pathways in galactodendritic conjugated phthalocyanine uptake by bladder cancer cells

4.1 General overview

The uptake mechanisms and pathways of PSs in cancer cells are highly complex and not fully understood. Nevertheless, the mechanism by which PSs are accumulated in cancer cells can influence the outcome of PDT. In the previous chapter of this thesis, we demonstrated that the uptake of **PcGal$_{16}$** is mediated in somehow by galactose-binding proteins overexpressed in cancer cells (such as galectin-1 and GLUT1). We hypothesized that these proteins increase the accumulation of **PcGal$_{16}$** around cancer cell membranes. In the present study we seek to investigate by which endocytic mechanisms **PcGal$_{16}$** is internalized by HT-1376 and UM-UC-3 bladder cancer cells.

Endocytosis is defined as the process by which molecules are internalized from the cell surface into internal membrane compartments. Endocytosis can be divided into two main pathways: the clathrin-mediated endocytic pathway and the clathrin-independent pathway (the lipid-raft-dependent route) [1]. The clathrin-mediated endocytosis is the most well characterized mechanism for the uptake of molecules into cells. In this pathway, specific adaptor-protein complexes bind directly to clathrin and cargo proteins to for the clathrin-coated vesicles. After endocytosis, the clathrin-coated vesicles are uncoated and fuse with the early endosome. The early endosome can later mature into late endosomes and fuse with lysosomes for degradation. Nevertheless, clathrin-mediated endocytosis can also target cargo molecules to other intracellular compartments such as the Golgi [2]. One division of the non-clathrin endocytic pathway is the caveolae-mediated pathway. The caveolae-mediated pathway involves the clustering of lipid raft components on the plasma membrane into caveolae. Caveolae are flask-shaped invaginations abundant on the cell surface and they contain sphingolipids, cholesterol and the caveolin proteins. Studies have demonstrated that caveolin-1 protein is of utmost importance in the formation of caveolae, because caveolin-1-null mice lack caveolar structures [3].

Endocytosis inhibition results demonstrated that **PcGal$_{16}$** entered UM-UC-3 bladder cancer cells mainly through the clathrin-mediated endocytosis pathway, and that caveolae-mediated endocytosis was involved to a small extent. In HT-1376 bladder cancer cells, both clathrin- and caveolae-mediated endocytosis were involved on the uptake of **PcGal$_{16}$**. Interestingly, knockdown of caveolin-1 protein in HT-1376 cells increased GLUT1 protein levels in the plasma membrane and increased the uptake and phototoxicity of **PcGal$_{16}$** (Figure 4.1).

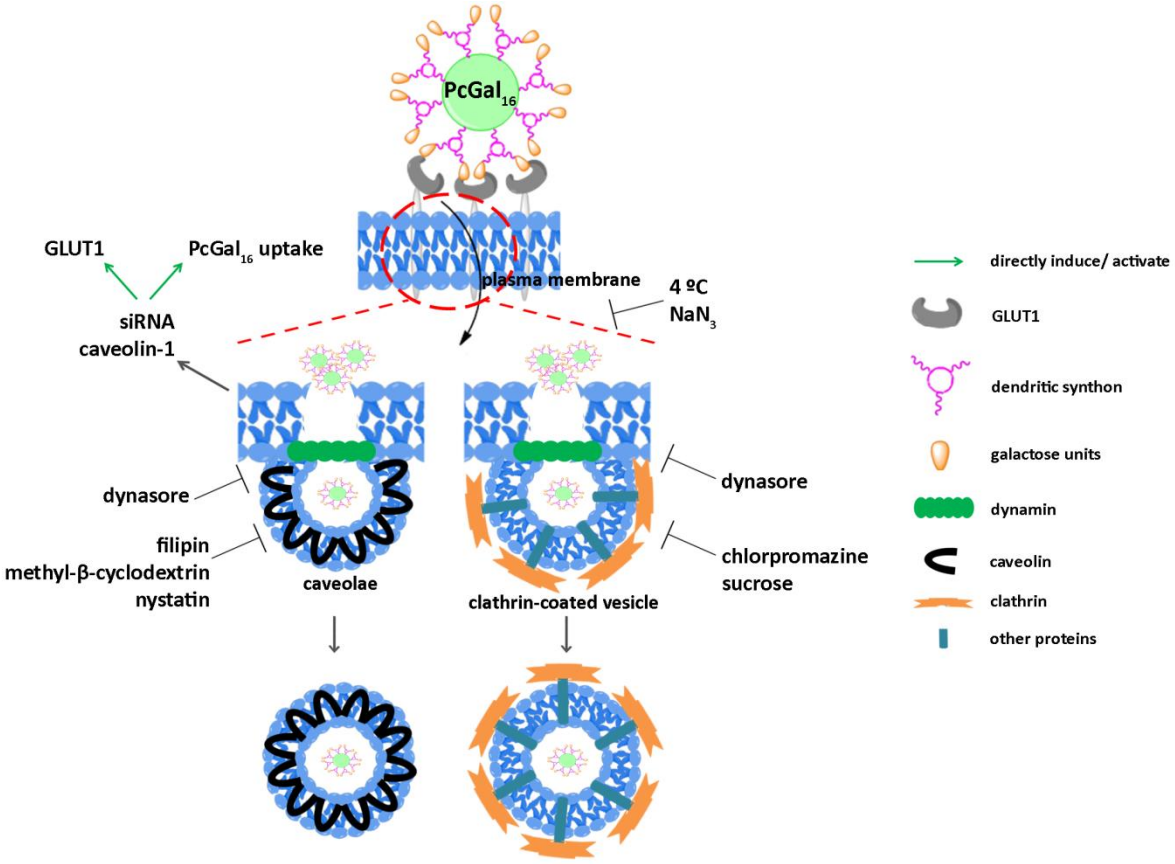

Figure 4.1 Hypothetic illustration of endocytic internalization of PcGal$_{16}$ in human bladder cancer cells. The accumulation of **PcGal$_{16}$** around cancer cell membranes is modulated by the presence of carbohydrate-binding proteins such as GLUT1. The internalization of **PcGal$_{16}$** is an energy dependent process, which makes use of both clathrin- and caveolae-endocytic pathways. Knockdown of caveolin-1 protein increases the uptake of **PcGal$_{16}$** and GLUT1 protein levels at the cell surface.

4.1.1 Methods

The following experimental protocols (please see Methods and Materials chapter IX) were used to obtain the data presented in this chapter:

- Biological models – Culture of HT-1376 and UM-UC-3 bladder cancer cells (9.3.8A)
- Fluorescence spectroscopy – uptake of **PcGal$_{16}$** (9.3.8C,D)
- PDT treatments – Photosensitizer **PcGal$_{16}$** (9.3.8F)
- Cell viability assays – MTT assay (9.3.8G)
- Transfection assays – knockdown of caveolin-1 using siRNA (9.3.8I)
- Western blotting assays – EEA1, Clathrin HC, Flotillin-1, Caveolin-1, GLUT1, EGFR, β-actin (9.3.8L)
- Endocytic inhibitors assays – NaN_3, chlorpromazine, sucrose, dynasore, filipin, methyl-β-cyclodextrin, nystatin (9.3.8N)
- Cell-surface biotinylation assays – GLUT1, EGFR (9.3.8O)

4.1.2 Publication

This chapter comprises the following publication:

Patrícia M.R. Pereira, Teresa M. Ribeiro-Rodrigues, Sandrina Silva, Carlos A.F. Ribeiro, José A. S. Cavaleiro, Henrique Girão, João P.C. Tomé, Rosa Fernandes, Role of clathrin- and caveolae-mediated pathways in galactodendritic conjugated phthalocyanine uptake by bladder cancer cells, *under final preparation.*

4.2 Clathrin- and caveolae-mediated endocytic pathways are required for internalization of $PcGal_{16}$

PSs accumulation in cancer cells can occur through diffusion (few cases) or endocytosis [4-6]. Regarding endocytosis, PSs can enter *via* clathrin-dependent and -independent pathways (such as caveolae-mediated endocytosis). Previous studies using fluorescence microcopy demonstrated that **$PcGal_{16}$** is efficiently accumulated in UM-UC-3 and HT-1376 bladder cancer cells [7]. To understand the mechanisms of cellular internalization of **$PcGal_{16}$** in HT-1376 and UM-UC-3 bladder cancer cells, we determined the expression of different proteins involved in endocytic pathways. Next, we studied the effects of various endocytic inhibitors on the uptake and further phototoxicity of **$PcGal_{16}$**.

The presence of endocytic proteins, EEA1 (early endosome antigen 1), clathrin heavy chain (HC), flotillin-1 and caveolin-1 was determined in whole cells lysates of HT-1376 and UM-UC-3 bladder cancer cells. EEA1 is a membrane-bound protein that is an effector of Rab5 (a small GTPase) controlling early endosome fusion dynamics; flotillin-1 and caverolin-1 are integral membrane proteins and constituents of lipid rafts and clathrin is a major protein component of chlatrin-coated pits [1]. Western blot analysis of whole cell lysates revealed similar levels of EEA1, clathrin HC and flotillin-1 proteins in HT-1376 and UM-UC-3 bladder cancer cells (Figure 4.2). Additionally, the caveolin-1 protein levels were almost two times higher in HT-1376 cells than in UM-UC-3 cells (Figure 4.2).

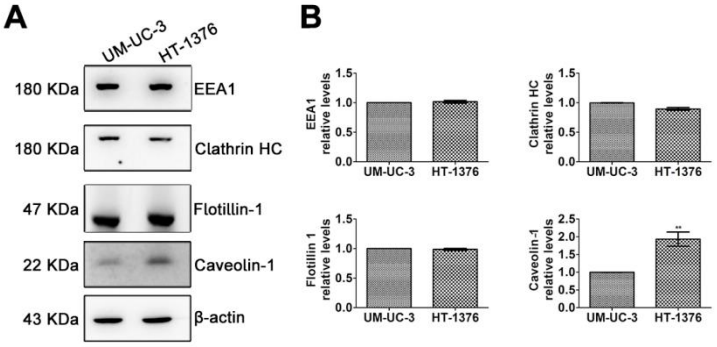

Figure 4.2 HT-1376 and UM-UC-3 bladder cancer cell lines express different endocytic uptake proteins. (A) Western blotting analysis of EEA1, clathrin heavy chain (HC), flotillin-1 and caveolin-1 proteins in UM-UC-3 and HT-1376 bladder cancer cells. β-actin was used as a loading control. (B) Quantitative analysis of EEA1, clathrin HC, flotillin-1 and caveolin-1 (normalized to β -actin) proteins expressed as a ratio of the levels found in

UM-UC-3 cells. Data are the mean ± S.D. of at least five independent experiments. $^{**}P< 0.01$ compared to UM-UC-3 bladder cancer cells.

Next, we examined whether **PcGal$_{16}$** uptake was an active or passive process. We performed uptake assays at 4 ºC, because at this temperature all energy dependent processes (including endocytosis) are inhibited. Additionally, we also performed uptake assays with NaN_3 to inhibit ATP hydrolysis required for active transport [8]. Incubation of HT-1376 and UM-UC-3 bladder cancer cells with **PcGal$_{16}$** at 4 ºC and treatment with NaN_3 resulted in a reduction of uptake by about 90% (Figures 4.3 and SI4.1, Tables SI4.1,SI4.2).

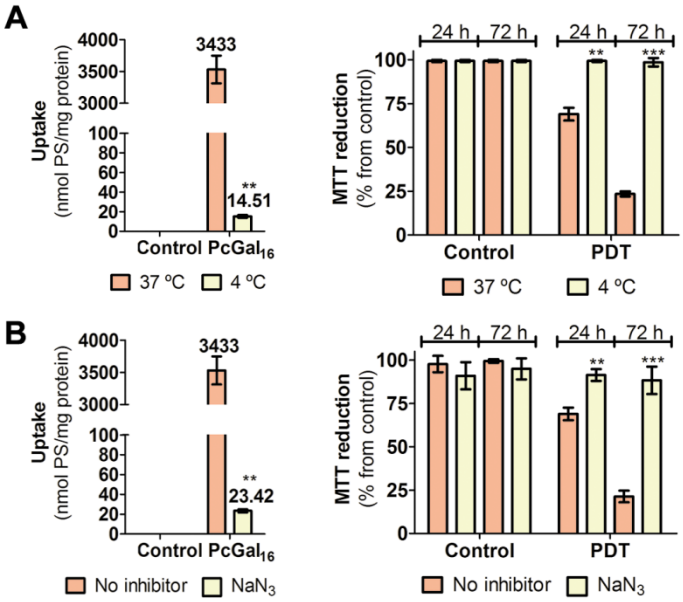

Figure 4.3 Low temperature and pre-incubation of HT-1376 bladder cancer cells with NaN_3 reduce the uptake and phototoxicity of PcGal$_{16}$. Intracellular uptake and phototoxicity of **PcGal$_{16}$** in HT-1376 bladder cancer cells at 4 ºC (A); or after pre-incubation with 20 mM NaN_3. Data are the mean ± S.D. of at least three independent experiments performed in triplicates. $^{**}P< 0.01$, $^{***}P< 0.001$ compared to uptake or phototoxicity at 37 ºC (A) or in the absence of NaN_3 (B).

Specific compounds known to affect endocytic processes were used to understand the uptake mechanisms of **PcGal$_{16}$** in HT-1376 and UM-UC-3 bladder cancer cells. Clathrin-dependent endocytosis was inhibited with hypertonic sucrose and chlorpromazine [9]. Dynasore was used to inhibit dynamin-dependent endocytosis [10]. Filipin, methyl-β-cyclodextrin and nystatin were used to inhibit caveolae-dependent endocytosis [9]. To

determine an optimal protocol for the use of endocytic inhibitors for a certain cell type, it is important to determine their *in vitro* cellular toxicity. We investigated the viability of HT-1376 and UM-UC-3 cancer cells after exposure to different concentrations of sucrose, chlorpromazine, dynasore, filipin, methyl-β-cyclodextrin or nystatin. The inhibitor was diluted in PBS and incubated with the cells for 2 h and toxicity was determined using the MTT assay at 24 h after cells incubation with inhibitors (Figures SI4.2,SI4.3). Based on these results, we determined non-toxic concentrations of endocytic inhibitors to be used in further assays. To study the effect of endocytic inhibitors on the uptake and phototoxicity of **$PcGal_{16}$**, cells were pre-incubated during 30 min with 0.45 mM sucrose, 5 µM chlorpromazine, 40 µM dynasore, 2.5 µg/mL filipin, 5 mM methyl-β-cyclodextrin or 25 µM nystatin. Next, cells were incubated with 5 µM **$PcGal_{16}$** (in the continued presence of the respective inhibitor) for 1.5 h (Figures 4.4-4.6, SI4.4-SI4.6) and the PDT assays were performed by irradiating cells with light at 2.5 mW/cm^2 for 40 min (6 J/cm^2). As phototoxicity is higher in HT-1376 cancer cells at 72 h after PDT when compared with that at 24 h [7], the effect of endocytic inhibitors in this cell line were evaluated at 24 and 72 h after PDT. In UM-UC-3 bladder cancer cells, MTT assay was performed at 24 h after PDT.

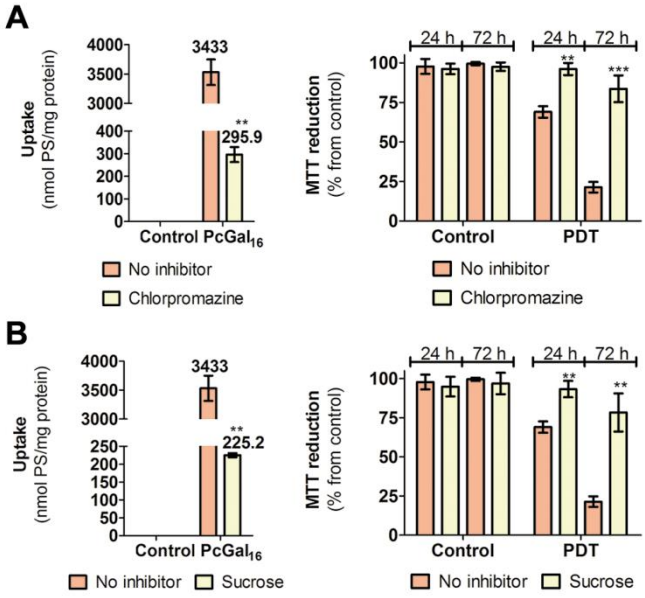

Figure 4.4 Pre-incubation of HT-1376 bladder cancer cells with chlorpromazine and sucrose reduce the uptake and phototoxicity of $PcGal_{16}$. Intracellular uptake and phototoxicity of **$PcGal_{16}$** in HT-1376 bladder cancer cells pre-incubated with 5 µM chlorpromazine (A) or 0.45 mM sucrose (B). Data are the mean ± S.D. of at

least three independent experiments performed in triplicates. $^{**}P< 0.01$, $^{***}P< 0.001$ compared to uptake or phototoxicity in the absence of endocytic inhibitor.

Chlorpromazine and sucrose considerably decreased the **PcGal$_{16}$** uptake and phototoxicity in both HT-1376 (Figure 4.4, Table SI4.1) and UM-UC-3 (Figure SI4.4, Table SI4.2) bladder cancer cells, indicating the involvement of clathrin-mediated endocytosis in **PcGal$_{16}$** uptake. Dynasore decreased the uptake of **PcGal$_{16}$** by 66% and 21% in HT-1376 and UM-UC-3 cells, respectively (Figures 4.5, SI4.5 and Tables SI4.1,SI4.2).

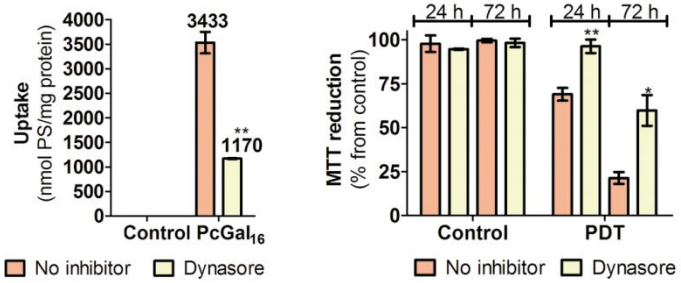

Figure 4.5 Pre-incubation of HT-1376 bladder cancer cells with dynasore reduces the uptake and phototoxicity of PcGal$_{16}$. Intracellular uptake and phototoxicity of **PcGal$_{16}$** in HT-1376 bladder cancer cells pre-incubated with 40 μM dynasore. Data are the mean ± S.D. of at least three independent experiments performed in triplicates. $^{*}P< 0.05$, $^{**}P< 0.01$ compared to uptake or phototoxicity in the absence of dynasore.

Filipin, methyl-β-cyclodextrin and nystatin decreased the uptake and phototoxicity of **PcGal$_{16}$** in a higher extent in HT-1376 cells (Figure 4.6, Table SI4.1) than in UM-UC-3 cells (Figure SI4.6, Table SI4.2), indicating that caveolae-mediated endocytosis was more important for the uptake of **PcGal$_{16}$** in HT-1376 cells than in UM-UC-3 cells.

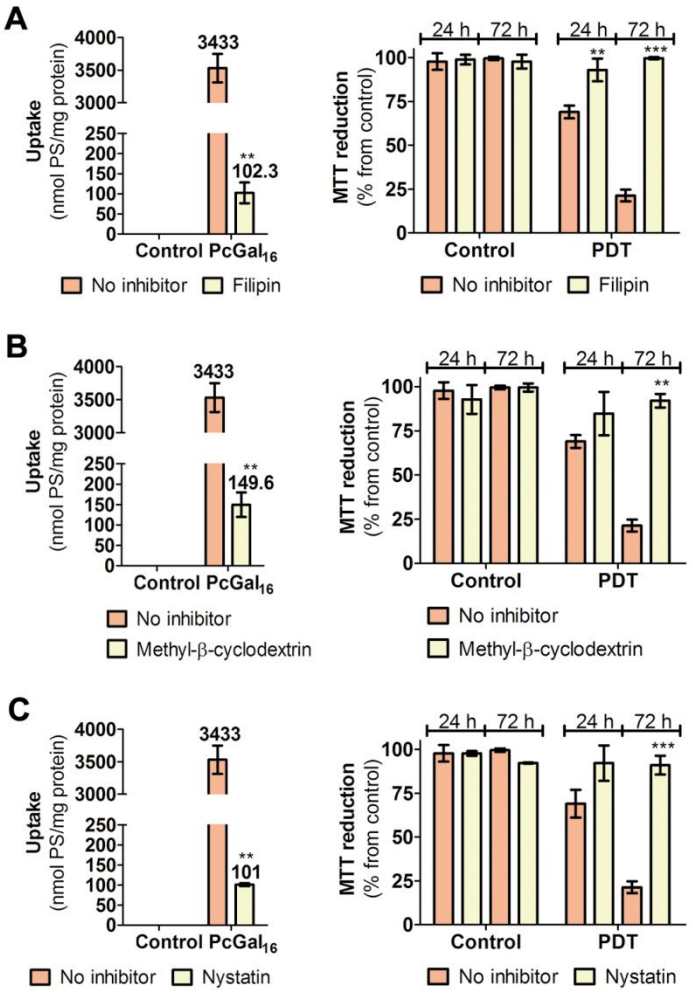

Figure 4.6 Pre-incubation of HT-1376 bladder cancer cells with filipin, methyl-β-cyclodextrin and nystatin reduce the uptake and phototoxicity of PcGal$_{16}$. Intracellular uptake and phototoxicity of **PcGal$_{16}$** in HT-1376 bladder cancer cells pre-incubated with 2.5 μg/mL filipin (A), 5 mM methyl-β-cyclodextrin (B) or 25 μM nystatin (C). Data are the mean ± S.D. of at least three independent experiments performed in triplicates. $^{**}P< 0.01$, $^{***}P< 0.001$ compared to uptake or phototoxicity in the absence of endocytic inhibitor.

4.3 Knockdown of caveolin-1 protein increases uptake and phototoxicity of PDT with PcGal$_{16}$ in HT-1376 cancer cells

Previous studies demonstrated that HT-1376 bladder cancer cells induce an antioxidant response after PDT with **PcGal$_{16}$**[7]. But MTT assays performed at 24 and 72 h after PDT demonstrated that these cells were unable to recover from the photo-effects for at least 72 h

after PDT [7]. On the other hand, UM-UC-3 cells were quite sensitive to PDT with **PcGal$_{16}$** [7]. In an attempt to correlate PcGal$_{l6}$ internalization pathway with the resistance of HT-1376 cancer cells to PDT, we decided to extend our study with this cell line. Incubation of HT-1376 cancer cells with **PcGal$_{16}$** induced an increase in the phosphorylated form of caveolin-1 (phospho-caveolin-1, Figure 4.7A) without alteration on the levels of caveolin-1 protein as observed by Western blotting.

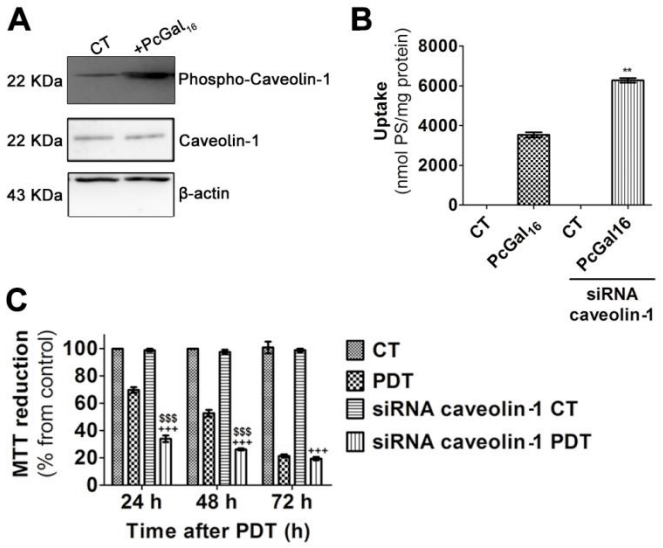

Figure 4.7 Caveolin-1 protein has a key role on the uptake of PcGal$_{16}$ by HT-1376 bladder cancer cells. (A) Western blotting analysis of phospho-caveolin-1 and caveolin-1 proteins levels in HT-1376 cells after PcGal$_{16}$ uptake. β-actin was used as a loading control. (B) Intracellular uptake of PcGal$_{16}$ by HT-1376 bladder cancer cells transfected with caveolin-1 siRNA. Cells were incubated with PcGal$_{16}$ 48 h post-transfection with caveolin-1 siRNA. Data are the mean ± S.D. of at least three independent experiments performed in triplicates. $^{**}P< 0.01$ compared to uptake in non-transfected cells. (C) Photocytotoxic effects after PcGal$_{16}$-PDT in HT-1376 cells transfected with caveolin-1 siRNA. Phototoxicity was evaluated 24, 48 and 72 h after PDT. Data are the mean ± S.D. of at least three independent experiments performed in triplicates. $^{+++}P< 0.001$ compared to phototoxicity in transfected control cells. $^{\$\$\$}P< 0.001$ compared to phototoxicity in non-transfected cells.

Having found that **PcGal$_{16}$** uptake increases the levels of phospho-caveolin-1 and that it is inhibited more significantly by caveolae-inhibitors in the cell line where caveolin-1 is more abundant (HT-1376), we investigated the role of caveolin-1 in **PcGal$_{16}$** internalization by HT-1376 cells. To determine whether caveolin-1 plays a role in the uptake of **PcGal$_{16}$** by HT-1376

cancer cells, siRNA was used to knockdown caveolin-1 (Figure SI4.7). As shown in Figure 4.7B,C, transfected cells displayed a markedly increased uptake and phototoxicity of **PcGal$_{16}$**.

4.4 Knockdown of caveolin-1 protein increases GLUT1 protein levels at the plasma membrane of HT-1376 cancer cells

GLUT1 is a glucose transporter overexpressed in cancer cells [11] and it is able to bind glyco-PSs increasing their concentration in cancer cells [7]. Previous studies demonstrated that GLUT1 protein contributes to the uptake of **PcGal$_{16}$** in HT-1376 cancer cells, because knockdown of this protein was associated with a marked decrease of **PcGal$_{16}$** uptake and phototoxicity [7]. The increase in the uptake of **PcGal$_{16}$** after knockdown of caveolin-1 prompted us to study whether knockdown of caveolin-1 protein induced changes on the levels of GLUT1 protein in HT-1376 cancer cells. Knockdown of caveolin-1 protein was specific for this endocytic protein, because it did not induce changes in the levels of other endocytic proteins (such as chlatrin HC, Figure 4.8A,B). Interestingly, an increase in the GLUT1 protein levels were observed after knockdown of caveolin-1 (Figure 4.8A,B).

Having established that knockdown of caveolin-1 protein increases the uptake of **PcGal$_{16}$** and the expression levels of GLUT1, we hypothesized that caveolin-1 regulates in somehow the internalization of GLUT1. To address this question we used cell-surface biotinylation assays to follow GLUT1 at the plasma membrane before and after uptake of **PcGal$_{16}$** in HT-1376 cells expressing caveolin-1 and HT-1376 cells depleted of caveolin-1. The results presented in Figure 4.8C show that, the amount of GLUT1 at the plasma membrane (biotinylated fraction) increases in cells depleted of caveolin-1. After cells incubation with **PcGal$_{16}$** GLUT1 decreases in the plasma membrane of both HT-1376 cells expressing caveolin-1 and depleted of this protein. In agreement with the data presented above, uptake of **PcGal$_{16}$** by HT-1376 bladder cancer cells increased the intracellular levels of GLUT1 protein (non-biotinylated fraction).

The clathrin-dependent endocytosis is the main pathway involved in the down-regulation of cell-surface receptors such as epidermal growth factor receptor (EGFR) [12]. Interestingly, cell-surface biotinylation assays demonstrated that EGFR increases in the

plasma membrane of HT-1376 cells depleted of caveolin-1 and it is internalized after uptake of **PcGal$_{16}$** Figure 4.8C.

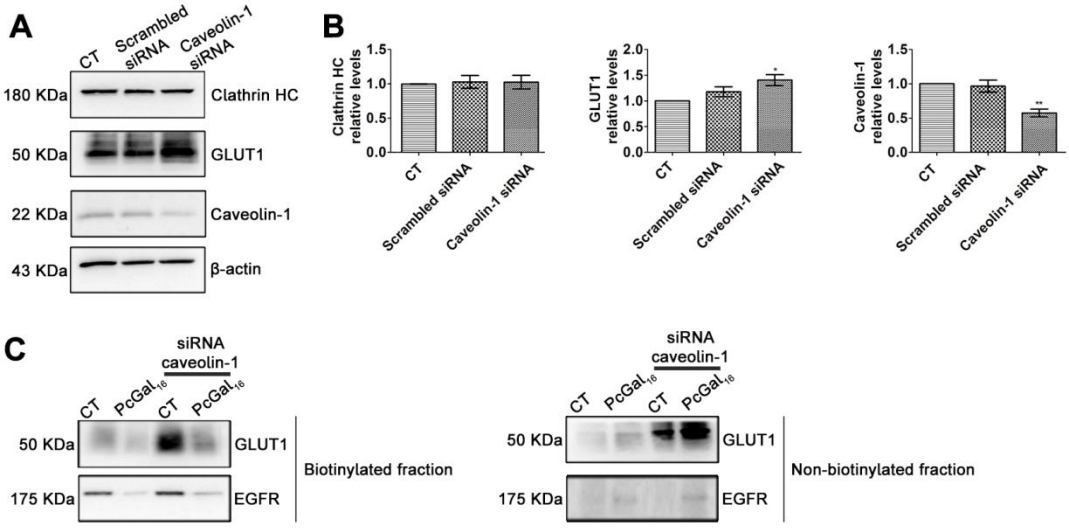

Figure 4.8 Knockdown of caveolin-1 protein increases the expression of GLUT1 protein in the plasma membrane of HT-1376 bladder cancer cells. Western blotting analysis (A) of clathrin heavy chain (HC), GLUT 1 and caveolin-1 proteins in HT-1376 cells transfected with caveolin-1 siRNA. β-actin was used as a loading control. (B) Quantitative analysis of clathrin HC, GLUT 1 and caveolin-1 GLUT1 (normalized to β-actin) expressed as a ratio of the levels found in control non-transfected control cells. Data represents mean ± S.D. of five independent experiments. $^{*}P< 0.05$, $^{**}P< 0.01$ compared to non-transfected control cells. (C) Western blotting analysis of GLUT 1 and EGFR after **PcGal$_{16}$** uptake in HT-1376 cells transfected with caveolin-1 siRNA and subjected to cell surface protein biotinylation. Cells were incubated with **PcGal$_{16}$** 48 h post-transfection with caveolin-1 siRNA. Cells were then subjeted to cell surface protein biotinylation, and the biotin-labeled and biotin-unlabeled proteins were separated using NeutrAvidin beads. NeutrAvidin supernatant (non-biotinylated proteins) and NeutrAvidin-bound proteins (biotinylated proteins) were then analyzed by Western blotting using antibodies against GLUT1 or EGFR.

4.5 Discussion

The internalization of PSs in cells is modulated by their degree of lipophilicity and asymmetry in the molecular structure, type and number of neutral and charged peripheral groups [4]; and by cell type and cell-specific features. These factors generally determine the subcellular compartment in which the PS accumulates. Taking into account the limited lifetime of ROS generated with PDT, the subcellular localization of the PS determines the targets of the primary damages. A study regarding the analysis of the endocytic pathways through which a PS is internalized, is of great importance in the design of an effective PS. Quantitative insight into the contribution of different endocytic pathways to the cellular uptake of a PS can be very helpful to understand how cellular uptake influences phototoxicity of a certain PS.

Previously, we demonstrated that the uptake of a phthalocyanine conjugated with dendritic units of galactose (**$PcGal_{16}$**) is dependent on the presence of galactose-binding proteins overexpressed in cancer cells (such as galectin-1 and GLUT1) [7]. We hypothesized that noncovalent interactions between **$PcGal_{16}$** and galactose-binding proteins will increase the concentration of this PS around cancer cell membranes, and the PS is then internalized by endocytosis. In the present study we demonstrated that **$PcGal_{16}$** endocytosis is highly dependent on the cell line used and both clathrin- and caveolae-mediated pathways are involved. Additionally, we demonstrated that **$PcGal_{16}$** uptake and further phototoxicity can be improved, in HT-1376 cell line resistant at the first times after PDT, by interfering with the endocytic machinery.

The internalization of a PS can be studied by different approaches but all have their limitations [9]. The use of inhibitors that affect a specific cellular uptake mechanism is a common approach. Additionally, knockdown of proteins required for specific endocytic pathways can also be used. In this study, we have focused on the use of chemical inhibitors and knockdown of caveolin-1 protein to investigate the endocytic internalization of **$PcGal_{16}$** [7, 13]. Further studies must consider the effect of the PS on the activity of endocytic pathways.

Sucrose hypertonic solution inhibits endocytosis because it blocks clathrin-coated pit formation [14]. Chlorpromazine is a cationic amphiphilic molecule which inhibits Rho GTPase activity needed for several mechanisms including clathrin-dependent endocytosis [9]. Dynasore is a cell-permeable small molecule that inhibits dynamin GTPase and mitochondrial dynamin activities, blocking dynamin-dependent endocytosis and interfering with both clathrin- and caveolin-dependent endocytosis [10]. Filipin changes the properties of cholesterol-rich membrane domains, interfering with caveolae-mediated endocytosis [15]. Methyl-β-cyclodextrin induces depletion of cholesterol (the main component of lipid rafts) from the plasma membrane and it has been used to determine if endocytosis is dependent on the integrity of lipid rafts [9]. Nystatin is an inhibitor of caveolae-mediated endocytosis, which disrupts lipid-raft caveolae structure and function [16].

PcGal$_{16}$ uptake was highly reduced when active processes were inhibited (studies at 4 ^{o}C or in the presence of NaN_3), which indicates that **PcGal$_{16}$** uptake is energy-dependent. None of the pharmacological inhibitors could fully inhibit **PcGal$_{16}$** uptake indicating that cells use multiple pathways simultaneously to internalize the same PS. Nevertheless, some inhibitors inhibited more strongly in one cell type than others. For instance, filipin, methyl-b-cyclodextrin and nystatin inhibited the **PcGal$_{16}$** uptake in HT-1376 cancer cells more strongly than in UM-UC-3 cancer cells. In spite of having high inhibitory effects in the phototoxicity of **PcGal$_{16}$**, dynasore inhibited the uptake only about 66% and 21% in HT-1376 and UM-UC-3 cells, respectively. The lack of correlation between reduction in phototoxicity and uptake when dynasore is used as endocytic inhibitor can be due to the fluorescent properties of dynasore, because it has emission bands in the same region of **PcGal$_{16}$**[17]. The compounds used to inhibit clathrin-mediated endocytosis (chlorpromazine and sucrose) were able to inhibit uptake and phototoxicity of **PcGal$_{16}$** in both cell lines.

Our data suggests that **PcGal$_{16}$** uptake in UM-UC-3 bladder cancer cells, which express caveolin-1 protein in lower levels when compared with HT-1376 cells, occurred mainly by clathrin internalization. Additionally, **PcGal$_{16}$** uptake in HT-1376 cells resulted on the stimulation of the phospho-caveolin-1. Phosphorylation of caveolin-1 has been indirectly related to the endocytic activity of caveolae [18]. For example, the addition of glycosphingolipids to cells resulted on the phosphorylation of caveolin-1 and increased

dynamics of caveolae [19]. It seems therefore evident that caveolin-1 protein has a role on the uptake of **PcGal$_{16}$** by HT-1376 bladder cancer cells.

Previous studies have demonstrated that blocking one uptake pathway can lead to the upregulation of other endocytic mechanisms [20]. Therefore, the increase in the uptake of **PcGal$_{16}$** after knockdown of caveolin-1 protein in HT-1376 bladder cancer cells can be due to the activation of other endocytic pathways that results in even higher accumulation of **PcGal$_{16}$**. Cell-surface biotinylation assays demonstrated an increase in the internalization of EGFR after uptake of **PcGal$_{16}$** in cells depleted of caveolin-1. An upregulation in clathrin-mediated endocytosis is expected in HT-1376 cancer cells depleted of caveolin-1, because EGFR internalization is mainly mediated by clathrin-dependent endocytosis [12]. In this study, we used siRNA to inhibit caveolin-1 mediated endocytosis. Although this is a great methodology to inhibit protein expression, the knockdown is not 100% efficient. The small amount of caveolin-1 observed by Western blotting upon siRNA treatment might be also involved in the uptake of **PcGal$_{16}$**. Importantly, studies have demonstrated that endocytic uptake of virus particles and exosomes is increased in caveolin-1 knock out cells suggesting that their uptake is negatively regulated by caveolin-1 [21, 22]. Somewhat unexpectedly, the increase in the uptake of **PcGal$_{16}$** after knockdown of caveolin-1 protein in HT-1376 bladder cancer cells also suggests a negative regulatory role of caveolin-1 in **PcGal$_{16}$** uptake.

In a previous study, we demonstrated that **PcGal$_{16}$** phototoxicity is higher in UM-UC-3 cells than in HT-1376 cells at 24 h after PDT [7]. The resistance of HT-1376 at the first 24 h after PDT was explained by the fact that an antioxidant response is developed after PDT in HT-1376 cancer cells [7]. Some studies have proposed that the acquisition of resistance to different compounds by cancer cells might be associated with high expression of caveolin-1 [23]. Considering the role of caveolin-1 protein in the resistance of cancer cells to therapy, we hypothesize that knockdown of this protein will increase the sensitivity of HT-1376 cancer cells to PDT.

The reduction of GLUT1 in the plasma membrane and its intracellular increase after **PcGal$_{16}$** uptake supports our previous study demonstrating that GLUT1 has a key role on the uptake of **PcGal$_{16}$** by HT-1376 bladder cancer cells [7]. Interestingly, knockdown of caveolin-1 protein increases GLUT1 protein levels at the plasma membrane of HT-1376 cancer cells.

These results led us to hypothesize that knockdown of caveolin-1 protein increases **PcGal$_{16}$** uptake and further phototoxicity through an increment of GLUT1 in the plasma membrane. Studies have demonstrated that the activity of GLUT1 is sensitive to changes in the lipid environment of the transporter, such as changes in phospholipids and cholesterol composing the membrane [24]. Although the mechanism by which depletion of caveolin-1 increases GLUT1 at the plasma membrane is not clear, studies have reported that GLUT1 protein is distributed in caveolin-rich membrane fractions [24-26]. Mechanisms of plasma membrane protein degradation (endocytic recycling) can also explain these results.

The accumulation of **PcGal$_{16}$** is not only dependent on the presence of galactose-binding proteins (as we have previously demonstrated in another study [7]), but it is a complex mechanism which results from the interplay between the mechanisms by which cells are able to endocytose PSs. The data presented here also suggest that **PcGal$_{16}$** might be internalized *via* different pathways in different cell types.

4.6 References

1. Le Roy C, Wrana JL (2005) Clathrin- and non-clathrin-mediated endocytic regulation of cell signalling. Nat Rev Mol Cell Biol 6: 112-126.

2. Gruenberg J, Stenmark H (2004) The biogenesis of multivesicular endosomes. Nat Rev Mol Cell Biol 5: 317-323.

3. Drab M, Verkade P, Elger M, Kasper M, Lohn M, Lauterbach B, et al. (2001) Loss of caveolae, vascular dysfunction, and pulmonary defects in caveolin-1 gene-disrupted mice. Science 293: 2449-2452.

4. Ezzeddine R, Al-Banaw A, Tovmasyan A, Craik JD, Batinic-Haberle I, Benov LT (2013) Effect of molecular characteristics on cellular uptake, subcellular localization, and phototoxicity of Zn(II) *N*-Alkylpyridylporphyrins. J Biol Chem 288: 36579-36588.

5. Soriano J, Stockert JC, Villanueva A, Can˜ete M (2010) Cell uptake of Zn(II)-phthalocyanine-containing liposomes by clathrin-mediated endocytosis. Histochem Cell Biol 133: 449-454.

6. Soriano J, Villanueva A, Stockert JC, Can˜ete M (2013) Vehiculization determines the endocytic internalization mechanism of Zn(II)-phthalocyanine. Histochem Cell Biol 139: 149-160.

7. Pereira PMR, Silva S, Cavaleiro JAS, Ribeiro CAF, Tomé JPC, Fernandes R (2014) Galactodendritic phthalocyanine targets carbohydrate-binding proteins enhancing photodynamic therapy. PLoS One 9: e95529.

8. Vasilyeva E, Forgac M (1998) Interaction of the clathrin-coated vesicle V-ATPase with ADP and sodium azide. J Biol Chem 273: 23823-23829.

9. Vercauteren D, Vandenbroucke RE, Jones AT, Rejman J, Demeester J, De Smedt SC, et al. (2010) The use of inhibitors to study endocytic pathways of gene carriers: optimization and pitfalls. Mol Ther 18: 561-569.

10. Kirchhausen T, Macia E, Pelish HE (2008) Use of dynasore, the small molecule inhibitor of dynamin, in the regulation of endocytosis. Methods Enzymol 438: 77-93.

11. Hiyoshi Y, Watanabe M, Imamura Y, Nagai Y, Baba Y, Yoshida N, et al. (2009) The relationship between the Glucose Transporter Type 1 expression and ^{18}F-fluorodeoxyglucose uptake in esophageal squamous cell carcinoma. Oncology-Basel 76: 286-292.

12. Kirchhausen T (2002) Clathrin adaptors really adapt. Cell 109: 413-416.

13. Silva S, Pereira PMR, Silva P, Paz FAA, Faustino MAF, Cavaleiro JAS, et al. (2012) Porphyrin and phthalocyanine glycodendritic conjugates: synthesis, photophysical and photochemical properties. Chem Commun 48: 3608-3610.

14. Heuser JE, Anderson RGW (1989) Hypertonic media inhibit receptor-mediated endocytosis by blocking clathrin-coated pit formation. J Cell Biol 108: 389-400.

15. Orlandi PA, Fishman PH (1998) Filipin-dependent inhibition of cholera toxin: evidence for toxin internalization and activation through caveolae-like domains. J Cell Biol 141: 905-915.

16. Chen C-L, Hou W-H, Liu I-H, Hsiao G, Huang SS, Huang JS (2009) Inhibitors of clathrin-dependent endocytosis enhance TGFβ signaling and responses. J Cell Sci 122: 1863-1871.

17. Matthews DR, Fruhwirth GO, Weitsman G, Carlin LM, Ofo E, Keppler M, et al. (2012) A multi-functional imaging approach to high-content protein interaction screening. PLoS One 7: e33231.

18. Pelkmans L (2005) Secrets of caveolae- and lipid raft-mediated endocytosis revealed by mammalian viruses. BBA-Mol Cell 1746: 295-304.

19. Sharma DK, Brown JC, Choudhury A, Peterson TE, Holicky E, Marks DL, et al. (2004) Selective stimulation of caveolar endocytosis by glycosphingolipids and cholesterol. Mol Biol Cell 15: 3114-3122.

20. Harush-Frenkel O, Debotton N, Benita S, Altschuler Y (2007) Targeting of nanoparticles to the clathrin-mediated endocytic pathway. Biochem Biophys Res Commun 353: 26-32.

21. Le PU, Guay G, Altschuler Y, Nabi IR (2002) Caveolin-1 is a negative regulator of caveolae-mediated endocytosis to the endoplasmic reticulum. J Biol Chem 277: 3371-3379.

22. Svensson KJ, Christianson HC, Wittrup A, Bourseau-Guilmain E, Lindqvist E, Svensson LM, et al. (2013) Exosome uptake depends on ERK1/2-heat shock protein 27

signaling and lipid raft-mediated endocytosis negatively regulated by caveolin-1. J Biol Chem 288: 17713-17724.

23. Chatterjee M, Ben-Josef E, Thomas DG, Morgan MA, Zalupski MM, Khan G, et al. (2015) Caveolin-1 is associated with tumor progression and confers a multi-modality resistance phenotype in pancreatic cancer. Sci Rep 5: 10867

24. Barnes K, Ingram JC, Bennett MDM, Stewart GW, Baldwin SA (2004) Methyl-beta-cyclodextrin stimulates glucose uptake in Clone 9 cells: a possible role for lipid rafts. Biochem J 378: 343-351.

25. Grant BD, Donaldson JG (2009) Pathways and mechanisms of endocytic recycling. Nat Rev Mol Cell Biol 10: 597-608.

26. Sakyo T, Kitagawa T (2002) Differential localization of glucose transporter isoforms in non-polarized mammalian cells: distribution of GLUT1 but not GLUT3 to detergent-resistant membrane domains. BBA-Biomemb 1567: 165-175.

4.7 Supporting Information

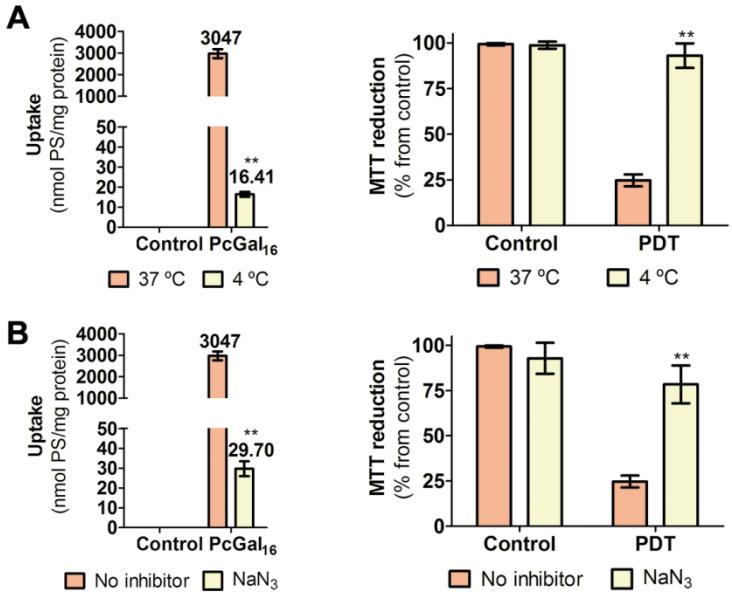

Figure SI4.1 Intracellular uptake and phototoxicity of **$PcGal_{16}$** in UM-UC-3 bladder cancer cells at 4 ºC (A); or after pre-incubation with 20 mM NaN_3. Data are the mean ± S.D. of at least three independent experiments performed in triplicates. $^{**}P< 0.01$ compared to uptake or phototoxicity at 37 ºC (A) or in the absence of NaN_3 (B).

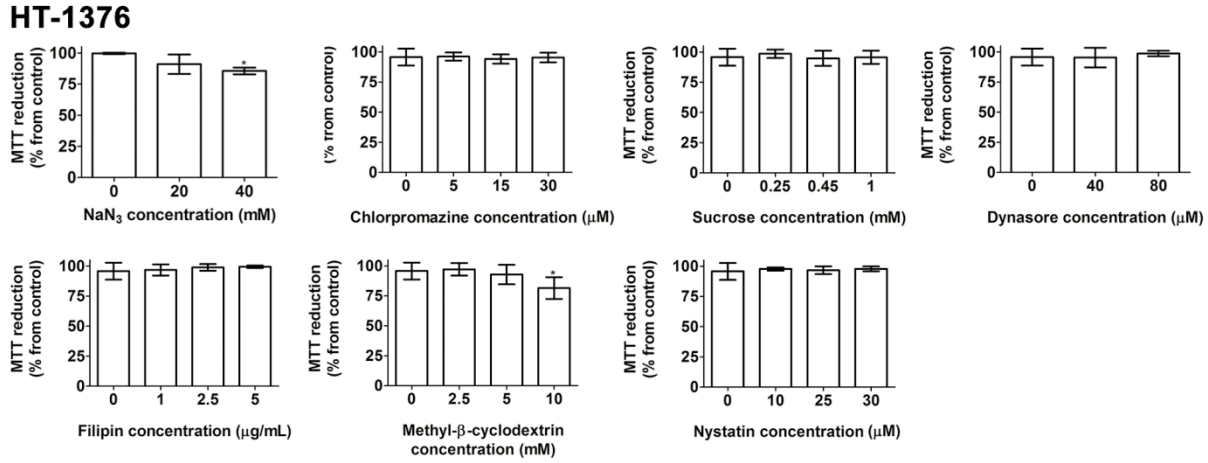

Figure SI4.2 Cytotoxic effects after HT-1376 cancer cells incubation with different concentrations of endocytic inhibitors (NaN_3, chlorpromazine, sucrose, dynasore, filipin, methyl-β-cyclodextrin and nystatin) was evaluated 24 h after treatment using the MTT assay. The percentage of toxicity was calculated relatively to control cells

(cells incubated with PBS). Data are the mean ± S.D. of at least three independent experiments performed in triplicates. $^{*}P< 0.05$ compared to control cells.

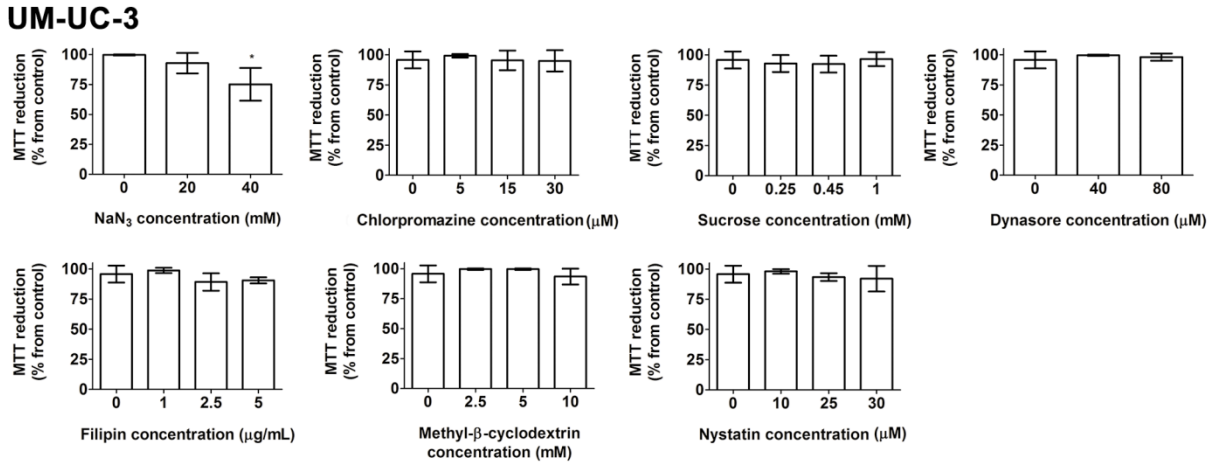

Figure SI4.3 Cytotoxic effects after UM-UC-3 cancer cells incubation with different concentrations of endocytic inhibitors (NaN_3, chlorpromazine, sucrose, dynasore, filipin, methyl-β-cyclodextrin and nystatin) was evaluated 24 h after treatment using the MTT assay. The percentage of toxicity was calculated relatively to control cells (cells incubated with PBS). Data are the mean ± S.D. of at least three independent experiments performed in triplicates. $^{*}P< 0.05$ compared to control cells.

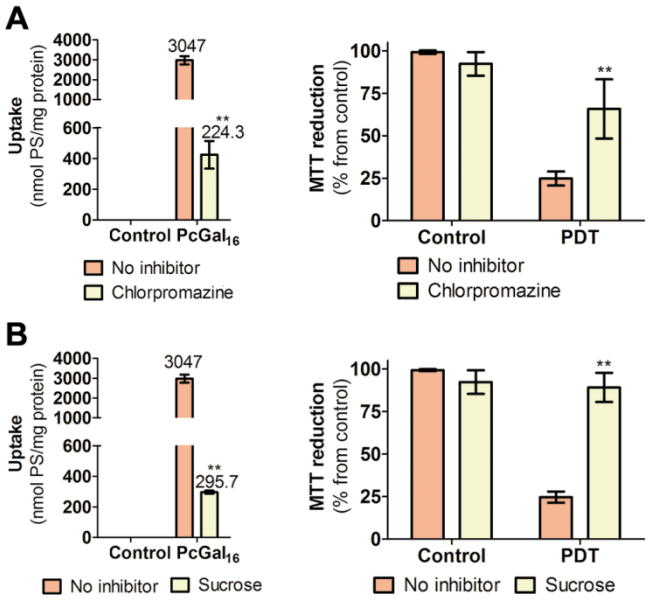

Figure SI4.4 Intracellular uptake and phototoxicity of **$PcGal_{16}$** in UM-UC-3 bladder cancer cells pre-incubated with 5 μM chlorpromazine (A) or 0.45 mM sucrose (B). Data are the mean ± S.D. of at least three independent

experiments performed in triplicates.$^{**}P< 0.01$ compared to uptake or phototoxicity in the absence of endocytic inhibitor.

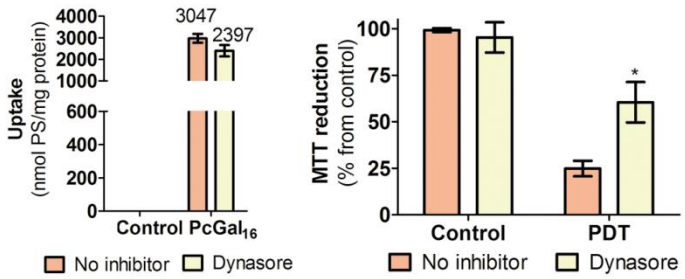

Figure SI4.5 Intracellular uptake and phototoxicity of **$PcGal_{16}$** in UM-UC-3 bladder cancer cells pre-incubated with 40 μM dynasore. Data are the mean ± S.D. of at least three independent experiments performed in triplicates. $^{*}P< 0.05$ to phototoxicity in the absence of endocytic inhibitor.

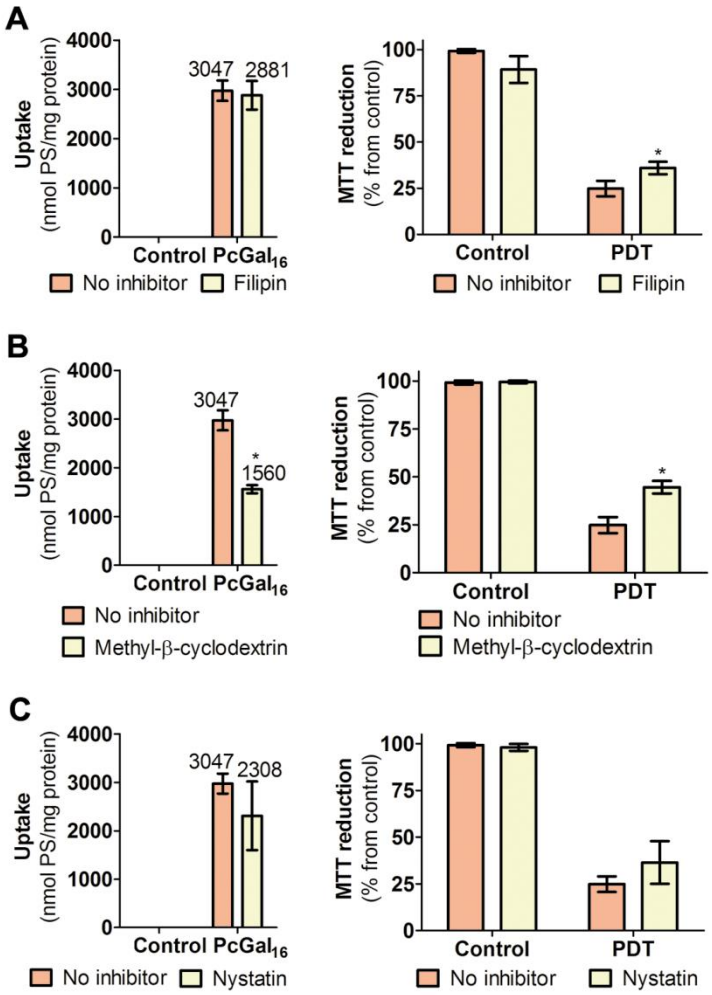

Figure SI4.6 Intracellular uptake and phototoxicity of **PcGal$_{16}$** in UM-UC-3 bladder cancer cells pre-incubated with 2.5 μg/mL filipin (A), 5 mM methyl-β-cyclodextrin (B) or 25 μM nystatin (C). Data are the mean ± S.D. of at least three independent experiments performed in triplicates. $^{*}P< 0.05$ compared to uptake or phototoxicity in the absence of endocytic inhibitor.

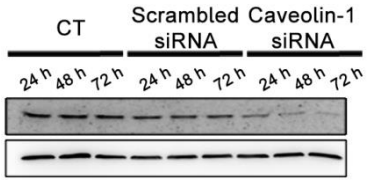

Figure SI4.7 Knockdown of caveolin-1 in HT-1376 bladder cancer cells as determined by Western blotting 24, 48 and 72 h post-transfection. β-actin was used as a loading control.

Table SI4.1 Analysis of the different endocytic inhibitors in HT-1376 bladder cancer cells, regarding **$PcGal_{16}$** uptake and phototoxicity, before and after transfection with caveolin 1 siRNA.

Condition	**Inhibitor concentration**	**Uptake (nmol $PcGal_{16}$/mg protein)**		**MTT reduction (% from control)**			
		Non-transfected cells	Transfected cells	Non-transfected cells			Transfected cells
				24 h after PDT	72 h after PDT	24 h after PDT	72 after PDT
No inhibitor, 37 ºC	___	3433	6274	65.07	23.46	28.38	16.53
4 ºC	___	14.51	___	99.3	98.59	___	___
NaN_3	20 mM	23.42	___	91.4	88.32	___	___
Sucrose	0.45 mM	225.2	7662	93.2	78.29	5.6	5.7
Chlorpromazine	5 µM	295.9	8309	96.0	83.61	3.1	4.8
Dynasore	40 µM	1170	___	96.2	59.79	___	___
Filipin	2.5 µg/mL	102.3	6444	93.0	98.23	14.1	13.9
Methyl-β-Cyclodextrin	5 mM	149.6	5837	84.7	91.98	17.1	16.5
Nystatin	25 µM	101	6464	92.1	91	13.0	13.8

Table SI4.2 Analysis of the different endocytic inhibitors in UM-UC-3 bladder cancer cells, regarding **$PcGal_{16}$** uptake and phototoxicity.

Condition	**Inhibitor concentration**	**Uptake (nmol $PcGal_{16}$/mg protein)**	**MTT reduction at 24 h after PDT (% from control)**
No inhibitor, 37 ºC	___	3047	24.68
4 ºC	___	16.41	93.01
NaN_3	20 mM	29.70	78.41
Sucrose	0.45 mM	295.7	89.13
Chlorpromazine	5 µM	424.3	64.19
Dynasore	40 µM	2397	60.44
Filipin	2.5 µg/mL	2881	35.97
Methyl-β-Cyclodextrin	5 mM	1560	44.62
Nystatin	25 µM	2308	36.40

The role of galectin-1 in *in vitro* and *in vivo* photodynamic therapy with a galactodendritic porphyrin

CHAPTER V

Chapter V The role of galectin-1 in *in vitro* and *in vivo* photodynamic therapy with a galactodendritic porphyrin

5.1 General overview

Most of the clinically-approved agents used in PDT for cancer treatment are porphyrin-based photosensitizers (*e.g.* Photofrin, ALA/PpIX, BPD-MA). Several porphyrin-based PSs have been synthesized through conjugation with biomolecules in order to influence their water/lipid solubility, amphiphilicity, pKa, stability, intracellular localization and pharmacokinetics [1-7]. The conjugation of galactose targeting moieties with a porphyrinoid is a valuable approach to achieve a high local concentration of PSs in tumor tissues, since certain galactose-binding proteins are overexpressed on cancer tissues [8, 9] increasing their tumor selectivity/uptake and reducing the unwanted phototoxicity in the surrounding healthy tissues. Galectin-1, the first discovered galectin, exhibits extracellular and intracellular localization [10], being able to form homodimers that can cross-link ligands containing appropriate carbohydrate moieties. The overexpression of galectin-1 has been described for several tumor types (namely bladder tumors) [11-13] and this has been associated with low prognosis and high metastatic potential [13]. This protein abundantly expressed in tumor environments can modulate several functions such as angiogenesis, cell migration adhesion and tumor-immune escape [11-13].

We previously reported **PorGal$_8$**, a porphyrin conjugated with dendritic units of galactose (Figure SI5.1), as a new water soluble PS able to generate ROS after photoactivation [14]. In the present chapter, we validated **PorGal$_8$** as a novel therapeutic agent in PDT for the treatment of tumors containing high levels of galectin-1 (Figure 5.1). We showed a specific uptake of **PorGal$_8$** and induction of apoptotic cell death by generating oxidative stress and alterations in the cytoskeleton of bladder cancer cells overexpressing galectin-1. We further validated the photodynamic efficiency of **PorGal$_8$** in athymic nude mice (Balb/c *nu*/*nu*) bearing subcutaneously implanted luciferase-positive bladder cancer xenografts, overexpressing galectin-1 protein. **PorGal$_8$** (5 μmol/kg, i.p.), injected 24 h before light delivery (50.4 J/cm^2), inhibited tumor growth. We conclude that the use of **PorGal$_8$** enables

selective target and cytotoxicity by PDT in cancer cells overexpressing galectin-1, preventing undesired phototoxicity in the surrounding healthy tissues.

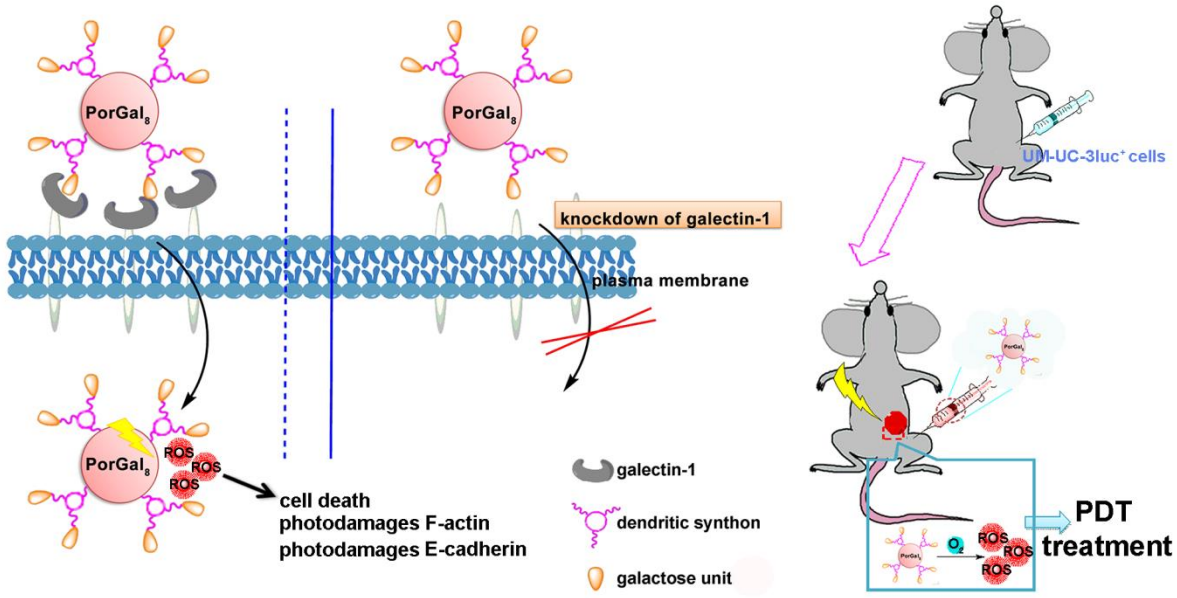

Figure 5.1 Hypothetic illustration of phototoxicity of PorGal$_8$ in *in vitro* and *in vivo* biological models containing high levels of galectin-1 protein.

5.1.1 Methods

The following experimental protocols (please see Methods and Materials chapter IX) were used to obtain the data presented in this chapter:

- Protein interaction assays – galectin-1 (9.2.2E)
- Biological models – Culture of HT-1376 and UM-UC-3 bladder cancer cells (9.3.8A)
- Fluorescence spectroscopy and microscopy – uptake of **PorGal$_8$** (9.3.8C-E)
- PDT treatments – Photosensitizer **PorGal$_8$** (9.3.8F)
- Cell viability assays – MTT, Trypan blue and TUNEL assays (9.3.8G)
- Transfection assays – knockdown of galectin-1 using siRNA (9.3.8I)
- Intracellular levels of Reactive Oxygen Species (9.3.8J)
- Redox quenching assays (9.3.8K)
- Western blotting assays – galectin-1, E-cadherin, β-actin (9.3.8L)

- Immunocytochemistry assays – E-cadherin (9.3.8M)
- *In vivo assays* (9.4.8A)
- Immunohistochemistry assays – E-cadherin, Ki-67, Phalloidin-TRICT, galectin-1 (9.3.8C)

5.1.2 Publication

This chapter comprises the following publication:

Patrícia M. R. Pereira, Sandrina Silva, José S. Ramalho, Célia M. Gomes, Henrique Girão, José A. S. Cavaleiro, Carlos A. F. Ribeiro, João P. C. Tomé, Rosa Fernandes,The role of galectin-1 in in vitro and in vivo photodynamic therapy with a galactodendritic porphyrin, *accepted European Journal of Cancer.*

5.2 PorGal$_8$ interacts with galectin-1 and its accumulation in bladder cancer cells is dependent on the expression of this protein

Porphyrin conjugated with four dendritic units of galactose (**PorGal$_8$**) showed a high binding affinity to human galectin-1, as assessed by fluorescence quenching on the tryptophan residue of the protein (Figure 5.2A, Figure SI5.1B). The values determined for affinity constant (K_a) and the number of binding sites (*n*) for **PorGal$_8$** with galectin-1 were 1.27 x 10^7 M^{-1} and 1.40, respectively. A strong interaction between **PorGal$_8$** and lectin-recombinant human galectin-1 was also confirmed by the measured apparent dissociation constant (K_D), of 1.44 ± 0.062 μM (mean ± s.d.), see Figure 5.2A**.** We assessed the cellular uptake of **PorGal$_8$** in two bladder cancer cell lines derived from transitional cell carcinoma, HT-1376 and UM-UC-3, (Figure SI5.1C), which have different galectin-1 protein levels. The uptake of **PorGal$_8$** was both concentration- and time-dependent, reaching a plateau in less than 2 h (Figure 5.2B). Moreover, cellular uptake of **PorGal$_8$** was higher in UM-UC-3 cells that express higher levels of galectin-1 protein than HT-1376 cells (Figure 5.2C) [15]. A stronger fluorescence of **PorGal$_8$** (with occasional bright spots in the perinuclear region) was observed in UM-UC-3 cells when compared with HT-1376 cells (Figure SI5.2). Knockdown of galectin-1 *via* siRNA in UM-UC-3 cells (Figure 5.2D) clearly showed a decreased uptake of **PorGal$_8$** ($P < 0.01$, Figure 5.2E)**.**

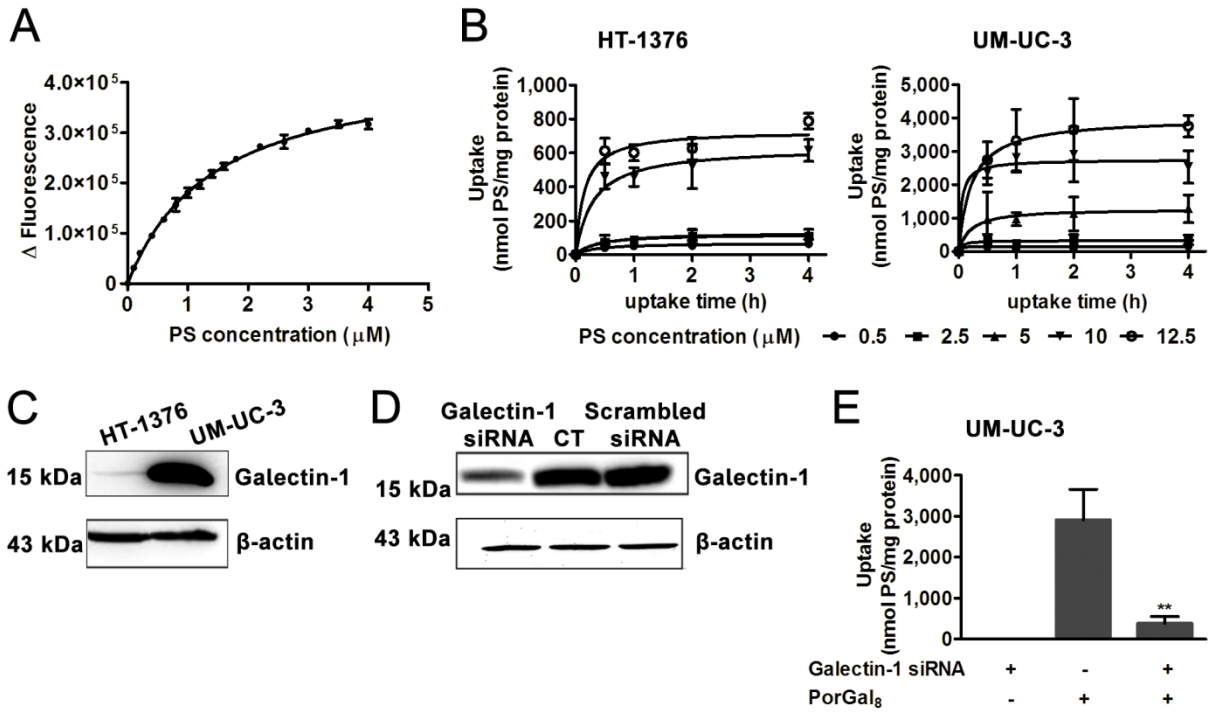

Figure 5.2 Galectin-1 plays a role in the uptake of PorGal$_8$ by HT-1376 and UM-UC-3 bladder cancer cells. (A) Fluorescence variation on the emission spectra of galectin-1 after addition of **PorGal$_8$**. Data are means ± s.e.m. of two independent experiments. (B) Intracellular uptake of **PorGal$_8$** by HT-1376 and UM-UC-3 bladder cancer cells. Data are means ± s.e.m. of at least three independent experiments performed in triplicates. (C) Western blotting analysis of galectin-1 protein in HT-1376 and UM-UC-3 bladder cancer cells. β-actin was used as a loading control. (D) Knockdown of galectin-1 in UM-UC-3 bladder cancer cells as determined by Western blotting 48 h post-transfection. (E) Intracellular uptake of **PorGal$_8$** by UM-UC-3 bladder cancer cells transfected with galectin-1 siRNA. ** $P < 0.01$ compared to non-transfected control cells using a Student´s *t* test. Data are means ± s.e.m. of at least three independent experiments performed in triplicates.

5.3 PorGal$_8$ induces cytotoxicity after photodynamic activation

Although **PorGal$_8$** is non toxic in the dark (at concentrations up to 12.5 μM and exposure times up to 4 h, Figure SI5.3A), it causes phototoxicity against bladder cancer cells. In fact, when HT-1376 and UM-UC-3 cells were incubated with **PorGal$_8$** and then irradiated (with a LEDs array system emitting white light, delivered at 8.4 mW/cm^2), there was an increased phototoxicity in a concentration- and uptake time-dependent manner (Figure SI5.3B). No cytotoxicity was observed in the untreated sham irradiated cells (Figure SI5.3B)

or untreated irradiated cells in the presence of 0.45% (v/v) or less DMSO in PBS (data not shown). **PorGal$_8$** led to a significantly higher phototoxicity on UM-UC-3 cells compared to HT-1376 cells (Figure 5.3A).

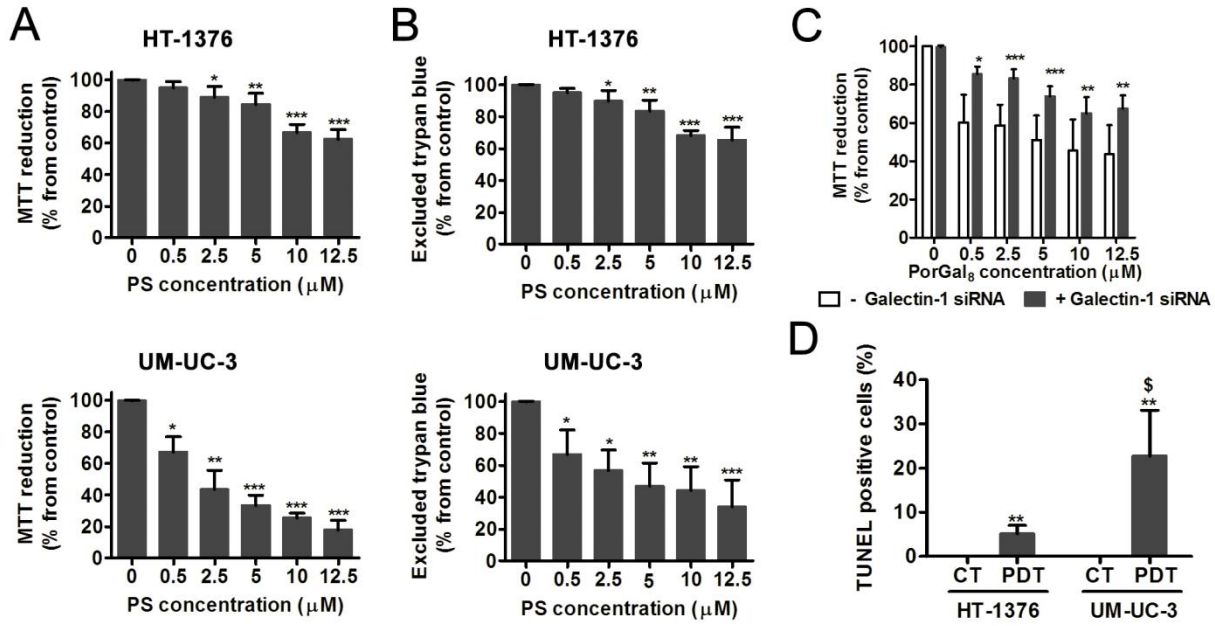

Figure 5.3 PDT with PorGal$_8$ induces cytotoxicity in HT-1376 and UM-UC-3 bladder cancer cells. (A) and (B) Cytotoxicity 24 h after PDT with **PorGal$_8$** was determined using the MTT and trypan blue staining assays, respectively. * $P < 0.05$, ** $P < 0.01$, *** $P < 0.001$ compared to MTT reduction (%) or excluded trypan blue (%) at 24 h after PDT for the respective control using a Student´s *t* test. Data are means ± s.e.m. of at least three independent experiments performed in triplicates. (C) Photocytotoxic effects after PDT with **PorGal$_8$** in UM-UC-3 cells transfected with galectin-1 siRNA. * $P < 0.05$, ** $P < 0.01$, *** $P < 0.001$ compared to MTT reduction (%) at 24 h after PDT for the respective non-transfected cells using a Student´s *t* test. Data are means ± s.e.m. of at least three independent experiments performed in triplicates. (D) Quantification of TUNEL-positive cells at 24 h after PDT with **PorGal$_8$** obtained from counts of randomly chosen microscopic fields.** $P < 0.01$ compared to control cells, $^{\$}P < 0.05$ compared to TUNEL-positive HT-1376 cells at 24 h after PDT using the multiple pairwise Kurskal-Wallis ANOVA.

The percentage of cell death in treated cells compared to untreated controls was also significantly influenced by the dose of light (2.52, 5.04, 10.08 and 20.16 J/cm^2). Based on the MTT data (Figure SI5.3B), we estimated the light dose necessary to induce significant phototoxicity in both cell lines. In subsequent experiments, a light dose of 8.4 mW/cm^2 for 40 min (*i.e.* 20.16 J/cm^2, Figure 5.3A) was used to perform the PDT assays. Trypan blue viability

assay (cell membrane activity) confirmed that, compared to control cells, phototoxicity was higher in UM-UC-3 than in HT-1376 cells (Figure 5.3B). Additional studies indicated that in UM-UC-3 transfected cells with galectin-1 siRNA (Figure 5.3C) there was a decrease in cytotoxicity induced by PDT with **PorGal$_8$**. Moreover, although increased apoptotic responses were observed in both cell lines (Figure 5.3D and Figure SI5.4A), 24 h after PDT with **PorGal$_8$**, as assessed by the Terminal deoxynucleotidyl transferase dUTP nick end labeling (TUNEL) assay, UM-UC-3 cell line was markedly more sensitive than HT-1376 cell line ($P < 0.05$). Additional MTT and TUNEL assays demonstrated that a certain percentage of HT-1376 cancer cells are able to recover from the photodynamic effect between 24 to 72 h after treatment (Figure SI5.4B). In UM-UC-3 cancer cells, a stronger phototoxic effect was observed at 72 h after treatment.

5.4 Photodynamic therapy with PorGal$_8$ induces ROS-mediated cytotoxicity

ROS production in cancer cells after PDT can be determined using specific solid traps or fluorescent probes such as 2´,7´-dichlorodihydrofluorescein diacetate (H_2DCFDA) and dihydroethidium (DHE).The H_2DCFDA and DHE, two oxidation-sensitive fluorescent dyes, demonstrated the production of ROS immediately after PDT 20.16 J/cm^2 in bladder cancer cells previously treated with 10 μM **PorGal$_8$** for 1.5 h (Figure 5.4A,B and Figure SI5.4C). Although both cell lines showed almost similar anion superoxide generation after PDT with **PorGal$_8$** (Figure SI5.4C), ROS generation detected with H_2DCFDA in UM-UC-3 cells was almost twice of the HT-1376 cells (Figure 5.4A,B).

PDT assays in bladder cancer cells incubated with non-toxic concentrations of ROS quenchers (histidine, sodium azideand cysteine) demonstrated that sodium azide (a quencher of $^1O_2$) significantly decreased the percentage of cell death ($P < 0.001$, Figure 5.4C). Histidine and cysteine at the employed concentrations were also able to decrease the cytotoxicity induced by PDT with **PorGal$_8$** in UM-UC-3 cells (Figure 5.4C). Additionally, the oxygen levels in the medium of both cancer cell lines gradually decreased due to PDT-induced photochemical oxygen consumption (Figure 5.4D). Furthermore, the oxygen consumption was higher in UM-UC-3 cells when compared to HT-1376 cells.

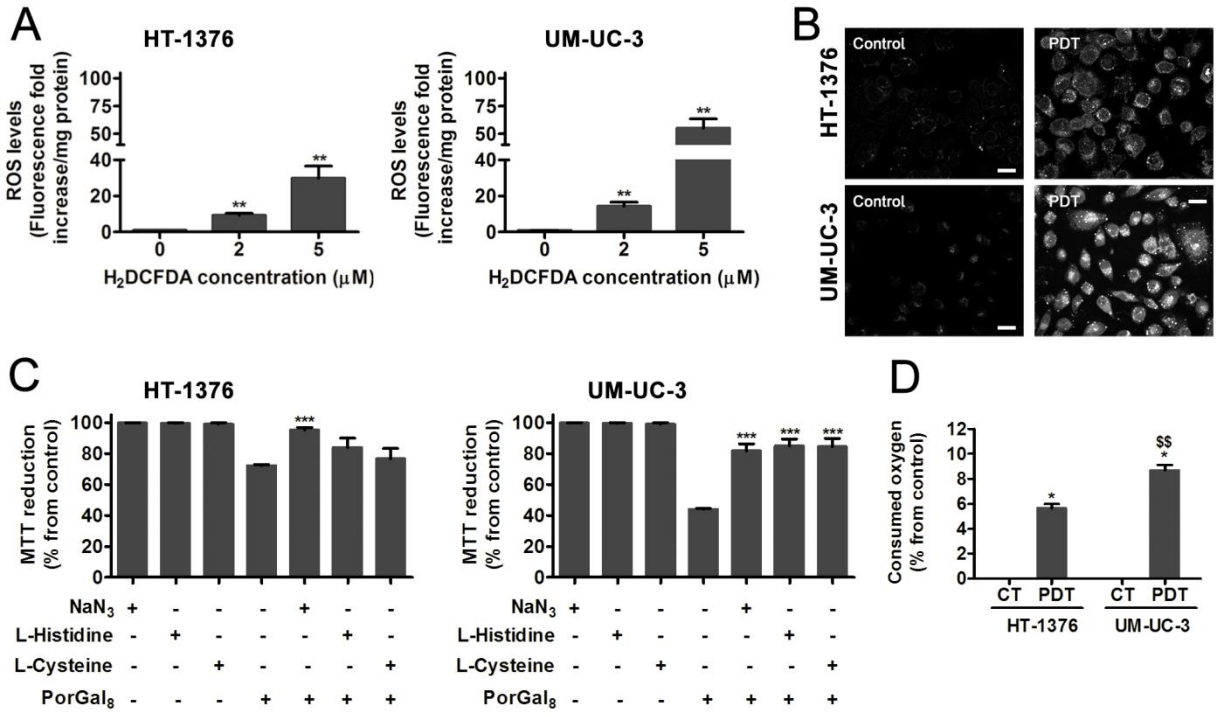

Figure 5.4 PorGal$_8$ generates ROS after PDT. (A) Quantification and (B) representative fluorescence images of DCF fluorescence increase (as a measure of ROS production) in HT-1376 and UM-UC-3, after PDT with **PorGal$_8$**. *Scale bars* 20 μm. ** $P < 0.01$ compared to control cells using a Student´s *t* test. Data are means ± s.e.m. of at least three independent experiments performed in triplicates. (C) Phototoxicity after PDT with **PorGal$_8$** in the presence of 50 nM of ROS quenchers (sodium azide, histidine and cysteine) in HT-1376 and UM-UC-3 cells. Cytotoxicity was assessed 24 h after treatment using the MTT assay. The percentage of cytotoxicity was calculated relatively to control cells (untreated cells). *** $P < 0.001$ compared to MTT reduction (%) 24 h after PDT with **PorGal$_8$** using a Student´s *t* test. Data are means ± s.e.m. of at least three independent experiments performed in triplicates. (D) Oxygen consumption in HT-1376 and UM-UC-3 cells after PDT with **PorGal$_8$**. *$P < 0.05$, $^{\$\$}P < 0.01$compared to control cells and HT-1376 cells after PDT, respectively, using the multiple pairwise Kurskal-Wallis ANOVA. Data are means ± s.e.m. of at least three independent experiments performed in triplicates.

5.5 Photodynamic therapy with PorGal$_8$ induces tumor shrinkage

To examine the effectiveness of **PorGal$_8$** *in vivo*, we developed a xenograft tumor model that included mice with UM-UC-3luc$^+$ cells (containing high levels of galectin-1 protein) in the dorsum (Figure SI5.5, Figure 5.5A).

Human UM-UC-3 bladder cancer cells were transduced by the lentiviral vector containing the firefly reporter gene pCMVLuc (pVR1216) and stable clones were selected using blasticidin (Figure SI5.5A). Human UM-UC-3luc$^+$ bladder cancer cells were generated from clones (clone B6, Figure SI5.5A) that stably expressed luciferase protein. A cell titration curve with UM-UC-3luc$^+$ cells demonstrated an elevated expression of luciferase expression over the background level in UM-UC-3 cells (Figure SI5.5B). To confirm that no alterations of cellular physiology occurred during the cloning process, we compared the UM-UC-3luc$^+$ clones to the original UM-UC-3 cells and we found that they had similar growth patterns and cytotoxicity after PDT (Figure SI5.5C).

A xenograft tumor model prepared by subcutaneous inoculation of 2 x 10^6 UM-UC-3luc$^+$ cancer cells in the dorsum of immunocompromised nude (Balb/c *nu/nu*) mice was followed continuously from the time of implantation by non-invasive bioluminescent imaging (Figure SI5.5D,E). Although non-invasive bioluminescent imaging allowed us to detect tumor burdens from the time of implantation of 2 x 10^6 UM-UC-3luc$^+$ cancer cells, the tumors could not be detected with the caliper before day 9.

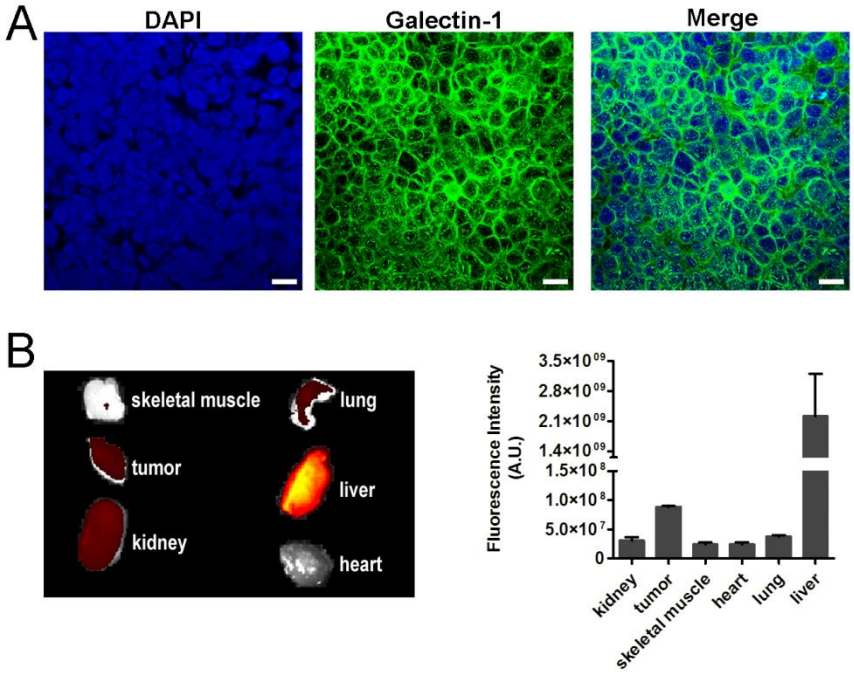

Figure 5.5 PorGal$_8$ accumulated in tumors expressing galectin-1 protein. (A) Representative fluorescence images of galectin-1 protein (green) in UM-UC-3luc$^+$ tumors, with DAPI staining the nucleus (blue). *Scale*

*bars*20 μm. (B) Representative fluorescence images and quantification of **PorGal$_8$** in dissected organs (skeletal muscle, tumor, kidney, heart, lung and liver) obtained 24 h post intraperitoneal injection of **PorGal$_8$**. Data are means ± s.e.m. (n = 3 mice).

The strongest fluorescence intensity of **PorGal$_8$** was observed in the tumor at 24 h after injection (Figure 5.5B). At this time point, **PorGal$_8$** fluorescence is almost absent in the skeletal muscle and heart; and it could be also detected in the primary routes of drug excretion and metabolism, such as the lung, kidney and liver (Figure 5.5B). One day post-injection of **PorGal$_8$** was chosen as the optimal time to perform the PDT studies once at this time point, the tumor-to-background ratio (TBR) was about 2.0.

After confirming the preferential accumulation of **PorGal$_8$** in the UM-UC-3luc$^+$ tumors (24 h after intraperitoneal injection of 5 μmol/kg, Figure 5.5B), PDT was performed with a single dose of light (white light 400–800 nm of a LumaCare irradiation system, with a fluence rate of 28 mW/cm^2 for 30 min, *i.e.* 50.4 J/cm^2).

The tumor growth and volume were significantly reduced in UM-UC-3luc$^+$ tumors after PDT with **PorGal$_8$** when compared to control groups (Figure SI5.6A and Figure 5.6A,B). Immunohistochemical analysis of Ki-67 nuclear protein in tumors revealed that Ki-67-positive UM-UC-3luc$^+$ cells were rare after PDT with **PorGal$_8$** (Figure 5.6C), presumably because of the paucity of residual viable cells. Immunohistochemical analysis of E-cadherin demonstrated a well organized distribution of this protein in tumors of control animals and its disorganization in the tumors of animals treated with PDT (Figure SI5.6B). Western blot analysis demonstrated a decrease of both full-length E-cadherin (E-cadherin/FL) and its fragments 120 kDa after PDT with **PorGal$_8$** (Figure 5.6D). Furthermore, staining with Phalloidin-TRICT showed a reorganization of filamentous actin (F-actin) in the tumors of the animals treated with PDT (Figure 5.6E).

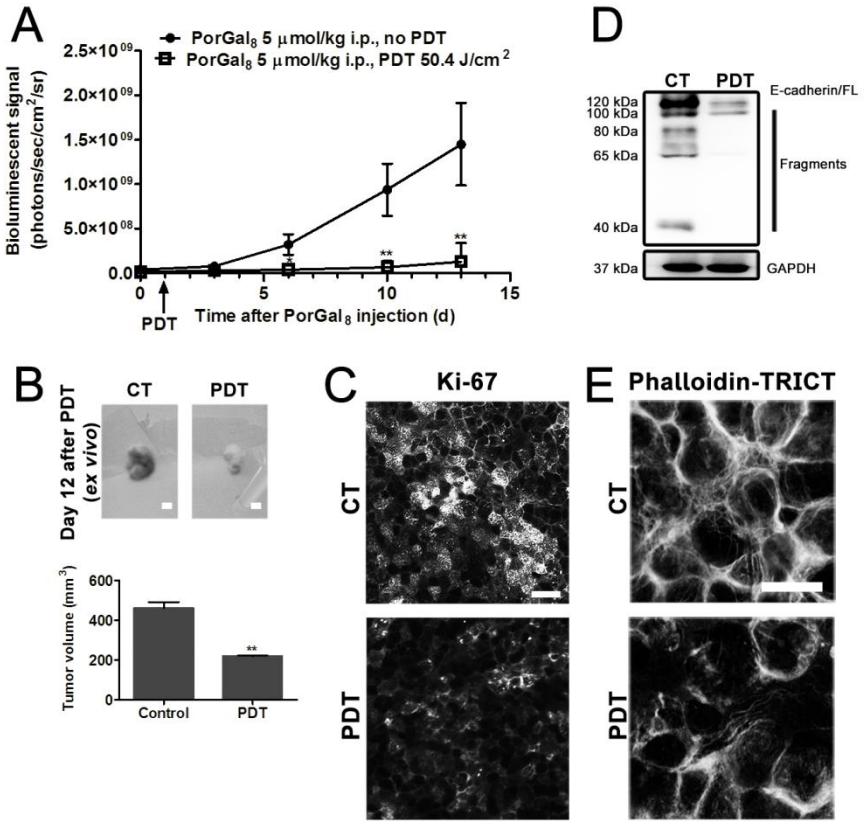

Figure 5.6 PorGal$_8$ has an anticancer photodynamic effect on UM-UC-3luc$^+$ tumors inoculated in nude mice. (A) Tumor growth inhibition by PDT with **PorGal$_8$** in UM-UC-3luc$^+$ tumors. * $P < 0.05$, ** $P < 0.01$ compared to the control group using a Student´s *t* test. Data are means ± s.e.m. ($n \geq 6$ mice in each group). (B) Representative photographs of dissected tumors in control group and animals treated with PDT. *Scale bars* 5 mm. Tumor volumes in untreated mice and mice treated with PDT at 12 days post PDT with **PorGal$_8$**. ** $P < 0.01$ compared to the control group using a Student´s *t* test. (C) Representative fluorescence images of Ki-67 protein (red) in UM-UC-3luc$^+$ tumors of control and treated group, with DAPI staining the nucleus (blue). *Scale bars* 20 μm. (D) Western blotting analysis of E-cadherin protein in UM-UC-3luc$^+$ tumors in control and treated group. GAPDH was blotted as loading control. (E) Representative fluorescence images of Phalloidin-TRICT in control and treated group. *Scale bars* 20 μm.

5.6 Discussion

Many existing PSs used in clinic lack tumor selectivity which leads to undesired damage in normal tissues. Thus, there have been many attempts to develop new PSs, that show specific accumulation within the target tumor tissue, through conjugation with various active targeting approaches, such as conjugation with carbohydrates [1-3], peptides or antibodies [4-7], incorporation within liposomes [16], and encapsulation within polymeric nanoparticles [17]. Among carbohydrates, the galactose one in the form of dendritic units could have potential in the development of new PSs since it improves the solubility of the PSs and it is able to promote multivalent interactions with galectins (namely galectin-1 [12]) overexpressed in many cancers [8]. In this study, **PorGal$_8$** was developed by linking four dendritic units of galactose to the photosensitizer porphyrin [14]. **PorGal$_8$**, has several advantages in PDT, including improved water-solubility, photostability, high ability to generate ROS (namely $^1O_2$) [14] and selectivity to cancer cells. The selectivity of **PorGal$_8$** is derived from its phototoxicity after preferential accumulation in cancer cells overexpressing galectin-1; the accumulation of this PS and its further phototoxicity is reduced in cancer cells containing low levels of galectin-1.

In vitro studies indicated that **PorGal$_8$** binds to galectin-1 with relative high affinity (K_D of 1.435±0.06175 μM and K_a of 1.27 x 10^7 M^{-1}). Human lectins are involved not only in carbohydrate interactions [18, 19], but they are also enrolled in protein-protein/lipid interactions *via* a hydrophobic binding site [20], different from the CRD. The tryptophan residue Trp68 has been determined as the one responsible for the fluorescence emission of galectin-1 protein [21]. This residue is found on the CRD [21] and it is important in the binding of lactose with galectin-1 [22], which is shown by the decrease of the Trp fluorescence intensity. Therefore, we can speculate that the molecules of galactose around the macrocycle of the porphyrin can promote the binding of **PorGal$_8$** with galectin-1 *via* a carbohydrate interaction with the CRD. In addition to the CRD, galectin-1 protein has also a well-conserved hydrophobic core, which is responsible for the existence of dimeric galectin-1 protein in solution due to hydrophobic interactions [21]. Therefore, we also hypothesize that, in addition to the carbohydrate interaction between **PorGal$_8$** and galectin-1, the spatial

clustering of hydrophobic amino acid side chains in human galectin-1 might hold the hydrophobic porphyrinic macrocycle. Previous studies have demonstrated that porphyrins (not conjugated with sugar moieties) interact with galectin-1 *via* hydrophobic binding sites [22]. Furthermore, the role of galectin-1 in **PorGal$_8$** selectivity was also shown when galectin-1 was knockdown in UM-UC-3 bladder cancer cells, which was associated with a marked decrease of PS uptake and phototoxicity.

In vivo studies performed in a xenograft tumor model which includes mice with UM-UC-3luc$^+$ cells (containing high levels of galectin-1) in the dorsum, validated the ability of **PorGal$_8$** to be accumulated in the tumor tissue. Based on previous data of the lactose-mediated liver-targeting effect [23], the strong fluorescence intensities of **PorGal$_8$** in the mice were obtained from 12 h to 24 h. **PorGal$_8$** fluorescence was found in the whole body with no selectivity at initial several hours and the strongest fluorescence in the tumor site was found at 24 h after intraperitoneal injection. At this time point, **PorGal$_8$** could be detected clearly also in the main excretory organs, such as kidney, liver and lung. Together, these data indicate that the linkage of dendritic units of galactose may be a useful tool for PS delivery in cancer tissues overexpressing galectin-1. In addition to being overexpressed in a spectrum of cancers, galectin-1 expression is also heightened in the tumor-associated stroma or neovascular endothelium where it contributes to tumor immune escape, metastasis and angiogenesis [11]. Even being PDT with **PorGal$_8$** twice selective (first **PorGal$_8$** is accumulated in the tumor and second only the tumor is light irradiated), this strategy can also result in indirect PDT effects on the cellular and molecular components of the tumor microenvironment.

PDT with **PorGal$_8$** in the xenograft tumor model demonstrated efficient tumor shrinkage with a single administration of **PorGal$_8$** followed by a single exposure of light. In a group of six animals, we detected complete elimination of the tumor in one of them. Previous PDT experiments with the PSs photofrin and/or talaporfin used irradiation doses superior to 100 J/cm^2 in carcinoma xenograft models [24, 25]. In our study, PDT with **PorGal$_8$** showed antitumor effects *in vivo* with a relatively low irradiation dose 50.4 J/cm^2. This indicates that the high cancer cell selectivity and specificity of **PorGal$_8$** could reduce the total energy of light irradiation needed in PDT treatment. This reduction may further reduce the risk or severity of side effects of PSs related to the damage to adjacent normal tissue.

The cytoskeleton components (actin microfilaments, microtubules and intermediate filaments) are potential targets in the development of new anti-cancer drugs, due to its role in cell morphology and membrane integrity. Cytoskeletal structures as well as cell adhesion proteins have been shown to be affected by PDT [26]. Our previous unpublished *in vitro* studies demonstrated that PDT with **PorGal$_8$** induces alterations of F-actin organization [27]. In the present study we observed that PDT with **PorGal$_8$** was also able to induce *in vivo* changes in the distribution pattern of the cell adhesion protein E-cadherin. E-cadherin, the prototypic member of the classic cadherin family, mediates cell–cell adhesion in epithelia and to function, the cytoplasmic domain of cadherins must bind to the actin cytoskeleton *via* proteins called catenins [28]. It is tempting to speculate that rearrangements of the actin cytoskeleton and of E-cadherin observed in the present study may play an important role in regulating cell death triggered by PDT with **PorGal$_8$**. Knowing that galectin-1 is also involved in cell motility and reorganization of the actin cytoskeleton in cells with increased expression of RhoA [29] (a protein involved in actin polymerization and depolymerisation processes), further assays are warranted to determine whether RhoA protein is involved in the photodamage induced by PDT with **PorGal$_8$** in the cytoskeleton of bladder cancer cells.

In the present study, we used a porphyrin conjugated with dendritic units of galactose as an agent of PDT *in vitro* and *in vivo*. The potential of PDT with **PorGal$_8$** seems to be primarily dependent on the expression of galectin-1 in bladder cancer cells and, then on ROS formation and alterations on the cytoskeleton of cancer cells. PDT with **PorGal$_8$** led to successful shrinkage of subcutaneously xenografted tumors after only a single administration of **PorGal$_8$** followed by a single exposure of light. Thus, we believe that our present study is the first to provide the *in vivo* potential of PSs conjugated with dendritic units of galactose in PDT of tumors overexpressing galectin-1.

5.7 References

1. Zheng G, Graham A, Shibata M, Missert JR, Oseroff AR, Dougherty TJ, Pandey RK (2001) Synthesis of β-galactose-conjugated chlorins derived by enyne metathesis as galectin-specific photosensitizers for photodynamic therapy. J Org Chem 66: 8709-8716.

2. Vedachalam S, Choi B-H, Pasunooti KK, Ching KM, Lee K, Yoon HS, Liu X-W (2011) Glycosylated porphyrin derivatives and their photodynamic activity in cancer cells. Med Chem Commun 2: 371-377.

3. Lourenço LMO, Pereira PMR, Maciel E, Valega M, Domingues FM, Domingues MR, Neves MGPMS, Cavaleiro JAS, Fernandes R, Tomé JPC (2014) Amphiphilic phthalocyanine-cyclodextrin conjugates for cancer photodynamic therapy. Chem Commun 50: 8363-8366.

4. Ding X, Xu Q, Liu F, Zhou P, Gu Y, Zeng J, An J, Dai W, Li X (2004) Hematoporphyrin monomethyl ether photodynamic damage on HeLa cells by means of reactive oxygen species production and cytosolic free calcium concentration elevation. Cancer Lett 216: 43-54.

5. Mitsunaga M, Ogawa M, Kosaka N, Rosenblum LT, Choyke PL, Kobayashi H (2011) Cancer cell-selective in vivo near infrared photoimmunotherapy targeting specific membrane molecules. Nat Med 17: 1685-1691.

6. Pereira PMR, Korsak B, Sarmento B, Schneider RJ, Fernandes R, Tomé JPC (2015) Antibodies armed with photosensitizers: from chemical synthesis to photobiological applications. Org Biomol Chem 13: 2518-2529.

7. Pereira PMR, Carvalho JJ, Silva S, Cavaleiro JAS, Schneider RJ, Fernandes R, Tomé JPC (2014) Porphyrin conjugated with serum albumins and monoclonal antibodies boosts efficiency in targeted destruction of human bladder cancer cells. Org Biomol Chem 12: 1804-1811.

8. Thijssen VL, Heusschen R, Caers J, Griffioen AWG (2015) Galectin expression in cancer diagnosis and prognosis: A systematic review. BBA -Rev Cancer 1855: 235-247.

9. Yau T, Dan XL, Ng CCW, Ng TB (2015) Lectins with potential for anti-cancer therapy. Molecules 20: 3791-3810.

10. Hasan SS, Ashraf GM, Banu N (2007) Galectins - potential targets for cancer therapy. Cancer Lett 253: 25-33.

11. Camby I, Le Mercier M, Lefranc F, Kiss R (2006) Galectin-1: a small protein with major functions. Glycobiology 16: 137R-157R.

12. Cindolo L, Benvenuto G, Salvatore P, Pero R, Salvatore G, Mirone V, Prezioso D, Altieri V, Bruni CB, Chiariotti L (1999) Galectin-1 and galectin-3 expression in human bladder transitional-cell carcinomas. Int J Cancer 84: 39-43.

13. Kim H-J, Jeon H-K, Cho YJ, Park YA, Choi J-J, Do I-G, Song SY, Lee Y-Y, Choi CH, Kim T-J, Bae D-S, Lee J-W, Kim B-G (2012) High galectin-1 expression correlates with poor prognosis and is involved in epithelial ovarian cancer proliferation and invasion. Eur J Cancer 48: 1914-1921.

14. Silva S, Pereira PMR, Silva P, Paz FAA, Faustino MAF, Cavaleiro JAS, Tomé JPC (2012) Porphyrin and phthalocyanine glycodendritic conjugates: synthesis, photophysical and photochemical properties. Chem Commun 48: 3608-3610.

15. Pereira PMR, Silva S, Cavaleiro JAS, Ribeiro CAF, Tomé JPC, Fernandes R (2014) Galactodendritic phthalocyanine targets carbohydrate-binding proteins enhancing photodynamic therapy. PLoS One 9: e95529.

16. Skupin-Mrugalska P, Piskorz J, Goslinski T, Mielcarek J, Konopka K, Düzgüneş N (2013) Current status of liposomal porphyrinoid photosensitizers. Drug Discov Today 18: 776-784.

17. Camerin M, Magaraggia M, Soncin M, Jori G, Moreno M, Chambrier I, Cook MJ, Russell DA (2010) The *in vivo* efficacy of phthalocyanine-nanoparticle conjugates for the photodynamic therapy of amelanotic melanoma. Eur J Cancer 46: 1910-1918.

18. Gabius H-J (1994) Noncarbohydrate Binding Partners/Domains of Animal Lectins. Int J Biochem 26: 469-477.

19. Bogoeva VP, Russev GC (2008) Fluorescence study of steroid hormone binding activity of Helix pomatia agglutinin. Steroids 73: 1060-1065.

20. Barondes SH (1981) Lectins - Their Multiple Endogenous Cellular Functions. Annu Rev Biochemistry 50: 207-231.

21. López-Lucendo MF, Solís D, André S, Hirabayashi J, Kasai K-I, Kaltner H, Gabius H-J, Romero A (2004) Growth-regulatory human galectin-1: Crystallographic characterisation of the structural changes induced by single-site mutations and their impact on the thermodynamics of ligand binding. J Mol Biol 343: 957-970.

22. Iglesias MM, Elola MT, Martinez V, Fink N, Wolfenstein-Todel C (2003) Identification of an equilibrium intermediate in the unfolding process of galectin-1, which retains its carbohydrate-binding specificity. Bba-Proteins Proteom 1648: 164-173.

23. Ma PA, Liu S, Huang Y, Chen X, Zhang L, Jing X (2010) Lactose mediated liver-targeting effect observed by ex vivo imaging technology. Biomaterials 31: 2646-2654.

24. Peng Q, Warloe T, Moan J, Godal A, Apricena F, Giercksky K-E, Nesland JM (2001) Antitumor effect of 5-aminolevulinic acid-mediated photodynamic therapy can be enhanced by the use of a low dose of photofrin in human tumor xenografts. Cancer Res 61: 5824-5832.

25. Schastak S, Jean B, Handzel R, Kostenich G, Hermann R, Sack U, Orenstein A, Wang Y-S, Wiedemann P (2005) Improved pharmacokinetics, biodistribution and necrosis in vivo using a new near infra-red photo sensitizer: tetrahydroporphyrin tetratosylat. J Photoch and Photobio B 78: 203-213.

26. Uzdensky A, Kolpakova E, Juzeniene A, Juzenas P, Moan J (2005) The effect of sub-lethal ALA-PDT on the cytoskeleton and adhesion of cultured human cancer cells. Biochim Biophys Acta 1722: 43-50.

27. Pereira PMR (2012) Cojugados fotoativos para tratamento do cancro da bexiga. Tese de Mestrado, Universidade de Aveiro.

28. Gumbiner BM (2005) Regulation of cadherin-mediated adhesion in morphogenesis. Nat Rev Mol Cell Biol 6: 622-634.

29. Camby I, Belot N, Lefranc F, Sadeghi N, de Launoit Y, Kaltner H, Musette S, Darro F, Danguy A, Salmon I, Gabius HJ, Kiss R (2002) Galectin-1 modulates human glioblastoma cell migration into the brain through modifications to the actin cytoskeleton and levels of expression of small GTPases. J Neuropathol Exp Neurol 61: 585-596.

5.8 Supporting Information

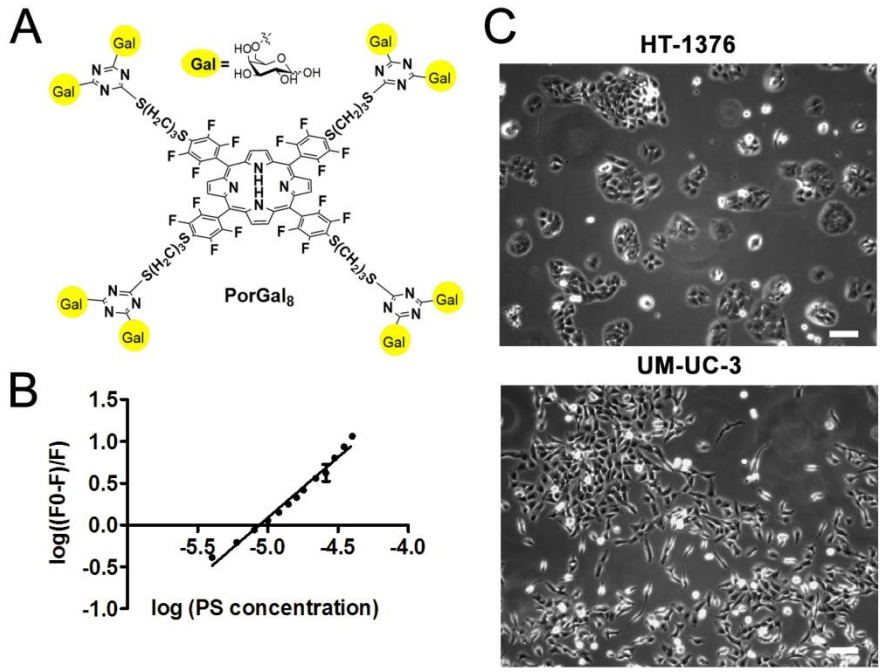

Figure SI5.1 (A) Chemical structure of porphyrin conjugated with four dendritic units of galactose (**PorGal$_8$**). (B) Linear plot obtained by plotting the changes in the fluorescence of human galectin-1, *log((F$_0$-F)/F)vs.* log(PS concentration) where log(Ka) and n are the ordinate at the origin and slope, respectively. (C) Bright field images of monolayer culture of HT-1376 and UM-UC-3 human bladder cancer cell lines. *Scale bars* 20 µm.

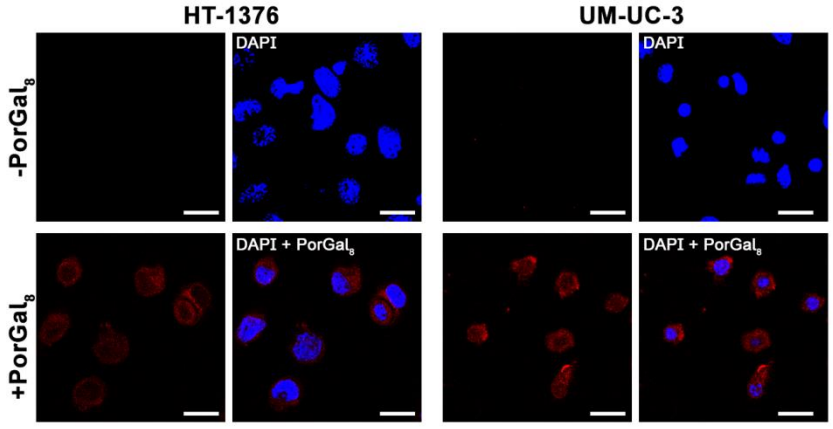

Figure SI5.2 Representative fluorescence images of bladder cancer cells incubated with **PorGal$_8$** (red) in darkness and cell nucleus stained with DAPI (blue). *Scale bars* 20 µm.

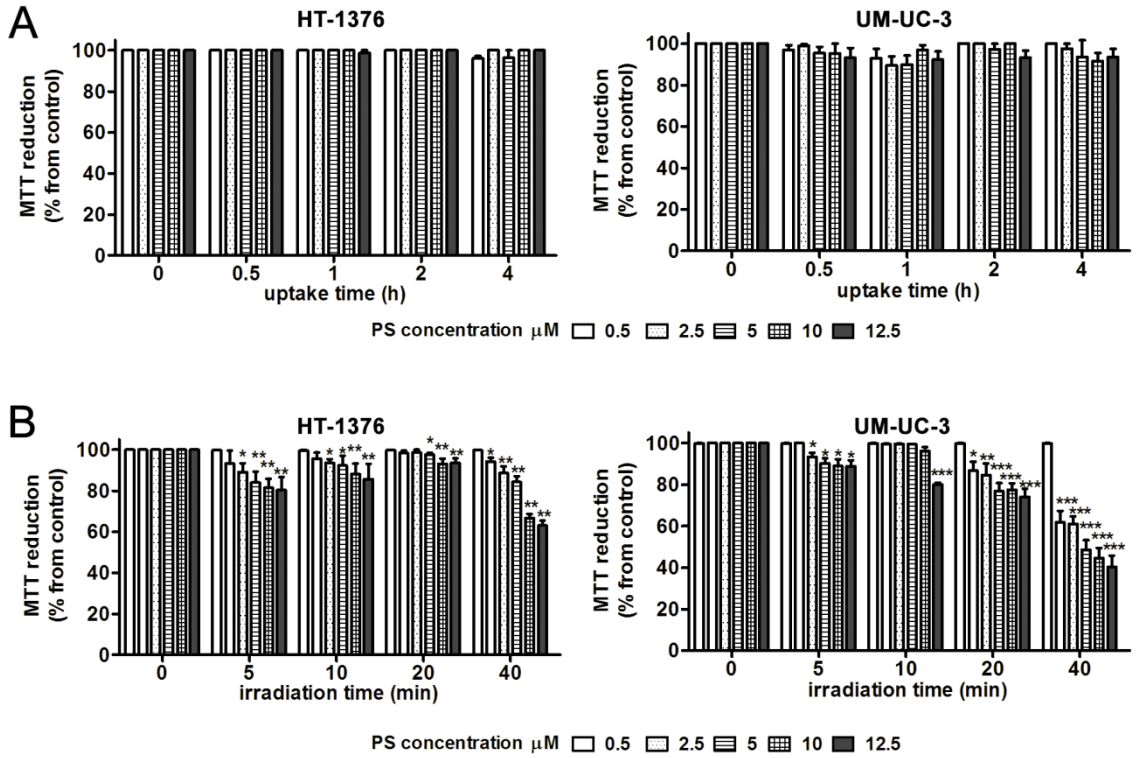

Figure SI5.3 (A) Non-dark toxicity of **PorGal$_8$** determined 24 h after treatment using the MTT assay. The percentage of cytotoxicity was calculated relatively to control cells (untreated cells). Data are means ± s.e.m. of at least three independent experiments performed in triplicates. (B)Irradiation dose-dependent cell death in response to PDT with **PorGal$_8$**. Cytotoxicity was assessed 24 h after treatment using the MTT assay. The percentage of cytotoxicity was calculated relatively to control cells (untreated cells). Data are means ± s.e.m. of at least three independent experiments performed in triplicates. * $P < 0.05$, ** $P < 0.01$, *** $P < 0.001$ compared to MTT reduction (%) or excluded trypan blue (%) at 24 h after PDT for the respective control using a Student´s t test.

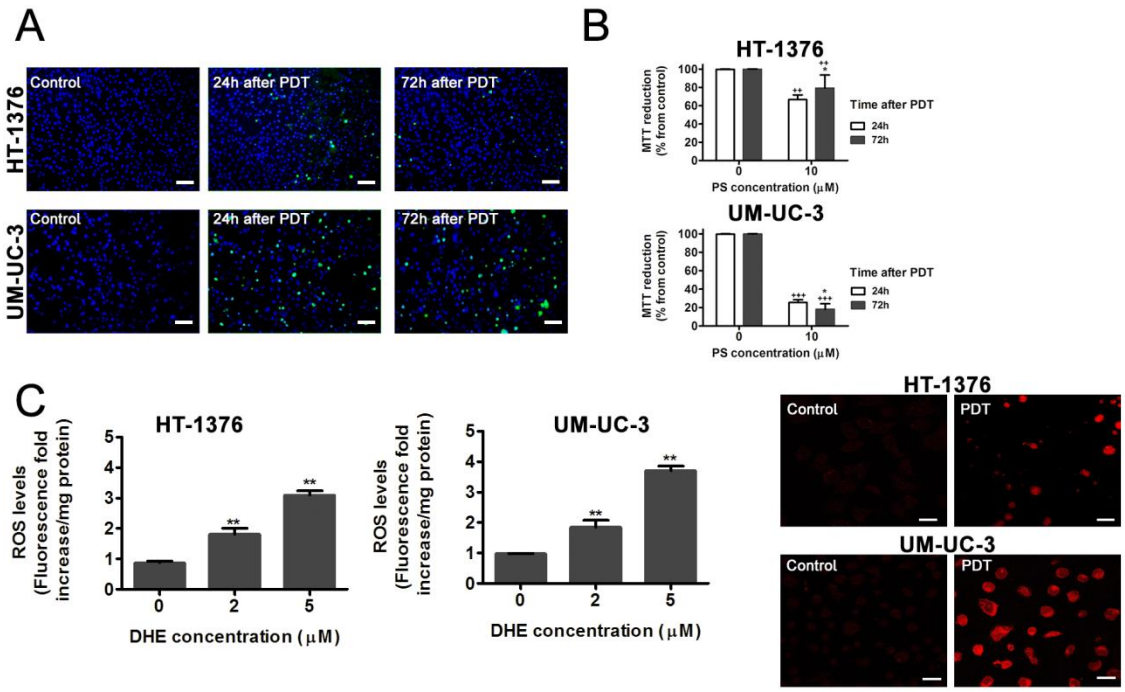

Figure SI5.4 (A) Representative fluorescence images of apoptotic cell death using TUNEL assay in HT-1376 and UM-UC-3 cells at 24 and 72 h after PDT with **PorGal$_8$**. DAPI was used for nuclear region staining (blue) and TUNEL staining was used to visualize dead cells (green). *Scale bars* 20 μm. (B) Phototoxicity at 24 and 72 h after treatment using the MTT assay. The percentage of cytotoxicity was calculated relatively to control cells (untreated cells). Data are means ± s.e.m. of at least three independent experiments performed in triplicates. $^{++}P < 0.01$, $^{+++}P < 0.001$ compared to MTT reduction (%) in control cells 24 or 72h after PDT using a Student´s t test. * $P < 0.05$, compared to MTT reduction at 24 h for the respective treated cells. (C) Quantification and representative fluorescence images of DHE fluorescence increase (as a measure of ROS production) in HT-1376 and UM-UC-3 cancer cells, after PDT with **PorGal$_8$**. *Scale bars* 20 μm. Data are means ± s.e.m. of at least three independent experiments performed in triplicates. ** $P < 0.01$ compared to control cells using a Student´s *t* test.

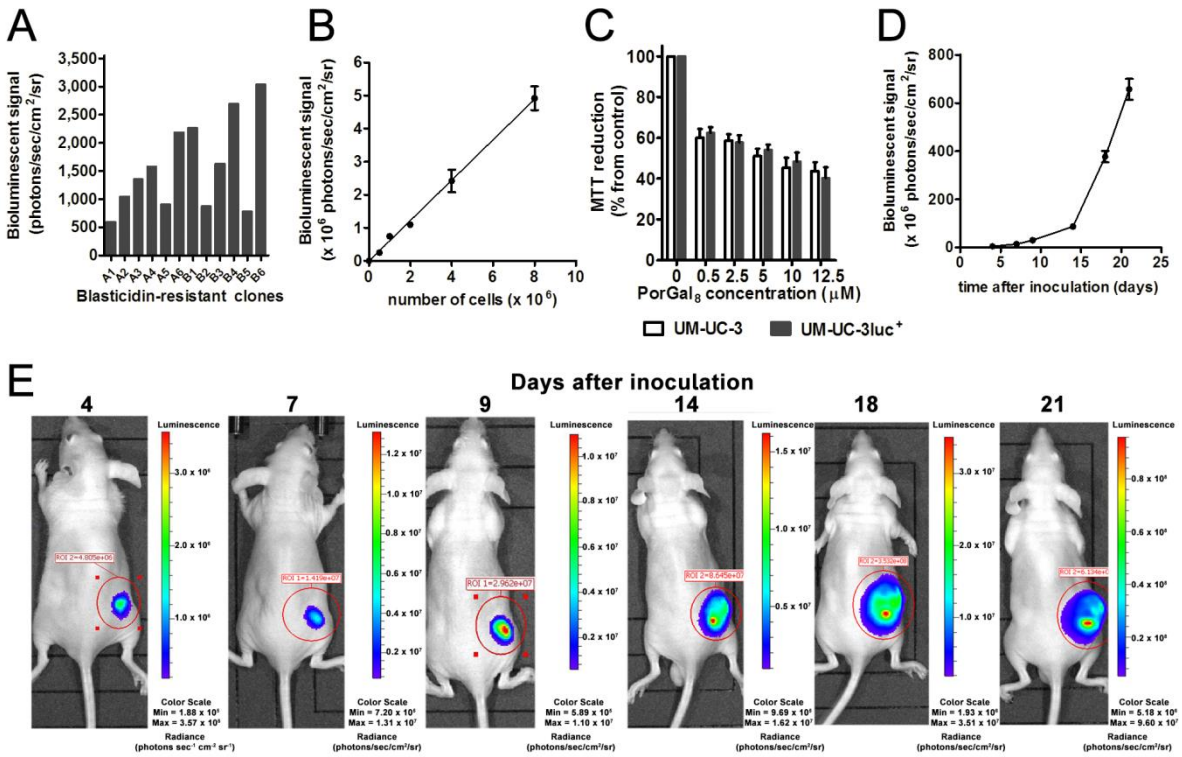

Figure SI5.5 (A) Bioluminescent signal of blasticidin-resistant clones isolated from UM-UC-3 bladder cancer cells transduced with the pLenti6 lentiviral vector containing the firefly reporter gene. Data are means ± s.e.m. of one independent experiment performed in duplicates. (B) *In vitro* correlation between the bioluminescent signal of clone B6 and the cell number. Data are means ± s.e.m. of one independent experiment performed in triplicates. (C) Phototoxicity after PDT with **PorGal$_8$** in UM-UC-3 and UM-UC-3luc$^+$ bladder cancer cells. Cytotoxicity was assessed 24 h after treatment using the MTT assay. The percentage of cytotoxicity was calculated relatively to control cells (untreated cells).Data are means ± s.e.m. of at least three independent experiments performed in triplicates. (D) and (E) Bioluminescent signals at 4, 7, 9, 14, 18 and 21 days post-implantation of UM-UC-3luc$^+$ cancer cells into the flanks of athymic nude mice. Data are means ± s.e.m. (n = 6 mice).

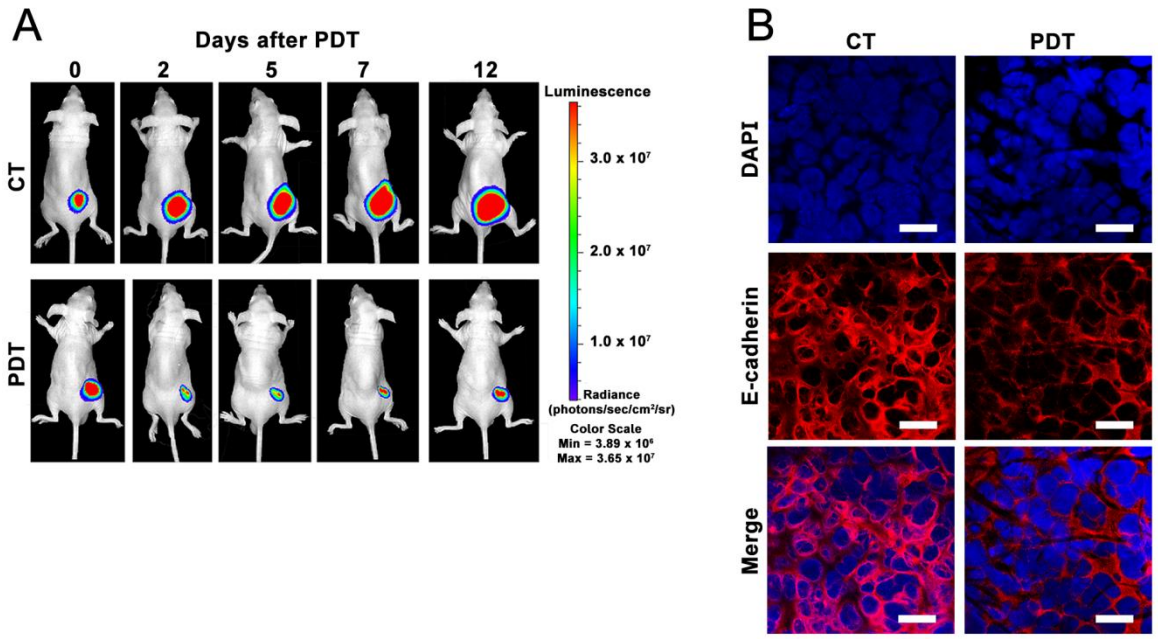

Figure SI5.6 (A) Representative bioluminescent images of mice at 2, 5, 7 and 12 days post PDT with **PorGal$_8$**. PDT 50.4 J/cm^2 was performed 24 h after intraperitoneal injection with 5 μmol/kg of **PorGal$_8$**. (B) Representative fluorescence images of E-cadherin protein (red) in UM-UC-3luc$^+$ tumors of control and treated group, with DAPI staining the nucleus (blue). *Scale bars* 20 μm.

Mitochondria-targeted photodynamic therapy with a galactodendritic chlorin to enhance cell death in resistant human bladder cancer cells

CHAPTER VI

Chapter VI Mitochondria-targeted photodynamic therapy with a galactodendritic chlorin to enhance cell death in resistant human bladder cancer cells

6.1 General overview

The photodynamic efficiency could be improved when PS reach and accumulate in hypersensitive subcellular sites [1]. The physicochemical properties of the PSs such as chemical structure, lipophilicity and charge have a key role on their accumulation in cell structures or organelles such as plasma membranes, lysossomes and mitochondria [2]. The mitochondrion is an attractive target for PDT due to its central role in energy metabolism and regulation of apoptosis [3, 4]. PSs able to target primarily mitochondria, such as cationic compounds or agents containing a mitochondrial localization peptide sequence have demonstrated enhanced phototoxicity, through mitochondria-mediated apoptosis [5-7]. However, a major limitation of the existing PS is the lack of high selectivity for cancer cells.

In the design of new PSs for cancer treatment, reduction of porphyrins to Chls results on an increase in the extinction coefficient of the last Q band [8, 9]. Particularly, perfluorophenylchlorin (**ChlF$_{20}$**) has demonstrated to be a useful core platform in the development of new PSs [10]. Based on our recent research, we envisaged that the conjugation of **ChlF$_{20}$** with dendritic units of galactose could improve not only the solubility of the PS in an aqueous medium [11] but also increase its specificity for tumor tissues [12]. The high local concentration of galactodendritic PSs in the tumor tissues is due to the possible interaction of galactose molecules with galactose-binding proteins (such as galectin-1 and glucose transporter 1 GLUT1) overexpressed in these tissues [13].

Here we report the rational design of a new third-generation PS, a chlorin conjugated with galactodendritic units, **ChlGal$_8$**, to improve the effectiveness of bladder cancer treatment. **ChlGal$_8$** shows better photo-chemical and -physical properties than the homologous porphyrin, **PorGal$_8$**. In addition to inheriting excellent photostability, ability to generate $^1O_2$ and to interact with the proteins galectin-1 and HSA, **ChlGal$_8$** exhibits high absorption in the

red region of the electromagnetic spectrum. *In vitro* studies of anticancer activity of **ChlGal$_8$** revealed that once this PS is taken up by UM-UC-3 bladder cancer cells, induces high cytotoxicity after a single dose of light irradiation. In HT-1376 bladder cancer cells resistant to therapy, enhanced photodynamic efficacy both *in vitro* and *in vivo* was achieved after a second light irradiation. The enhanced phototoxicity in HT-1376 cancer cells seems to be due to **ChlGal$_8$** ability to accumulate in the mitochondria, *via* GLUT1, in the period of time between single and repeated irradiation. A PDT regimen by using an extra dose of light irradiation and **ChlGal$_8$** as PS, represents a promising strategy in treating resistant cancers in clinic (Figure 6.1).

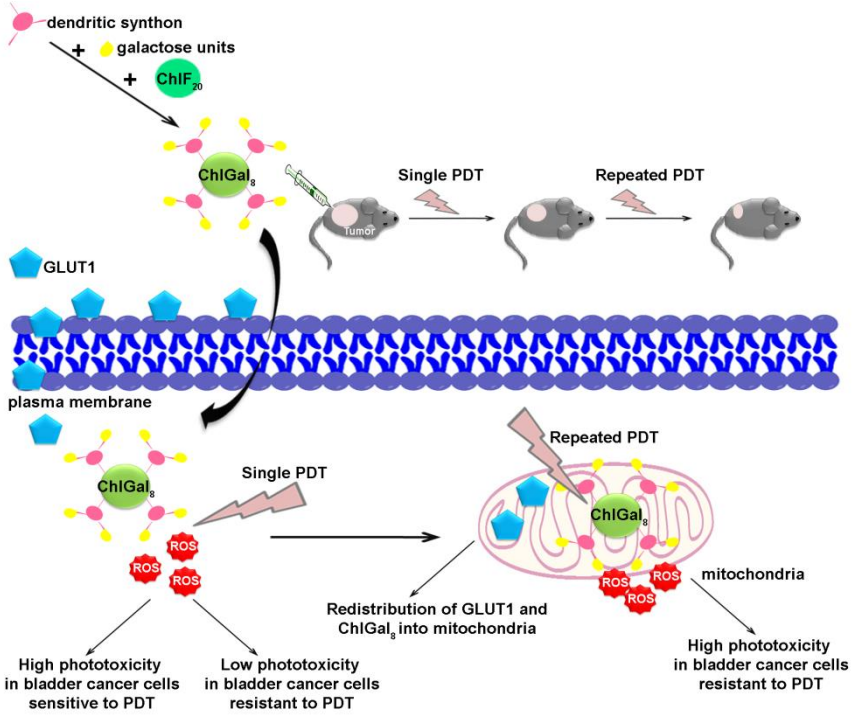

Figure 6.1 Hypothetic illustration of phototoxicity of ChlGal$_8$ in *in vitro* and *in vivo* biological models.ChlGal$_8$ is accumulated in bladder cancer cells. After single PDT, **ChlGal$_8$** generates ROS which induce high cell death in bladder cancer cells sensitive to PDT. Before repeated PDT, **ChlGal$_8$** is preferentially accumulated in the mitochondria (as well as GLUT1 protein) and induces high phototoxicity in bladder cancer cells resistant to PDT. As the animal model is the essential link between cell-based experiments and translational of this new PS into patients with bladder cancer, we have established a xenograft tumor model by subcutaneous injection of HT-1376 human bladder cancer cells in the dorsum of immunocompromised nude mice. A significant inhibition in the tumor growth was observed after repeated PDT with **ChlGal$_8$**.

6.1.1 Methods

The following experimental protocols (please see Methods and Materials chapter IX) were used to obtain the data presented in this chapter:

- Aggregation assays (9.2.2A)
- Fluorescence assays (9.2.2B)
- Photostability assays (9.2.2C)
- Singlet oxygen assays (9.2.2D)
- Protein interaction assays – galectin-1 and HSA (9.2.2E)
- Partition coefficients (9.2.2F)
- Biological models – Culture of HT-1376 and UM-UC-3 bladder cancer cells (9.3.8A)
- Fluorescence spectroscopy – uptake of **ChlGal$_8$** (9.3.8C-E)
- PDT treatments – Photosensitizer **ChlGal$_8$** (9.3.8F)
- Cell viability assays – MTT assays (9.3.8G)
- Transfection assays – knockdown of GLUT1 using siRNA (9.3.8I)
- Intracellular levels of Reactive Oxygen Species (9.3.8J)
- Redox quenching assays (9.3.8K)
- Western blotting assays – Lamin B, GLUT1, β-actin, Tom20, ZO-1 (9.3.8L)
- Cellular fractionation (9.3.8P)
- *In vivo* assays (9.4.8B)

6.1.2 Publication

This chapter comprises the following publication:

Patrícia M. R. Pereira, Sandrina Silva, Mafalda Bispo, Mónica Zuzarte, Célia Gomes, Henrique Girão, José A. S. Cavaleiro, Carlos A. F. Ribeiro, João P. C. Tomé, Rosa Fernandes, Mitochondria-targeted photodynamic therapy with a galactodendritic chlorin to enhance cell death in resistant bladder cancer cells, *submitted*.

6.2 ChlGal$_8$ exhibits excellent photo-physical and -chemical properties for PDT

ChlGal$_8$ (Figure 6.2A) was synthesized as described in chapter II. The steady-state fluorescence emission spectrum of **ChlGal$_8$** was acquired in dimethylformamide (DMF) and the fluorescence quantum yield (Φ_F) was determined (Table 6.1). These studies demonstrated that **ChlGal$_8$** has emission bands in the red spectral region at 653 nm and 714 nm. The electronic absorption spectra of **ChlGal$_8$** were measured in DMSO and their extinction coefficients (ε) in this solvent are summarized in Table 6.1. **ChlGal$_8$** at 4 μM (in DMSO) exhibit a very sharp Soret (around 410 nm) and Q bands (around 650 nm), which are typical of non-aggregated PSs (Figure 6.2B).

Table 6.1 UV-Visible and fluorescence data of the galactose-conjugate **ChlGal$_8$**.

Galactose-conjugate	Solvent	λabsorption bands[nm] (log ε)[a]	λemission (nm)	Φ_F
ChlGal$_8$	DMF	411 (4.5), 651 (3.80)	653, 714	0.60b
	DMSO	411 (4.41), 650 (3.83)	___	___
	PBS	416 (4.35), 652 (3.78)	___	___

[a]logε $M^{-1}cm^{-1}$, [b]Reference: 5,10,15,20-tetraphenylporphyrin (TPP) in DMF Φ_F = 0.11 [14] excitation at 601 nm.

To determine the solubility of **ChlGal$_8$** in aqueous buffered solution, their absorption spectra were also acquired in PBS. In this solvent, **ChlGal$_8$** demonstrated a lowering intensity and a broadening of the Soret and Q bands, which are related with reasonable water solubility (Figure 6.2B). The galactose-conjugate strictly follows the Beer-Lambert law at concentrations between 0 to 10 μM suggesting no aggregation in PBS at concentrations below 10 μM (Figure SI6.1A,B). To predict a priori the ability of **ChlGal$_8$** to diffuse across cancer cell membranes and to reach the inside of cancer cells, the partition coefficient value (log *P*, which is the log of the concentration of compounds in n-octanol/PBS system) was determined using the classic shake flask method [10]. Data show that the values of log *P* are higher for **PorGal$_8$** when compared with **ChlGal$_8$** (Table 6.2), indicating that **ChlGal$_8$** has less water solubility when compared with the corresponding porphyrin **PorGal$_8$**.

Table 6.2 Partition coefficient (log *P* in n-octanol/PBS system) values of the galactose-conjugates **PorGal$_8$** and **ChlGal$_8$**.

Compound	log *P*
PorGal$_8$	-4.00
ChlGal$_8$	-2.65

The photostability of **ChlGal$_8$** was evaluated, by monitoring the intensity of Soret band of a PBS solution containing 4 µM **ChlGal$_8$**, after irradiation with red light (>500 nm) at a fluence rate of 150 mW/cm^2 (Table SI6.1). The results demonstrate that this galactose-conjugate is photostable when exposed to strong light power over the investigated irradiation period (30 min). The generation of $^1O_2$ by **ChlGal$_8$** was determined in DMF:H_2O (9:1, v:v) using DPBF as $^1O_2$ scavenger. The well known $^1O_2$ generator, **TPPF$_{20}$**, was used as reference [15]. The ability of **ChlGal$_8$** to generate $^1O_2$ was also compared with the corresponding porphyrin **PorGal$_8$**. **ChlGal$_8$**, **PorGal$_8$** and **TPPF$_{20}$** (both at 0.67 µM) were able to photo-oxidize DPBF (at 16.15 µM, Figure 6.2C). Under the conditions of the assay, **ChlGal$_8$** demonstrated higher ability to photo-oxidize DPBF when compared to the corresponding porphyrin **PorGal$_8$**.

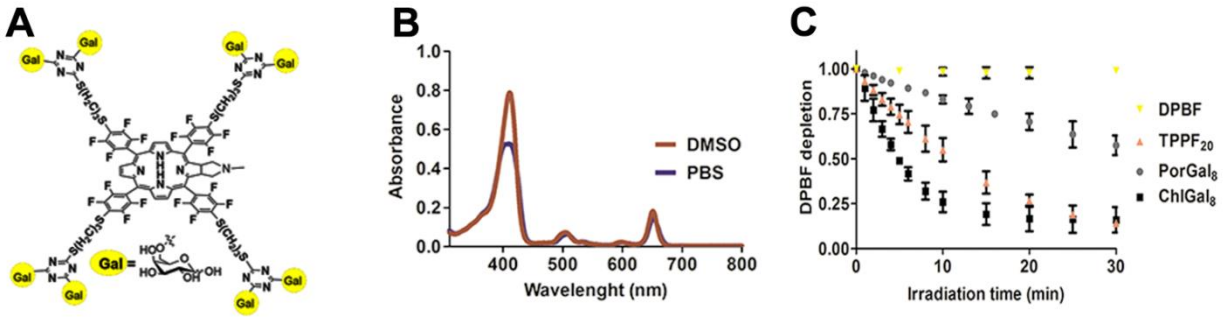

Figure 6.2 ChlGal$_8$ exhibits excellent photo-chemical and -physical properties. (A) Chemical structure of **ChlGal$_8$**. (B) Electronic absorption spectra of **ChlGal$_8$** at 4 µM in DMSO and PBS. (C) Photo-oxidation of DPBF (16.15 µM) with or without **ChlGal$_8$**, **PorGal$_8$** or **TPPF$_{20}$** at 0.67 µM, after irradiation with red light (λ > 500 nm, 14 mW/cm^2). The DPBF absorbance was recorded at 415 nm. Data are means ± s.e.m. of at least two independent experiments.

6.3 ChlGal$_8$ interacts with human serum albumin and galectin-1 proteins

To predict the *in vivo* pharmacokinetics and pharmacological properties of **ChlGal$_8$**, its interaction with the most abundant plasma protein (HSA) was studied by fluorescence spectroscopy [11, 16]. A quenching on the fluorescence emission (Figure SI6.1C) of the single tryptophan residue present in the protein (Trp214 [17] located in subdomain IIA of site I) occurred after addition of **ChlGal$_8$** (0 to 40 µM) to HSA samples (2 µM). K_a and n for **ChlGal$_8$** were 3.28 x 104 M^{-1} and 1.0, respectively. The value of n equal to 1 indicates that **ChlGal$_8$** binds HSA in the molar ratio of 1:1.

We previously reported that the galactose binding proteins overexpressed in bladder cancer cells, galectin-1 and GLUT1, have a key role on the uptake of galactodendritic PSs [12]. The addition of **ChlGal$_8$** (0 to 4 µM) to recombinant human galectin-1 (2 µM) produced fluorescence quenching (Figure 6.3A) of the tryptophan residue (Trp68 [18, 19] present on the carbohydrate-recognition domain of the protein). The values of K_a and n equal to 1.76 x 107 M^{-1} and 1.5, respectively, as well as the $K_D$equal to 3.79 ± 2.22 µM indicate that **ChlGal$_8$** has high interaction for galectin-1.

6.4 ChlGal$_8$ accumulates and induces phototoxicity in bladder cancer cells

Encouraged by the excellent photo-physical and -chemical properties of **ChlGal$_8$**, we tested the PDT efficacy of **ChlGal$_8$** in two bladder cancer cell lines derived from transitional cell carcinoma, HT-1376 and UM-UC-3. Bladder cancer is a especially well suited for PDT since bladder is an easily accessible organ for both intravesical instillation and illumination [20]. Cancer cell uptake of **ChlGal$_8$** (0.5 to 10 µM) for up to 4 h was evaluated by fluorescence spectroscopy. Both HT-1376 and UM-UC-3 cells took up **ChlGal$_8$** quite readily with similar uptake profile and a slower steady increase was observed after 1.5 h (Figure 6.3B).

To evaluate the efficacy of PDT by **ChlGal$_8$** in bladder cancer cells, UM-UC-3 and HT-1376 were treated with **ChlGal$_8$** at various concentrations, and cells were then irradiated with red light (> 500 nm) at 2.5 mW/cm^2 for 40 min (*i.e.* 6 J/cm^2). No cytotoxicity was observed in

cells incubated with **ChlGal$_8$** in the dark (Figure SI6.2) for at least 72 h after treatment. However, when UM-UC-3 and HT-1376 bladder cancer cells were incubated with **ChlGal$_8$** and then irradiated there was an increased phototoxicity in a concentration-dependent manner (Figure 6.3C).

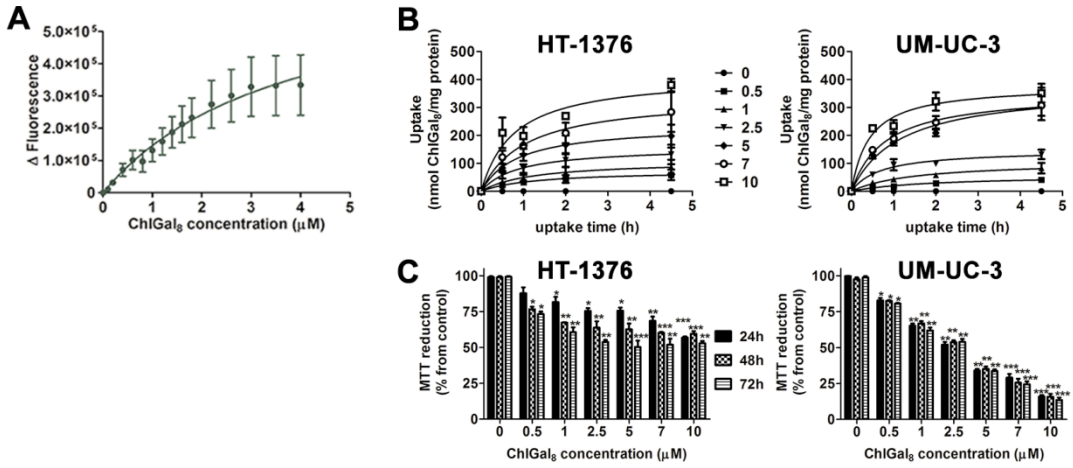

Figure 6.3 ChlGal$_8$ interacts with galectin-1 protein, accumulates and induces phototoxicity in bladder cancer cells. (A) Fluorescence variation on the emission spectrum of 2 μM galectin-1 protein after addition of **ChlGal$_8$** (0-4 μM). Data are means ± s.e.m. of at least two independent experiments. (B) Intracellular uptake of **ChlGal$_8$** by HT-1376 and UM-UC-3 bladder cancer cells. Data are means ± s.e.m. of at least three independent experiments performed in triplicate. (C) Cytotoxicity 24, 48 and 72 h after PDT with **ChlGal$_8$**, determined using the MTT assay. Data are means ± s.e.m. of at least three independent experiments performed in triplicate. $^{*}P<$ 0.05, $^{**}P<$ 0.01, $^{***}P<$ 0.001 compared to MTT reduction (%) of control cells (untreated cells) using a Student´s *t* test.

Although PDT with **ChlGal$_8$** is more active against UM-UC-3 cells than HT-1376 cells, both cell lines were unable to recover from the PDT-induced damage effects (up to 72 h). The degree of cytotoxic effect of PDT with **ChlGal$_8$** in the two cell lines can be partially explained by the different intracellular amount of ROS produced immediately after irradiation, as detected with the oxidation-sensitive fluorescent dye 2´,7´-dichlorohydrofluorescin (H_2DCFDA, Figure 6.4A).

6.5 A second light irradiation enhances photodynamic efficacy of ChlGal$_8$ in bladder cancer cells

The resistance of HT-1376 cancer cells to PDT with **ChlGal$_8$** prompted us to investigate the optimization of treatment regimens by repeated dose of light irradiation in order to enhance the effectiveness of PDT (Figure 6.4A). Cells were subjected to two irradiations for 40 min at 2.5 mW/cm^2 (6 J/cm^2) with a time interval of 1.5 h. The phototoxicity was determined 24 h after treatment. Data show that the repeated PDT treatment was similar to the single PDT in UM-UC-3 bladder cancer cells (Figure 6.4B). In HT-1376 bladder cancer cells, the repeated PDT was shown to be more effective (Figure 6.4B).

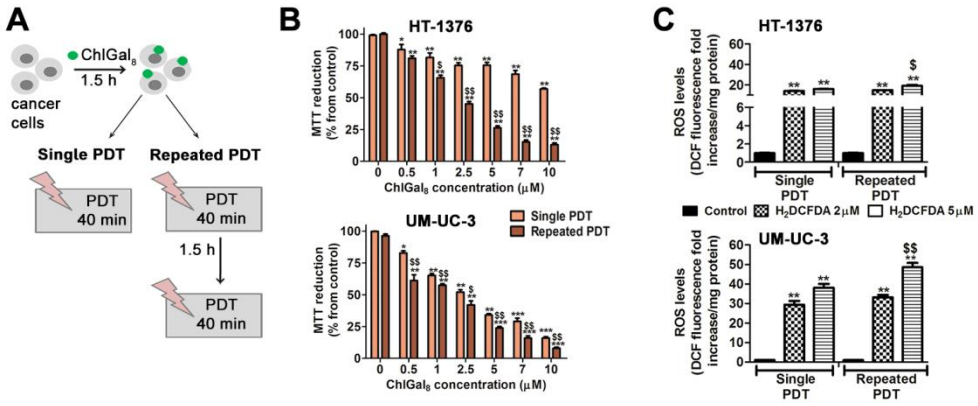

Figure 6.4 A second irradiation improves PDT efficacy in bladder cancer cells resistant to therapy. (A) Schematic illustration of single and repeated PDT experiments performed with **ChlGal$_8$** in bladder cancer cells. (B) Cytotoxicity 24 h after single and repeated PDT with **ChlGal$_8$**, in HT-1376 and UM-UC-3 cancer cells, was evaluated using the MTT assay. Data are means ± s.e.m. of at least three independent experiments performed in triplicate. $^{*}P< 0.05$, $^{**}P< 0.01$, $^{***}P< 0.001$ compared to MTT reduction (%) at 24 h after PDT for control cells (untreated cells) using a Student´s *t* test. $^{\$}P< 0.05$, $^{\$\$}P<0.01$ compared to MTT reduction (%) at 24 h after PDT for single PDT at the respective concentration of **ChlGal$_8$** using a Student´s *t* test. (C) Quantification of oxidized H_2DCFDA (DCF) fluorescence increase (as a measure of ROS production) in HT-1376 and UM-UC-3 cancer cells, after single and repeated PDT with **ChlGal$_8$**. Data are means ± s.e.m. of at least three independent experiments performed in triplicate. $^{**}P< 0.01$ compared to control cells (untreated cells) using a Student´s *t* test. $^{\$}P< 0.05$, $^{\$\$}P< 0.01$ compared to single PDT using a Student´s *t* test.

The concentrations of **ChlGal$_8$** necessary to inhibit the metabolic activity of UM-UC-3 and HT-1376 bladder cancer cells in 50% (IC_{50}), after single and repeated light irradiation, were estimated from Figure 6.3C and Figure 6.4B. IC_{50} value is higher for HT-1376 cells treated with single PDT when compared with these cells treated with repeated PDT (Table 6.3).

Table 6.3 Values for photocytotoxic concentration (IC_{50}, μM) of photoactivated$ChlGal_8$ after single and repeated PDT on human bladder cancer cell lines, HT-1376 and UM-UC-3.

	IC_{50} (μM), $CI_{95\%}$	
	UM-UC-3	**HT-1376**
Single PDT	1.4 [0.83; 2.3]	4.0 [0.93;17.4]
Repeated PDT	1.3 [0.58;3.1]	1.3 [0.84;1.9]

IC_{50} is the incubation concentration that inhibits the metabolic activity of cancer cells in 50%, after single and repeated PDT with $ChlGal_8$. IC_{50}values were calculated using the MTT dose response curves (24 h after treatment).$CI_{95\%}$: 95% Confidence interval.

We further showed that the increased phototoxicity after repeated PDT with **ChlGal$_8$** in resistant HT-1376 bladder cancer cells was accompanied by increased ROS production (Figure 6.4C). Additional studies performed with the corresponding porphyrin **PorGal$_8$** demonstrated that the high phototoxicity induced after repeated PDT, in resistant HT-1376 cancer cells, is a specific characteristic of **ChlGal$_8$** (Figure SI6.3).

6.6 ChlGal$_8$ accumulation in mitochondrial fraction is enhanced after a single irradiation

The improved efficacy of **ChlGal$_8$** after repeated PDT in resistant HT-1376 bladder cancer cells, prompted us to study the intracellular localization of **ChlGal$_8$** before single and repeated treatment. Subcellular fractions were prepared by the differential centrifugation method [21] and the amount of **ChlGal$_8$** in such fractions was determined by fluorescence spectroscopy. To ensure proper fraction enrichment, the subcellular fractions were also tested by western blot for specific markers, such as lamin B (nuclear marker), β-actin (cytosol

marker), Tom20 (mitochondrial marker) and ZO-1 (membrane marker). After **ChlGal$_8$** uptake (before single PDT), the intracellular concentration of this PS in the subcellular fractions of UM-UC-3 and HT-1376 bladder cancer cells decreased in the following order: nuclei *plus* cell debris (intact cells and large membranes) > mitochondria > plasma membrane > cytosol (Figure SI6.4 and Figure 6.5). The distribution of **ChlGal$_8$** was similar in the subcellular fractions obtained before first and repeated PDT (Figure SI6.4) in UM-UC-3 bladder cancer cells. In HT-1376 bladder cancer cells, there was an increase of **ChlGal$_8$** in the mitochondrial fraction obtained before repeated PDT (Figure 6.5A). The increase of **ChlGal$_8$** in the mitochondrial fraction of HT-1376 cells was accompanied with a decrease of this PS in the "nucleus *plus* cell debris" fraction. Interestingly, Western blot analysis of GLUT1 demonstrated that in the period of time between single and repeated PDT there is an increase of GLUT1 protein in the mitochondrial fraction of HT-1376 cells (Figure 6.5B,C). In control experiments where HT-1376 bladder cancer cells were incubated with PBS and then repeated PDT was performed, no changes were observed in GLUT1present in the mitochondria-enriched fraction (Figure SI6.5).

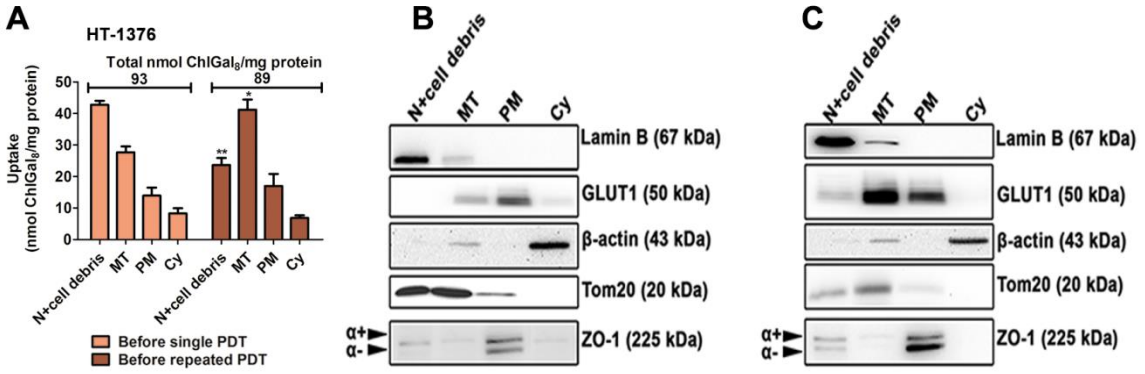

Figure 6.5 ChlGal$_8$ promotes translocation of GLUT1 to the mitochondria after a single irradiation. (A) Distribution of **ChlGal$_8$** in the subcellular fractions "nucleus (N) *plus* cell debris", mitochondria (MT), plasma membrane (PM) and cytosol (Cy) of HT-1376 cancer cells, obtained before single and repeated PDT. Data are means ± s.e.m. of at least three independent experiments performed in triplicates. $^{*}P< 0.05$, $^{**}P< 0.01$ compared to uptake (nmol PS/mg protein) of **ChlGal$_8$** before single PDT for the respective subcellular fraction using a Student´s *t* test. (B,C) Western blot analysis of lamin B (nuclear marker), GLUT1, β-actin (cytosol marker), Tom20 (mitochondrial marker) and ZO-1 (plasma membrane marker) in the subcellular fractions of HT-1376 bladder cancer cells, obtained before (B) single and (C) repeated PDT.

To determine whether the preferential accumulation of **ChlGal$_8$** in the mitochondria before repeated PDT is involved on the increment of mitochondrial ROS production and further enhancement of phototoxicity, additional experiments were performed with the mitochondria-targeted superoxide scavenger (MitoTEMPO) and with the fluorescent mitochondrial probe for highly reactive species, the mitochondria peroxy yellow 1 (MitoPY1) [22]. Overall, we found that phototoxicity was attenuated when PDT assays were performed in HT-1376 cells incubated with MitoTEMPO (Figure 6.6A). Additionally, the increase in phototoxicity after repeated PDT with **ChlGal$_8$** in HT-1376 cells demonstrated to be dependent on the production of mitochondrial ROS (namely hydrogen peroxide), as detected with MitoPY1 (Figure 6.6B).

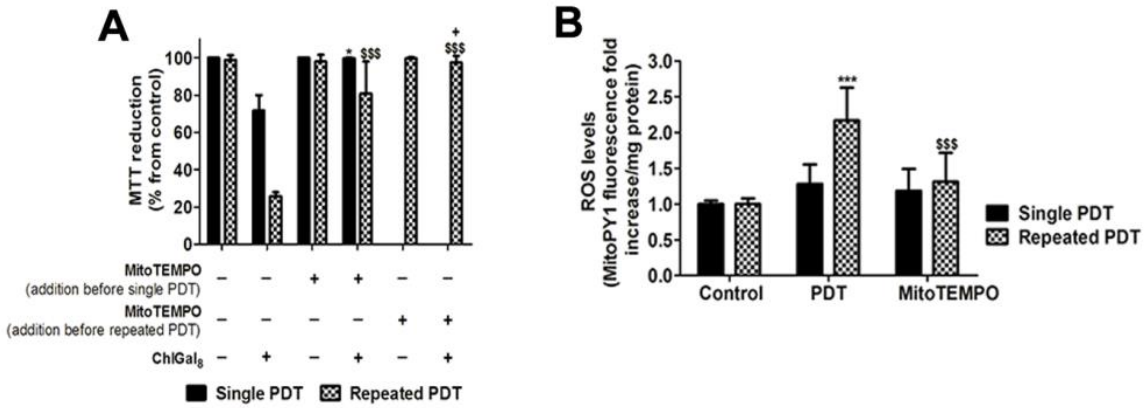

Figure 6.6 ChlGal$_8$ induces higher mitochondrial ROS production after repeated irradiation. (A) Phototoxicity 24 h after single and repeated PDT in the presence of 10 μM MitoTEMPO (a specific scavenger of mitochondrial hydrogen superoxide) in HT-1376 cancer cells, determined using the MTT assay. Data are means ± s.e.m. of at least three independent experiments performed in triplicate. $^{*}P$<0.05, $^{\$\$\$}P$< 0.001 compared to MTT reduction (%) at 24 h after single and repeated PDT, respectively, using a Student´s *t* test. ^{+}P< 0.05 compared to MTT reduction (%) at 24 h after repeated PDT in the presence of 10 μM MitoTEMPO (added before single PDT) using a Student´s *t* test. (B) Quantification of MitoPY1 fluorescence increase (as a measure of hydrogen peroxide production in mitochondria) in HT-1376 cells in the absence and presence of MitoTEMPO, after single and repeated PDT with **ChlGal$_8$**. Data are means ± s.e.m. of at least three independent experiments performed in triplicate. $^{***}P$< 0.001 compared to control cells (untreated cells) using a Student´s *t* test. $^{\$\$\$}P$< 0.001 compared to repeated PDT using a Student´s *t* test.

6.7 $ChlGal_8$ promotes translocation of GLUT1 to the mitochondria after a single irradiation and induces high phototoxicity after repeated irradiation

To determine whether GLUT1 plays a role in PDT efficacy with **$ChlGal_8$**, siRNA was used to knockdown GLUT1 within HT-1376 cancer cells (Figure SI6.6A). No significant differences were detected on the uptake of **$ChlGal_8$** by HT-1376 cells after knockdown of GLUT1 protein (Figure SI6.6B). However, knockdown of GLUT1 significantly reduced ROS production and phototoxicity (Figure 6.7A,B). Furthermore, we showed that GLUT1 siRNA prevented the irradiation-induced increase of **$ChlGal_8$** in the mitochondrial fraction of HT-1376 cells (Figure 6.7C).

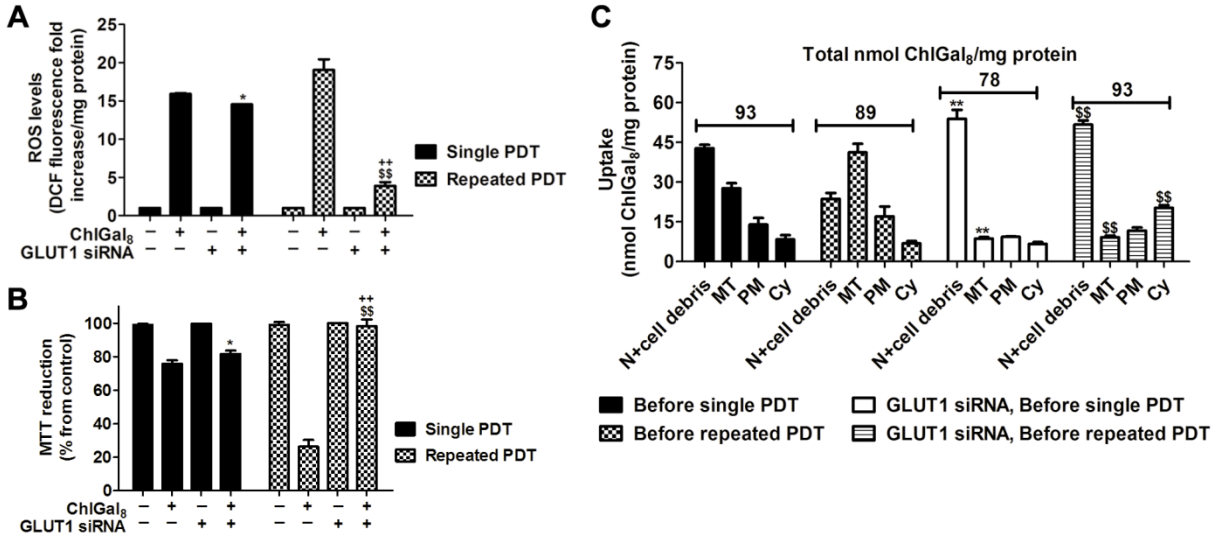

Figure 6.7 GLUT1 has a key role in increased $ChlGal_8$-induced phototoxicity after repeated PDT. (A) Quantification of DCF fluorescence increase (as a measure of ROS production) in HT-1376 cells transfected with GLUT1 siRNA after single and repeated PDT with **$ChlGal_8$**. Data are means ± s.e.m. of at least three independent experiments performed in triplicates. $^{*}P< 0.05$, $^{\$\$}P< 0.01$ compared to single and repeated PDT, respectively, in non-transfected HT-1376 cells. $^{++}P< 0.01$ compared to single PDT in transfected HT-1376 cells. (B) Photocytotoxic effects after single and repeated PDT with **$ChlGal_8$** in HT-1376 cells transfected with GLUT1 siRNA. Data are means ± s.e.m. of at least three independent experiments performed in triplicate. $^{*}P< 0.05$, $^{\$\$}P< 0.01$ compared to MTT reduction (%) at 24 h after single and repeated PDT, respectively, using a Student´s *t* test. $^{++}P< 0.01$ compared to MTT reduction (%) at 24 h after single PDT in HT-1376 cells transfected with GLUT1 siRNA, using a Student´s *t* test. (C) Distribution of **$ChlGal_8$** in the subcellular fractions "nucleus (N) *plus* cell debris", mitochondria (MT), plasma membrane (PM) and cytosol (Cy) of HT-1376 cells transfected with GLUT1

siRNA, obtained before single and repeated PDT. Data are means ± s.e.m. of at least three independent experiments performed in triplicate. $^{**}P< 0.01$, $^{\$\$}P< 0.01$ compared to the respective subcellular fractions obtained before the first and second irradiation times, respectively, in non-transfected HT-1376 cells.

6.8 Repeated PDT with ChlGal$_8$ improves the *in vivo* photodynamic efficacy against HT-1376 tumors inoculated in nude mice

Subcutaneous xenograft HT-1376 tumors were used to evaluate the PDT efficacy of **ChlGal$_8$** after single and repeated treatments (Figure 6.8A). In single PDT, the HT-1376 tumors were treated with a single dose of light (>500 nm) with a fluence rate of 30 mW/cm^2 for 20 min, *i.e.* 36 J/cm^2) at 1.5 h after intratumoral injection of **ChlGal$_8$** (3.33 µmol/kg). In repeated PDT, the tumors were irradiated for an additional time (36 J/cm^2) at 40 min after the first PDT session. As illustrated in Figure 6.8B, a single intratumoral administration of **ChlGal$_8$** and exposure to repeated photo-irradiation was significantly more efficacious in the inhibition of tumor growth than single shot photo-irradiation. The tumor growth of mice treated with single treatment was slightly suppressed after PDT, however, accelerated after 6 days and exhibited almost no difference to the control group at the endpoint.

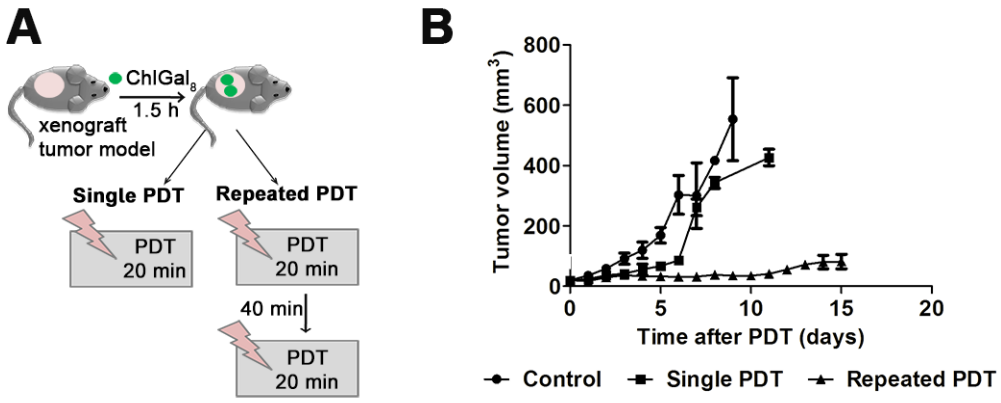

Figure 6.8 Repeated PDT with ChlGal$_8$ improves the *in vivo* photodynamic efficacy against HT-1376 tumors inoculated in nude mice. (A) Schematic illustration of single and repeated PDT experiments performed *in vivo* with **ChlGal$_8$**. (B) Tumor volumes in control mice, mice treated with single and repeated PDT at days 1-15 after treatment. Values are means ± s.e.m. (n = 6 mice per group).

6.9 Discussion

ChlGal$_8$ is an interesting third generation PS for PDT of bladder cancer because dendritic galactose molecules around chlorin macrocycle can be recognized by galactose binding proteins (such as galectin-1 and GLUT1) overexpressed in cancer cells. The synthesis of **ChlGal$_8$** was motivated by the interesting *in vitro* and *in vivo* results of **PorGal$_8$** (please see Chapter V).

ChlGal$_8$ has a more than 50-fold higher extinction coefficient (6800 $M^{-1}.cm^{-1}$) at the absorption maximum of 650 nm than the corresponding previously reported porphyrin **PorGal$_8$** in the previous chapter, 100 $M^{-1}.cm^{-1}$ at 655 nm) [11]. Due to its higher absorption at 650 nm, where tissue light penetration is rather high [23], **ChlGal$_8$** could be advantageous for PDT when compared with the corresponding **PorGal$_8$**.

In addition to water solubility, $^1O_2$ generation and photostability, **ChlGal$_8$** also demonstrated interaction with HSA and galectin-1 proteins. HSA is able to bind and transport anticancer drugs. Moreover, increased vascular permeability exhibited in solid tumors, leads to the accumulation of drug albumin conjugates in the tumor interstitium, affecting the unbound (free) drug quantity in the circulation, its distribution, metabolism, elimination and biological activity [24]. The interaction of **ChlGal$_8$** with galectin-1 can be explained by carbohydrate interactions of the galactose units with the carbohydrate-recognition domain of the protein [19], and hydrophobic interactions between the chlorin macrocycle and the well-conserved hydrophobic core of the protein [18, 25, 26].

We have previously reported that HT-1376 and UM-UC-3 bladder cancer cells express high levels of the galactose binding proteins GLUT1 and galectin-1 (chapter III), respectively [12]. Therefore, it is envisaged that specific domains, enriched in these proteins, at the cell surface can promote the interaction with the galactodendritic units on the chlorin macrocycle of **ChlGal$_8$**, enhancing somehow its cellular uptake. The association of **ChlGal$_8$** with galactose binding proteins promotes high local concentration of the PS around cancer cell membrane, which induces PS macrocycle partition into the membrane. Thus, uptake of **ChlGal$_8$** is also dependent on its relative hydrophobicity [27].

When compared with **PorGal$_8$** data (chapter V), the uptake of **ChlGal$_8$** was lower which can be due to its higher partition coefficient value. Although the lower uptake of **ChlGal$_8$** by bladder cancer cells when compared with **PorGal$_8$**, the photoxicity induced 24 h after PDT was higher with **ChlGal$_8$** than with **PorGal$_8$** in UM-UC-3 bladder cancer cells. Another interesting result was that although the similar uptake of **ChlGal$_8$** by UM-UC-3 and HT-1376 bladder cancer cells, the phototoxicity induced by **ChlGal$_8$** was higher in UM-UC-3 than in HT-1376 cells. Previous studies have demonstrated that HT-1376 cells exhibit a protective mechanism after PDT by inducing an antioxidant response [12]. The key role of microenvironment-related molecules, particularly the extracellular matrix-metalloproteinase inducer CD147 on the resistance of HT-1376 cancer cells to cisplatin-based chemotherapy has also been reported [28].

In this study, we demonstrated that a repeated PDT was more effective in inducing cell death in resistant HT-1376 cancer cells when compared with single PDT. These results can be explained by disaggregation of **ChlGal$_8$** molecules between the first and second light irradiation steps. Interestingly, after a single irradiation both **ChlGal$_8$** and GLUT1 are localized in the mitochondrial fraction. GLUT1 is ubiquitously expressed in most mammalian cells [29]. Although the role of GLUT1 in the mitochondria is not completely clear, it is speculated that GLUT1 is mostly involved on the transport of the oxidized form of vitamin C, the dehydroascorbic acid [30]. Once inside mitochondria, dehydroascorbic acid is reduced to ascorbic acid [29] that quenches ROS, inhibits mitochondrial membrane depolarization and protects mitochondria from oxidative injury [30]. Our results collectively point to an antioxidant response of HT-1376 cancer cells after single PDT, which stimulates the translocation of GLUT1 to the mitochondria. As a first stage, it is expected that GLUT1 translocation to the mitochondria contributes to a protective response against ROS-mediated damage. However, upon accumulation of **ChlGal$_8$** in mitochondria, if a repeated PDT occurs, this PS is highly efficient in inducing phototoxicity.

Mitochondria have been recognized as a key target for the initiation of apoptosis in PDT. **ChlGal$_8$** bound to mitochondria can generate large amounts of ROS after irradiation, which can lead to mitochondrial damage triggering cell death signaling cascades and the mitochondria-dependent apoptosis [31].

Given that **ChlGal$_8$** was demonstrated to be a powerful PS in *in vitro* assays, we next conducted a proof-of-concept study to demonstrate its increased efficacy after a repeated irradiation treatment in a xenograft tumor. A single administration of **ChlGal$_8$** followed by a repeated PDT demonstrated to be more effective than the conventional single treatment.

6.10 References

1. Oleinick NL, Morris RL, Belichenko T (2002) The role of apoptosis in response to photodynamic therapy: what, where, why, and how. Photoch Photobio Sci 1: 1-21.

2. Rosenkranz AA, Jans DA, Sobolev AS (2000) Targeted intracellular delivery of photosensitizers to enhance photodynamic efficiency. Immunol Cell Biol 78: 452-464.

3. Szewczyk A, Wojtczak L (2002) Mitochondria as a pharmacological target. Pharmacol Rev 54: 101-127.

4. Pathania D, Millard M, Neamati N (2009) Opportunities in discovery and delivery of anticancer drugs targeting mitochondria and cancer cell metabolism. Adv Drug Deliver Rev 61: 1250-1275.

5. Zhao ZX, Chan PS, Li HG, Wong KL, Wong RNS, Mak NK, Zhang J, Tam HL, Wong WY, Kwong DWJ, Wong WK (2012) Highly selective mitochondria-targeting amphiphilic Silicon(IV) phthalocyanines with axially ligated rhodannine B for Photodynamic Therapy. Inorg Chem 51: 812-821.

6. Xu J, Zeng F, Wu H, Hu C, Wu S (2014) Enhanced Photodynamic efficiency achieved via a dual-targeted strategy based on photosensitizer/micelle structure. Biomacromolecules 15: 4249-4259.

7. Zhang S, Yang L, Ling X, Shao P, Wang X, Edwards WB, Bai M (2015) Tumor mitochondria-targeted photodynamic therapy with a translocator protein (TSPO)-specific photosensitizer. Acta Biomater 28: 160-170.

8. Senge MO, Brandt JC (2011) Temoporfin (Foscan®, 5,10,15,20-tetra(*m*-hydroxyphenyl)chlorin)-a second-generation photosensitizer. Photochem Photobiol 87: 1240-1296.

9. Lu K, He C, Lin W (2015) A chlorin-based nanoscale metal-organic framework for Photodynamic Therapy of colon cancers. J Am Chem Soc 137: 7600-7603.

10. Singh S, Aggarwal A, Thompson S, Tomé JPC, Zhu XC, Samaroo D, Vinodu M, Gao RM, Drain CM (2010) Synthesis and photophysical properties of thioglycosylated chlorins, isobacteriochlorins, and bacteriochlorins for bioimaging and diagnostics. Bioconjugate Chem 21: 2136-2146.

11. Silva S, Pereira PMR, Silva P, Paz FAA, Faustino MAF, Cavaleiro JAS, Tomé JPC (2012) Porphyrin and phthalocyanine glycodendritic conjugates: synthesis, photophysical and photochemical properties. Chem Commun 48: 3608-3610.

12. Pereira PMR, Silva S, Cavaleiro JAS, Ribeiro CAF, Tomé JPC, Fernandes R (2014) Galactodendritic phthalocyanine targets carbohydrate-binding proteins enhancing Photodynamic Therapy. Plos One 9: e95529.

13. Thijssen VL, Heusschen R, Caers J, Griffioen AW (2015) Galectin expression in cancer diagnosis and prognosis: A systematic review. BBA -Rev Cancer 1855: 235-247.

14. Seybold PG, Gouterma M (1969) Porphyrins. XIII: Fluorescence spectra and quantum yields. J Mol Spectrosc 31: 1-13.

15. Williams ATR, Winfield SA, Miller JN (1983) Relative fluorescence quantum yields using a computer-controlled luminescence spectrometer. Analyst 108: 1067-1071.

16. Zhang Y-Z, Zhou B, Zhang X-P, Huang P, Li C-H, Liu Y (2009) Interaction of malachite green with bovine serum albumin: Determination of the binding mechanism and binding site by spectroscopic methods. J Hazard Mater 163: 1345-1352.

17. He XM, Carter DC (1992) Atomic-structure and chemistry of Human Serum-Albumin. Nature 358: 209-215.

18. López-Lucendo MF, Solís D, André S, Hirabayashi J, Kasai K, Kaltner H, Gabius HJ, Romero A (2004) Growth-regulatory human galectin-1: Crystallographic characterisation of the structural changes induced by single-site mutations and their impact on the thermodynamics of ligand binding. J Mol Biol 343: 957-970.

19. Iglesias MM, Rabinovich GA, Ivanovic V, Sotomayor C, Wolfenstein-Todel C (1998) Galectin-1 from ovine placenta - amino-acid sequence, physicochemical properties and implications in T-cell death. Eur J Biochem 252: 400-407.

20. Dhallewin MA, Baert L, Marijnissen JPA, Star WM (1992) Whole bladder wall Photodynamic Therapy with *in situ* light dosimetry for carcinoma *in situ* of the bladder. J Urology 148: 1152-1155.

21. Rangel R, Dobroff AS, Guzman-Rojas L, Salmeron CC, Gelovani JG, Sidman RL, Pasqualini R, Arap W (2013) Targeting mammalian organelles with internalizing phage (iPhage) libraries. Nat Protoc 8: 1916-1939.

22. Dickinson BC, Srikun D, Chang CJ (2010) Mitochondrial-targeted fluorescent probes for reactive oxygen species. Curr Opin Chem Biol 14: 50-56.

23. Agostinis P, Berg K, Cengel KA, Foster TH, Girotti AW, Gollnick SO, Hahn SM, Hamblin MR, Juzeniene A, Kessel D, Korbelik M, Moan J, Mroz P, Nowis D, Piette J, Wilson BC, Golab J (2011) Photodynamic Therapy of cancer: An update. Ca-Cancer J Clin 61: 250-281.

24. Yang F, Zhang Y, Liang H (2014) Interactive association of drugs binding to Human Serum Albumin. Int J Mol Sci 15: 3580-3595.

25. D'Auria S, Petrova L, John C, Russev G, Varriale A, Bogoeva V (2009) Tumor-specific protein human galectin-1 interacts with anticancer agents. Mol Biosyst 5: 1331-1336.

26. Gegg CV, Roberts DD, Segel IH, Etzler ME (1992) Characterization of the adenine binding-sites of 2 Dolichos-Biflorus lectins. Biochemistry-Us 31: 6938-6942.

27. Mishra PP, Patel S, Datta A (2006) Effect of increased hydrophobicity on the binding of two model amphiphilic chlorin drugs for photodynamic therapy with blood plasma and its components. J Phys Chem B 110: 21238-21244.

28. Afonso J, Santos LL, Miranda-Gonçalves V, Morais A, Amaro T, Longatto-Filho A, Baltazar F (2014) CD147 and MCT1-potential partners in bladder cancer aggressiveness and cisplatin resistance. Mol Carcinogen 54: 1451-1466.

29. Vatassery GT, Smith WE, Quach HT, Lai JCK (1995) *In vitro* oxidation of vitamin-E, vitamin-C, thiols and cholesterol in rat-brain mitochondria incubated with free-radicals. Neurochem Int 26: 527-535.

30. Sagun KC, Cárcamo JM, Golde DW (2005) Vitamin C enters mitochondria via facilitative glucose transporter 1 (GLUT1) and confers mitochondrial protection against oxidative injury. Faseb J 19: 1657-1667.

31. Green DR, Kroemer G (2004) The pathophysiology of mitochondrial cell death. Science 305: 626-629.

6.11 Supporting information

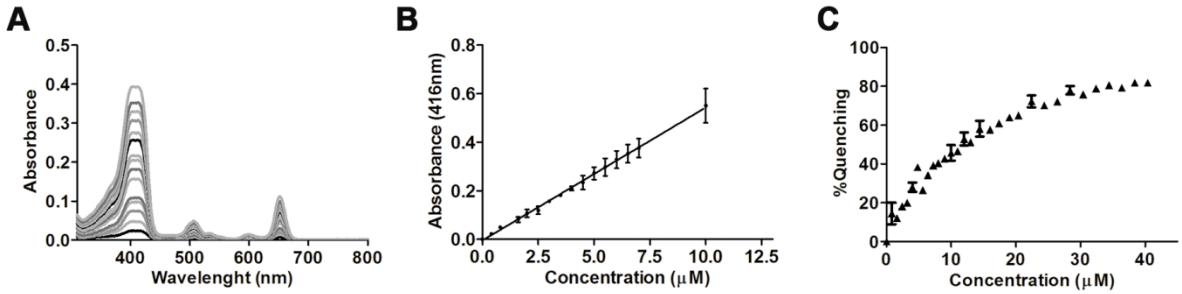

Figure SI6.1 (A) UV-Visible spectra of **ChlGal$_8$** in PBS at different concentrations (0 µM to 10 µM). (B) Linear plot obtained by plotting **ChlGal$_8$**-Soret band at 416 nm *vs.* concentration of the galactose-conjugate in PBS. Data are means ± s.e.m. of at least two independent experiments. (C) Fluorescence quenching curves of 2 µM of HSA, after addition of **ChlGal$_8$** at several concentrations (between 0 µM to 40.4 µM). *Quenching (%)=(F0-F)/F0*, where F0 and F are the HSA fluorescence intensities in the absence and presence of **ChlGal$_8$** (λexcitation at 280 nm and wavelength emission range between 300 nm to 400 nm). Data are means ± s.e.m. of at least two independent experiments.

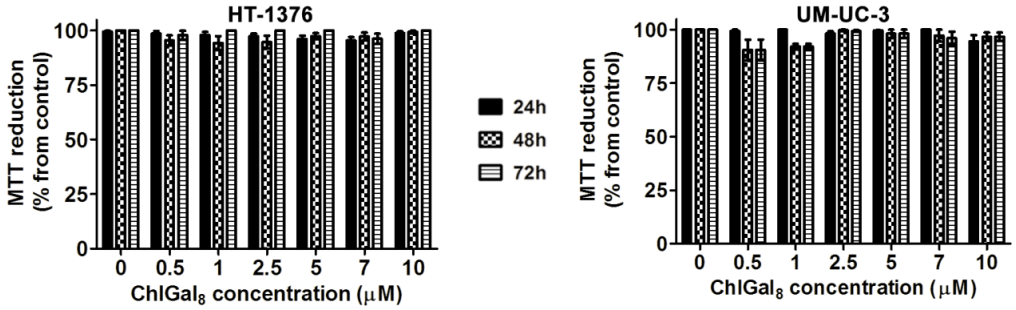

Figure SI6.2 Non-dark toxicity of **ChlGal$_8$** determined 24, 48 and 72 h after treatment using the MTT assay. The percentage of cytotoxicity was calculated relatively to control cells (untreated cells). Data are means ± s.e.m. of at least three independent experiments performed in triplicate.

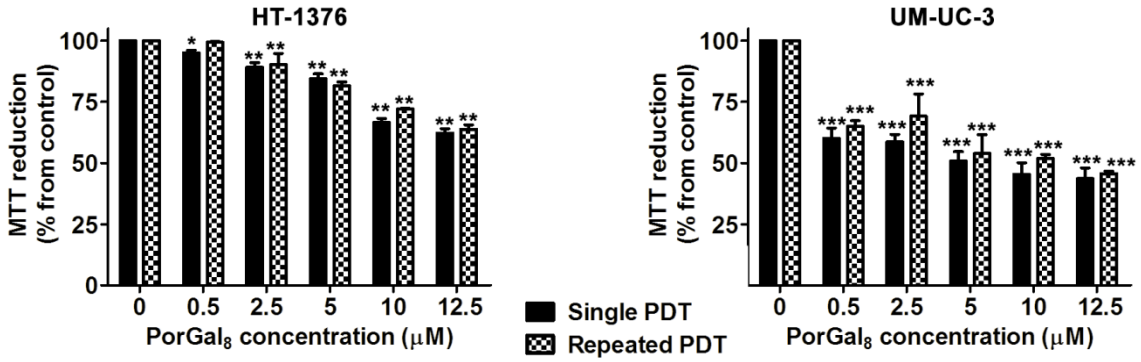

Figure SI6.3 Irradiation dose-dependent cell death in response to single and repeated PDT with **PorGal$_8$**. Cytotoxicity was assessed 24 h after treatment using the MTT assay. The percentage of cytotoxicity was calculated relatively to control cells (untreated cells). Data are means ± s.e.m. of at least three independent experiments performed in triplicate. $^{*}P< 0.05$, $^{**}P< 0.01$, $^{***}P< 0.001$ compared to control cells (untreated cells) using a Student´s *t* test.

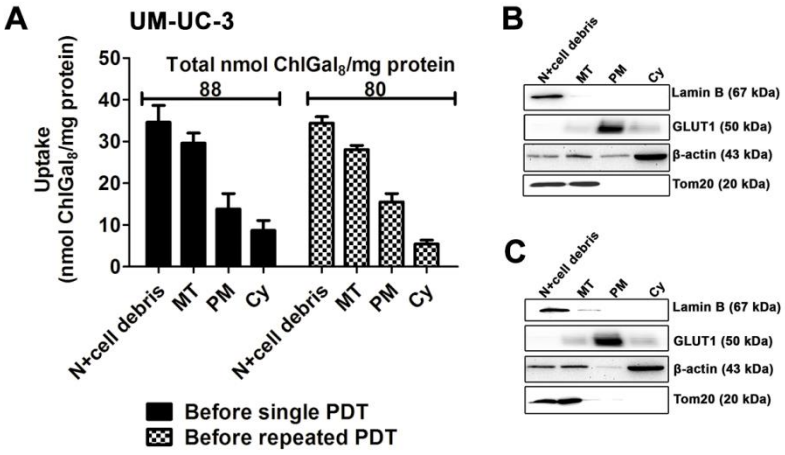

Figure SI6.4 (A) Distribution of **ChlGal$_8$** in the subcellular fractions "nucleus (N) *plus* cell debris", mitochondria (MT), plasma membrane (PM) and cytosol (Cy) of UM-UC-3 cancer cells, obtained before single and repeated PDT. Data are means ± s.e.m. of at least three independent experiments performed in triplicate. (B,C) Western blot analysis of lamin B (nuclear marker), GLUT1, β-actin (cytosol marker) and Tom20 (mitochondrial marker) in the subcellular fractions of UM-UC-3 bladder cancer cells, obtained before (B) single and (C) repeated PDT.

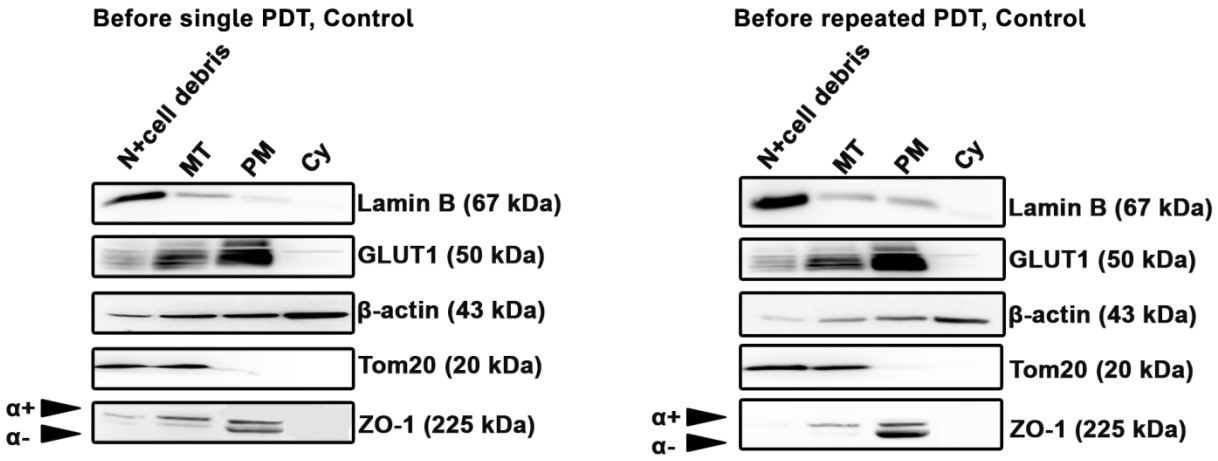

Figure SI6.5 Western blot analysis of lamin B (nuclear marker), GLUT1, β-actin (cytosol marker), Tom20 (mitochondrial marker) and ZO-1 (plasma membrane marker) in the subcellular fractions "nucleus (N) *plus* cell debris", mitochondria (MT), plasma membrane (PM) and cytosol (Cy), of HT-1376 bladder cancer cells, obtained before single and repeated PDT in control cells (untreated cells).

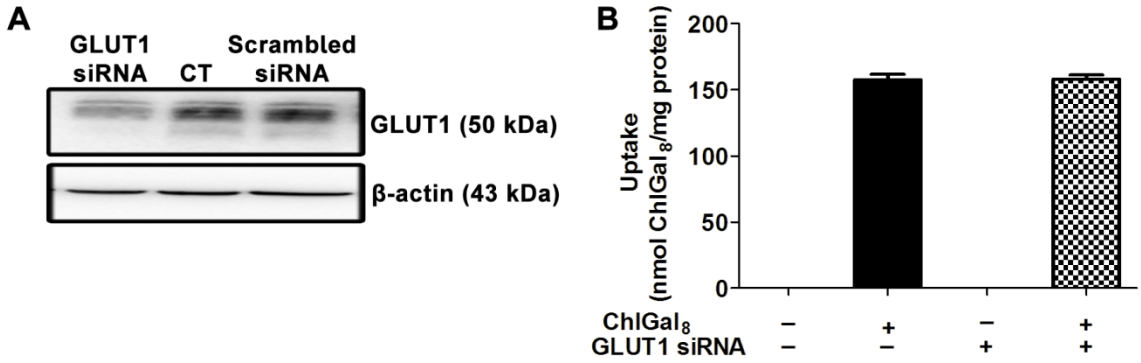

Figure SI6.6 (A) Knockdown of GLUT1 in HT-1376 bladder cancer cells as determined by Western blot 24 h post-transfection. (B) Intracellular uptake of **ChlGal$_8$** by HT-1376 bladder cancer cells transfected with GLUT1 siRNA. Data are means ± s.e.m. of at least three independent experiments performed in triplicate.

Table SI6.1 Photostability of **ChlGal$_8$** at 4 μM in PBS, after irradiation with red light (620-750 nm) at a fluence rate of 150 mW/cm^2 for different periods of time (0-30 min). The results are presented in percentage calculated by the ratio of residual absorbance (at 416 nm) at different periods of time and absorbance before irradiation. Data are means ± s.e.m. of at least two independent experiments.

Galactose-conjugate	**Irradiation time (min)**									
	0	1	3	4	5	10	15	20	25	30
ChlGal$_8$	100	100	100	99	99	99	99	98	98	98

Establishment and characterization of tumor spheroids for evaluating photodynamic efficacy of a porphyrin attached to the carbon-3 of galactose

CHAPTER VII

Chapter VII Establishment and characterization of tumor spheroids for evaluating photodynamic efficacy of a porphyrin attached to the carbon-3 of galactose

7.1 General overview

Galactosylated photosensitizers have been developed *viaN*-, *S*-, *C*- and *O*-galactosylation by attaching the anomeric carbon or carbon-6 of the sugar to the macrocycle of the porphyrinoid [1]. To gain affinity for galactose-binding proteins, the galactosylated porphyrinoids have been also developed by using galactose sugar in a multivalent format [2, 3]. Besides this, optimization of monovalent galactose by derivatization of the galactose carbon-3 yielded compounds with high affinity to galectin-1 [4].

Most work on PDT has been done on either *in vivo* animal models or *in vitro* two-dimensional monolayers. Monolayer culture of cancer cells are easily handled and offer some information about cellular processes at a much lower cost than animal studies. However, monolayers represent a highly artificial cellular environment and lack the three-dimensional aspects of a tumor [5-8]. Therefore, they are less reliable in predicting effectiveness of treatments *in vivo*. Moreover, tumors are known to have a necrotic core [9] characterized by hypoxia at its center. This necrotic core has been shown to make cancer cells more resistant to ROS-dependent radiation [10], and chemotherapy [7]. Because PDT relies on the availability of oxygen to cells for generation of ROS, a monolayer model is not sufficient to understand what happens *in vivo*.

To address this issue, researchers have turned to a more complex model using spheroids [11-13]. To a certain degree, spheroids with specific size can mimic the behavior of tumors because they are likewise three-dimensional cell aggregates with a necrotic core at the center and healthy cells at the surface. This is particularly important because it allows for the formation of a gradient of nutrients, such as oxygen which can influence PDT efficacy. Both the three-dimensional structure and the oxygen gradient make spheroids a better model to predict photodynamic efficiency of a new galactose-PS.

In an attempt to increase the affinity of porphyrinoids to galectin-1 protein, we have attached galactose units through carbon-3 to a porphyrin by click conjugation (**Por-C3-Gal$_4$**). Furthermore, to validate the potential of **Por-C3-Gal$_4$**,the same tetrapyrrolic macrocycle was also attached to the carbon-1 of galactose sugar (**Por-C1-Gal$_4$**). The aim of the present study was to investigate the photophysical properties, uptake and photodynamic efficiency of **Por-C3-Gal$_4$** and **Por-C1-Gal$_4$** in *in vitro* cancer models. *In vitro* studies were performed in monolayers of cancer cells (HCT-116 colon cancer cells, MCF-7 breast cancer cells, UM-UC-3 bladder cancer cells and HeLa cervical cancer cells) expressing different levels of galectin-1 protein. Attempting to mimic the several heterogeneous treatment effects found *in vivo*, *in vitro* studies were also performed in the corresponding three-dimensional spheroid cancer cell cultures. Using agarose-coated plates, we obtained viable spheroids from human tumor cell lines from different origins (HCT-116, MCF-7, UM-UC-3 and HELA cells) with appropriate size (volume of approximately 0.05 mm^3 and diameter of approximately 443μm) for screening PDT agents. We observed that detachment from monolayer culture and growth as tumor spheroids was accompanied by changes in both glucose metabolism, endogenous ROS levels and galectin-1 and GLUT1 protein levels.

The uptake and phototoxocity of the new galactose-Pors are dependent on the galactose moiety (C1 *vs.* C3), partition coefficient, levels of galectin-1 in cancer cells and on the *in vitro* (monolayer or spheroid cultures) model used. Porphyrin attached to the carbon-3 of galactose sugar exhibits higher potodynamic activity in bladder cancer cells expressing galectin-1 protein, than the corresponding porphyrin attached to the carbon-1 of galactose sugar (Figure 7.1).

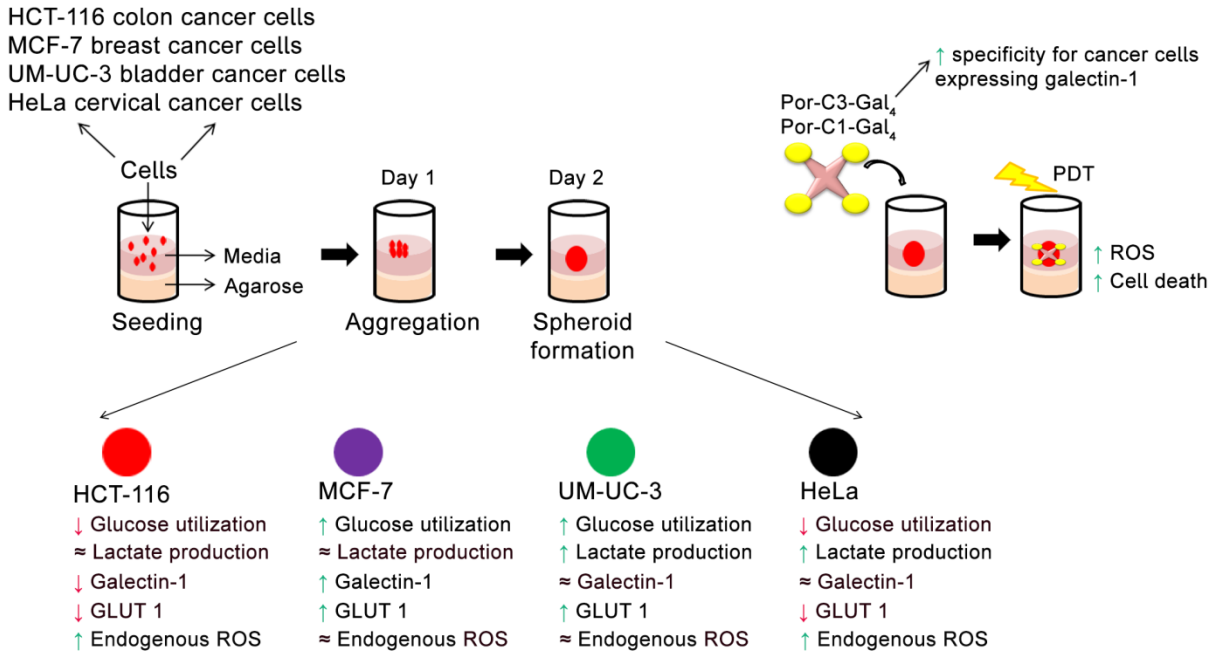

Figure 7.1 Illustration of spheroids formation with HCT-116, MCF-7, UM-UC-3 and HeLa cancer cells; and phototoxicity with Por-C3-Gal$_4$ and Por-C1-Gal$_4$. The initial aggregation of monolayer cancer cells plated for spheroid formation lasted for 24 h. Within 48-72 h the small clumps were replaced by compact spheroids. The glycolotic status (glucose usage and lactate production), endogenous levels of ROS and expression of the proteins galectin-1 and GLUT1 are altered during spheroids formation. **Por-C3-Gal$_4$** and **Por-C1-Gal$_4$** are non toxic compounds *per se* and have high toxicity after PDT.

7.1.1 Methods

The following experimental protocols (please see Methods and Materials chapter IX) were used to obtain the data presented in this chapter:

- Partition coefficients (9.2.2F)
- Biological models – Culture of HCT-116 colon cancer cells, MCF-7 breast cancer cells, UM-UC-3 bladder cancer cells and HeLa cervical cancer cells as monolayers and spheroids (9.3.8A,B)
- Fluorescence spectroscopy – uptake of **Por-C3-Gal$_4$** and **Por-C1-Gal$_4$** (9.3.8C-E)
- PDT treatments – Photosensitizer **Por-C3-Gal$_4$** and **Por-C1-Gal$_4$** (9.3.8F)
- Cell viability assays – MTT and LDH assays (9.3.8G)

- Intracellular levels of Reactive Oxygen Species (9.3.8J)
- Western blotting assays – galectin-1, GLUT1, β-actin (9.3.8L)

7.1.2 Publication

This chapter comprises the following publications:

Patrícia M.R. Pereira, N. V. S. Dinesh K. Bhupathiraju, Naxhije Berisha, Rosa Fernandes, João P.C. Tomé, Charles M. Drain, Application of Cancer Cell Spheroids to Screen Photodynamic Efficiency of Glyco-Photosensitizers, *under final preparation*.

Patrícia M.R. Pereira, N. V. S. Dinesh K. Bhupathiraju, Waqar Rizvi, Rosa Fernandes, João P.C. Tomé, Charles M. Drain, Comparative studies of porphyrin C3-galactose and porphyrin C1-galactose conjugates for enhanced photodynamic therapy, *under final preparation*.

7.2 Kinetics of spheroids growth

The culture of certain type of cells on surfaces not favourable for cell attachment led to enhancement of homotypic cell-cell interactions, resulting in formation of three-dimensional structures (spheroids, Figure 7.2A) [8]. In our study, five different types of cells were tested for spheroid formation in agarose-coated wells of a 96-well plate (Table 7.1). The HCT-116 colon cancer cells, MCF-7 and MDA-MB-231 breast cancer cells, UM-UC-3 bladder cancer cells and HeLa cervical cancer cells were cultured in suspension on agarose bed which forms a thin non-adherent film and prevents cell attachment. Agarose is one of the most efficient substrates to prevent cell attachment to the plate and has been used in several studies regarding spheroid cultures [7, 14-17].

Table 7.1 Human cell lines tested for spheroids formation and their respective doubling times (h).

Cell line	**Origin**	**Doubling time (h)**	
		Monolayers [Reference]	Spheroids
HCT-116	Colon Cancer	17 [18]	19
MCF-7	Breast Cancer	25 [18]	38
UM-UC-3	Bladder Cancer	20 [19]	23
HeLa	Cervival Cancer	19 [18]	23
MDA-MB-231	Breast Cancer	42 [18]	N.D.

After seeding on the agarose-coated wells, cells started to cluster, and the first loose aggregates were already seen after 2 h of incubation. During the first 24 h of incubation, the cells formed aggregates which were easily dissociated by mechanical force. Most of the tumor cells tested (HCT-116, MCF-7, UM-UC-3 and HeLa) gave rise to compact, rigid and spherically-shaped spheroids (Figures 7.2 and 7.3) by 48 h after cell plating. When spheroid cultures were observed under phase contrast microscope, a multilayer cell assembly was observed. The absence of necrotic core formation within spheroids was evident at all time points examined, indicative of cell viability in the interior of the spherical structures. Besides, these cultures were resistant to gentle agitation or physical transfer and only enzymatic digestion could separate these three-dimensional structures into single cells. MDA-MB-231

breast cancer cells remained as single suspended cells forming aggregates which were not stable enough for harvest and further experiments.

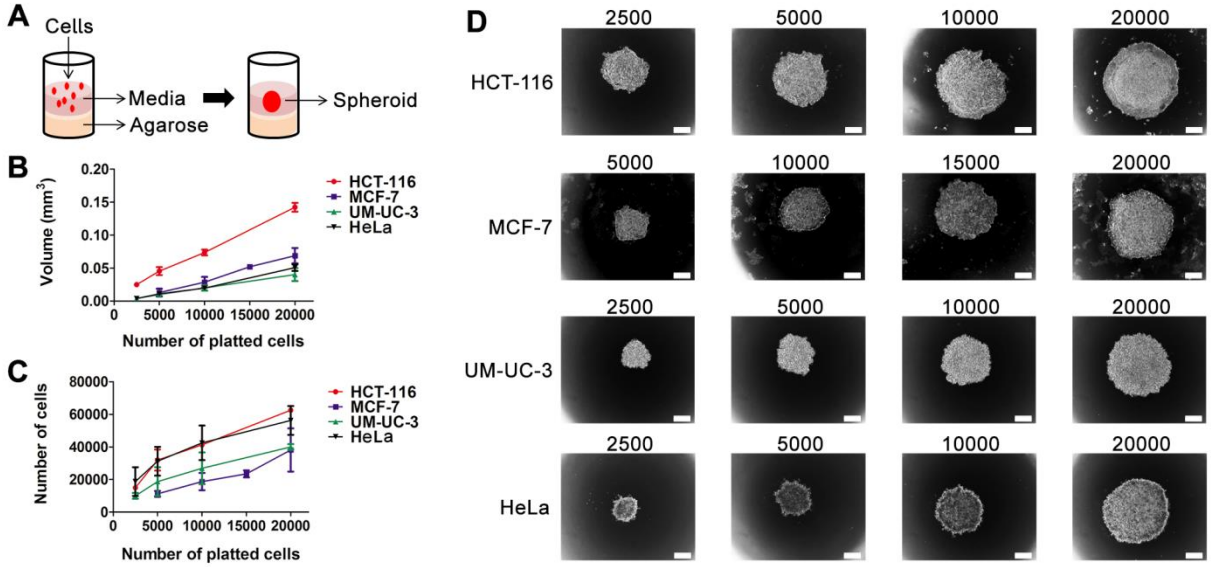

Figure 7.2 Spheroid size is dependent on cell seeding number. (A) Spheroid plating scheme: one spheroid *per* well was formed in agarose-coated 96-well plates. (B,C)Volume (mm^3) and number of cells of HCT-116, MCF-7, UM-UC-3 and HeLa cancer cells at 48 h after plating with seeding densities of 2,500- 20,000 cells per well for HCT-116, UM-UC-3 and HeLa cancer cells and 5,000-20,000 cells per well for MCF-7 cancer cells. Data are mean ± S.D. of at least 30 spheroids. (D)representative brightfield images of spheroids at 48 h after plating with seeding densities of 2,500- 20,000 cells per well for HCT-116, UM-UC-3 and HeLa cancer cells and 5,000-20,000 cells per well for MCF-7 cancer cells. *Scale bars* 100 µm.

We analysed the growth kinetic of spheroid HCT-116, MCF-7, UM-UC-3 and HeLa cancer cells (Figures 7.2 and 7.3, Tables SI7.1-SI7.4). Figure 7.2D shows representative optical images of spheroids with different initial cell seeding density (2,500 – 20,000 cells per well). A higher cell density in the initial suspension gave rise to spheroids with bigger volume and number of cells *per* spheroid than lower cell densities (Figures 7.2B-D). HCT-116, MCF-7, UM-UC-3 and HeLa spheroids showed similar growth pattern, *i.e.* the volume decreased significantly until 48 h in culture, then maintaining until 72 h with small fluctuations (Figures 7.3A,C). Between 48 to 72 h after cell plating, the border of the spheroids became ruffled, indicating proliferation at the spheroid periphery (Figure 7.3C). The number of viable cells per

spheroid increased with time after cell seeding (Figure 7.3B) with doubling times lower when compared with monolayer cultures (Table 7.1).

In an attempt to use spheroids with similar volume in our studies to guarantee the homogeneity of our three-dimensional populations, we determined the cell seeding densities by which spheroids of different cell lines can be obtained with similar size after 48 h in culture (Tables SI7.1-SI7.4, Figure 7.3A). The culture of 5,000 HCT-116 cells per well, 15,000 MCF-7 cells per well, 20,000 UM-UC-3 cells per well, 20,000 HeLa cells per well gave rise to spheroids with volume and average size of approximately 0.05 mm^3 and 443 µm, respectively.

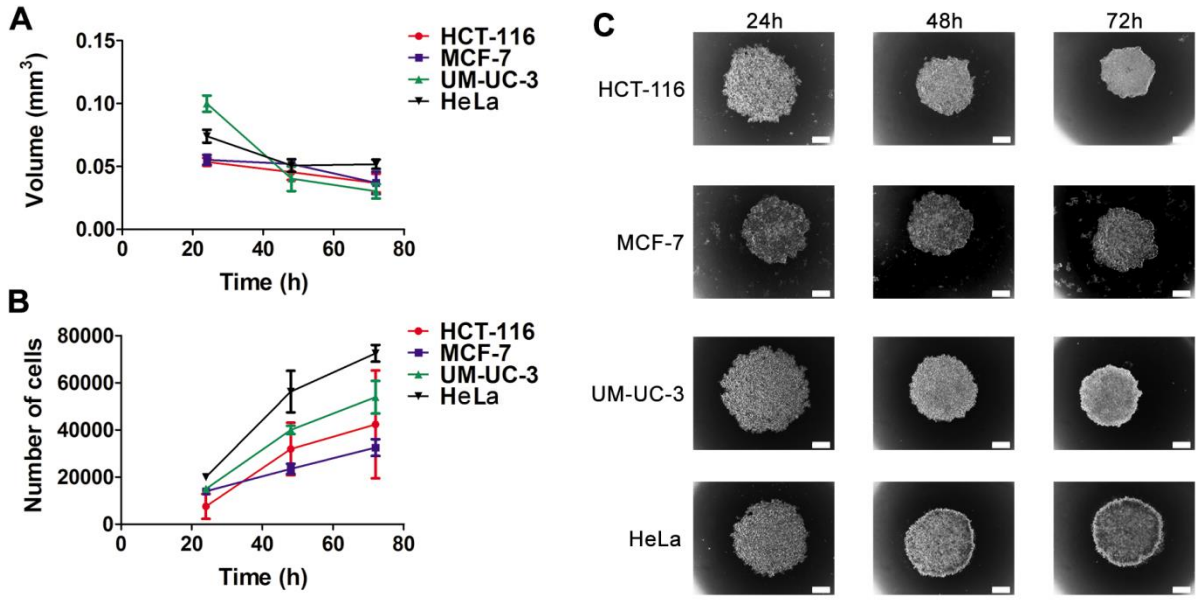

Figure 7.3 Spheroid size is dependent on time after cell seeding. (A, B)Volume (mm^3) and number of cells of HCT-116, MCF-7, UM-UC-3 and HeLa cancer cells at 24, 48 and 72 h after plating with seeding densities of 5,000 HCT-116 cells per well, 15,000 MCF-7 cells per well, 20,000 UM-UC-3 cells per well and 20,000 HeLa cells per well. Data are mean ± S.D. of at least 30 spheroids. (C) representative brightfield images of spheroids at 24, 48 and 72 h after plating with seeding densities of 5,000 HCT-116 cells per well, 15,000 MCF-7 cells per well, 20,000 UM-UC-3 cells per well and 20,000 HeLa cells per well. *Scale bars* 100 µm.

7.3 Cells of resulting spheroids are viable and have altered pattern of metabolism

To assess cellular viability of spheroid cultures, the MTT assay (which measures cell metabolic activity) was performed in intact or dissociated spheroids [9, 20]. Unlike other studies reporting the use of MTT to study spheroids viability, the MTT assay could not be

applied on the evaluation of spheroids viability since this assay did not result in reproducible and constant results (data not shown). The determination of cell death *via* measurement of molecules released from membrane-defective cells into the extracellular medium demonstrated be preferable in the evaluation of spheroids viability. Therefore, culture media from monolayer or spheroid cultures were used for estimation of lactate dehydrogenase (LDH) release by cells that have membrane damaged due to necrosis or apoptosis [20]. The amounts of LDH release by spheroids at 48 and 72 h were similar to those at 24 h after cell plating (Figure 7.4A). LHD release by spheroids was similar to those by the respective monolayer cultures (Figure 7.4B), which demonstrates that the generated spheroids are viable structures for at least 72 h after cell plating.

Spheroids, which are high cell-density and closely packed three-dimensional-tumor like structures, closely simulate conditions existing in the under-perfused solid tumors, wherein hypoxia and related alterations in cellular metabolism occur due to increasing distances from the nourishing blood capillaries. In fact, the diffusion of small molecules such as glucose and oxygen can be limited, leading to low concentrations of glucose and oxygen in the inner regions of spheroids [10, 21]. The glycolytic flux of cells in culture can be determined by measuring glucose consumption and lactate excretion [22]. To determine the glucose consumption by cells, we used the fluorescent glucose analog (2-deoxy-2-[(7-nitro-2,1,3-benzoxadiazol-4-yl)amino]-D-glucose (2-NBDG), which was added to the cells during 1 h of incubation and its intracellular accumulation was measured by fluorescence spectroscopy. The glucose utilization (nmol per mg of protein) in monolayer cultures decreased in the following order HeLa > HCT-116 >UM-UC-3 > MCF-7 (Figure SI7.1). The glucose consumption by MCF-7 and UM-UC-3 spheroids was higher than the corresponding cells growing in monolayers (Figure 7.4C). On the other hand, spheroids of HCT-116 and HeLa demonstrated lower glucose consumption than monolayer cultures. Lactate production (nmol/mg of protein) was determined in the culture medium using a commercially available colorimetric kit. The lactate production in monolayer cultures decreased in the following order: HeLa > HCT-116 ≈ MCF-7 >UM-UC-3 (Figure SI7.2). A significant increment in lactate production was observed during the formation of UM-UC-3 and HeLa spheroids (Figure 7.4D). Interestingly, no

alterations in lactate production were observed during HCT-116 and MCF-7 spheroid development.

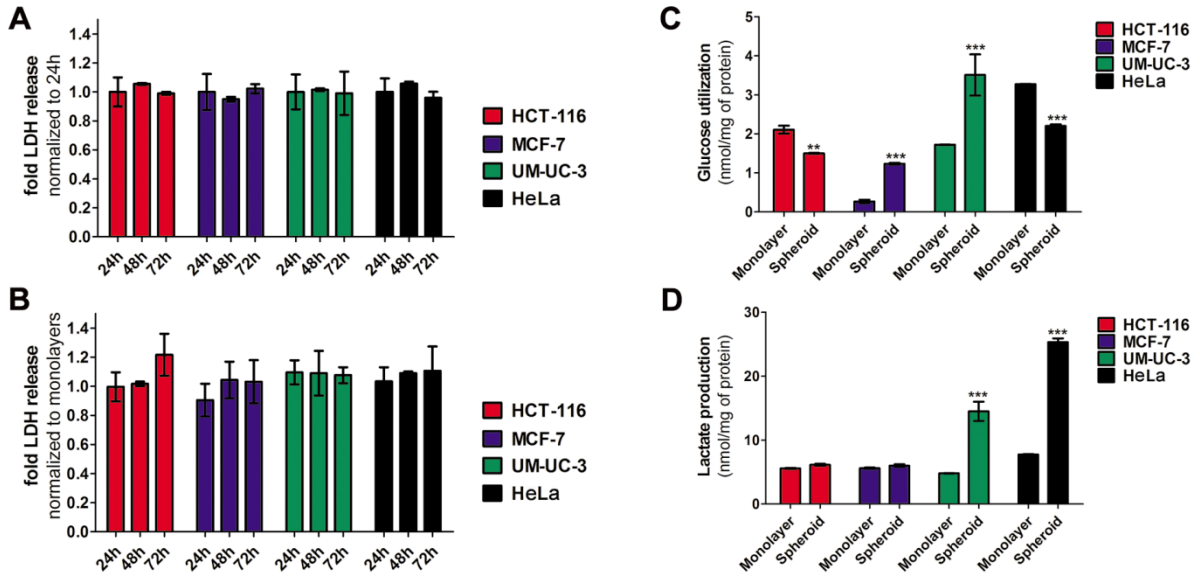

Figure 7.4 Cells of resulting spheroids are viable and have altered pattern of metabolism. (A, B)Spheroids viability at 24, 48 and 72 h after plating with seeding densities of 5,000 HCT-116 cells per well, 15,000 MCF-7 cells per well, 20,000 UM-UC-3 cells per well and 20,000 HeLa cells per well. Viability was determined using the lactate dehydrogenase (LDH) assay. LDH activity was measured in the culture supernatant and data were normalized to LDH activity of spheroids at 24 h after cell plating (A) or LDH activity of cells growing in monolayers (B). Data are means ± S.D. of at least three independent experiments performed in triplicate. C, DGlucose utilization and lactate production of cancer cells growing in monolayers and in spheroids at 48 h after plating with seeding densities of 5,000 HCT-116 cells per well, 15,000 MCF-7 cells per well, 20,000 UM-UC-3 cells per well and 20,000 HeLa cells per well. The amount of glucose (nmol, C) and lactate (nmol, D) were estimated using enzymatic assays and the results were normalized for mg of protein. Data are means ± S.D. of at least three independent experiments performed in triplicate. $^{**}P< 0.01$, $^{***}P< 0.001$ compared to glucose utilization or lactate production of the respective cancer cell line growing in monolayers, using a Student´s *t* test.

7.4 Expression of galectin-1 and GLUT1 proteins; and endogenous ROS are altered during spheroids formation

In our research related with the development of new PSs to be used in cancer PDT, we are particularly interested in porphyrinoids conjugated with sugars such as glucose and

galactose [1-3, 23]. Galectin-1 and GLUT1 are glyco-binding proteins overexpressed in cancer cells [24, 25] with a key role in the uptake and further phototoxicity of glyco-PSs [2, 26, 27]. Therefore we have evaluated the protein levels of galectin-1 and GLUT1 in monolayers of HCT-116, MCF-7, UM-UC-3 and HeLa cancer cells, by Western Blotting (Figure 7.5A,B). To determine whether the expression of these proteins is altered during spheroids development, we have also performed Western Blotting in cellular extracts of spheroid cultures (Figures 7.5C,D). Galectin-1 and GLUT1 expression was higher in MCF-7 spheroids when compared with monolayer cultures. No alterations in galectin-1 expression occurred during growth of HeLa and UM-UC-3 spheroids. Galectin-1 protein levels were lower in spheroids of HCT-116 and GLUT1 protein levels were lower in spheroids of HCT-116 and HELA. The expression of galectin-1 spheroids decreased in the following order: UM-UC-3 > HeLa > MCF-7 > HCT-116 (Figure SI7.3). Additionally GLUT1 protein levels in spheroids decreased in the following order: MCF-7 > UM-UC-3 > HeLa ≈ HCT-116 (Figure SI7.4).

Previous studies have reported alterations in endogenous ROS during spheroid development [10]. To determine endogenous levels of ROS in monolayer and spheroids, these cultures were stained with the redox sensitive dye H_2DCFDA and the fluorescence of ROS converted into DCF (oxidized H_2DCFDA) was monitored by fluorescence spectroscopy. Endogenous levels were similar in monolayers and spheroids of MCF-7 and UM-UC-3 cancer cells (Figure SI7.5). In HCT-116 and HELA spheroids there was an increase in endogenous ROS generation during spheroid formation.

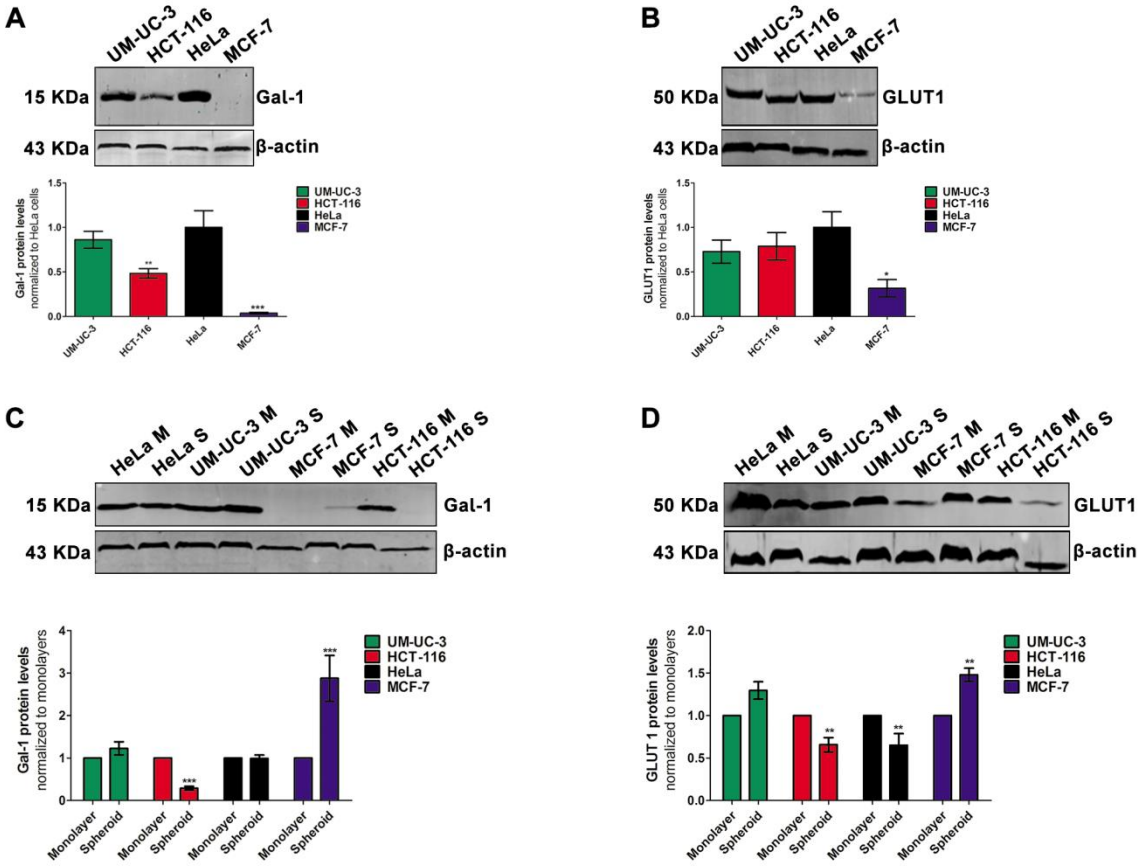

Figure 7.5 Cells of resulting spheroids have altered expression of galectin-1 and GLUT1 proteins. (A, C)Western blotting analysis and quantification of galectin-1 protein levels in monolayers of HCT-116, MCF-7, UM-UC-3 and HeLa cancer cells growing in monolayers (A) or in spheroids (C). M means monolayer and S, spheroid. Quantitative analysis of galectin-1 (normalized to β-actin) expressed as a ratio of the levels found in HeLa cells (A) or in cancer monolayers (C). Data are means ± S.D. of at least five independent experiments. $^{***}P< 0.001$ compared to galectin-1 protein levels in HeLa cells (A) or in respective cancer cell line growing in monolayers (C), using a Student´s *t* test. (B, D)Western blotting analysis and quantification of GLUT1 protein levels in monolayers of HCT-116, MCF-7, UM-UC-3 and HeLa cancer cells growing in monolayers (B) or in spheroids (D). M means monolayer and S, spheroid. Quantitative analysis of GLUT1 (normalized to β-actin) expressed as a ratio of the levels found in HeLa cells (B) or in cancer monolayers (D). Data are means ± S.D. of at least five independent experiments. $^{*}P< 0.05$, $^{**}P< 0.01$ compared to GLUT1 protein levels in HeLa cells (B) or in respective cancer cell line growing in monolayers (D), using a Student´s *t* test.

7.5 Por-C3-Gal$_4$ and Por-C1-Gal$_4$ accumulate in cancer cells growing as monolayer and spheroid cultures and are non-toxic in darkness

Resistance of cancer cells to PDT agents arises not only due to decreased PS photoactivity *in vivo*, but also due to PS delivery barriers and penetration kinetics. The three-dimensional structure of spheroidsmimics some of the physical and physiological barriers found *in vivo* [7, 8, 13]. To validate the use of HCT-116, MCF-7, UM-UC-3 and HeLa spheroid cultures in the screening of galactose-PSs we performed uptake and PDT studies (Figure 7.6A) with new porphyrin containing galactose units attached through carbon-3 (**Por-C3-Gal$_4$**). It is expected that **Por-C3-Gal$_4$** will have increased affinity to galactin-1 protein [4]. Furthermore, to validate the potential of **Por-C3-Gal$_4$,** the same tetrapyrrolic macrocycle was also attached to the carbon-1 of galactose sugar (**Por-C1-Gal$_4$**). (Figure SI7.6) [23].

Octanol-PBS partition coefficient values were determined for **Por-C3-Gal$_4$** and **Por-C1-Gal$_4$** using the classic shake flask method [28]. Data show that the values of log *P* are higher for **Por-C3-Gal$_4$** when compared with **Por-C1-Gal$_4$** (Table 7.1), indicating that **Por-C1-Gal$_4$** has less water solubility when compared with the corresponding porphyrin **Por-C3-Gal$_4$**.

Table 7.1 Partition coefficient (log *P* in n-octanol/PBS system) values of the galactose-conjugates **Por-C3-Gal$_4$** and **Por-C1-Gal$_4$**.

Compound	*logP*
Por-C1-Gal$_4$	-1.36
Por-C3-Gal$_4$	-1.50

Monolayer cultures of cancer cells were incubated with increasing concentrations (2.25, 4.5 and 9 μM) of **Por-C3-Gal$_4$** and **Por-C1-Gal$_4$** in PBS (containing a maximum of 0.5% v/v DMSO) for up to 4 h. No toxicity was observed in untreated cells (up to 4 h) in the presence of 0.5% (v/v) DMSO in the incubation medium (Figure SI7.7).

Moreover, **Por-C3-Gal$_4$** and **Por-C1-Gal$_4$** showed no significant dark cytotoxicity in monolayer and spheroid cultures at concentrations up to 9 μM (Figures SI7.8 and Figure SI7.9). We evaluated **Por-C3-Gal$_4$** and **Por-C1-Gal$_4$** accumulation in monolayer and spheroid cultures using fluorescence spectroscopy (Figure 7.6).

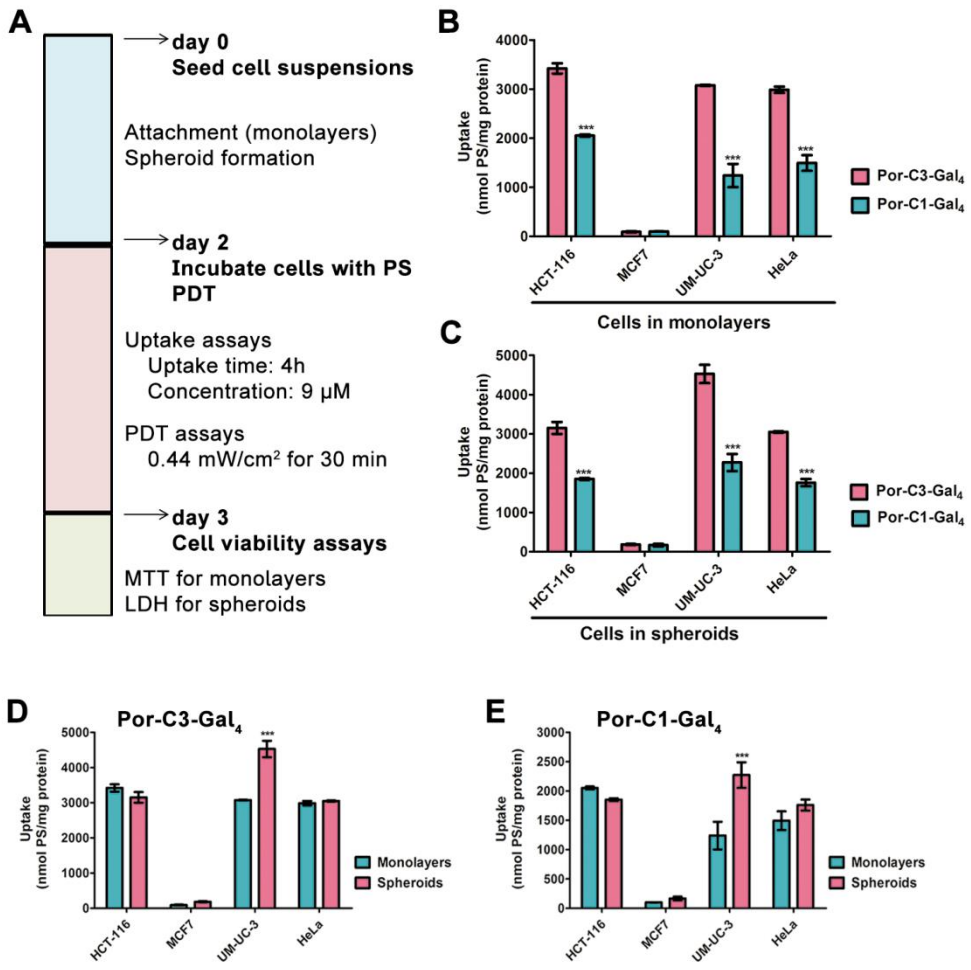

Figure 7.6 Por-C3-Gal$_4$ and Por-C1-Gal$_4$ accumulate in cancer cells growing as monolayer and spheroid cultures. (A**)** Uptake and PDT studies scheme. Intracellular uptake of **Por-C3-Gal$_4$** and **Por-C1-Gal$_4$** by HCT-116, MCF-7, UM-UC-3 and HeLa cancer cells growing as monolayers (B) or spheroids (C). The concentration of PSs was determined by fluorescence spectroscopy ($\lambda_{excitation}$ at 410 nm and $\lambda_{emission}$ at 702 nm) after incubation of cancer cells with 9 μM of PSs during 4 h and the results were normalized to protein quantity. Data are means ± S.D. of at least three independent experiments performed in triplicate. $^{***}P< 0.001$ compared uptake of **Por-C3-Gal$_4$** in the respective cell line, using a Student´s *t* test. (D)**Por-C3-Gal$_4$** and (E) **Por-C1-Gal$_4$** uptake in cancer cells growing as monolayers and spheroids. Data are means ± S.D. of at least three independent experiments performed in triplicate. $^{***}P< 0.001$ compared uptake by cancer cells growing as monolayers, using a Student´s *t* test.

The uptake by HCT-116, UM-UC-3 and HeLa cancer cells growing as monolayers or spheroids was higher for **Por-C3-Gal$_4$** when compared with**Por-C1-Gal$_4$** (Figures 7.6B,C). A

decrease in the uptake of **Por-C3-Gal$_4$** and **Por-C1-Gal$_4$** by monolayer cultures was observed in the following order: HCT-116 > HeLa ≈ UM-UC-3 > MCF-7 (Figures 7.6B). When spheroids were used as cell culture model, a decrease in the uptake of **Por-C3-Gal$_4$** and **Por-C1-Gal$_4$** was observed in the following order: UM-UC-3 > HCT-116 > HeLa > MCF-7 (Figures 7.6C).

We compared the uptake of **Por-C3-Gal$_4$** and **Por-C1-Gal$_4$** into monolayer cultures *vs.* spheroids. Spheroid structures of HCT-116, MCF-7 and HeLa cells did not alter the extent of uptake of **Por-C3-Gal$_4$** and **Por-C1-Gal$_4$** (Figures 7.6D,E). Interestingly, an increase in the uptake of **Por-C3-Gal$_4$** and **Por-C1-Gal$_4$** was observed when UM-UC-3 cancer cells were culture in three-dimensional structures.

7.6 Por-C3-Gal$_4$ and Por-C1-Gal$_4$ induce cytotoxicity in monolayer and spheroid cultures after photodynamic activation

After characterization of spheroids formation and uptake assays, we investigated the effect of **Por-C3-Gal$_4$** and **Por-C1-Gal$_4$** mediated PDT efficacy in monolayer and spheroid cultures (Figure 7.6A). For these studies, we used spheroids with volume and average size of approximately 0.05 mm^3 and 443 µm, respectively, which were obtained from the human cancer cell lines, as previously described.

The cells were treated 48 h after plating, with 9 µM of **Por-C3-Gal$_4$** and **Por-C1-Gal$_4$** for 4 h, and then exposed to light (420-700 nm) delivered at 0.44 mW/cm^2 during 30 min (0.792 J/cm^2). The 48 h time point following cell seeding was chosen based on the time needed for spheroids of the different cell lines to form and achieve reproducible and similar compactness (based on spheroid volume and shape) in each well. In all monolayer cultures, the light activation of **Por-C3-Gal$_4$** and **Por-C1-Gal$_4$** induced reduction of cells viability (Figure 7.7A).

As shown in Figure 7.7A, the phototoxicity of **Por-C3-Gal$_4$** and **Por-C1-Gal$_4$** was higher in cell monolayers of HCT-116, UM-UC-3 and HELA when compared with that in MCF-7 cells. When PDT was performed in spheroid cultures, the release of LDH into the culture medium was increased when compared with control cells (Figure 7.7B). After PDT,

LDH released by HCT-166, UM-UC-3 and HELA spheroids was higher than that by MCF-7 spheroid cultures. However, the amount of LDH leakage into the extracellular medium was lower for all cancer spheroid cultures when compared to their monolayer counterparts (Figure 7.7C,D).

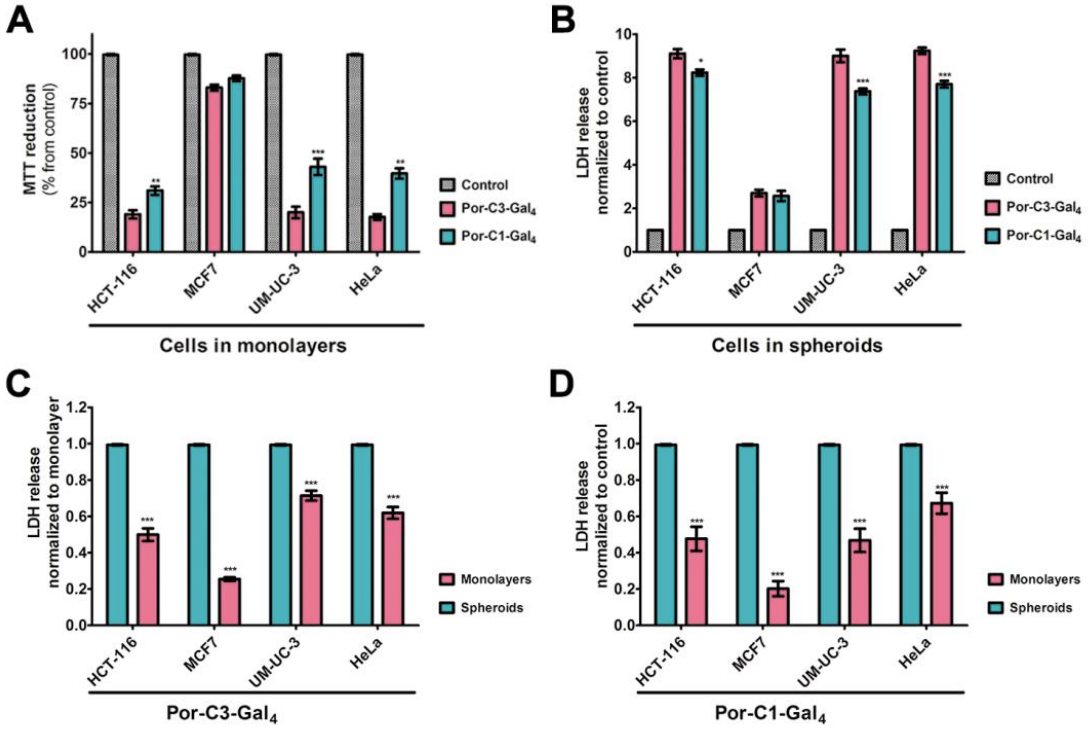

Figure 7.7 Por-C3-Gal$_4$ and Por-C1-Gal$_4$ produces toxicity after PDT in cancer cells growing as monolayers or spheroids. (A) Cytotoxicity at 24 h after PDT with **Por-C3-Gal$_4$** and **Por-C1-Gal$_4$** in cancer cells growing in monolayers, determined using the MTT assay. Cells were incubated with 9 µM PS for 4 h and PDT was performed during 30 min at 0.44 mW/cm^2. Data are means ± S.D. of at least three independent experiments performed in triplicate. $^{**}P< 0.01$, $^{***}P< 0.001$ compared to phototoxicity with **Por-C3-Gal$_4$**. (B) Cytotoxicity at 24 h after PDT with **Por-C3-Gal$_4$** and **Por-C1-Gal$_4$** in cancer cells growing in spheroids, determined using the LDH assay. Spheroids were incubated with 9 µM PS for 4 h and PDT was performed during 30 min at 0.44 mW/cm^2. Data are means ± S.D. of at least three independent experiments performed in triplicate. $^{*}P< 0.05$, $^{***}P< 0.001$ compared to phototoxicity with **Por-C3-Gal$_4$**, using a Student´s *t* test. (C,D) Cytotoxicity at 24 h after PDT with (C) **Por-C3-Gal$_4$** and (D) **Por-C1-Gal$_4$** in cancer cells growing in monolayers or spheroids, determined using the LDH assay. $^{***}P< 0.001$ compared to phototoxicity in monolayers, using a Student´s *t* test.

7.7 Discussion

The development of reliable *in vitro* models for the screening of anticancer agents plays a key role in extracting biologically relevant knowledge. Tumor spheroid cultures with appropriate size and shape simulate the three-dimensional tumor micro-milieu and *in vivo* environment in which cancer cells reside [7, 8], namely the physic-chemical conditions (oxygen, pH and nutrient gradients). The advantage of using spheroid cultures in PS screening has been previously reported [5, 12, 29-33]. However, a high throughput screening that involves the use of different cancer cell lines is limiting due to the difficulty to obtain homogeneous spheroid cultures. To analyze uptake and cytotoxicity of an anticancer compound, in *in vitro* three-dimensional tumor structure, it is necessary to obtain spheroids with a compact structure and reproducible diameters. Of the five tested tumor cells, HCT-116 colon cancer cells, MCF-7 breast cancer cells, UM-UC-3 bladder cancer cells and HeLa cervical cancer cells grew as viable, stable, structurally and functionally mature spheroids by 48 h after cell seeding. MDA-MB-231 breast cancer cells failed to form spheroids in agarose-coated 96-well plates, instead, formed loose aggregates, which may be attributed to weak cell-cell aggregation.

HCT-116, MCF-7, UM-UC-3 and HeLa spheroids formed 48 h after cell plating showed appropriate size (approximately 0.05 mm^3 in volume and 443 μm in average cellular diameter) for use in the screening of PDT agents. Spheroids with a size lower than 200 μm may be sufficient to mimic three-dimensional cell-cell and cell-matrix interactions but they are inappropriate to reflect pathophysiological conditions with hypoxic areas in the spheroid center or to mimic proliferation gradients [6]. Spheroids with diameter starting from 200 μm mimic the chemical gradients (oxygen, nutrients or catabolites) found *in vivo* [13]. Cells cultured in spheroids with sizes beyond 500 μm may become quiescent with formation of a necrotic core and undergo cell death due to limited diffusion of oxygen and nutrients inside spheroids [34, 35]. Studies have demonstrated that not only spheroid volume, but also spheroid shape may be a source of variability when these three-dimensional structures are used on the evaluation of a new anticancer compound [13]. In spheroids with an irregular shape it is usually observed the formation of two necrotic cores instead of only one which

results in inconsistent viability in these cells. In our study, we optimized conditions to obtain spherically-shaped spheroids of homogenous size and preserved cell viability for at least 72 h after cell seeding.

Glycolysis is the process characterized by conversion of glucose into pyruvate and then to lactic acid. In the presence of oxygen, most of the mitochondria of mammalian cells oxidize pyruvate to carbon dioxide and water, inhibiting glycolysis [21]. On the other hand, cancer cells have increased glycolysis (in which glucose is converted to lactic acid) even if oxygen is available [36, 37]. The high glucose consumption is a unique property of cancer cells and might have a key role in promoting tumor development [21]. When compared with tumors under "normal" oxygen levels, hypoxic tumors require increased glycolysis to survive [21]. The development of hypoxic regions in three-dimensional cultures will increase glycolysis which will result in an increase in glucose utilization and lactate production [38].

In our study we observed alterations in glucose metabolism during spheroid formation. Glucose utilization by cancer cells was measured using the fluorescent glucose analog 2-NBDG which is taken into cells through glucose transporters [22, 39]. We observed an increase in glucose utilization by MCF-7 and UM-UC-3 cancer cells during spheroid development when compared with the respective monolayer cultures. These results suggest that, concomitant to the development of MCF-7 and UM-UC-3 spheroid structures, there is alteration in the pattern of metabolism with increase in glucose dependence. As the uptake of glucose by cancer cells is dependent on the expression of glucose transporters (such as GLUT1) [21]; increased GLUT1 protein levels can explain the increased glucose consumption by MCF-7 and UM-UC-3 spheroid cancer cells. Interestingly, HCT-116 and HeLa spheroids demonstrated a decrease in the consumption of glucose as well as a decrease in GLUT1 expression levels. Previous studies have also demonstrated that dephosphorylation of 2-NBDG by hexokinase can result in efflux from cells [39]. Additionally, alterations in hexokinase expression have been observed during spheroids development [38]. Therefore, alterations in hexokinase expression during HCT-116 and HeLa spheroids can result in dephosphorylation and efflux of 2-NBDG which lead to decreased glucose consumption.

Lactate production was measured enzimatically in the culture cell media of monolayers or spheroids cultures by using an appropriate commercial kit [22]. The development of UM-

UC-3 and HeLa spheroids resulted in an increment of lactate production, while no alterations were detected during the development of HCT-116 and MCF-7 spheroids. The increment in the production of lactate by UM-UC-3 spheroids can be due to increased glycolysis in these cells. Previous studies have demonstrated that lactate production and utilization (oxidation for energetic purposes, amino acid production or shuttles for anabolic purposes) can occur simultaneously and these processes are highly dependent on the external lactate concentrations [40]. Therefore, the increase in lactate in the culture medium of HeLa spheroids (in spite of decrease in glucose utilization by these cells) can be due to alterations in lactate efflux [41]. The breakdown of cellular macromolecules or the catabolism of other fuels (besides glucose) can also justify the increase of lactate levels found in HeLa spheroids [38]. As lactate efflux is dependent on monocarboxylate transporter 1 (MCT 1) at the cell membrane [41], alterations in the expression of MCT 1 during spheroids development can explain the alterations in lactate production.

The oxygen sensor transcription factor hypoxia-inducible factor-1α (HIF1α) has a key role in the glycolytic response [42]. Under hypoxic stress, the upregulation of HF1α induces the expression of survival genes such as glucose transporters [43], haematopoeitic factors (*e.g.* transferrin and erythropoietin) [44], hexokinase II [45], angiogenic growth factors (vascular endothelial growth factor, VEGF). Additionally, HIF1α overexpression increases galectin-1 expression and its inhibition attenuates hypoxia induction of galectin-1 [46].

In our research we are particularly interested in the screening of new galactose-PSs to be used in cancer PDT [1, 3, 47], since this type of compounds can interact in somehow with proteins able to bind galactose (such as galectin-1 and GLUT1) overexpressed in cancer cells improving the selectivity of the PS for cancer cells. In both MCF-7 and UM-UC-3 cancer cells, galectin-1 and GLUT1 protein levels were found to be increased in spheroids compared to the respective monolayers. In HCT-116 spheroids the expression of these proteins was lower when compared with monolayer cultures. Galectin-1 expression was unaltered in HeLa spheroids, while GLUT1 protein expression was reduced. The precise changes in the spheroids setting underlying these alterations require further investigation, yet it is well known that the expression of both galectin-1 and GLUT1 is altered during hypoxic conditions due to upregulation of HIF1α [43, 46].

Herein we used cell lines growing in monolayer and spheroid cultures which express galectin-1 and GLUT1 in different levels. Therefore, we could not only study how the expression of these proteins influences the uptake and further phototoxicity of galactose-PSs but also compare the *in vitro* PDT efficacy of a galactose-PS in monolayer *vs.* spheroid cultures.

In an attempt to increase the affinity of galactose-PSs to galectin-1, a porphyrin was conjugated to the carbon-3 of galactose sugar (**Por-C3-Gal$_4$**). To determine the *in vitro* photodynamic properties of **Por-C3-Gal$_4$** we used monolayer and spheroid cultures in our studies. **Por-C3-Gal$_4$** results were also compared to the results for the same porphyrin conjugated to carbon-1 of galactose sugar (**Por-C1-Gal$_4$**). The uptake and phototoxicity induced by PDT with **Por-C3-Gal$_4$** and **Por-C1-Gal$_4$** were dependent on the cell line and on the *in vitro* model. The uptake of PSs was higher in cell lines containing high levels of galectin-1 and GLUT1 proteins than in cell lines containing low levels of these proteins. Additionally, the increment in the levels of galectin-1 and GLUT1 proteins during the development of UM-UC-3 spheroids resulted in an improvement of **Por-C3-Gal$_4$** and **Por-C1-Gal$_4$** uptake. Porphyrin attached to the carbon-3 of galactose sugar exhibited higher potodynamic activity in cancer cells expressing galectin-1 protein, than the corresponding porphyrin attached to the carbon-1 of galactose sugar. However, the three-dimensional culture model demonstrated higher resistance to phototoxicity when compared with monolayer cultures which is consistent with previous studies [12].

Many factors associated with PS accumulation in spheroids, hypoxia and related alterations in the metabolism have influence on the phototoxicity response of spheroids. Additionally, the slower proliferation of spheroids (characterized by increased doubling times) when compared with monolayer cultures can contribute to the lower phototoxicity in spheroids. In monolayer cultures, the cells are exposed to uniform **Por-C3-Gal$_4$** and **Por-C1-Gal$_4$** and oxygen levels. On the other hand, **Por-C3-Gal$_4$** and **Por-C1-Gal$_4$** and oxygen need to diffuse to the center of spheroids which decreases PS and oxygen in the core of these three-dimensional structures. As PDT is dependent not only on the photo-activation of the PS but also on the generation of ROS [48], the low concentration of PS and low levels of oxygen in the center of the spheroid can decrease the photodynamic efficacy. Previous studies have

reported the formation of a necrotic core during spheroid development due to lack of nutrition and oxygen in the middle of these three-dimensional structures [8]. In our study we did not observe that phenomenon (usually detected by observation of a darkest region in the spheroid core imaged in brightfield [13]), because we used spheroids with 443 μm size which were cultured during short time (72 h).

Alteration in cell redox status, with increasing generation of ROS has been observed during spheroids development [10]. This is a biochemical property that can explain the resistance of spheroid cultures when compared with cells growing in monolayers. In our study, an increase in endogenous ROS generation was detected during the development of HCT-116 and HeLa spheroids. GLUT1 protein has antioxidant functions in cells due to its ability to import the oxidized form of vitamin C (dehydroascorbic acid) [49] to the mitochondria. Therefore, it is expected that the decrease in GLUT1 protein expression in HCT-116 and HeLa spheroids will result in an increase of endogenous ROS.

7.8 References

1. Singh S, Aggarwal A, Bhupathiraju NVSDK, Arianna G, Tiwari K, Drain CM (2015) Glycosylated porphyrins, phthalocyanines, and other porphyrinoids for diagnostics and therapeutics. Chem Rev 115: 10261-10306.

2. Pereira PMR, Silva S, Cavaleiro JAS, Ribeiro CAF, Tomé JPC, Fernandes R (2014) Galactodendritic phthalocyanine targets carbohydrate-binding proteins enhancing Photodynamic Therapy. Plos One 9: e95529.

3. Silva S, Pereira PMR, Silva P, Paz FAA, Faustino MAF, Cavaleiro JAS, Tomé JPC (2012) Porphyrin and phthalocyanine glycodendritic conjugates: synthesis, photophysical and photochemical properties. Chem Commun 48: 3608-3610.

4. van Hattum H, Branderhorst HM, Moret EE, Nilsson UJ, Leffler H, Pieters RJ (2013) Tuning the preference of thiodigalactoside- and lactosamine-based ligands to galectin-3 over galectin-1. J Med Chem 56: 1350-1354.

5. Madsen SJ, Sun C-H, Tromberg BJ, Cristini V, De Magalhães N, Hirschberg H (2006) Multicell tumor spheroids in photodynamic therapy. Laser Surg Med 38: 555-564.

6. Friedrich J, Seidel C, Ebner R, Kunz-Schughart LA (2009) Spheroid-based drug screen: considerations and practical approach. Nat Protoc 4: 309-324.

7. Perche F, Torchilin VP (2012) Cancer cell spheroids as a model to evaluate chemotherapy protocols. Cancer Biol Ther 13: 1205-1213.

8. Breslin S, O'Driscoll L (2013) Three-dimensional cell culture: the missing link in drug discovery. Drug Discov Today 18: 240-249.

9. Bizik J, Kankuri E, Ristimäki A, Taïeb A, Vapaatalo H, Lubitz W, Vaheri A (2004) Cell-cell contacts trigger programmed necrosis and induce cyclooxygenase-2 expression. Cell Death Differ 11: 183-195.

10. Khaitan D, Chandna S, Arya MB, Dwarakanath BS (2006) Establishment and characterization of multicellular spheroids from a human glioma cell line; Implications for tumor therapy. J Transl Med 4: 1-13.

11. Charoen KM, Fallica B, Colson YL, Zaman MH, Grinstaff MW (2014) Embedded multicellular spheroids as a biomimetic 3D cancer model for evaluating drug and drug-device combinations. Biomaterials 35: 2264-2271.

12. Chen Y-C, Lou X, Zhang Z, Ingram P, Yoon E (2015) High-throughput cancer cell sphere formation for characterizing the efficacy of photodynamic therapy in 3D cell cultures. Sci Rep 5: 12175-12187.

13. Zanoni M, Piccinini F, Arienti C, Zamagni A, Santi S, Polico R, Bevilacqua A, Tesei A (2016) 3D tumor spheroid models for *in vitro* therapeutic screening: a systematic approach to enhance the biological relevance of data obtained. Sci Rep-Uk 6: 19103-19117.

14. Gong X, Lin C, Cheng J, Su J, Zhao H, Liu T, Wen XJ, Zhao P (2015) Generation of multicellular tumor spheroids with microwell-based agarose scaffolds for drug testing. Plos One 10: e0130348.

15. Jendželovský R, Jendželovská Z, Hiľovská L, Kovaľ J, Mikeš J, Fedoročko P (2016) Proadifen sensitizes resistant ovarian adenocarcinoma cells to cisplatin. Toxicol Lett 243: 56-66.

16. Byeon HJ, Thao QL, Lee S, Min SY, Lee ES, Shin BS, Choi H-G, Youn YS (2016) Doxorubicin-loaded nanoparticles consisted of cationic- and mannose-modified-albumins for dual-targeting in brain tumors. J Controlled Release 225: 301-313.

17. Liu J, Chen Y, Li G, Zhang P, Jin CZ, Zeng L, Ji L, Chao H (2015) Ruthenium(II) polypyridyl complexes as mitochondria-targeted two-photon photodynamic anticancer agents. Biomaterials 56: 140-153.

18. Kim M, Wu X, Song I, Fu M, Chang S-H, Lisanti MP, Pestell R (2008) Selective cytotoxicity of synthesized procyanidin 3-O-galloylepicatechin-4b, 8-3-O-galloylcatechin to human cancer cells. Cell Cycle 7: 1648-1657.

19. McKeown SR, Robson T, Price ME, Ho ETS, Hirst DG, McKelvey-Martin VJ (2003) Potential use of the alkaline comet assay as a predictor of bladder tumour response to radiation. Brit J Cancer 89: 2264-2270.

20. Ho WY, Yeap SK, Ho CL, Rahim RA, Alitheen NB (2012) Development of multicellular tumor spheroid (MCTS) culture from breast cancer cell and a high throughput screening method using the MTT assay. Plos One 7: e44640.

21. Gatenby RA, Gillies RJ (2004) Why do cancers have high aerobic glycolysis? Nat Rev Cancer 4: 891-899.

22. TeSlaa T, Teitell MA (2014) Techniques to monitor glycolysis. Methods Enzymol 542: 91-114.

23. Chen X, Hui L, Foster DA, Drain CM (2004) Efficient synthesis and photodynamic activity of porphyrin-saccharide conjugates: Targeting and incapacitating cancer cells. Biochemistry-Us 43: 10918-10929.

24. Medina RA, Owen GI (2002) Glucose transporters: expression, regulation and cancer. Biol Res 35: 9-26.

25. Thijssen VL, Heusschen R, Caers J, Oen AWG (2015) Galectin expression in cancer diagnosis and prognosis: A systematic review. BBA -Rev Cancer 1855: 235-247.

26. Li GL, Pandey SK, Graham A, Dobhal MP, Mehta R, Chen YH, Gryshuk A, Rittenhouse-Olson K, Oseroff A, Pandey RK (2004) Functionalization of OEP-based benzochlorins to develop carbohydrate-conjugated photosensitizers. Attempt to target beta-galactoside-recognized proteins. J Org Chem 69: 158-172.

27. Laville I, Pigaglio S, Blais JC, Doz F, Loock B, Maillard P, Grierson DS, Blais J (2006) Photodynamic efficiency of diethylene glycol-linked glycoconjugated porphyrins in human retinoblastoma cells. J Med Chem 49: 2558-2567.

28. Singh S, Aggarwal A, Thompson S, Tomé JPC, Zhu XC, Samaroo D, Vinodu M, Gao RM, Drain CM (2010) Synthesis and photophysical properties of thioglycosylated chlorins, isobacteriochlorins, and bacteriochlorins for bioimaging and diagnostics. Bioconjugate Chem 21: 2136-2146.

29. Gaio E, Scheglmann D, Reddi E, Moret F (2016) Uptake and photo-toxicity of Foscan®, Foslip® and Fospeg® in multicellular tumor spheroids. J Photochem Photobiol B 161: 244-252.

30. Vera RE, Lamberti MJ, Rivarola VA, Vittar NBR (2015) Developing strategies to predict photodynamic therapy outcome: the role of melanoma microenvironment. Tumor Biol 36: 9127-9136.

31. Yuan A, Yang B, Wu J, Hu Y, Ming X (2015) Dendritic nanoconjugates of photosensitizer for targeted photodynamic therapy. Acta Biomater 21: 63-73.

32. Manoto SL, Houreld NN, Abrahamse H (2015) Resistance of lung cancer cells grown as multicellular tumour spheroids to Zinc Sulfophthalocyanine photosensitization. Int J Mol Sci 16: 10185-10200.

33. Muehlmann LA, Rodrigues MC, Longo JPF, Garcia MP, Py-Daniel KR, Veloso AB, de Souza PEN, da Silva SW, Azevedo RB (2015) Aluminium-phthalocyanine chloride nanoemulsions for anticancer photodynamic therapy: Development and *in vitro* activity against monolayers and spheroids of human mammary adenocarcinoma MCF-7 cells. J Nanobiotechnol 13: 36-47.

34. Carlsson J, Acker H (1988) Relations between pH, oxygen partial-pressure and growth in cultured-cell spheroids. Int J Cancer 42: 715-720.

35. Friedrich J, Eder W, Castaneda J, Doss M, Huber E, Ebner R, Kunz-Schughart LA (2007) A reliable tool to determine cell viability in complex 3-D culture: the acid phosphatase assay. J Biomol Screen 12: 925-937.

36. Semenza GL, Artemov D, Bedi A, Bhujwalla Z, Chiles K, Feldser D, Laughner E, Ravi R, Simons J, Taghavi P, Zhong H (2001) 'The metabolism of tumours': 70 years later. Novartis Found Symp 240: 251-260.

37. Tannock IF, Kopelyan I (1986) Influence of glucose-concentration on growth and formation of necrosis in spheroids derived from a human bladder-cancer cell-line. Cancer Res 46: 3105-3110.

38. Bloch K, Smith H, Parsons VvH, Gavaghan D, Kelly C, Fletcher A, Maini P, Callaghan R (2014) Metabolic alterations during the growth of tumour spheroids. Cell Biochem Biophys 68: 615-628.

39. O'Neil RG, Wu L, Mullani N (2005) Uptake of a fluorescent deoxyglucose analog (2-NBDG) in tumor cells. Mol Imaging Biol 7: 388-392.

40. Bourrat-Floeck B, Groebe K, Mueller-Klieser W (1991) Biological response of multicellular EMT6 spheroids to exogenous lactate. Int J Cancer 47: 792-799.

41. Kennedy KM, Dewhirst MW (2010) Tumor metabolism of lactate: the influence and therapeutic potential for MCT and CD147 regulation. Future Oncol 6: 127-151.

42. Semenza GL (1998) Hypoxia-inducible factor 1: master regulator of O_2 homeostasis. Curr Opin Genetics Dev 8: 588-594.

43. Hayashi M, Sakata M, Takeda T, Yamamoto T, Okamoto Y, Sawada K, Kimura A, Minekawa R, Tahara M, Tasaka K, Murata Y (2004) Induction of glucose transporter 1 expression through hypoxia-inducible factor 1 alpha under hypoxic conditions in trophoblast-derived cells. J Endocrinol 183: 145-154.

44. Carmeliet P, Dor Y, Herbert J-M, Fukumura D, Brusselmans K, Dewerchin M, Neeman M, Bono F, Abramovitch R, Maxwell P, Koch CJ, Ratcliffe P, Moons L, Jain RK, Collen D, Keshert E (1998) Role of HIF-1alpha in hypoxia-mediated apoptosis, cell proliferation and tumour angiogenesis. Nature 394: 485-490.

45. Yasuda S, Arii S, Mori A, Isobe N, Yang W, Oe H, Fujimoto A, Yonenaga Y, Sakashita H, Imamura M (2004) Hexokinase II and VEGF expression in liver tumors: correlation with hypoxia-inducible factor-1 alpha and its significance. J Hepatol 40: 117-123.

46. Zhao X-Y, Chen T-T, Xia L, Guo M, Xu Y, Yue F, Jiang Y, Chen G-Q, Zhao K-W (2010) Hypoxia inducible factor-1 mediates expression of galectin-1: the potential role in migration/invasion of colorectal cancer cells. Carcinogenesis 31: 1367-1375.

47. Silva LP, Neves BM, Moura L, Cruz MT, Carvalho E (2014) Neurotensin decreases the proinflammatory status of human skin fibroblasts and increases epidermal growth factor expression. Int J Inflam 2014: 1-9.

48. Dolmans DEJGJ, Fukumura D, Jain RK (2003) Photodynamic therapy for cancer. Nat Rev Cancer 3: 380-387.

49. Sagun KC, Cárcamo JM, Golde DW (2005) Vitamin C enters mitochondria via facilitative glucose transporter 1 (GLUT1) and confers mitochondrial protection against oxidative injury. Faseb J 19: 1657-1667.

7.9 Supporting information

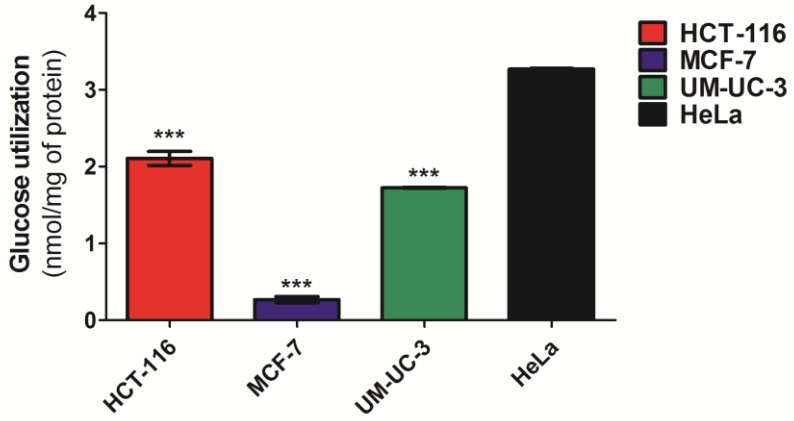

Figure SI7.1 Glucose utilization of cancer cells growing in monolayers at 48 h after plating with seeding densities of 5,000 HCT-116 cells per well, 15,000 MCF-7 cells per well, 20,000 UM-UC-3 cells per well and 20,000 HeLa cells per well. The amount of glucose (nmol) was estimated using the fluorescent glucose analog 2-NBDG and the results were normalized for mg of protein. Data are means ± S.D. of at least three independent experiments performed in triplicate. $^{***}P< 0.001$ compared to glucose utilization in HeLa cells, using a Student´s *t* test.

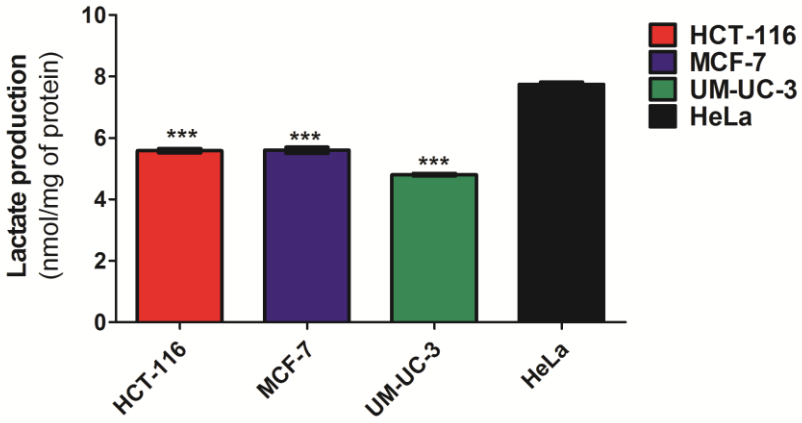

Figure SI7.2 Lactate utilization of cancer cells growing in monolayers at 48 h after plating with seeding densities of 5,000 HCT-116 cells per well, 15,000 MCF-7 cells per well, 20,000 UM-UC-3 cells per well and 20,000 HeLa cells per well. The amount of lactate (nmol) was estimated using an enzymatic assay and the results were normalized for mg of protein. Data are means ± S.D. of at least three independent experiments performed in triplicate. $^{***}P< 0.001$ compared to glucose utilization in HeLa cells, using a Student´s *t* test.

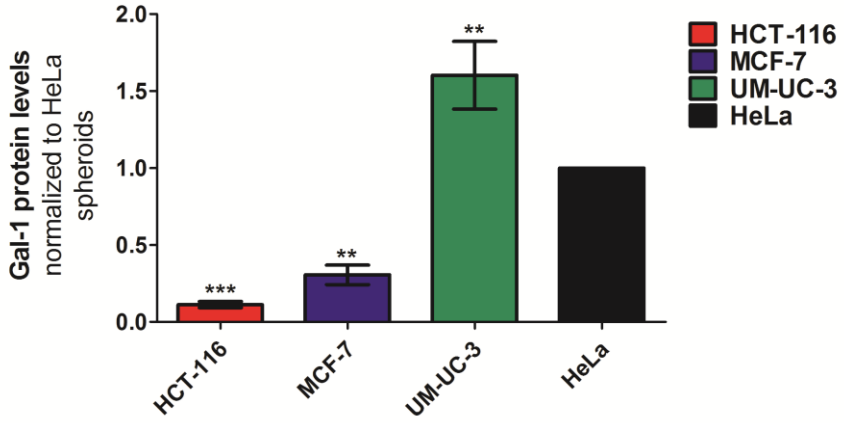

Figure SI7.3 Quantitative analysis of galectin-1 (normalized to β-actin) in spheroid cultures expressed as a ratio of the levels found in HeLa spheroids. Data are means ± S.D. of at least five independent experiments. $^{**}P< 0.01$, $^{***}P< 0.001$ compared to galectin-1 protein levels in HeLa spheroids, using a Student´s *t* test.

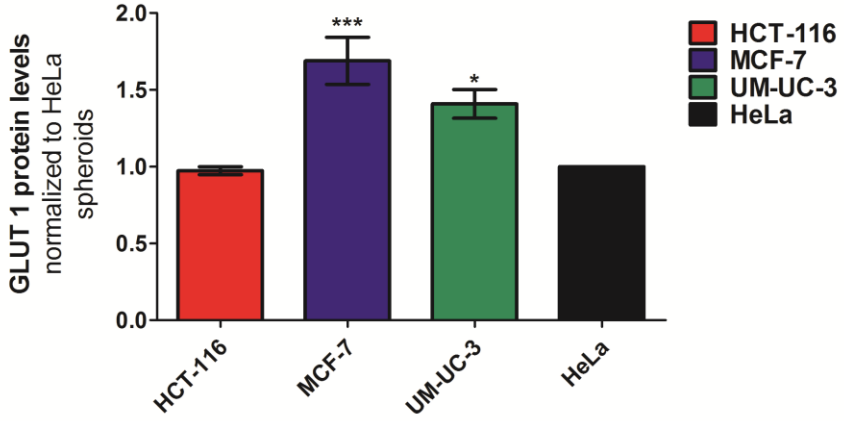

Figure SI7.4 Quantitative analysis of GLUT1 (normalized to β-actin) in spheroid cultures expressed as a ratio of the levels found in HeLa spheroids. Data are means ± S.D. of at least five independent experiments. $^{*}P< 0.05$, $^{***}P< 0.001$ compared to GLUT1 protein levels in HeLa spheroids, using a Student´s *t* test.

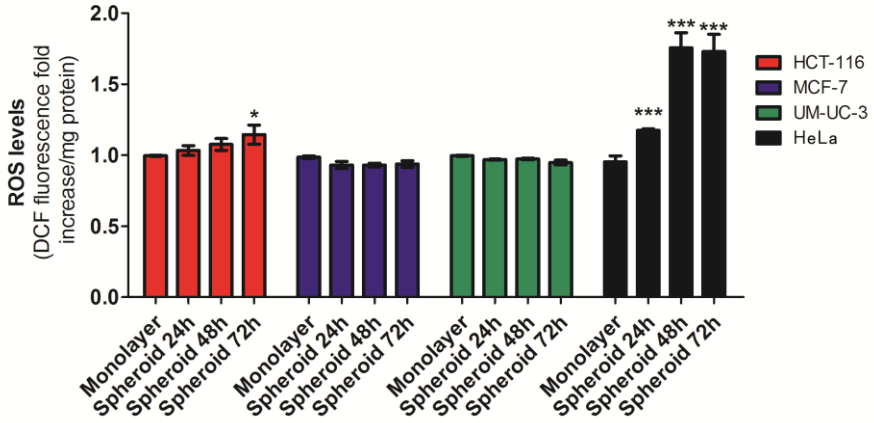

Figure SI7.5 Quantification of DCF fluorescence increase (as a measure of endogenous ROS) in cancer cells growing as monolayers or spheroids. ROS levels are expressed as a ratio of the levels found on the respective cell line growing in monolayers. Data are means ± S.D. of at least three independent experiments performed in triplicate. $^{**}P< 0.01$, $^{***}P< 0.001$ compared to DCF fluorescence in the respective cell line growing in monolayers, using a Student´s t test.

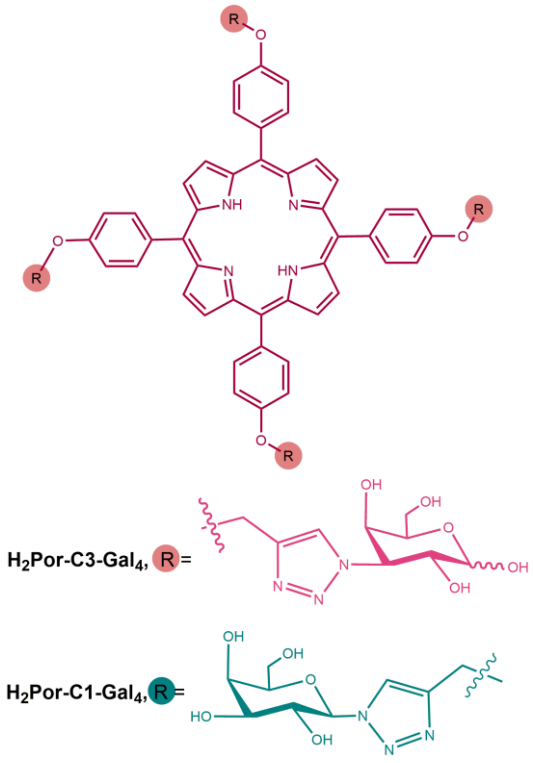

Figure SI7.6 Chemical structure of **Por-C3-Gal$_4$** and **Por-C1-Gal$_4$**.

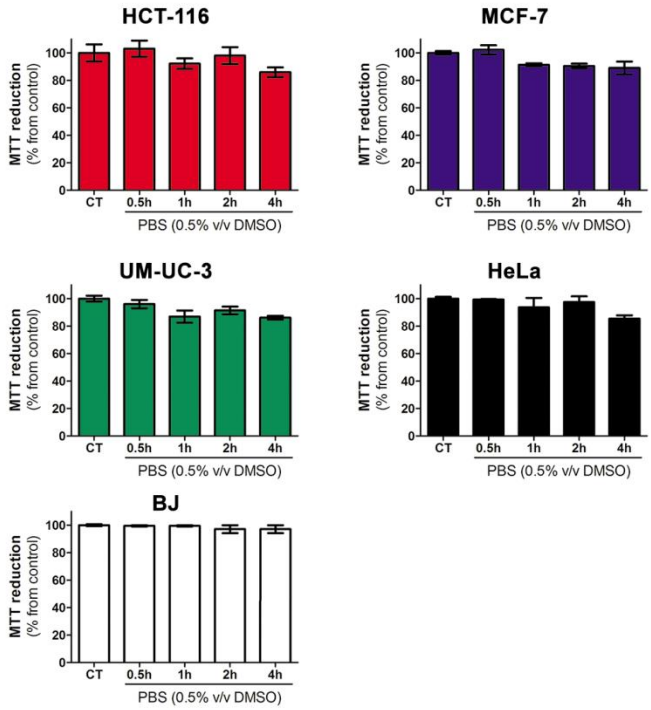

Figure SI7.7 Cytotoxicity of PBS solution containing 0.5% DMSO (v/v) in monolayer cultures at different incubation times (0.5, 1, 2 and 4 h). The percentage of cytotoxicity was calculated relatively to control cells (cells incubated with medium). Data are means ± S.D. of at least three independent experiments performed in triplicate.

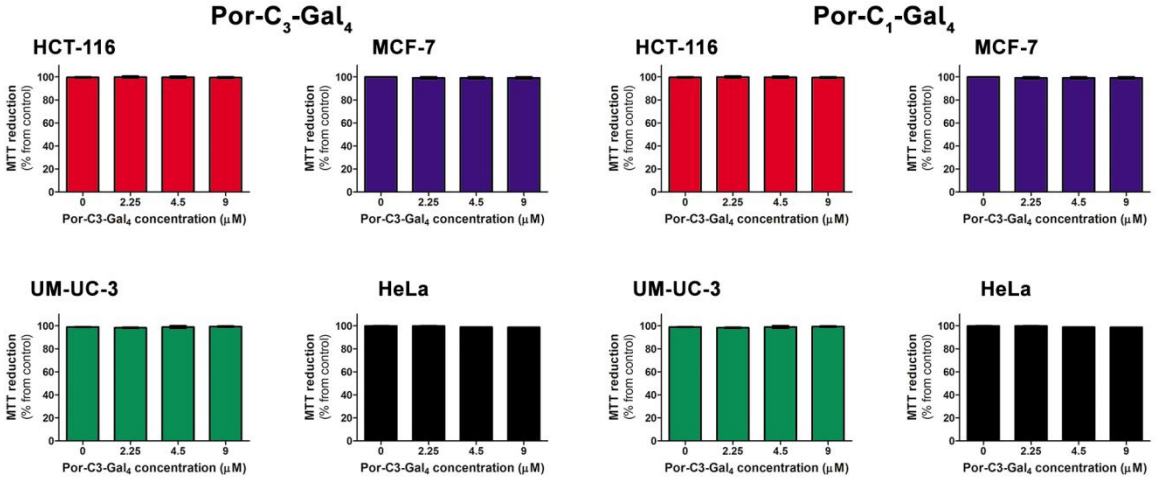

Figure SI7.8 Non-dark toxicity of **Por-C3-Gal$_4$** and **Por-C1-Gal$_4$** at different concentrations (0, 2.25, 4.5 and 9 μM) and uptake time of 4 h, in monolayer cultures. The percentage of cytotoxicity was calculated relatively to control cells (untreated cells). Data are means ± S.D. of at least three independent experiments performed in triplicate.

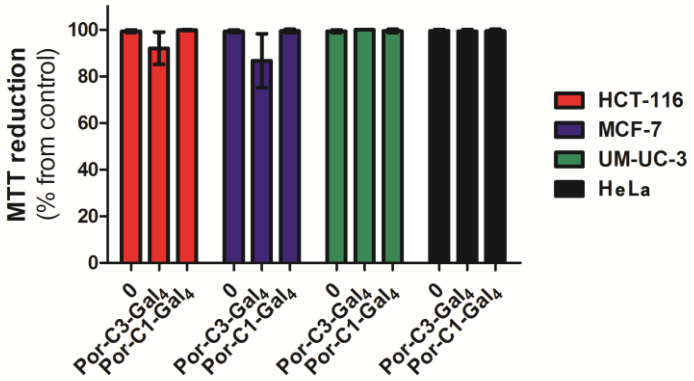

Figure SI7.9 Non-dark toxicity of **Por-C3-Gal$_4$** and **Por-C1-Gal$_4$** at 9 µM and uptake time of 4 h, in spheroids cultures. The percentage of cytotoxicity was calculated relatively to control cells (untreated cells). Data are means ± S.D. of at least three independent experiments performed in triplicate.

Table SI7.1 HCT-116 spheroid size and cellular characteristics as a function of age (24, 48 and 72 h) and number of platted cells (2,500, 5,000, 10,000 and 20,000 cells per well).

Number of platted cells/well	Age of spheroids (h)	Radius (μM) ± S.D.	Volume (mm^3)	Number of cells/spheroid	Average cellular diameter (μm) ± S.D.
2500	24	193±16	0,03515	8177	387±32
	48	174±8	0,02497	15000	349±15
	72	142±9	0,01299	25083	285±17
5000	24	231±5	0,05360	7581	463±10
	48	216±9	0,04541	31944	433±19
	72	194±14	0,03675	42363	388±28
10000	24	304±7	0,12160	17839	608±4
	48	259±5	0,07360	41250	520±11
	72	198±8	0,03334	49322	396±16
20000	24	378±3	0,22630	65000	756±7
	48	323±5	0,14230	62500	648±10
	72	247±17	0,06809	135000	495±34

Table SI7.2 MCF-7 spheroid size and cellular characteristics as a function of age (24, 48 and 72 h) and number of platted cells (5,000, 10,000, 15,000 and 20,000 cells per well).

Number of platted cells/well	Age of spheroids (h)	Radius (μM) ± S.D.	Volume (mm^3)	Number of cells/spheroid	Average cellular diameter (μm) ± S.D.
5000	24	151±3	0,01489	6625	304±6
	48	143±4	0,01292	9375	287±9
	72	138±6	0,01180	11250	276±12
10000	24	208±2	0,03816	14542	417±5
	48	188±4	0,02862	18750	378±8
	72	183±5	0,02706	30625	367±11
15000	24	236±4	0,05515	14000	467±3
	48	232±2	0,05198	23500	463±3
	72	206±8	0,03688	32500	412±17
20000	24	276±3	0,08893	25542	552±7
	48	253±3	0,06871	38125	507±6
	72	244±4	0,06180	38130	489±8

Table SI7.3 UM-UC-3 spheroid size and cellular characteristics as a function of age (24, 48 and 72 h) and number of platted cells (2,500, 5,000, 10,000 and 20,000 cells per well).

Number of platted cells/well	Age of spheroids (h)	Radius (µM) ± S.D.	Volume (mm^3)	Number of cells/spheroid	Average cellular diameter (µm) ± S.D.
2500	24	126±2	0,008440	4833	253±4
	48	99±1	0,004145	10000	199±2
	72	101±1	0,004405	13833	203±3
5000	24	171±2	0,021190	8458	343±3
	48	134±1	0,010000	18750	267±2
	72	126±1	0,008473	26833	253±3
10000	24	222±2	0,045640	13750	444±3
	48	167±3	0,019930	26875	335±6
	72	155±2	0,015680	40083	310±3
20000	24	288±1	0,099910	15000	576±3
	48	211±4	0,040230	40000	423±8
	72	193±3	0,030280	53875	386±6

Table SI7.4 HeLa spheroid size and cellular characteristics as a function of age (24, 48 and 72 h) and number of platted cells (2,500, 5,000, 10,000 and 20,000 cells per well).

Number of platted cells/well	Age of spheroids (h)	Radius (µM) ± S.D.	Volume (mm^3)	Number of cells/spheroid	Average cellular diameter (µm) ± S.D.
2500	24	110±3	0,005588	6250	220±6
	48	98±3	0,003991	18750	196±7
	72	94±2	0,003491	21250	188±3
5000	24	147±4	0,013480	8750	295±8
	48	137±3	0,010860	31250	274±6
	72	126±2	0,008347	45000	252±3
10000	24	192±2	0,029870	17500	385±4
	48	167±2	0,019630	42500	335±4
	72	171±2	0,020810	52500	341±4
20000	24	260±2	0,073960	20000	521±5
	48	229±3	0,050690	56250	460±6
	72	231±2	0,051750	72500	463±4

Conclusions and future perspectives

CHAPTER VIII

Chapter VIII Conclusions and future perspectives

8.1 Conclusions

Porphyrinoids were successfully conjugated with dendritic units of galactose (**PorGal$_8$**, **ChlGal$_8$** and **PcGal$_{16}$**) and with galactose through carbon-3 (**Por-C3-Gal$_4$**). Although structurally different, all of these bioconjugates have a common purpose – molecular targeted photodynamic therapy of cancer cells. **PorGal$_8$** and **ChlGal$_8$** contain in their structure a porphyrin and a chlorin, respectively, conjugated with eight galactose units distributed in a dendritic manner. **PcGal$_{16}$** is a phthalocyanine conjugated with sixteen galactose units distributed in a dendritic manner. **Por-C3-Gal$_4$** is a porphyrin conjugated with four galactose sugars through carbon-3.

The new galactose-PSs exhibited excellent properties as PSs: i) water solubility, ii) interaction with galectin-1 protein which is overexpressed in many tumor types,iii) ability to generate $^1O_2$, iv) photostability and v) interaction with the most abundant protein of blood plasma (HSA).

PcGal$_{16}$ demonstrated high absorption in the wavelength range between 650 and 850 nm and strong ROS production. Monolayers of UM-UC-3 and HT-1376 bladder cancer cells were used to evaluate the potential of **PcGal$_{16}$**. In comparison with the non-conjugated Pc, **PcGal$_{16}$** readily accumulated in bladder cancer cells. **PcGal$_{16}$** was accumulated by UM-UC-3 and HT-1376 cells expressing high levels of galectin-1 and GLUT1 proteins, respectively. We conclude that galectin-1 and GLUT1 proteins are essential in the uptake of **PcGal$_{16}$** by bladder cancer cells based on the observations that i) knockdown of these proteins significantly decreased the uptake of **PcGal$_{16}$** and ii) **PcGal$_{16}$** colocalizes with galectin-1 and GLUT1 proteins. The intracellular uptake of the photosensitizers studied in this work was determined by fluorescence spectroscopy and validated using fluorescence microscopy.

Temperature-dependent studies suggested the contribution of an energy-dependent process to **PcGal$_{16}$** transport across UM-UC-3 and HT-1376 cells. Studies with inhibitors of clathrin-mediated endocytosis revealed an impeded uptake of **PcGal$_{16}$** by UM-UC-3 cells. The uptake of **PcGal$_{16}$** in HT-1376 cells was inhibited after depletion of cholesterol in the plasma

membrane (preventing caveolin-mediated endocytosis) and inhibition of clathrin-coated vesicles (preventing clathrin-mediated endocytosis). UM-UC-3 cells express lower levels of caveolin-1 (a protein involved in the formation of caveolae during endocytosis) when compared with HT-1376 cells. Interestingly, knockdown of caveolin-1 protein in HT-1376 cells significantly increased the uptake of **PcGal$_{16}$** and the expression of GLUT1 protein at the plasma membrane. We conclude that uptake of **PcGal$_{16}$** is a complex process that i) is dependent on the cell line used, ii) requires the expression of galactose-binding proteins present at the plasma membrane of cancer cells and iii) occurs through a combination of specific endocytic uptake mechanisms. *In vitro* PDT studies with **PcGal$_{16}$** demonstrated phototoxicity associated with increased levels of intracellular ROS. Phototoxicity was higher in UM-UC-3 cells than in HT-1376 cells at 24 h after treatment. In this study, we observed that HT-1376 cells generate an antioxidant response to counteract the effects of oxidative stress induced by PDT with **PcGal$_{16}$**. The increase in the uptake of **PcGal$_{16}$** after knockdown of caveolin-1 protein decreased the resistance of HT-1376 cells to PDT.

PorGal$_8$ binds to galectin-1 protein with high affinity. The photodynamic efficiency of **PorGal$_8$** was evaluated *in vitro* using monolayers of UM-UC-3 and HT-1376 bladder cancer cells and *in vivo* in athymic nude mice (Balb/c *nu/nu*) bearing subcutaneously implanted luciferase-positive UM-UC-3 bladder cancer xenografts. The uptake of **PorGal$_8$** was higher in UM-UC-3 cells than in HT-1376 cells and it can be somehow related to the higher protein levels of galectin-1 in UM-UC-3 cell line. Galectin-1 knockdown reduces uptake of **PorGal$_8$** by UM-UC-3 bladder cancer cells. **PorGal$_8$** was nontoxic to cancer cells until activated by light. The phototoxicity after PDT with **PorGal$_8$** was higher for the cell line UM-UC-3 than for the cell line HT-1376, being mediated by ROS production. PDT with **PorGal$_8$** induced apoptotic cell death and alterations in the cytoskeleton of UM-UC-3 bladder cancer cells. Biodistribution studies, at 24 h after intraperitoneal injection of **PorGal$_8$**, revealed that this PS accumulates in the main excretory organs (*e.g.* kidney, liver and lung) and in the tumor. Highly efficient tumor ablation was achieved with a single intraperitoneal administration of **PorGal$_8$** followed by a single exposure of light.

ChlGal$_8$ exhibited a more than 50-fold increase in the extinction coefficient at the lowest-energy Q band relative to the porphyrin **PorGal$_8$**. The photodynamic efficiency of

ChlGal$_8$ was evaluated *in vitro* using monolayers of UM-UC-3 and HT-1376 bladder cancer cells and *in vivo* in athymic nude mice (Swiss *nu/nu*) bearing subcutaneously implanted HT-1376 bladder cancer xenografts. In spite of better photo-chemical and –physical properties, **ChlGal$_8$** uptake by bladder cancer cells was lower when compared with **PorGal$_8$**. *In vitro*, a single dose of **ChlGal$_8$** and irradiation induced high photosensitivity in UM-UC-3 bladder cancer cells sensitive to therapy. HT-1376 cells were resistant to PDT as previously observed for PDT with **PcGal$_{16}$** and **PorGal$_8$**. Interestingly, both **ChlGal$_8$** and GLUT1 protein were localized in the mitochondrial fraction of HT-1376 cells after a single irradiation. We further demonstrated, using both *in vitro* and in vivo assays, that a repeated irradiation treatment (instead of the traditional single irradiation treatment) could improve phototoxicity with **ChlGal$_8$** in HT-1376 bladder cancer cells resistant to PDT. The particular ability of **ChlGal$_8$** to be accumulated in the mitochondria in the period of time between single and repeated PDT provides new insights into the optimization of treatment regimens by fractionated dosing of light irradiation to achieve enhanced PDT efficacy.

The attachment of porphyrin to C3-galactose (**Por-C3-Gal$_4$**) demonstrated to be an effective way to increase the specificity of a PS to cancer cells overexpressing galectin-1 protein. The uptake and phototoxicity of **Por-C3-Gal$_4$** were studied in monolayers and spheroid cultures of HCT-116 colon cancer cells, MCF-7 breast cancer cells, UM-UC-3 bladder cancer cells and HeLa cervical cancer cells. **Por-C3-Gal$_4$** exhibited higher uptake by cancer cells expressing high levels of galectin-1 protein when compared with cells containing low levels of this protein. Additionally, PDT effects in cancer cells expressing galectin-1 were higher with **Por-C3-Gal$_4$** when compared with the same porphyrin attached to C1-galactose.

8.2 Future perspectives

PDT is a clinically approved cancer therapy with unquestionable advantages when compared with conventional cancer therapies. It has intrinsic dual cancer cell selectivity due to the specificity of the PS and the precise light delivery in the target lesions. However, none of the clinically approved PSs fulfill all the criteria of an ideal one for cancer PDT. As light delivery technologies advance, the success of PDT seems to be highly dependent on the development of new PSs able to target selectively cancer cells. The conjugation of porphyrinoids (porphyrins, chlorins, phthalocyanines and others) with galactose molecules increases their water solubility and provides the possibility for specific (non-covalent) interaction with galactose-binding proteins overexpressed in cancer cells. A careful planning of the organic synthetic strategy, considering both galactose moieties and PSs suited for conjugation, should allow very efficient PDT treatments. In this work, the use of dendritic units of galactose and C3-galactose demonstrated to be promising strategies in the synthesis of new galactose-PSs.

The synthesis of dendritic units of galactose through carbon-3 of the sugar seems indeed very promising in the development of new galactose-PSs. Our *in vitro* and *in vivo* data demonstrated that galectin-1 protein has a great potential in molecular-targeted PDT. We envisage that the conjugation of a porphyrinoid with an antibody recognizing this antigen could improve its targeting efficiency and further photoxicity.

The photo-properties of new galactose-conjugated PSs are only one aspect among the many *in vitro* and *in vivo* steps that matter for their efficiency in cancer PDT. Photophysical and photochemical studies were performed *prior* to *in vitro/in vivo* studies. In our study, the production of $^1O_2$ by galactose-PSs was determined before *in vitro* and *in vivo* studies by using a qualitatively methodology. A quantitative assay is necessary in further studies. Intracellular ROS were determined using ROS-sensitive fluorescent probes (*i.e.* H_2DCFDA, DHE and MitoPY1) which are very useful for quick screening experiments and to measure general aspects of intracellular oxidative stress and redox status. However, these probes are often unspecific and the results obtained do not always correlate with the photocytotoxic effects. The use of new and more accurate techniques to determine *in vitro* and *in vivo* generation of

ROS will be helpful in further studies to gain insight into the contribution of specific ROS in galactose-PS-mediated cell death after PDT.

In vitro studies demonstrated that galactose-PSs bind to galectin-1 protein. However, the molecular mechanisms of this interaction are still unknown and further studies should be performed to interpret these results. Further studies using immunoanalytical assays can be interesting to gain insight about PSs uptake through mediated interaction with specific galactose-binding proteins.

There is a lack of knowledge about the mechanisms by which a PS is accumulated inside cancer cells. Our data demonstrated that i) galactose-binding proteins overexpressed at the plasma membrane of cancer cells are important in the uptake of galactose-PSs and ii) caveolae- and clathrin-mediated endocytosis are involved in the internalization of galactose-PSs. We demonstrated that interfering with endocytosis *in vitro* can lead to increased uptake and further phototoxicity of **PcGal$_{16}$**.Although we provide convincing evidence that knockdown of caveolin-1 increases uptake and further phototoxicity of **PcGal$_{16}$** by increasing the amount of GLUT1 in the plasma membrane of cancer cells, our studies do not fully elucidate the mechanisms by which GLUT1 protein levels are increased in cells depleted of caveolin-1. Future studies should explore if after accumulation around cancer cell membranes, **PcGal$_{16}$** follows the same endocytic pathway as GLUT1.

The *in vitro* studies with galactodendritic-PSs were based in two-dimensional monolayer cell culture systems, which are too simple to replicate the tumor heterogeneity present *in vivo*. Further studies using cancer cells growing in a three-dimensional environment (*e.g.* spheroid or organotypic cultures) will be helpful to investigate the selectivity and phototototoxicity of galactose-PSs.

In vivo studies with galactose-PSs were performed in xenograft tumor models. Further studies in orthotropic tumor models are needed to gain insight into the importance of tumor host environment in determining tumor response to PDT with a galactose-PS. Further investigations using repeated administrations of the therapy (galactose-PS plus light) must be considered in the treatment of cancer cells resistant to PDT.

Methods and Materials

CHAPTER IX

Chapter IX Methods and Materials

9.1 Synthesis of galactose-conjugates

9.1.1 Equipment and reagents

The starting reagents were commercially available and used without further purification.

^{1}H, ^{13}C, and ^{19}F Nuclear Magnetic Resonance (NMR) spectra were recorded on a *Bruker Avance-300* instrument at 300.13, 75.47 and 282.38 MHz, respectively. The deuterated solvents chloroform ($CDCl_3$)and dimethyl sulfoxide (DMSO-d_6) were used for the acquisition of NMR spectra. Tetramethylsilane (TMS) at δ 0 ppm was used as internal reference in ^{1}H and ^{13}C NMR spectra. For ^{19}F NMR spectra, hexafluorobenzene (C_6F_6) was used as internal standard at δ-163 ppm. The chemical shifts are expressed in δ (ppm) and the coupling constants (*J*) in Hertz (Hz). Spin multiplicities are indicated by the following symbols: s (singlet), d (doublet), t (triplet), q (quartet), m (multiplet). Unequivocal ^{1}H assignments were made with aid of 2D COSY ($^{1}H/^{1}H$), while ^{13}C assignments were made on the basis of 2D HSQC ($^{1}H/^{13}C$).

High Resolution Mass Spectrometric (HRMS) analysis was performed at the University of Vigo using a VG AutoSpec Q and M mass spectrometers, $CHCl_3$ as solvent and nitrobenzyl alcohol (NBA) as matrix (unless otherwise stated).

Column chromatography was carried out using silica gel (Merck, 35-70 mesh). Reverse phase column chromatography was carried out using Sep-Pak® Vac 35 cc (10 g) columns. Analytical TLC was carried out on precoated sheets with silica gel 60 F_{254} (0.2 mm thick, Merck).

All chemicals were supplied by Sigma–Aldrich. Solvents were purified or dried according to the literature procedures. $TPPF_{20}$ was commercially available.

The UV-visible assays were performed on the UVIKON 922 spectrophotometer from Biotek Instruments.

9.1.2 Softwares

ChemDraw Ultra 12.00 from CambridgeSoft was the software used to draw chemical structures. MestReNova LITE (version 5.2.5-5780) was used to analyze NMR spectra.

9.1.3 Synthetic procedures

A. Synthesis of galactodendritic-photosensitizers

*Synthesis of 2-chloro-4,6-di-O-isopropilidene-α-D-galactopyranose-1,3,5-triazine (**1**)*

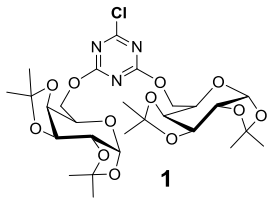

1

The compound **1** (2-chloro-4,6-di-*O*-isopropilidene-α-D-galactopyranose-1,3,5-triazine) was synthesized as previously described in the literature [1]. Under N_2, 1,2:3,4-di-*O*-isopropylidene-α-D-galactopyranose (4.0 g, 15.4 mmol) was dissolved in dry toluene (40 mL) and a large excess of *N*,*N*-diisopropylethylamine (DIPEA, 2.0 mL) was added. The reaction was then cooled at 0 ºC and 2,4,6-trichloro-1,3,5-triazine (1.4 g, 7.33 mmol) was joined to the mixture. The reaction mixture was stirred at 60 ºC during 48 h. After concentration under vacuum, the residue was purified by column chromatography (light petroleum/ethyl acetate, 8:2 to 2:1 v/v) to afford compound **1** (4.28 g, 80%) as a white solid.

^{1}H NMR (300 MHz, $CDCl_3$): δ 1.27, 1.28, 1.39 and 1.45 (4s, 4 x 6H, CH_3), 4.14 (ddd, $J_{4'\text{-}5'}$= 1.7, $J_{5'\text{-}6'a}$=6.5, $J_{5'\text{-}6'b}$= 7.9, 2H, H-5'), 4.26-4.29 (m, 4H, H-2', H-4'), 4.48-4.50 (m, 4H, H-6'a, H-6'b), 4.58 (dd, $J_{2'\text{-}3'}$= 7.9, $J_{3'\text{-}4'}$= 2.5, 2H, H-3'), 5.48 (d, $J_{1'\text{-}2'}$= 5.0, 2H, H-1').

^{13}C NMR (75 MHz, $CDCl_3$): δ 24.4, 24.9, 25.9, 26.0 (Me-isop), 65.4 (C-5'), 67.4 (C-6'), 70.4 (C-3'), 70.5 (C-2', C-4'), 96.2 (C-1'), 108.8, 109.6 (Cq-isop), 171.9 (C-4, C-6), 172.6 (C-2).

HRMS-ESI:*m/z* calculated for $C_{27}H_{39}ClN_3O_{12}$ $[M+H]^+$: 632.2222, found: 632.2212. *m/z* calculated for $C_{27}H_{38}ClN_3O_{12}Na$ $[M+Na]^+$: 654.2042, found: 654.2033. *m/z* calculated for $C_{27}H_{38}ClN_3O_{12}K$ $[M+K]^+$: 670.1781, found: 670.1771.

*Synthesis of 3-[(4,6-bis(1,2:3,4-di-O-isopropylidene-α-D-galactopyran-6-yl)-1,3,5-triazin-2-yl) thio]propane-1-thiol (**2**)*

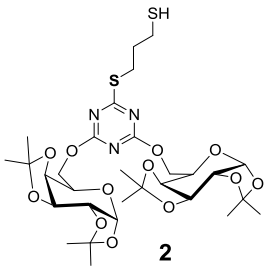

2

The compound **2** (3-[(4,6-bis(1,2:3,4-di-*O*-isopropylidene-α-D-galactopyran-6-yl)-1,3,5-triazin-2-yl) thio]propane-1-thiol) was synthesized as previously described in the literature [1]. Under N_2, compound **1** (4.3 g, 6.8 mmol) was dissolved in dry toluene (40 mL). DIPEA (5.9 mL, 34 mmol) and 1,3-dimercaptopropane (2.7 mL, 27.2 mmol) were then added and the mixture stirred at 70 ºC during 12 h. After concentration under vacuum, the residue was purified by column chromatography (hexane/ethyl acetate, 9:1 to 6.5:3.5 v/v) to afford compound **2** (4.2 g, 72%) as a viscous colorless oil.

^{1}H NMR (300 MHz, $CDCl_3$): δ 1.33, 1.34, 1.45, 1.51 and 1.61 (4s, 4 x 6H, CH_3), 1.97-2.09 (m, 2H, $CH_2\underline{CH_2}CH_2SH$), 2.61-2.69 (m, 2H, $CH_2CH_2\underline{CH_2}SH$), 2.77–2.81 (m, 1H, SH), 3.21-3.27 (m, 2H, $\underline{CH_2}CH_2CH_2SH$), 4.19 (ddd, $J_{4'\text{-}5'}$= 1.7, $J_{5'\text{-}6'a}$=6.5, $J_{5'\text{-}6'b}$= 8.2, 2H, H-5'), 4.32-4.36 (m, 4H, H-2', H-4'), 4.50-4.52 (m, 4H, H-6'a, H-6'b), 4.63 (dd, $J_{2'\text{-}3'}$= 7.9, $J_{3'\text{-}4'}$= 2.4, 2H, H-3'), 5.54 (d, $J_{1'\text{-}2'}$= 5.0, 2H, H-1').

^{13}C NMR (75 MHz, $CDCl_3$): δ 23.5 ($CH_2CH_2\underline{CH_2}SH$), 24.6, 25.1, 26.1 and 26.2 (Me-isop), 28.9 ($CH_2\underline{CH_2}CH_2SH$), 33.3 ($\underline{CH_2}CH_2CH_2SH$), 65.6 (C-5'), 66.5 (C-6'), 70.7 (C-3', C-2'), 70.8 (C-4'), 96.4 (C-1'), 108.9, 109.7 (Cq-isop), 170.6 (C-4, C-6), 185.0 (C-2).

HRMS-ESI:*m/z* calculated for $C_{30}H_{46}N_3O_{12}S_2$ $[M+H]^+$: 704.2523, found: 704.2510. *m/z* calculated for $C_{30}H_{45}N_3O_{12}S_2Na$ $[M+Na]^+$: 726.2342, found: 726.2333.

*Synthesis of protected galactodendritic porphyrin (**protectedPorGal$_8$**)*

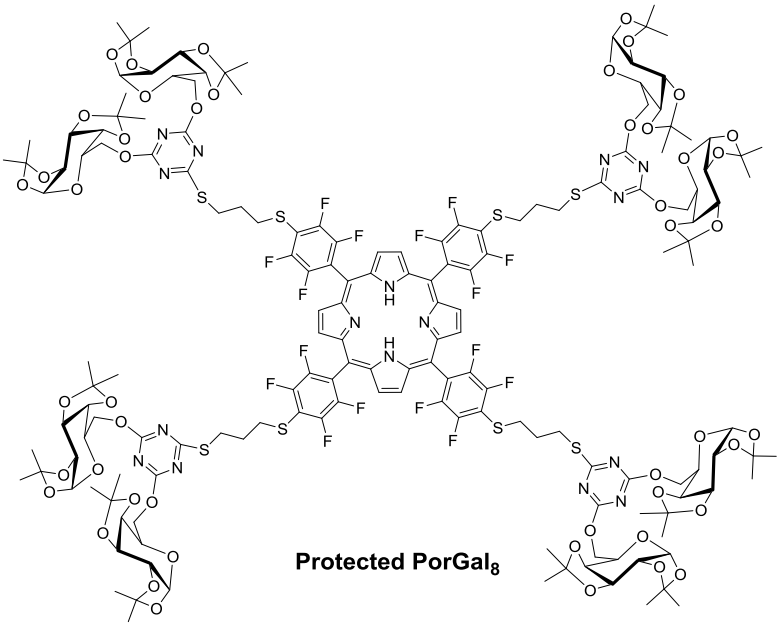

The **protectedPorGal$_8$** was synthesized as previously described in the literature [1]. Under N_2, **TPPF$_{20}$** (50.0 mg, 51.3 µmol) was dissolved in dimethylformamide (DMF).

DIPEA (0.9 mL, 5.13 mmol) and compound **2** (155.0 mg, 0.22 mmol) were added and the mixture stirred at 40 ºC during 24 h.

After co-evaporation of DMF with toluene, the residue was purified by column chromatography (light petroleum/ethyl acetate/dichloromethane (CH_2Cl_2)/acetone, 6:1:2:1 to 4:1:2:1 v/v). The eluent was evaporated to dryness under reduced pressure and the solid was dissolved in $CH_2Cl_2$and precipitated with light petroleum affording **protectedPorGal$_8$** (148.4 mg, 78%) as a red solid.

^{1}H NMR (300 MHz, $CDCl_3$): δ -2.88 (brs, 2H, NH), 1.31 and 1.34 (2s, 2 x 24H, CH_3), 1.47 (m, 24H, CH_3,), 1.52 (s, 24H, CH_3), 2.30 (q, *J*= 6.9, 8H, $SCH_2\underline{CH_2}CH_2SPor$), 3.40-3.49 (m, 16H, $S\underline{CH_2}CH_2\underline{CH_2}SPor$), 4.23 (ddd, $J_{4'\text{-}5'}$= 1.5, $J_{5'\text{-}6'a}$= 6.4, $J_{5'\text{-}6'b}$= 8.0, 8H, H-5'), 4.34 (dd, $J_{1'\text{-}2'}$= 5.0, $J_{2'\text{-}3'}$= 2.4, 8H, H-2'), 4.37 (dd, $J_{3'\text{-}4'}$= 7.9, $J_{4'\text{-}5'}$= 1.5, 8H, H-4'), 4.56-4.58 (m, 16H, H-6'a, H-6'b), 4.64 (dd, $J_{2'\text{-}3'}$= 2.4, $J_{3'\text{-}4'}$= 7.9, 8H, H-3'), 5.55 (d, $J_{1'\text{-}2'}$= 5.0, 8H, H-1'), 8.94 (brs, 8H, pyrrolic β-H).

^{19}F NMR (282 MHz, $CDCl_3$): δ -160.2 (q, $J_{o\text{-}m}$= 12.5, 8F, F-*ortho*), -157.4 (q, $J_{o\text{-}m}$ = 12.5, 8F, F-*meta*).

^{13}C NMR (75 MHz, $CDCl_3$): δ 24.6, 25.1, 26.1 and 26.2 (Me-isop), 29.0 ($S\underline{CH_2}CH_2CH_2SPor$), 29.5 ($SCH_2\underline{CH_2}CH_2SPor$), 33.6 ($SCH_2CH_2\underline{CH_2}SPor$), 65.6 (C-5'), 66.6 (C-6'), 70.7 (C-3', C-2'), 70.8 (C-4'), 96.4 (C-1'), 108.9, 109.7 (Cq-isop), 119.9, 120.4 and 134.7 (C-Por), 145.4, 148.3, 148.5 and 149.6 (C-Por, C-F), 155.1 (C-Por), 170.7 (C-4, C-6), 184.8 (C-2).

HRMS-ESI:*m/z* calculated for $C_{164}H_{188}F_{16}N_{16}O_{48}S_8$ $[M+2H]^{2+}$: 1854.5103, found: 1854.5131.

UV-Vis in DMSO λ_{max}(log ε): 412 (4.31), 508 (3.14), 582 (2.78), 656 (1.12).

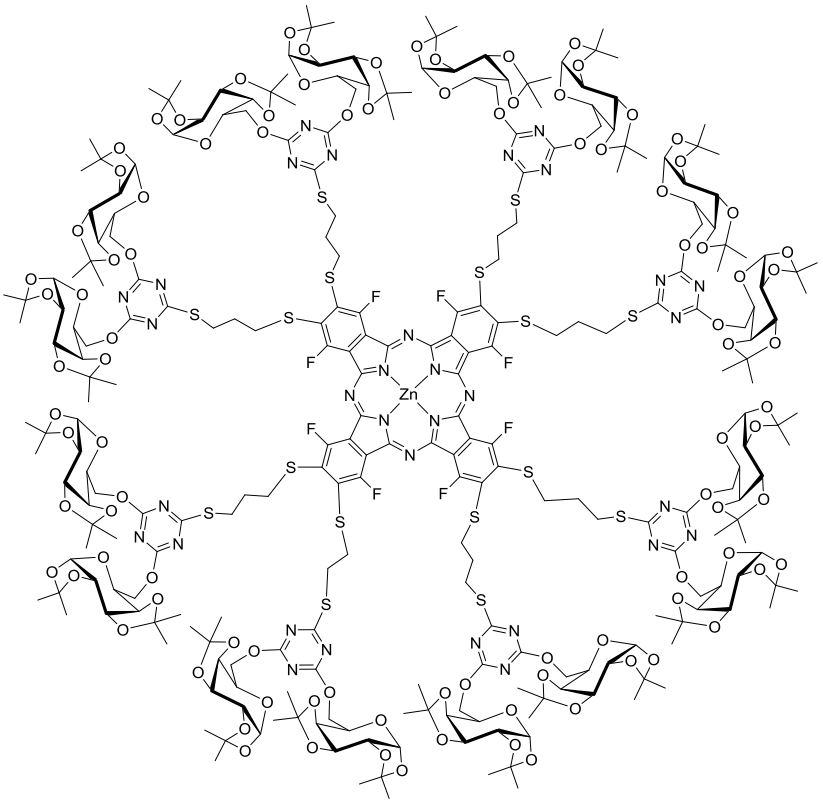

Protected PcGal$_{16}$

*Synthesis of protected galactodendritic phthalocyanine (**protectedPcGal$_{16}$**)*

The **protectedPcGal$_{16}$** was synthesized as previously described in the literature [1]. The synthesis and characterization of **protectedPcGal$_{16}$** were performed by Doctor Sandrina Silva, postdoc student, in the laboratory of Doctor João Tomé, Department of Chemistry – University of Aveiro, Aveiro, Portugal.

*Synthesis of **ChlF$_{20}$***

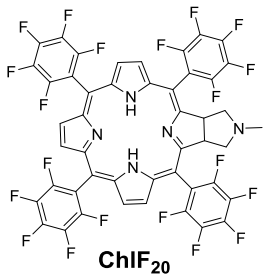

ChlF$_{20}$

The **ChlF$_{20}$** was synthesized as previously described in the literature [2, 3]. Under N_2, the commercially available **TPPF$_{20}$** (100 mg, 102.6 µmol) was dissolved in dry toluene. *N*-methylglycine (20

mg, 224.5 µmol) and paraformaldehyde (17 mg, 566.1 µmol) were added and the mixture was heated at reflux for 5 h. After evaporation of toluene, the residue was purified by column chromatography (light petroleum/ethyl acetate, 9:1 to 7:3 v/v). The eluent was evaporated to dryness under reduced pressure and the solid was dissolved in CH_2Cl_2 and precipitated with hexane affording **ChlF$_{20}$** (74 mg, 70%) as a green solid.

^{1}H NMR (300 MHz, $CDCl_3$): δ -1.82 (s, 2H, NH), 2.21 (s, 3H, N-CH_3), 2.46-2.67 (m, 2H, H-pyrrolidine), 3.06-3.22 (m, 2H, H-pyrrolidine), 5.16-5.33 (m, 2H, *β*-H [C (sp^3)]), 8.39 (d, 2H, *J*=4.9Hz, pyrrolic *β*-H), 8.48 (s, 2H, pyrrolic *β*-H), 8.71 (d, 2H, *J*=4.9Hz, pyrrolic *β*-H).

^{19}F NMR (282 MHz, $CDCl_3$): δ -161.39 to -161.78, -162.72 to -162.78 (2m, 8F, F-*meta*), -152.66 to -153.01 (m, 4F, F-*para*), -136.62 to -138.17, -138.25 to -138.63 (2m, 8F, F-*ortho*).

*Synthesis of protected galactodendritic chlorin (**protectedChlGal$_8$**)*

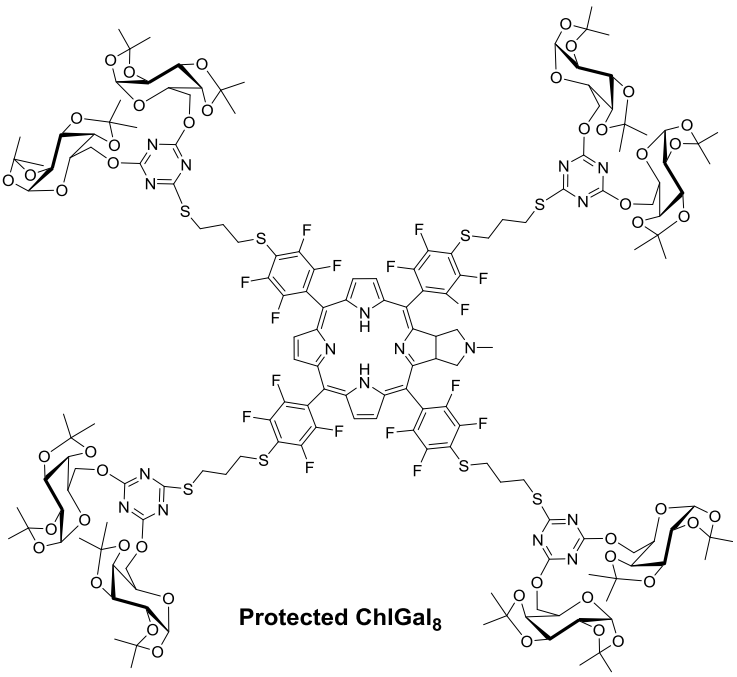

The conjugation of **ChlF$_{20}$** with galactodendritic unit was performed as previously described for **PorGal$_8$** described in the literature [1]. Under N_2, **ChlF$_{20}$** (70.0 mg, 67.85 µmol) was dissolved in DMF. DIPEA (3.0 mL, 166.9 mmol) and compound **2** (215.0 mg, 0.304 mmol) were added and the mixture stirred at 40ºC during 44 h. After co-evaporation of DMF with toluene, the crude was dissolved in CH_2Cl_2, neutralized with an aqueous solution of sodium bicarbonate ($NaHCO_3$) and the organic layer was washed with water (H_2O) and dried under diminished pressure. Then, the mixture was concentrated and submitted to column chromatography (hexane/ethyl acetate/ CH_2Cl_2/acetone, 6:1:2:1 to 4:2:2:1 v/v). The eluent was evaporated to

dryness under reduced pressure and the solid was dissolved in CH_2Cl_2 and precipitated with light petroleum affording **protected ChlGal$_8$** (164.0 mg, 70%) as a dark-green solid.

^{1}H NMR (300 MHz, $CDCl_3$): δ -1.78 (s, 2H, NH); 1.32 e 1.34 (2s, 2 x 24H, CH_3); 1.46 (s, 24H, CH_3); 1.52 (s, 24H, CH_3); 2.20 (s, 3H, N-CH_3); 2.26 (q, *J*=6.2 Hz, 8H, $SCH_2\underline{CH_2}CH_2SChl$); 2.52-2.62 (m, 2H, H-pyrrolidine); 3.07-3.17 (m, 2H, H-pyrrolidine);3.34-3.49 (m, 16H, $S\underline{CH_2}CH_2\underline{CH_2}SChl$); 4.22 (td, $J_{5'\text{-}6á}$= $J_{5'\text{-}6'b}$= 6.5Hz, $J_{5'\text{-}4'}$ = 1.6Hz, 8H, H-5´); 4.33 (dd, J2'-3' = 2.4 Hz, J2'-1' = 5.0 Hz, 8H, H-2'); 4.37 (dd, $J_{4'\text{-}3'}$ = 8.0 Hz, $J_{4'\text{-}5'}$ = 1.6 Hz, 8H, H-4'); 4.50-4.58 (m, 16 H, H-6´a and H-6´b); 4.64 (dd, J3'-2' = 2.4 Hz, J3'-4' = 8.0 Hz, 8H, H-3´); 5.25-5.34 (m, 2H, *β*-H [C (sp^3)]); 5.54 (d, $J_{1'\text{-}2'}$= 5.0 Hz, 8H, H-1´); 8.41 (d, 2H, *J*=4.9Hz, pyrrolic *β*-H); 8.51 (s, 2H, pyrrolic *β*-H); 8.73 (d, 2H, *J*=4.9Hz, pyrrolic *β*-H).

^{19}F NMR (282 MHz, $CDCl_3$): δ -156.1 to -156.2 and -156.6 to -156.7 (2m, 4F, F-meta); -157.4 to -157.6 (m, 4F, F-meta); -159.0 to -159.2 and -160.4 to -160.6 (2m, 6F, F-orto); -161.0 to -161.1 (m, 2F, F-orto).

^{13}C NMR (75 MHz, $CDCl_3$):δ 22.9,24.6, 25.1, 26.1, 26.2 , 29.0, 29.5,29.8; 32.1,33.6, 65.6, 66.6, 70.6, 70.7, 70.8, 96.4, 108.9, 109.7, 128.2, 135.1, 140.1, 145.0, 146.0, 145.8, 147.8,170.7, 184.7.

HRMS-ESI:*m/z* calculated for $C_{167}H_{194}F_{16}N_{17}O_{48}S_8/3$ $[M/3 + H]^+$ 1256,36670, found 1256.36755. *m/z* calculated for $C_{167}H_{194}F_{16}N_{17}O_{48}S_8/2$ $[M/2 + H]^+$ 1884.04605, found 1884,05136.

General procedure for the cleavage of the isopropylidene acetals of the ***protectedPorGal$_8$, protected PcGal$_{16}$*** *and* ***protected ChlGal$_8$***

A suspension of galactose-conjugated porphyrinoids was stirred in a mixture of trifluoroacetic acid (TFA)/H_2O (9:1 v/v) at room temperature during 5 h. The mixture was then neutralized with aqueous potassium carbonate (K_2CO_3) and the product was purified by reverse phase column chromatography using a gradient of H_2O and tetrahydrofuran (THF) as eluent. The desired compound was precipitated, filtered, washed and dried under reduced pressure.

Synthesis of ***PorGal$_8$***

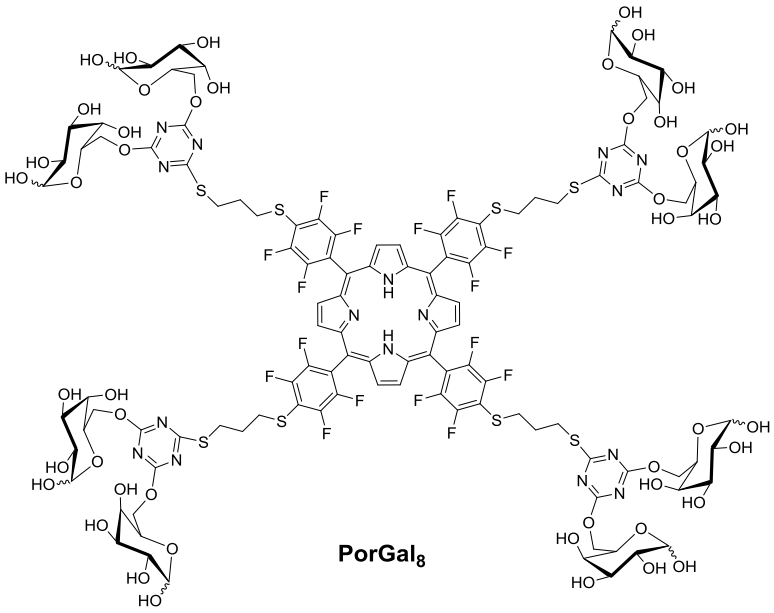

PorGal$_{16}$ was synthesized as previously described in the literature [1].According to the aforementioned general procedure, **protected PorGal$_8$** (35.0 mg, 9.43 μmoL) was treated with 3 mL of TFA/H_2O (9:1 v/v). After neutralization with the aqueous solution of K_2CO_3 and reverse phase column chromatography, **PorGal$_8$** was precipitated with CH_2Cl_2, filtered, washed, with acetone and dried under reduced pressure (23.2 mg, 80%).

^{1}H NMR (300 MHz, DMSO-d_6):δ -3.20 (brs, 2H, NH), 2.19–2.32 (m, 8H, $SCH_2\underline{CH_2}CH_2SPor$), 3.64-3.92 (m, 16H, $S\underline{CH_2}CH_2\underline{CH_2}SPor$), 4.17–4.51 (m, 24H, H-5', H-2', H-4'), 4.61-4.82 (m, 16H, H-6'a, H-6'b), 4.93–4.99 and 5.17 – 5.28 (2m, 8H, H-3'), 6.29–6.36 (m, 4H, H-1'α), 6.65-6.76 (m, 4H, H-1'β), 9.41 (brs, 8H, pyrrolic β-H).

^{19}F NMR (282 MHz, DMSO-d_6): δ -162.8 to -162.7 (m, 8F, F-*ortho*), -158.1 to -158.0 (m, 8F, F-*meta*).

HRMS-ESI:*m/z* calculated for $C_{116}H_{122}F_{16}N_{16}O_{46}S_8$ $[M+2H-2OH]^{2+}$: 1517.2605, found: 1517.2562. *m/z* calculated for $C_{116}H_{123}F_{16}N_{16}O_{47}S_8$ $[M+2H-OH]^{2+}$: 1525.7618, found: 1525.7622. *m/z* calculated for $C_{116}H_{124}F_{16}N_{16}O_{48}S_8$ $[M+2H]^{2+}$: 1534.2632, found: 1534.7648. *m/z* calculated for $C_{116}H_{123}F_{16}N_{16}O_{48}S_8Na$ $[M+H+Na]^{2+}$: 1545.2542, found: 1545.2570.

UV-Vis in DMSO λ_{max} (log ε): 415 (5.24), 505 (4.20), 575 (3.80), 655 (2.00).

Synthesis of ***PcGal$_{16}$***

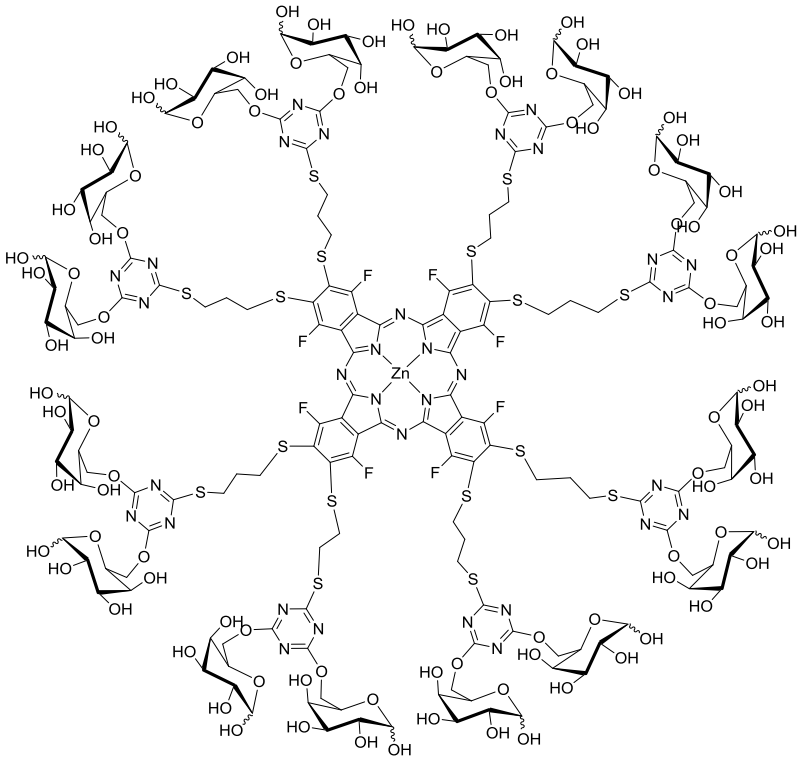

PcGal$_{16}$

PcGal$_{16}$ was synthesized as previously described in the literature [1]. The synthesis and characterization were **PcGal$_{16}$** was performed by Doctor Sandrina Silva, postdoc student, in the laboratory of Doctor João Tomé, Department of Chemistry – University of Aveiro, Aveiro, Portugal.

Synthesis of ***ChlGal$_8$***

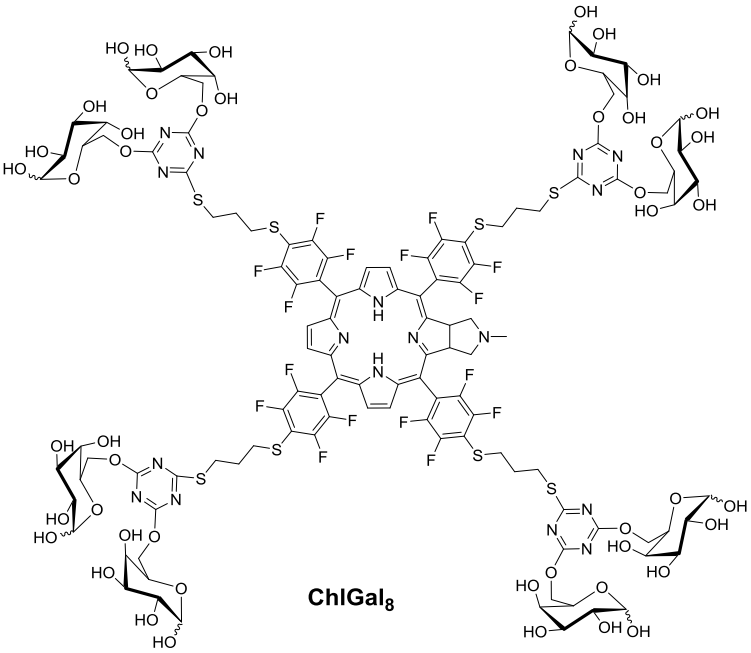

ChlGal$_8$

According to the aforementioned general procedure, **protected ChlGal$_8$** (103.1 mg, 27.37 µmoL) was treated with 10 mL of TFA/H_2O (9:1 v/v). After neutralization with the aqueous solution of K_2CO_3 and reverse phase column chromatography, **ChlGal$_8$** was precipitated with

methanol/CH_2Cl_2, filtered, washed, with acetone and dried under reduced pressure (74.4 mg, 87%).

^{1}H NMR (300 MHz, DMSO-d_6):δ -2.01 (s, 2H, NH); 2.04 (s, 3H, N-CH_3); 2.33-2.49 (m, 8H, $SCH_2\underline{CH_2}CH_2SChl$); 2.70-2.76 (m, 2H,H-pyrrolidine); 3.04-3.14 (m, 2H, H-pyrrolidine); 3.37-3.49 (m, 16H, $S\underline{CH_2}CH_2\underline{CH_2}SChl$);3.50-4.13 (m, 16H, H-5', H-2'); 4.31-4.57 (m, 8H, H-4'); 4.62-5.14 (m, 16H, H-6'a, H-6'b); 5.16-5.63 (m, 8H, H-3'); (m, 8H, H-1'α, H-1'β); 8.75 (d, 2H, *J*=4.0Hz, pyrrolic *β*-H); 8.82 (s, 2H, H pyrrolic *β*-H); 9.16 (d, 2H, *J*=4.0Hz, pyrrolic *β*-H).

^{1}H NMR (300 MHz, DMSO-d_6): δ-155.3 to -155.8 and -156.0 to -156.7 and -156.8 to -157.2 and -157.7 to -158.3 (4m, 8F, F-meta); -160.4 to -161.1and -162.1 to -162.5 and -162.9 to -163.3 (3m, 8F, F-orto).

HRMS-ESI:*m/z* calculated for $C_{119}H_{130}F_{16}N_{17}O_{48}S_8$ $[M/2 + H]^+$ 1563.2938, found 1563.2934.

UV-Vis in DMSO λ_{max} (log ε): 411 (4.41), 505 (3.14), 530 (2.32), 597 (2.75), 650 (3.83).

B. Synthesis of porphyrin C3-galactose and porphyrin C1-galactose

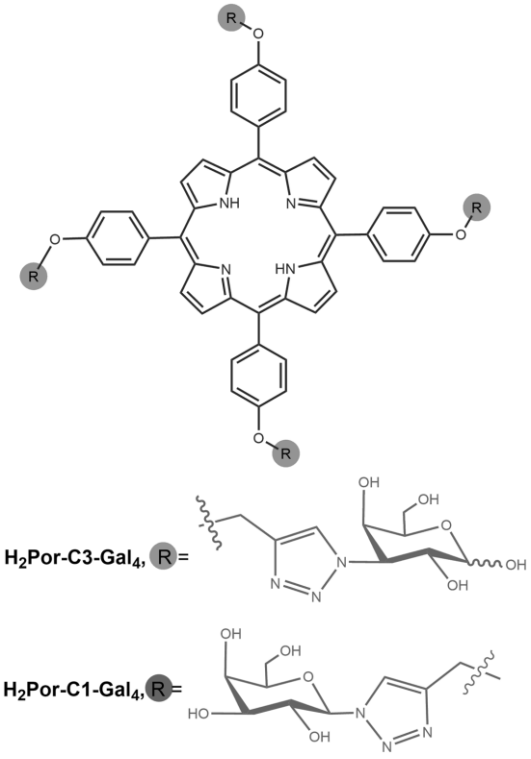

Por-C3-Gal$_4$ and **Por-C1-Gal$_4$** were synthesized and characterized by Doctor Dinesh Bhupathiraju (postdoc student) and Waqar Rizvi (PhD student) in the laboratory of Professor Charles Michael Drain, Department of Chemistry – Hunter College of CUNY, New York, United States.

9.2 Photo -physical and -chemical assays of galactose-conjugates

9.2.1 Equipment and reagents

A. General instrumentation

Equipment and material for the UV-Visible absorbance and fluorescent measurements

The fluorescence assays were performed on FluoroMax-3 spectrofluorimeter from Horiba Jobin Yvon.The data acquisition and post processing/analysis were performed using its software DataMax.The UV-visible assays were performed on the UVIKON 922 spectrophotometer from Biotek Instruments.

Equipment for irradiation assays

The illumination system used to determine the photostability and $^1O_2$ generation of PSs was the Light Source Model Lc-122 from Lumacare, equipped with a halogen/quartz 250 W lamp coupled to the selected interchangeable optic fiber probes (400-800 nm or 620-750 nm). The fluence rates were determined with the energy meter Coherent FieldMaxII-Top with a Coherent PowerSens PS19Q energy sensor. Alternatively, a LEDs array system emitting red light (600-800 nm with maximum emission at 700 nm) was also used in the determination of $^1O_2$ generation.

Reagents, chemical products and buffers

Dimethyl sulfoxide (DMSO), *n*-octanol, dimethylformamide (DMF), 1,3-diphenylisobenzofuran (DPBF) were obtained from Sigma. Phosphate buffered saline (PBS) buffer was prepared in Milli-Q water at pH 7.60: 10 mM NaH_2PO_4, 70 mM Na_2HPO_4 and 145 mM NaCl. 5,10,15,20-tetraphenylporphyrin (TPP) was from Sigma.

The Human Serum Albumin (HSA) lyophilized powder, essentially protease free; ≥96% (agarose gel electrophoresis) was purchased from Sigma. The human galectin-1 lyophilized powder, recombinant, expressed in E. coli was obtained from Sigma.

B. Softwares

GraphPad Prism (v.5.00, GraphPad Software) was used for most of the displayed graphs and ChemDraw Ultra 12.00 from CambridgeSoft was the software used to draw the chemical structures. DataMax software was used to acquire fluorescence emission spectra.

9.2.2 Protocols

A. Aggregation assays

Principle

The aggregation behaviour of PSs in PBS buffer is studied at different concentrations by Lambert-Beer´s law plots, where the relation of absorbance and concentration is linear: $A = \varepsilon \; x \; b \; x \; c$. *A* is the absorbance, ε is the molar absorptivity of the compound ($L.mol^{-1}.cm^{-1}$), *b* is the length of the light path (cm) and *c* is the concentration of the compound in solution (mol/L).

Protocol

Stock solutions of the galactose-conjugates at a concentration of 20 mM were prepared in DMSO and stored in the dark at room temperature. The working solutions were freshly prepared prior to use, by diluting the stock solutions in PBS buffer with the concentration of DMSO being always inferior to 1% (v/v).

Two milliliters of working solutions (without air bubbles) was placed into quartz cuvettesand the absorbance was scanned for wavelengths between 300 to 900 nm.[2]The wavelengths of maximum absorption were determined and the molar absorptivity of the compounds was calculated by Lambert-Beer´s law after plotting the absorbance against the respective concentration.[3]

[2] The maximum absorbance was always inferior to 1.0, in all working solutions.

[3] It was considered that the length of the light path (*b*) is equal to 1 cm.

B. Fluorescence assays

Principle

The fluorescence quantum yields (Φ_F) of PSs can be calculated in DMF by comparison of the area below the corrected emission spectra (between 620 nm to 850 nm) using TPP as standard ($\lambda_{excitation}$ at 601 nm, Φ_f = 0.11 in DMF) [4]. For that, the following equation is used: $\Phi PS = \Phi TPP(F_{PS}/F_{TPP})(A_{TPP}/A_{PS})(n^2_{PS}/n^2_{TPP})$; F_{PS} and F_{TPP} are the fluorescence integral areas (under the fluorescence emission curves) of PS and TPP reference, respectively. A_{PS} and A_{TPP} are the absorbance of PS and TPP (near of 0.03 at 601 nm), respectively. n_{PS} and n_{TPP} are the refractive indices of solvents used for PS and TPP reference, respectively [5].

Protocol

PSs working solutions were freshly prepared in DMF to give absorbance near of 0.03[4] at 601 nm. The fluorescence emission spectra of PSs were measured between 620 to 850 nm, after excitation at 601 nm. The excitation and emission slits width were set at 2.0 nm. Using the DataMax software, the emission spectra were corrected and the area under the fluorescence emission curves was calculated.

C. Photostability assays

Principle

The photostability can be studied by monitoring the decrease of the absorbance of Soret and Q bands, after different times of irradiation with white light (400-800 nm) or red light (620-750 nm) delivered by an illumination system.

Protocol

Solutions of PSs were freshly prepared in PBS buffer (0.5% v/v DMSO) and kept in the dark at room temperature. The irradiation experiments were performed in magnetically stirred cuvette solutions (with 2 mL of sample) in a dark room, over a period of 30 min with white or red light (400-800 nm) at a fluence rate of 150 mW/cm^2. The absorbance of PSs was

[4] This condition minimizes reabsorption of radiation by the ground-state species.

determined before irradiation and at several periods of time after irradiation. The results were expressed as follows: Photostability (%) = (Abs at a given time of irradiation) / (Abs before irradiation.

D. Singlet oxygen assays

Principle

Singlet oxygen ($^1O_2$) can be qualitatively determined by a chemical method using 1,3-DPBF as $^1O_2$ scavenger. The yellow-colored DPBF reacts specifically with $^1O_2$ in a [4+2] cycloaddition reaction, being oxidized to the colorless o-dibenzoylbenzene (Figure 9.1). DPBF has an absorption maximum at 415 nm, thus it is possible to follow the ability of the PSs to generate $^1O_2$ by measuring the DPBF absorption decay, at this wavelength.

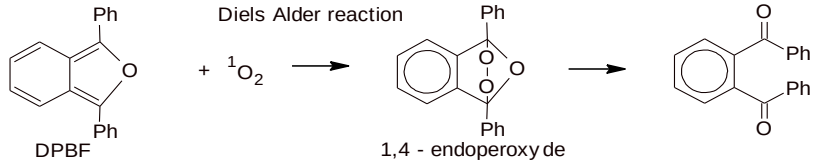

Figure 9.1 Reaction of diphenylisobenzofuran (DPBF) with singlet oxygen ($^1O_2$) by a Diels Alder reaction.

Protocol

Freshly prepared stock solutions of 50 µM DPBF, 10 µM of galactose-conjugates (DMF:H_2O; 9:1, v/v) were maintained in the dark at room temperature until use. Solutions containing DPBF with or without PSs were prepared in DMF:H_2O (9:1, v/v) in a quartz cuvette. The solutions were irradiated at room temperature and under gentle magnetic stirring. The breakdown of DPBF was monitored by measuring the decrease in absorbance at 415 nm at pre-established irradiation intervals. The results were expressed by plotting the DPBF depletion against the irradiation time. The depletion of DPBF was calculated as follows: $DPBF\ depletion = (Abs_t) / (Abs_0)$; Abs_0 and Abs_t are the absorbance values of DPBF at 415 nm before and after irradiation, respectively.

E. Human Serum Albumin and galectin-1 interaction assays

Principle

The interaction of the galactose-conjugates with HSA or galectin-1 proteins can be determined by measuring the intrinsic fluorescence quenching of tryptophan residues (excited at 280 nm) on the respective protein. If occurs interaction between conjugates and proteins, the binding constant (K_a) and the number of binding sites (n) can be determined by the following equation: *Trypthophan residues quenching (%)=(F0 – F)/(F0)x100*; *F0* and *F* are fluorescent intensities of tryptophan residues before and after addition of PS, respectively. K_a (binding constant) and n (number of binding sites) values were determined by plotting the *log((F0-F)/F)* against *log(PS concentration)*, giving a linear plot, where log(K_a) and n are the ordinate at the origin and slope, respectively [6].

Protocol

HSA was freshly prepared at a concentration of 2 μM in PBS buffer at room temperature. The concentration of galectin-1 was determined before the experiments by measuring the absorbance at 280 nm (ε_{Gal1} = 7 560 M^{-1} cm^{-1}, M = 14,000 g/mol) [7].

Two mL of protein solution at 2 μM was titrated with increasing concentrations of galactose-conjugates, keeping always the final concentration of DMSO to no more than 0.15% (v/v).[5] The fluorescence emission spectra of the protein´s tryptophan residues were acquired for the wavelength range between 300 nm to 450 nm upon excitation at 280 nm. The excitation and emission slits width were set at 2.0 nm. The fluorescence quenching curves were obtained by plotting the tryptophan residues quenching (in percentage) against conjugates concentration. The tryptophan residues quenching (in percentage) was calculated using the aforementioned equation.

The dissociation constants (K_D) of the galactose-conjugates to galectin-1 were calculated using the Boltzmann sigmoidal model of the program GraphPad Prism [8], according to the equation: $\Delta F=(B_{max}[PS])/(K_D+[PS])$; B_{max} is the maximal binding, and K_D is the concentration of PS required to reach half-maximal binding.

[5]Over a concentration range of 0-0.5% (v/v), DMSO did not quench HSA fluorescence.

F. Partition coefficients

Principle

The hydrophobic character of a drug can be measured experimentally by testing the drug´s relative distribution in an *n*-octanol/water mixture. Hydrophobic molecules will prefer to dissolve in the *n*-octanol layer of this two-phase system, whereas hydrophilic molecules will prefer the aqueous layer. The relative distribution is known as the partition coefficient (*P*) and it is obtained from the following equation: *P=(concentration of PS in octanol)/(concentration of PS in aqueous solution)*. Hydrophobic compounds have a high *P* value, whereas hydrophilic compounds have a low *P* value.

Protocol

The partition coefficient (*P*) of the galactose-conjugated PSs was measured in an *n*-octanol/PBS solvent system. The PSs were dissolved in a mixture of *n*-octanol/PBS (1:1 v/v) at a concentration of 15 μM, and the solution was shaken at room temperature. The two different phases formed were then separated by centrifugation (3 min at 3,000 *rpm*). The absorbance of the PS in each phase was determined and the concentration was calculated using molar absorptivity values. The partition coefficient value was then determined using the aforementioned equation.

9.3 *In vitro* biological assays

9.3.1 Equipment and common materials

A. General equipment

The centrifuge used was a SIGMA 2-16 and the microcentrifuge was a VWR MiniFuge Galaxy MiniStar C1413. The vortex was from VWR. The liquid aspirator system used was the Vacusip from Integra. The shaker used was a standard analog shaker from VWR. Dounce homogenizer was from Thomas Scientific.

B. Equipment for the UV-visible absorbance and fluorescence measurements

The UV-visible absorbance measurements were performed on a microplate reader Synergy™ HT (Biotek Instruments) controlled by BioTek's Gen5™ Data Analysis Software. For **PorGal$_8$** and **ChlGal$_8$**, the fluorescence measurements were also performed on this equipment. For **PcGal$_{16}$**, the fluorescence measurements were performed using the IVIS Lumina XR system (Caliper Life Sciences) in combination with its Living Image Software. For **Por-C3-Gal$_4$** and **Por-C1-Gal$_4$**, the fluorescence measurements were performed using the microplate reader Gemini EM Microplate Spectrofluorometer.

C. Equipment for the cells irradiation

Studies with **PorGal$_8$** were performed using a LEDs array system. The LEDs were prepared by Mr. Cândido Casqueira, electromechanic technician of the Department of Chemistry of the University of Aveiro, and they were used in the irradiation assays. They were composed of a matrix of 24 x 16 LEDs which makes a total of 384 light sources emitting white light with two emission peaks ($\lambda = 450 \pm 20$ and $\lambda = 550 \pm 50$ nm).

The illumination system used for PDT with **PcGal$_{16}$** and **ChlGal$_8$** was the Light Source Model Lc-122 from Lumacare, equipped with a halogen/quartz 250 W lamp coupled with the optic fiber probe (400-800 nm).

For **Por-C3-Gal$_4$** and **Por-C1-Gal$_4$**, the OLED Lumiblade Brite FL300 wm Level 4 (OLEDWorks)emitting light 420-700 nm was used for the PDT experiments.

The fluence rates were determined with the energy meter Coherent FieldMaxII-Top with a Coherent PowerSens PS19Q energy sensor.

D. Equipment for the Western blotting

The Mini Protean electrophoresis system and the Mini Trans-Blot system were from Bio-Rad Laboratories. The tube roller SRT6D was from Stuart. The chemiluminescence detection system used was the Chemi Doc™ XRS from Bio-Rad controlled by the software Quantity One. The fluorescence detection system was the Infrared Imaging System (LI-COR Biosciences).[6]

E. Microscopes

The fluorescence microscopes were purchased from Leica Microsystems (Model DFC350) or Nikon Eclipse Ti fluorescent microscope. Confocal microscopes were from Zeiss (LSM 710, Carl Zeiss) or Molecular Devices (Nikon Eclipse Ti With Ultra High Speed Wavelength Source).[7]

F. Materials

Canted neck cell culture flasks 75 cm^2 with 0.2 µM vent cap were purchased from Corning. CyroPure tubes were purchased from SARSTEDT. The tissue culture testplates and the conical tubes of 15 mL or 50 mL were from Orange Scientific. Rubber spatulas, cell scrappers were purchased from Greiner Bio-One. The Coverslip Glasses with diameters of 5 mm were purchased from Warner Instruments. The Neubauer chamber was from VWR. The Immun-Blot PVDF membranes were purchased from Bio-Rad. The plates used were transparent (Orange Scientific) and black (Greiner Bio-One) 96-wells microtiter plates for the absorbance and fluorescence studies, respectively.

[6] Fluorescence detection was used to acquire data of Chapter VII.

[7] The fluorescence and confocal microscopes from Leica Microsystems and Zeiss, respectively, were used to acquire data of Chapters III and V. The fluorescence and confocal microscopes from Nikon Eclipse Ti and Molecular Devices, respectively, were used to acquire data of Chapter VII.

9.3.2 Cell culture and trypsins

The cancer cells lines were from American Type Culture Collection (ATCC®). UM-UC-3 (ATCC Number: CRL-1749™) and HT-1376 (ATCC Number: CRL-1472™), human bladder transitional cell carcinoma cell lines, have been isolated from urinary bladder of a male and a female Caucasian aged 58 years, respectively, with a grade 3 bladder carcinoma. HCT-116 (ATCC Number: CCL-247™), colorectal carcinoma, have been isolated from colon of an adult male. MDA-MB-231 (ATCC Number: HTB-26™) and MCF-7 (ATCC Number: HTB-22™), adenocarcinoma, were obtained from mammary gland/breast (derived from metastatic site: pleural effusion) of females aged 51 and 69 years, respectively. HeLa (ATCC Number: CCL-2™), adenocarcinoma, have been isolated from cervix of a female 31 years.

All batches of culture media were supplemented with 10% (v/v) heat-inactivated Fetal Bovine Serum (FBS) from Gibco, 100 U/mL penicillin, 100 µg/mL streptomycin and 0.25 µg/mL amphotericin B (Sigma). UM-UC-3 and HT-1376 bladder cancer cells were cultured in Eagle´s Minimum Essential Medium (EMEM; Corning) with 1.5 g/L sodium bicarbonate, non-essential amino acids, L-glutamine and sodium pyruvate. Alternatively, UM-UC-3 and HT-1376 cells were also cultured in Roswell Park Memorial Institute (RPMI)-1640 medium (Sigma) supplemented with 2 g/L sodium bicarbonate (Sigma), 2 mM L-glutamine (Sigma).[8] HCT-116 colon cancer cells, MCF-7 and MDA-MB-231 breast cancer cells were cultured in Dulbecco´s Modified Eagle´s Medium (DMEM, Sigma). HELA cervical cancer cells were cultured in DMEM (Corning) with 4.5 g/L glucose, and L-glutamine without sodium pyruvate. All cells were maintained at 37 ºC in a 5% CO2 humidified atmosphere.

Trypsin-EDTA 0.25% (w/v) and Trypsin Tryple Express were purchased from Gibco.

[8] Data demonstrated in Chapter VI was acquired using UM-UC-3 and HT-1376 cells growing in (RPMI)-1640 medium.

9.3.3 Proteins, molecular weight marker, antibodies and hsiRNA

Bovine Serum Albumin (BSA), the lyophilized albumin fraction V was purchased from Biochemical. The protein standard for the Western blotting assays was the Precision Plus Protein^{TM} Dual Color standard, containing ten protein bands (10, 15, 20, 25, 37, 50, 75, 100, 150, and 250 kDa) from Bio-Rad. The pool of three target-specific 20-25 nt GLUT1 hsiRNA, galectin-1 hsiRNA or caveolin-1 hsiRNA, transfection medium, transfection reagent were obtained from Santa Cruz Biotechnology.

Table 9.1 Primary antibodies used in the Western blotting and immunofluorescence assays.

Antibody	**Antigen Molecular Weight (kDa)**	**Dilution**		**Supplier**
		Western blotting (v/v)	Immunofluorescence (v/v)	
Rabbit anti galectin-1	14	1:1,000	1:100	Abcam
Mouse anti **β**-actin	43	1:20,000	___	Sigma-Aldrich
Mouse anti-Lamin B	68	1:100	___	Oncogene Research Products
Rabbit anti-GLUT1	50	1:1,000	1:250	Chemicon
Rabbit anti-Tom20	20	1:1,000	___	Santa Cruz Biotechnology
Rabbit anti ZO-1	225	1:250	___	Invitrogen Life Technologies
Mouse anti E-cadherin	120	1:1,000	1:100	BD Biosciences
Rabbit anti-phospho-caveolin-1	22	1:100	___	Abcam
Rabbit anti-caveolin-1	22	1:500	___	Abcam
Mouse anti-chathrin heavy chain	180	1:1,000	___	BD Biosciences
Mouse anti-EEA1	180	1:1,000	___	BD Biosciences
Mouse anti-Flotillin-1	47	1:1,000	___	BD Biosciences
Mouse anti-Ki-67	359	___	1:100	Santa Cruz Biotechnology

The horseradish peroxidase-conjugated secondary anti-rabbit (GAR-HRP) or anti-mouse (GAM-HRP) antibodies, used in the Western blotting assays (chemiluminescence detection), were purchased from Bio-Rad. The secondary anti-rabbit IRDye® 800CW (Western blot, fluorescence detection) was from LI-COR Biosciences.

The secondary anti-rabbit or anti-mouse antibodies, used in the immunofluorescence assays, were the Alexa Fluor 488 Goat Anti-Rabbit and Alexa Fluor 568 Goat Anti-Mouse, purchased from Molecular Probes.

9.3.4 KITS and probes

The Immun-Star™ WesternC™ Chemiluminescent Kit (containing the chemiluminescent substrate: luminol/enhancer and peroxide solution) used in the Western blotting assays (chemiluminescence detection) was from Bio-Rad.

The PierceBCA Protein Assay Kit-Reducing Agent Compatible (containing the BCA Protein Assay Reagent and BSA standards at 2 mg/mL) was purchased from Thermo Scientific.

The 4′,6-Diamidino-2-phenylindole (DAPI) was purchased from Enzo Life Sciences. The VectaSHIELD mounting medium with DAPI was purchased from VECTOR.

The 2´,7´-dichlorohydrofluorescin (H_2DCFDA) and dihydroethidium (DHE) were purchased from Life Sciences. MitoPY1 was from Sigma.

TRITC (tetramethylrhodamine isothiocyanate)-conjugated phalloidin was purchased from Sigma.

Glucose uptake cell-based assay kit was from Cayman Chemical and lactate assay kit (colorimetric) was from Sigma. CytoTox 96® Non-Radioactive Cytotoxicity Assay was from Promega.

DeadEnd Fluorometric terminal deoxynucleotidyltransferasedUTP nick end-labeling (TUNEL) System was obtained from Promega.

9.3.5 Buffers, reagents and chemical products

Sodium Chloride (NaCl), Triton X-100, formaldehyde (PFA) and sodium azide (NaN_3) extra pure were from Merck. Tris Base ULTROL Grade was from CalbioChem. Protease inhibitor cocktail tablets were purchased from Complete Mini.

Glycerol electrophoresis reagent, DL-dithiothreitol 99%, bromophenol blue salt solution, sodium dodecyl sulfate (SDS), ethylene glycol tetraacetic acid (EGTA), iodoacetamide (IAD), phenylmethanesulfonyl fluoride (PMSF), sodium deoxycholate (DOC), Tween 20, dimethyl sulfoxide (DMSO) Hybri-Max™, 3-[4,5-dimethylthiazol-2-yl]-2,5-diphenyl-tetrazolium bromide (MTT), ammonium persulfate, Tetramethylethylenediamine (TEMED) electrophoresis reagent, glycine, L-histidine, L-cysteine were purchased from Sigma. Agarose was obtained from MP Biomedicals.

The trypan blue stain 0.4% was from BioWhittaker Reagents, Lonza. The 2-propanol was from J.T.Baker BAKER ANALYZED™ A.C.S reagents. The methanol (MeOH) was from EMSURE, Merck. The hydrochloric acid (HCl) 37% was from Panreac.

The acrylamide/Bis 20% solution was from BIO-RAD. The ECL reagent was from Amersham Biosciences. The Glycergel was purchased from DAKO. Poly-L-lysine was from Sigma.

Sucrose, chlorpromazine, dynasore filipin, methyl-β-cyclodextrin and nystatin were from Sigma.

NADPH, cytochrome c, xanthine and xanthine oxidase were obtained from Merck.

Glutathione-reduced form (GSH), glutathione reductase (GR), EDTA, tert-butyl hydroperoxide (t-BOOH), imidazole, glutathione-oxidised form, 1-chloro-2,4-dinitrobenzene (CDNB) were from Sigma. Sulfosuccinimidyl-2-(biotinamido)ethyl-1,3-dithiopropionate (Sulfo-NHS-SS-biotin) and NeutrAvidin beads were from Pierce. MitoTEMPO was from Sigma.

Table 9.2 Buffers used in the biological studies. All buffers were prepared in Milli-Q water unless other solvent is mentioned.

	Buffer name	**Composition**	**pH**
	PBS buffer	137 mM NaCl, 27 mM KCl, 81 mM Na_2HPO_4, 15 mM KH_2PO_4	7.30
	1% SDS lysis buffer	1% (w/v) SDS , Prepared in PBS buffer	7.00
	RIPA buffer	150 mM NaCl, 50 mM Tris base, 5 mM EGTA, 1% (v/v) Triton X-100, 0.5% (w/v) DOC, 0.1% (w/v) SDS, 2 mM PMSF, 2 mM IAD, 1 tablet of protease inhibitor cocktail	7.50
	6x Laemmli buffer	350 mM Tris-HCl, pH 6.8, 30% (w/v) glycerol, 10% (w/v) SDS, 600 mM DTT, 0.012% (w/v) bromophenol blue	6.80
	1.5 M Tris-HCl buffer	1.5 M Tris base	8.80
	0.5 M Tris-HCl buffer	0.5 M Tris base	6.80
	Fixation buffer	4% (v/v) PFA, Prepared in PBS buffer	7.30
	Hypotonic buffer	10 mM NaCl, 1.5 mM $MgCl_2$, 10 mM Tris-HCl	7.50
Western blot	Running buffer	25 mM Tris base, 192 mM Glicyine, 0.1% (w/v) SDS	8.80-8.50
	Transfer buffer	25 mM Tris base, 192 mM Glycine, 20% (v/v) MeOH, 0.005% (w/v) SDS	8.00-8.50
	Tris Buffer Saline Tween20 (TBST) buffer	20 mM Tris base, 150 mM NaCl, 0.1% (v/v) Tween 20	7.60
	Blocking buffer	5% (v/v) non-fat milk or 3% (v/v) BSA, Prepared in TBST buffer	7.60
Immunofluorescence	Blocking buffer	5% (v/v) BSA or 1:10 (v/v) goat serum, Prepared in PBS buffer	
	Permeabilization buffer	1% (v/v) Triton X-100, 0.02% (w/v) BSA, 0.02% (w/v) NaN_3, Prepared in PBS	7.30
	PBS Triton X-100 (PBST) buffer	0.25% (v/v) Triton X-100, 1% (w/v) BSA, 0.02% (w/v) NaN_3, Prepared in PBS	7.3
	Washing buffer	0.02% (w/v) BSA, 0.02% (w/v) NaN_3, Prepared in PBS	7.3

9.3.6 Softwares

Paint Shop Pro™ (v.6.00, Jasc Software) was used for the treatment of the images obtained in microscopy.

ImageJ 1.42n (Wayne Rasband, National Institutes of Health, USA) was used for the quantification of the proteins expression on Western blotting assays.

GraphPad Prism (v.5.00, GraphPad Software) was used for most of the displayed graphs, as well as for the statistical analysis.

Optimas® image analysis software (Optimas, version 5.0) was used for spheroids characterization.

9.3.7 Statistical Analysis

The results are presented as mean ± standard deviation (S.D.) with n indicating the number of experiments. Statistical significance among two conditions was assessed using the nonparametric Mann-Whitney test. Statistical significance among three conditions was assessed by the nonparametric Kruskal-Wallis test. Statistical significance among several conditions was assessed with the Friedman test. P-value was considered at the 5% level of significance to deduce inference of the significance of the data.

9.3.8 Protocols

A. Monolayer cultures

Principle

Animal cell lines, obtained from certain cancer cells and from genetic engineering, under the appropriate nutrients and strict aseptic conditions grow and replicate in culture.

Protocol: Defrosting Cells

The human bladder carcinoma cell lines were frozen in 1 mL vials in liquid nitrogen. The vial content was thawed, as fast as possible, in 37 ºC water bath and transferred to 5 mL

of prewarmed cell culture medium. After centrifugation at 1,000 *g* during 5 min, appropriate aliquots of cell suspension were added to new 25 cm^2 or 75 cm^2 cell culture flasks. Cells grown in monolayer at 37 ºC in a humidified incubator gassed with 5% carbon dioxide (CO_2) and 95% air. The cells were not cultured for more than three months following resuscitation.

Protocol: Subculturing

The cell culture medium was removed from culture flasks by aspiration and discarded. The cell layers were rinsed with 5 mL of warm sterile PBS, in order to remove traces of serum which would inhibit the action of the trypsin. Cells were treated with 0.033 mL/cm^2 of trypsin. The trypsinization progress was monitored under an inverted microscope. Flasks were incubated at 37 ºC until the cells rounded up and the cell layer begun being dispersed.Cell culture medium (0.1 mL/cm^2) was added to inhibit further trypsin activity and the cells were dispersed by repeated pippeting over the surface bearing the monolayer.The cells suspensions were then centrifuged at 1,000 *g* for 5 min. The supernatant was removed, the cells were re-suspended in cell culture medium and appropriate aliquots of cells were added to new 25 cm^2 or 75 cm^2 culture flasks. Cells were examined carefully every day by eye on an inverted microscope, for signs of contamination and the cell culture medium was changed two or three times per week.

Protocol: Freezing Cells

Cells were stored frozen as stocks in liquid nitrogen using cell culture medium containing 10% (v/v) DMSO at a density of 2-4 x 10^6 cells/mL. Cells were also frozen at -80 ºC for short times. Cells were harvested in the same manner used for routine subculture. The cell pellet was re-suspended in cell culture medium to give a final concentration of about 3 x 10^6 cells/mL and 900 µL were aliquot into each sterile vial containing 100 µL of sterile DMSO. The cells were frozen in a -80 ºC freezer prior to transfer to liquid nitrogen.

B. Spheroid cultures

Principle

Cells that usually grow as monolayers can be cultured in three-dimensional structures. Cells growing in three-dimensional structures mimic the physiological environment of living organisms compared to conventional monolayer culture systems. There are several methods available for the generation of spheroids. In this work, spheroids were generated by growing cancer cell suspensions in agarose-coated 96 well plates [9, 10]. The agarose prevents the cells from attaching to the bottom of the wells, thereby increasing interactions with neighboring cells (Figure 9.2).

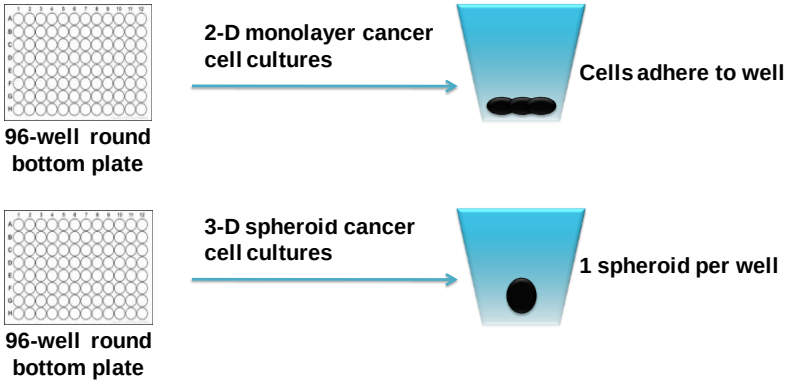

Figure 9.2 Schematic illustration of cells growing in monolayers or in spheroids.

Protocol: Spheroids culture

Spheroids culture were tried with HCT-116 colon cancer cells, MCF-7 and MDA-MB-231 breast cancer cells, UM-UC-3 bladder cancer cells and HeLa cervix cancer cells.[9] Agarose solution (1.5% w/v in PBS) was added to the wells of a 96-well microplate. Next, cells were seeded at densities ranging from 2,500 to 20,000 cells per well and the microplate was centrifuged for 15 min at 1,500 *g*. Clusters of cancer cells were observed after 24 h of seeding. For HCT-116, MCF-7, UM-UC-3 and HELA cancer cells, it took nearly 48 h for these clusters to form spheroids (*i.e.* clusters which are not dislodged by pipetting). MDA-MB-231 breast cancer cells did not form spheroids under these conditions for at least 72 h after cell seeding.

[9] Spheroid cultures were performed in the laboratory of Professor Charles Michael Drain, Department of Chemistry – Hunter College of CUNY, New York, United States.

Protocol: Spheroids volume and surface area

Images of spheroids were obtained at 24, 48 and 72 h after cell seeding using the image analysis system consisting of Nikon Eclipse Ti fluorescent microscope and an Andor iXon EMCCD camera. Volume and surface area were calculated using Optimas® image analysis software. The size of nearly 30 spheroids was calculated in each cell line [11] by measuring two orthogonal diameters (d1 and d2) using the line morphometry function. Volume was calculated using the formula $Volume=4/3\pi r^3$, where $r=1/2\sqrt{d1d2}$ is the geometric mean radius. Spheroids with volume ≈0.05 mm^3 were obtained 48 h after plating 5,000 HCT-116 cells per well, 15,000 MCF-7 cells per well, 20,000 UM-UC-3 cells per well and 20,000 HELA cells per well. These conditions were used to obtain spheroids for the determination of the doubling time, glucose utilization, lactate production, preparation of cells extracts, ROS determination, uptake and PDT assays.

Protocol: Spheroids average cell number

Average cell number per spheroid was determined at 24, 48 and 72 h after cell seeding by trypsinizing six spheroids, mixing the cell suspension with Trypan blue (Sigma) and counting the number of viable cells (details about trypan blue assay are described in cell viability assays section). The total number of cells obtained was divided by the number of spheroids trypsinized.

Protocol: Spheroids doubling times

The spheroid doubling times were determined by direct measurement of cell numbers, as described above. The spheroids were harvested at 24, 48 and 72 h after seeding cells in agarose-coated 96-well plate. Doubling times were determined using the formula: $N/N_0=e^{kt}$[12], where N is the cell number for a spheroid at a certain time (t) and N_0 is the corresponding cell number at time zero. The constant k was calculated for each spheroid by plotting $ln(N/N_0)vs.t$, between 24 and 72 h the period of time in which the cell growth rate was linear. The doubling time was then determined using the above formula and $N/N_0=2$.

Protocol: Spheroids glucose utilization and lactate production

Glucose utilization in monolayer and spheroid cultures was determined using the glucose uptake cell-based assay kit. The spheroids were obtained 48 h after plating cells in agarose-coated black, clear bottom 96-well plate. Monolayer and spheroid cultures were incubated in PBS for 2 h. The cultures were then incubated with 100 µg/mL of fluorescently-tagged glucose derivative 2-NBDG in PBS for 1 h. The supernatant was removed and cell cultures were washed with cell-based assay buffer. After removal of supernatant, 100 µL of cell-based assay buffer was added to each well and 2-NBDG taken up by cells was detected in a Gemini EM Microplate Spectrofluorometer with the excitation and emission filters set at 485 nm and 535 nm, respectively.

Lactate production in monolayer and spheroid cultures was determined using the lactate assay kit. The spheroids were obtained 48 h after plating cells in agarose-coated 96-well plate. After incubation of monolayer and spheroid cultures with PBS for 2 h, 50 µL of supernatant was collected to a new plate and mixed with 50 µL of master reaction mix (46 µL lactate assay buffer, 2 µL lactate enzyme mix, 2 µL lactate probe) during 30 min at room temperature. The lactate produced was detected by measuring the absorbance at 570 nm in a PowerWave HT Microplate Spectrophotometer.

Cells were lysed in 1% (w/v) sodium dodecyl sulfate solution in PBS (pH 7.0) and the protein concentration was determined by bicinchoninic acid reagent. Glucose consumed or lactate produced was normalized to protein concentration (details about protein determination are described in determination of intracellular photosensitizer concentration by fluorimetry section).

C. Preparation and treatment of cancer cells with photosensitizers

Principle

Cancer cells growing as monolayers of spheroids are treated with working sterile solutions of PSs.

Protocol: Preparing photosensitizers working solutions

Stock solutions of the PSs at a concentration of 2 mM were prepared in DMSO and stored at 0-4 ºC in dark conditions. Freshly working solutionswere prepared from the respective stock solution in sterile PBS, accounting their water solubility range. The concentration of DMSO was always lower than 0.45% (v/v), in all working solutions.

Protocol: Preparing cancer cell lines

Adherent cancer cells were detached with trypsin as described before. Cell culture medium was then added to inhibit trypsin activity and cells were dispersed by repeated pippeting up and down for 4 min. The cells suspensions were then centrifuged at 1,000 *g* for 5 min. For studies in monolayers, the cells were re-suspended in cell culture medium and seeded into cell culture plates (plates of 6, 12, 24, or 96-wells according to the experiment) at a density of 9.4 x 10^4 cells/cm^2 [10] and incubated overnight in an incubator at 37 ºC with 5% CO_2 and 95% air to promote cell adhesion. For studies in spheroids, three-dimensional cultures were obtained 48 h after platting 5,000 HCT-116 cells per well, 15,000 MCF-7 cells per well, 20,000 UM-UC-3 cells per well and 20,000 HELA cells per well in agarose-coated 96-well plates.

Protocol: Treatment of cancer cells with photosensitizers

After seeding the cells as monolayers or spheroids, the cell culture medium was removed and the cells were washed with PBS.[11] The cells were incubated in dark conditions at various periods of time with increasing concentrations of PSs in sterile PBS.

[10]The concentration of viable cells per milliliter of cell supession was calculated using the Trypan Blue Staining. Only cells with viability above 90% were used in all experiments. Details about trypan blue assay are described in cell viability assays section

[11] This washing step allows the elimination of serum proteins that are able to interact with the PSs.

D. Determination of intracellular photosensitizer concentration by fluorimetry

Principle

Taking into account the fluorescence properties of the PSs, their concentration inside cancer cells can be determined by fluorimetry (after cell lysis) and normalized to total protein quantity.

The concentration of proteins in a sample can be measured spectrophotometrically using the Bicinchoninic Acid Assay (BCA assay), also known as the Smith assay. The procedure involves two steps. The first is the biuret reaction, whose faint blue color results from the reduction of cupric ion (Cu^{2+}) to cuprous ion (Cu^{+}) by peptide bonds in protein, in an alkaline environment. Therefore, the amount of reduced Cu^{2+} is proportional to the amount of protein present in the solution. The second is the chelation of two molecules of BCA with one cuprous ion, resulting in an intense purple-colored product that strongly absorbs light at the wavelength of 562 nm. The BCA-copper complex exhibits a strong linear absorbance at 562 nm with increasing concentration of protein. The purple color can be measured at any wavelength between 550 and 570 nm with minimal loss of signal.

Protocol: Determination of intracellular photosensitizer fluorescence by fluorimetry

Cancer cells growing as monolayers or spheroids were incubated with PSs. After PSs uptake by cancer cells, cells were washed twice with PBS. Cells were mechanically scrapped in 130 µL of 1% (w/v) SDS solution in PBS (pH 7.0) and the plate was stirred on an automatic plate shaker in the dark at room temperature. One hundred µL of this cell suspension was transferred to 96-wells black plates and the intracellular fluorescence of the PSs was determined by fluorometric measurement (Table 9.3), using standard PSs solutions for calibration.

The PS concentration in the samples was directly obtained by plotting the average of the fluorescence for each PS standard in function of its concentration (µM).

Table 9.3 Equipments and filters used for determination of intracellular photosensitizer fluorescence by fluorimetry.

Compound	Equipment	$\lambda_{excitation}$ (nm)	$\lambda_{emission}$ (nm)
PorGal$_8$	microplate reader Synergy™ HT	360/40	645/40
ChlGal$_8$	microplate reader Synergy™ HT	360/40	645/40
PcGal$_{16}$	IVIS Lumina XR system	675	695-770
Por-C1-Gal$_4$	Gemini EM Microplate Spectrofluorometer	410	702
Por-C1-Gal$_4$	Gemini EM Microplate Spectrofluorometer	410	702

Protocol: Calculations

The PS uptake curves were obtained by non linear regression analysis (using GraphPad), accordingly to the following equation: *Uptake (nmol PS per mg of protein)= (B_{max}[PS])/(K_d+[PS]).* The B_{max} is the maximum extrapoled value of the PS uptake (nmol of PS per mg of protein) and K_d is the PS concentration needed to achieve a half maximum uptake at equilibrium.

Protocol: Determination of total protein

In a 96-wells plate, the following solutions were pipetted into each well:

- 25 µL of sample buffer: 1% (w/v) SDS in PBS (pH 7.0),

- 25 µL of sample, blank (sample buffer), standard (prepared in the sample buffer at concentrations ranging from 12.5-800 µg/mL using the BSA standard at 2 mg/mL),

- 200 µL of BCA working Reagent (50 parts of BCA reagent A mixed with one part of BCA reagent B).

The plate was incubated at 37 ºC for 30 min. Then, the absorbance at 570 nm was measured in the plate reader spectrophotometer. The protein concentration in the samples was directly obtained by plotting the average of the absorbance at 570 nm for each BSA standard in function of its concentration (µg/mL).

E. Determination of intracellular photosensitizer fluorescence by fluorescence microscopy

Principle

Based on the fluorescence properties of the porphyrin and phthalocyanine based PSs, their distribution inside the cells can be evaluated by fluorescence microscopy.

Protocol

Coverslips (three coverslips per well in 12-wells culture plates) were coated with poly-L-lysine (diluted 1:10, v/v, in sterile PBS) for 1 h at room temperature. The coverslips were allowed to dry completely at room temperature. The cells were plated for 24 h before treatment. After photosensitizer uptake and washing, cells were fixedwith 4% w/v PFA for 10 min at room temperature. The samples were washed with PBS (3 x 5 min). The coverslips were mounted using the VectaSHIELD mounting medium,[12] sealed with nail polish and stored at 4 ºC until visualization under the fluorescence microscope.

F. Photodynamic assays

Principle

The excitation of a potential PS (previously accumulated in cancer cells) with light at a specific wavelength induces cell toxicity, which is mediated by ROS generation. It is expected that, besides the preferential accumulation of the PS in cancer cells, they produce toxicity just after activation by light. Thus, it is important to evaluate both the PS toxicity in the absence of light and after light irradiation.

Protocol: Irradiation

After PSs incubation, the cells were washed twice with PBSand covered with 100 µL of fresh medium. In a dark room, the cells were irradiated for variable times with the desired light irradiation time (Table 9.4). After irradiation, cells were incubated for selected time points in the humidified incubator gassed with 5% CO_2 and 95% air.

[12] The mounting medium is applied on a slide and the coverslip with cells on top is added.

With **ChlGal$_8$**, a repeated PDT was performed 1.5 h after single photo-irradiation of the cells with red light at 2.5 mW/cm^2 for 40 min

Table 9.4 Light irradiation systems and conditions used during PDT assays.

Compound	Irradiation system	Potency (mW/cm^2)	Irradiation time (min)	PDT treatment
PorGal$_8$	white light with two emission peaks ($\lambda = 450 \pm 20$ and $\lambda = 550 \pm 50$ nm)	8.4	40	Single
ChlGal$_8$	Lumacare (> 500 nm)	2.5	40	Single Repetated (1.5 h dark period interval)
PcGal$_{16}$	Lumacare (620–750 nm	2.5	40	Single
Por-C1-Gal$_4$	OLED (420-700 nm)	0.44	30	Single
Por-C1-Gal$_4$	OLED (420-700 nm)	0.44	30	Single

G. Cell viability assays

- **MTT colorimetric assay**

Principle

3-[4,5-dimethylthiazol-2-yl]-2,5-diphenyl-tetrazolium bromide (MTT, yellow-colored) is added directly to the medium in the wells and incubated for 2-4 h. In living cells, MTT is reduced to an insoluble formazan (giving a blue purple colour), being this reduction proportional to the mitochondrial enzyme succinate dehydrogenase activity.

Protocol

The cells were treated with the photosensitizer and the photodynamic treatment was performed, as described before. Twenty four, 48, or 72 h after treatments, 50 µL of the medium was removed and 10 µL of MTT stock solution (3 mg/mL in PBS buffer) was added to each well at a final concentration of 0.5 mg/mL.The plates were thenwrapped in aluminium foil and incubated in the darkness at 37 ºC for 4 h. The resulting purple needle-shaped crystals were dissolved by the addition of 200 µL acidic isopropanol (0.04 M HCl in absolute isopropanol). To dissolve completely the converted dye, repetitive pipetting was applied and

the plate was stirred on an automatic plate shaker in the dark at room temperature. The absorbance was measured at 570 nm (using 620 nm as the background wavelength), in the plate reader spectrophotometer. The percentage of absorbance for each treated sample was normalized to that of the untreated control cells.

Calculations

For each well, the absorbance was expressed as: *Absorbance 570 nm – Abosrbance 620 nm*. The results were expressed as percentage of MTT reduction: *MTT reduction (%)=Absorbance treated wells/Absorbance control wells x 100*.

The IC_{50} values (*i.e.* concentration of PS that reduces cell survival by 50%) were calculated using non-linear regression analysis, sigmoidal dose-response curves (using GraphPad Prism) as shown in the equation below: $MTT\ reduction\ (\%)=Bottom+(Top-Bottom)/(1+10^{(logIC50-log[PS])Hillslope})$. *Bottom* represents the maximum value of response (maximum percent of MTT reduction) and *Top* is the minimum value of response (minimum percent of MTT reduction). The *log* IC_{50} is the log of the PS concentration ([PS]) that responses midway between *Top* and *Bottom*. The *Hillslope* is the steepness of the curve.

- **Trypan blue assay**

Principle

Trypan blue is an organic amine dye that is excluded by living cells with intact membranes, whereas dead or dying cells with compromised plasma membrane integrity take up the dye. Therefore, all the cells that exclude the dye are considered viable and appear brilliant under the microscope. By contrast, cells with damaged membranes appear with a distinctive blue color readily observed under the microscope.

Protocol

To check cell viability before plating the cells, they were trypsinized and resuspended in medium. Then, 20 µL of cell suspension and 20 µL of trypan blue stain were gently mixed, and the cells were counted using a haemocytometer. The percentage of viable cells and the

concentration of viable cells per milliliter of cell suspension were calculated. Only cells with viability above 90% were used in all experiments.

To check cell viability after PDT experiments, the cells were plated in 48-wells culture plates for 24 h before treatment. Next, the cells were treated with the photosensitizer and the photodynamic treatment was performed. Twenty four, 48, or 72 h after treatments, the cell suspension was diluted in the trypan blue stain and the cells were counted.

Calculations

Viable (bright cells) and nonviable cells (cells stained in blue) were counted and summed for the total number of cells. The viability was calculated as follows: *Viable cells(%)=Number of viable cells/Number of total cells x 100*. The concentration of viable cells per milliliter in the cell suspension was calculated considering the average of viable cells (*VCs*) per each counting square, the dilution made and the volume of each counting square:[13] $(Viable\ cells/mL)=(VCs \times dilution\ factor)/(1 \times 10^{-4})$.

- **TUNEL assay**

Principle

The photodynamic activation of PSs in cancer cells can trigger cell death pathways mediated by apoptosis. In many cell types, apoptosis is characterized by the generation of deoxyribonucleic acid (DNA) fragments through the activation of endogenous nucleases. The DeadEnd Fluorometric TUNEL System measures the fragmented DNA of apoptotic cells by catalytically incorporating fluorescein-12-dUTP and 3´-OH DNA ends using the Terminal Deoxynucleotidyl Transferase, Recombinant, enzyme (rTdT). The fluorescein-12-dUTP-labeled DNA can then be visualized using fluorescence microscopy.

Protocol

Cell death was detected by TUNEL assay, using the DeadEnd Fluorometric TUNEL System, according to the manufacturer´s instructions. Briefly, 24 and 72 h after PDT

[13] Considering the volume of each counting square to be 0.1 mm^3, the same as 1 x 10^{-4} mL.

treatment, bladder cancer cells were fixed in 4% (w/v) PFA and permeabilized with 0.2% v/v Triton X-100 in PBS solution. Cells were stained with TdT reaction cocktail for 60 min at 37 ºC. The nuclei were stained with DAPI and the cells were analyzed under a fluorescence microscope. TUNEL-positive DAPI-stained cells were counted in 10 randomly selected fields from three independent experiments. Percentage of dead cells was expressed as ratio of TUNEL-positive cell numbers to DAPI-stained cell numbers.

- **Lactate dehydrogenase assay**

Principle

Lactate dehydrogenase (LDH) is a soluble cytosolic enzyme which is released to the cell culture medium upon cell death due to damage of plasma membrane. The increase of the LDH activity is proportional to the number of lysed cells. The CytoTox 96® Non-Radioactive Cytotoxicity Assay is a colorimetric enzymatic assay which measures the release of LDH from damaged cells by combining lactate, Nicotinamide Adenine Dinucleotide (NAD+) and a tetrazolium salt (iodonitrotetrazolium violet, INT) as substrates in the presence of diaphorase to measure the absorbance at 490 nm of a red formazan product (Figure 9.3).

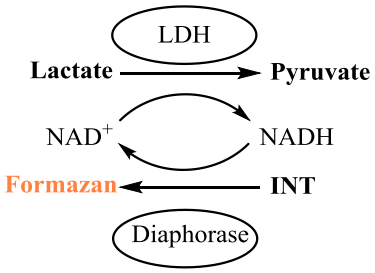

Figure 9.3 Schematic representation of Lactate dehydrogenase (LDH) activity assay using the CytoTox 96® Non-Radioactive Cytotoxicity Assay.

Protocol

The CytoTox 96® Non-Radioactive Cytotoxicity Assay measures LDH activity and it was used to determine cytotoxicity in spheroid cultures. Briefly, 50 µL of culture medium was collected from the 96-well plate containing cell spheroids and mixed with 50µl of the CytoTox 96® Reagent in dark for 30 min at room temperature. After incubation, 50µl of stop solution was added to each well and the absorbance was recorded at 490 nm using a microplate reader.

The average values of the culture medium background were subtracted from all values of experimental wells. The protein concentration was determined by Bicinchoninic Acid Assay[14]after scrapping spheroid cultures in 1% (w/v) SDS solution in PBS (pH 7.0); and LDH activity was normalized to protein concentration.

H. Antioxidant enzyme activities

Principle

As the induction of cell death by PDT is mediated by the production of ROS, the involvement of specific antioxidant enzymes in the detoxification of ROS and/or resulting toxic products can be measured by spectroscopy (Figure 9.4). Superoxide dismutase (SOD) catalyses the dismutation of superoxide radical anions into hydrogen peroxide and molecular oxygen. Hydrogen peroxide is then removed by catalase (CAT) when it is present at high concentrations or by glutathione peroxidase (GPox) when present at low concentrations. Glutathione reductase (GR) has an indirect antioxidant function of in the replenishment of gluthathione levels in reduced form (GSH) and glutathione S-transferase (GST) is involved in the elimination of reactive compounds through their conjugation with GSH.

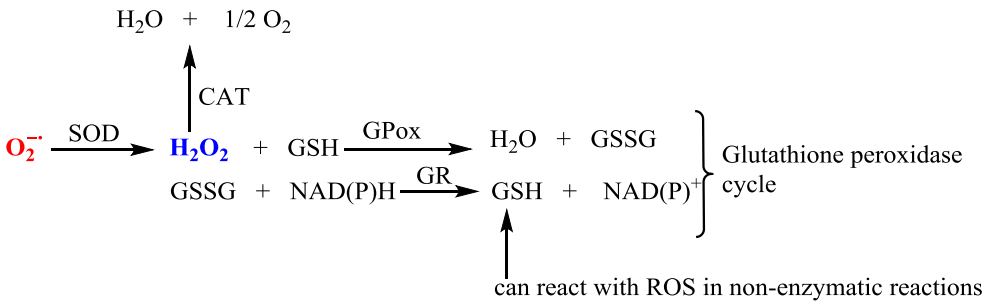

Figure 9.4 Schematic illustration of the involvement of specific antioxidant enzymes in the detoxification of ROS.

Protocol

Cell homogenates were obtained immediately after PDT and centrifuged at 10,000 g for 10 min at 4 ºC. The supernatants were used for measurements of glutathione peroxidase

[14]Details about protein determination are described in determination of intracellular photosensitizer concentration by fluorimetry section.

(GPox), glutathione reductase (GR), glutathione S-transferase (GST), superoxide dismutase (SOD) and catalase (CAT) activities in 96-well plates using a Biotek Synergy HT spectrophotometer. The activity was expressed as nmol of substrate oxidized per minute per mg of protein (mU/mg). The protein concentration was determined by Bicinchoninic Acid Assay.[15]

Glutathione peroxide (GPox) activity

GPox activity was determined at 30 ºC, measuring the NADPH oxidation at 340 nm. Supernatants were mixed with 1 mM of glutathione-reduced form (GSH), 0.5 U/mL GR, 0.18 mM NaDPH, 1 mM EDTA and 0.7 mM tert-butyl hydroperoxide (t-BOOH) in 50 mM imidazole at pH 7.4. The activity was calculated using the NADPH extinction coefficient of 0.62 m^2/mmoL.

Glutathione reductase (GR) activity

GR activity in cell supernatants was determined at 30 ºC by measuring the rate of NADPH oxidation at 340 nm in the presence of 3 mM glutathione-oxidised form, 0.12 mM NADPH, and 2.5 mM EDTA, in 50 mM Hepes (pH 7.4). The activity was calculated using the NADPH extinction coefficient of 0.62 m^2/mmoL.

Glutathione S-transferase (GST) activity

GST activity was determined at 30 ºC by monitoring the formation of GSH conjugate with 1-chloro-2,4-dinitrobenzene (CDNB) at 340 nm in the presence of 1 mM GSH and 1 mM CDNB in 50 mM Hepes (pH 7.4). The activity was calculated using the conjugate extinction coefficient of 0.96 m^2/mmoL.

Superoxide dismutase (SOD) activity

SOD activity was determined at 25 ºC measuring the cytochrome c reduction at 550 nm. The supernatants were mixed with 40 µM cytochrome c solution (0.05 M potassium

[15]Details about protein determination are described in determination of intracellular photosensitizer concentration by fluorimetry section.

phosphate, 0.5 mM EDTA, pH 7.8) containing 80 µM xanthine. To initiate the reaction, 2 U/mL xanthine oxidase was added. The increase in cytochrome c absorbance at 550 nm was recorded. SOD activity was calculated considering that one unit of SOD activity represents the inhibition of 50% in the rate of increase in absorbance at 550 nm when compared with control (sample without SOD under the conditions of the assay).

Catalase (CAT) activity

CAT activity was determined at 25 ºC by monitoring the rate of hydrogen peroxide (0.04% w/w) decomposition in 0.05 M potassium phosphate, pH 7.0. One unit of catalase activity was defined by the enzyme quantity that produced an absorbance reduction of 0.43 per minute at 240 nm in this system.

I. Transfection assays

Principle

Small interfering RNA (siRNA) also referred to as silencing RNA or short interfering RNA is used in the gene silencing technique to suppress gene expression (Figure 9.5). Typically consisting of 20-25 nucleotide double stranded RNA (dsRNA), siRNA is used to induce RNAi particularly in mammalian cells. Intracellular delivery of siRNA induces RNAi - a biological mechanism when siRNA molecules activate RNA-induced Silencing Complex (RISC). Guided by the antisense strand of the siRNA, RISC degrades the target mRNA thus inhibiting its translation.

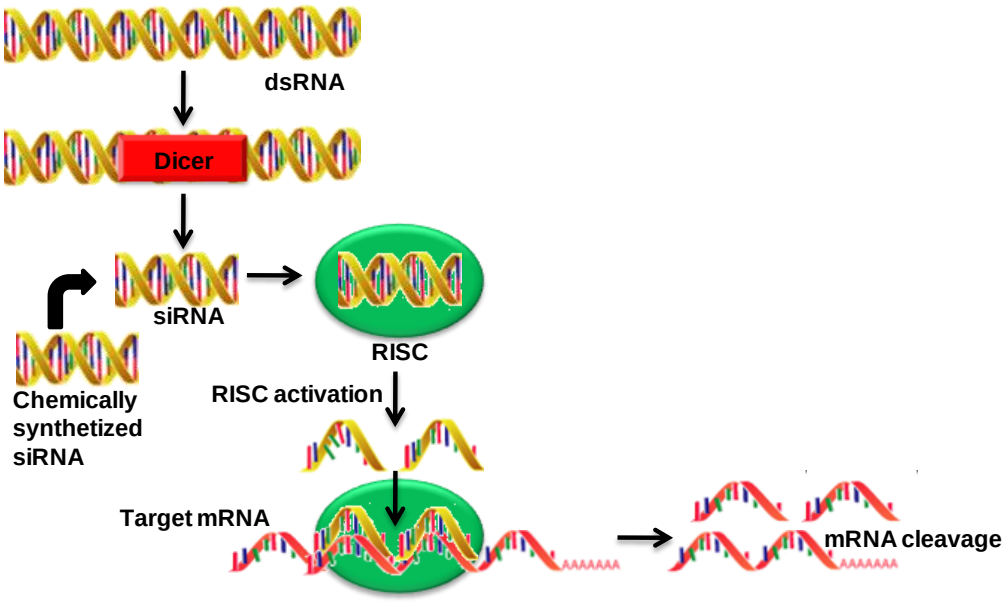

Figure 9.5 Schematic representation of transfection assays using small interfering RNA (siRNA).

Protocol

Galectin-1, GLUT1 or caveolin-1 were depleted in human bladder cancer cells using a pool of three target-specific 20-25 nt siRNA. UM-UC-3 bladder cancer cells were transfected in 6- or 96-well culture plates, at 60-80% confluence, with galectin-1 hsiRNA. HT-1376 bladder cancer cells were transfected in 6- or 96-well culture plates, at 60-80% confluence, with GLUT1 or caveolin-1 hsiRNA. Cells were also transfected with a scrambled siRNA in parallel as controls.

For each transfection, cells were treated for 5 h with 2.4 µM of siRNA in transfection medium containing 0.5 µL/cm^2 of transfection reagent. After incubation, complete media was added and the cells were incubated for 24, 48 or 72 h. Galectin-1 or GLUT1 downregulation was evaluated 24, 48 or 72h h post-transfection by Western blotting. The uptake and PDT experiments were performed 24 h post-transfection with GLUT1 hsiRNA, 48 h post-transfection with galectin-1 hsiRNA or caveolin-1 hsiRNA.

J. Intracellular levels of Reactive Oxygen Species after photodynamic assays

Principle

The ROS generation after PDT can be detected using the dichlorofluorescein (H_2DCFDA), dihydroethidium (DHE) and mitochondria peroxy yellow 1 (MitoPY1) probes, by fluorescence microscopy and fluorescence spectroscopy techniques. H_2DCFDA is able to cross the cell membrane and their acetate groups are removed by intracellular esterases, producing H_2DCF. H_2DCF reacts with several cytotoxic oxygen species producing DCF that can be used as a measure of intracellular ROS levels. DHE probe diffuses across cell membrane, exhibiting blue fluorescence. In the presence of ROS (particularly superoxide anion) this probe is oxidized to ethidium, which intercalates within the cell´s DNA, staining the nucleus with bright red fluorescence. MitoPY1 is a fluorescent probe used to detect mitochondrial ROS. The intracellular fluorescence of the probes was normalized to total protein quantity by Bicinchoninic Acid Assay.[16]

Protocol: Reactive oxygen species evaluation by fluorimetry

The cells were plated in 96-wells black plates. Immediately after photodynamic treatment and washings, cells were incubated with either 2 μM or 5 μM of H_2DCFDA, DHE or MitoPY1[17]in PBS (in dark conditions) for 1 h at 37°C. The excitation and emission filters used for the H_2DCFDA probe were 485/20 nm and 528/20 nm, respectively. For the DHE or MitoPY1 probes, the excitation and emission filters used were 485/20 nm and 590/35 nm, respectively. After fluorometric measurement, cells were lysed with 1% (w/v) SDS solution in PBS (pH 7.0) and total protein concentration was determined as previously described by Bicinchoninic Acid Assay.

Protocol: Reactive oxygen species evaluation by fluorescence microscopy

Coverslips were coated with poly-L-lysine (diluted 1:10, v/v, in sterile PBS) for 1 h at room temperature. The cells were plated carefully in 12-wells culture plates. The cells were

[16]Details about protein determination are described in determination of intracellular photosensitizer concentration by fluorimetry section

[17] H_2DCFDA and DHE were prepared in DMSO as stock solutions with a concentration of 5 mM, under a nitrogen atmosphere. The stock solutions were then kept in the dark at -20 ºC.

treated with the photosensitizer and the photodynamic treatment was performed. After PDT treatments, cells were incubated with 5 μM of ROS probe in PBS (in dark conditions) for 1 hour at 37°C. The cells were washed twice for 5 min each in PBS. After that, the cells were fixed in 4% w/v PFA for 10 min at room temperature. The samples were washed with PBS (3 x 5 min). The coverslips were mounted using the VectaSHIELD mounting medium, sealed with nail polish and stored at 4 ºC until visualization under the fluorescence microscope.

K. Redox quenching assays

Principle

The role of type I and type II oxidative mechanisms in cell toxicity after PDT, can be evaluated using specific quenchers of $^1O_2$ (sodium azide and histidine) and free radical scavengers (cysteine), respectively. MitoTEMPO can also be used as a specific scavenger of mitochondrial hydrogen superoxide.

Protocol

The cells were plated in 96-wells black plates for 24 h before treatment. Immediately after PS uptake, the cells were washed and the redox quenchers (sodium azide, histidine and cysteine at concentration of 50 nM or 10 μM MitoTEMPO) were added to the cells in growth culture medium. After incubation with the redox quenchers for 10 min, the photodynamic treatment (in the presence of the redox quenchers) was performed. The effect of the presence of quenchers on cell viability was evaluated 24 h after photodynamic therapy by the MTT viability assay.

L. Western blotting assays

Principle

The presence of specific proteins in a complex mixture extracted from cells can be studied by Western blotting using specific antibodies (Figure 9.6). Moreover, with this technique it is possible to quantify the levels of the proteins. For that, denaturated proteins present in the mixture are separated in a polyacrylamide gel by electrophoresis, accordingly to their size, following the methodology of Laemmli. Then, the separated proteins in the gel are

electrotransferred to a membrane using the method of Towbin and a specific unlabeled primary antibody is used to stain the target antigen. After wash, a labeled secondary antibody is used to detect the presence of the primary antibody, and thus the target protein. The proteins can be visualized as bands, using the ECL (enhanced chemiluminescence) or fluorescence detection methods. For ECL detection, the horseradish peroxidase (HRP), which is conjugated with the secondary antibody, in the presence of hydrogen peroxide and an enhancer, catalyzes the oxidation of luminol, emitting light. The emitted light can be detected using a CCD camera for light capture. For fluorescence detection, a secondary antibody coupled with a fluorescent dye is used.

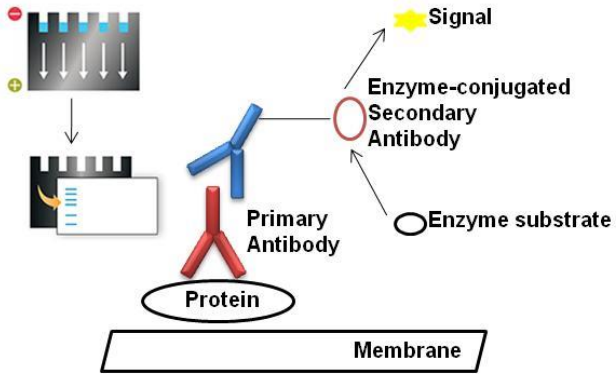

Figure 9.6 Schematic representation of Western blotting.

Protocol: Sample preparation

For immunodetection of proteins cells were plated in 6-wells culture plates before treatment. The cells were then treated with the photosensitizer and the photodynamic treatment was performed. After treatment, the cells were washed twice with ice-cold PBS and lysed by addition of ice-cold RIPA buffer with fresh protease inhibitors. The cell lysates were then transferred to microtubes with the help of a rubber policeman (cell scrapper) and incubated on ice during 30 min. During incubation, samples were vortexed 10 sec every 10 min.[18] The total cell lysates were centrifuged at 18,000 *g* for 16 min, at 4 ºC. The supernatant was transferred to a new microcentrifuge tube. The supernatants were used for protein concentration determination, followed by denaturation with Laemmli buffer.

[18] These vortex steps are important for the cell disruption.

Protocol: Determination of total protein

The protocol used for the determination of protein concentration was the same as described before, with some differences:

The samples were diluted in RIPA buffer 1:9 (v/v) and in a 96-wells plate, the following solutions were pipetted to each well:

- 25 µL of sample buffer: RIPA buffer,

- 25 µL of sample, blank (sample buffer), standard (prepared in the sample buffer at concentrations ranging from 12.5-800 µg/mL using the BSA standard at 2 mg/mL),

- 200 µL of BCA working Reagent (50 parts of BCA reagent A mixed with one part of BCA reagent B).

Protocol: Sodium Dodecyl Sulfate Polyacrylamide Gel Electrophoresis and Blotting

After determination of protein concentration, the samples were denaturated with 6x Laemmli buffer. The samples were heated at 37 ºC for 30 min, or boiled[19] during 5 min at 95 ºC. Protein samples (60 µg) was loaded on 8%, 10% or 12% polyacrylamide gels and the proteins were separated by electrophoresis. The electrophoresis was stopped when the dye front reached the bottom of the gel.

Following gel electrophoresis, the separated protein mixtures were transferred to a solid support for further analysis. The polyvinylidene difluoride membranes (PVDF) were first activated with 100% MeOH, and then soaked in Milli-Q water and equilibrated in transfer buffer. All the material used in the blotting (sponges, sheets of filter paper), as well as the gels were also equilibrated in transfer buffer. The gel and the PVDF membrane were assembled into a sandwich along with sheets of filter paper and sponges. The separated proteins were then transferred to the PVDF membranes (using ice cold transfer buffer) for 90 min under agitation, with the tank in ice (and using a cooling coil inside the tank). At the end, the baking of the membranes was performed by incubation at 50 ºC for 20 min.

[19] The samples should not be boiled when the analysis of GLUT1 protein is aimed due to the formation of GLUT1 aggregates after boiling.

Protocol: Antibodies incubations, detection and quantification

The membranes were placed into blocking buffer for 1 h at room temperature with gentle agitation. The membranes were incubated with the primary antibody (diluted in the blocking buffer) for 2 h at room temperature or overnight at 4 ºC, under low agitation. After incubation, the membranes were rinsed in TBST (3 x 10 min) at room temperature. The appropriate secondary antibody conjugated with the enzyme horseradish-peroxidase diluted 1:10,000 (v/v) or IRDye® 800CW 1:15,000 (v/v) in 2.5% (w/v) non-fat milk (prepared in TBST) was added, and the membranes were incubated for 1 h at room temperature, under moderate agitation. After incubation with the secondary antibodies, the membranes were washed in TBST (3 x 10 min), with agitation. To demonstrate equivalent protein loading, all the membranes were re-probed for the protein β-actin. For the detection using the secondary antibody conjugated with the enzyme horseradish-peroxidase, the membranes were placed on the chemiluminescence detection system[20] (proteins side up), incubated with the substrate solution (1:1, v/v, mixture of luminol/enhancer and peroxide buffer) for 1 min following manufacturer instructions, and then the images were acquired. For the detection using the secondary antibody IRDye® 800CW, membranes were imaged on the Odyssey Infrared Imaging System (proteins side down). The intensity signal of the bands was quantified using the software ImageJ 1.42q and the fold change in protein levels was expressed as follows and then normalized to the control situation: *Fold change in protein expression=Protein band intensity/β-actin band intensity*.

M. Immunocytochemistry assays

Principle

The distribution of specific proteins through the sample can be visualized by immunocytochemistry. First, the cells are fixed to retain their shape and structure (morphology) and location of all cellular proteins and to disable intrinsic proteolytic enzymes. The cells are then permeabilized with a mild detergent, so the antibodies could have access to the cytoplasm. After that, specific unlabeled primary antibody binds to the target molecule, and the secondary antibody (covalently attached to a fluorophore) recognizes the primary

[20] To prevent drying, the membranes were placed in a nylon transparent sheet.

antibody. At the end, the images can be obtained using a fluorescence microscope, showing the subcellular distribution of the protein of interest.

Protocol: Sample preparation, adherent cells

Coverslips were coated with poly-L-lysine (diluted 1:10, v/v, in sterile PBS) for 1 h at room temperature. Cells were plated in 12-wells culture plates before treatment. For the treatments with the PSs, the cells were treated and the photodynamic treatment was performed.

Protocol: Fixation, permeabilization, blocking and incubation with the antibodies

After washing with PBS, the cells were fixedin 4% w/v PFA for 10 min at room temperature. The samples were washed with PBS (3 x 5 min). The cells were treated with permeabilization buffer during 10 min. Then, the cells were washed with washing buffer, for 5 min. The cells were incubated with the blocking buffer for 30 min, in a humidified chamber. After blocking, the cells were incubated with the primary antibody diluted in PBST buffer during 1 h at room temperature, in a humidified chamber. The primary antibody solution was decanted and the samples were washed with washing buffer (3 x 5 min). The cells were incubated with the secondary antibody and DAPI (1 µg/mL) diluted in PBST buffer for 1 h (at room temperature) in a humidified chamber in the dark. The cells were washed in the dark three times with the washing buffer, 5 min each wash. The coverslips were mounted using the glycergel mounting medium and sealed with nail polish. The samples were stored in an appropriate box at 4 ºC until acquisition of images by fluorescence microscopy.

N. Endocytic inhibitors assays

Principle

Specific pathways of endocytosis involved in the uptake of PSs can be studied using pharmacological inhibitors that transiently block endocytic pathways. Uptake studies can be performed at 4 ºC and in the presence of NaN_3 to determine whether the uptake is an active process. Clathrin-dependent endocytosis can be inhibited using hypertonic sucrose and chlorpromazine [13]. Dynasore can be used to inhibit dynamin-dependent endocytosis [14].

Filipin, methyl-β-cyclodextrin and nystatin can be used to inhibit caveolae-dependent endocytosis [13].

Protocol

The cells were plated in 96-wells plates for 24 h before treatment. The cell culture medium was removed and the cells were washed with PBS. The cells were incubated during 30 min with 20 mM NaN_3, 0.45 mM sucrose, 5 µM chlorpromazine, 40 µM dynasore, 2.5 µg/mL filipin, 5 mM methyl-β-cyclodextrin or 25 µM nystatin at 37 ºC. The cells were then incubated in darkness with 5 µM **$PcGal_{16}$** (in the continued presence of the respective inhibitor) for 1.5 h at 37 ºC. For studies at 4 ºC, cells were incubated with 5 µM **$PcGal_{16}$** for 1.5 h at 4 ºC. Uptake and PDT assays were then performed as aforementioned.

O. Cell-surface biotinylation assays

Principle

Cell-surface proteins expression can be studied by Western blot after biotinylation and isolation of those proteins. Cells are labeled with a thiol-cleavable amine-reactive biotinylation reagent. The Sulfo-NHS-SS-biotin is a cell-membrane impermeable where the sulfo-NHS ester group reacts with an amine to form a stable amide bond with the amine-containing protein (Figure 9.7A and 9.7B). Cells are subsequently lysed with a mild detergent and the labeled proteins are isolated using immobilized beads (such as NeutrAvidin beads, Figure 9.7C). The bound proteins are released from the beads by incubating with a solution containing DTT (Figure 9.7C).

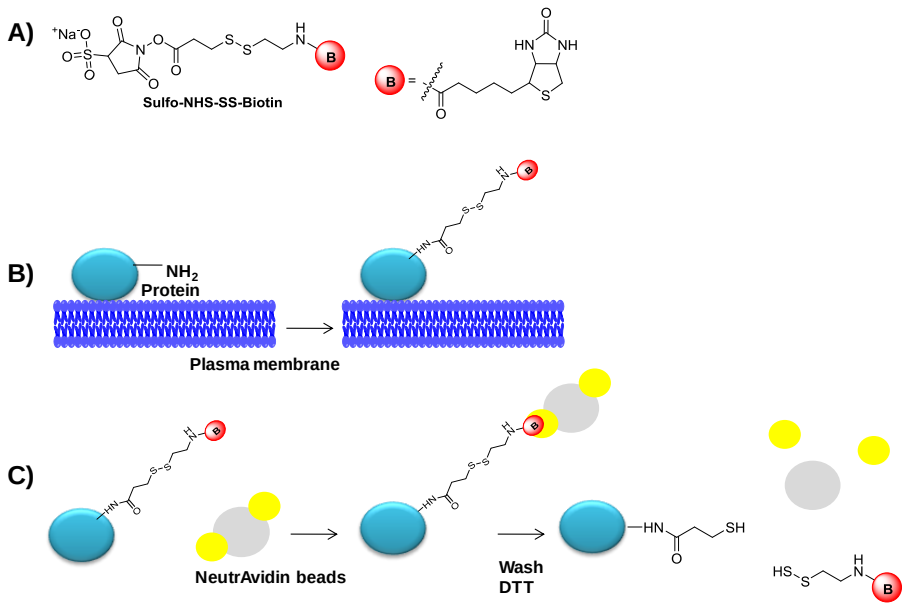

Figure 9.7 Schematic representation of cell-surface protein biotinylation.

Protocol

Cells were plated in 6-wells culture plates before treatment. Cell-surface biotinylation was performed as previously described [15]. Prior to surface protein biotinylation, all reagents were cooled to 4 ºC. The cells were washed twice with ice-cold PBS containing 0.5 mM $MgCl_2$ and 1 mM $CaCl_2$. Next, cells were incubated with 1 mL of the same ice-cold solution containing 1 mg/ml of freshly added Sulfo-NHS-SS-biotin[21] for 30 min at 4ºC, with gentle agitation. The medium was discarded and the plates were washed thrice with ice-cold PBS containing 0.5 mM $MgCl_2$, 1 mM $CaCl_2$, and 100 mM glycine[22]. The cells were scrapped in ice-cold RIPA buffer and kept on ice for 15 min. The cell homogenates were centrifuged at 18,000 *g* for 16 min at 4 ºC. The supernatants were then transferred to 1.5 mL eppendorf microfuge tubes containing 20 µL NeutrAvidin beads.[23] After 2 h incubation at 4°C under agitation, the NeutrAvidin supernatant (non-biotinylated proteins)[24] was collected and denaturated with Laemmli buffer and used for Western blotting. The beads were washed thrice

[21]Sulfo-NHS-SS-biotin does not penetrate the plasma membrane because of the charged sulfonate group, thus biotinylation is restricted to the cell surface.
[22]PBS containing glycine is used to quench any unreacted biotin reagent.
[23] Before use, NeutrAvidin beads were washed thrice with RIPA buffer.
[24] As the proteins at the cell surface are biotinylated, the non-biotinylated proteins correspond to intracellular proteins.

with RIPA buffer. The NeutrAvidin-bound proteins (biotinylated proteins) were eluted from the beads by adding 20 µL 2x Laemmli buffer[25], denaturated and used for Western blotting.

P. Cellular fractionation

Principle

Each organelle has characteristics (size, shape and density for example) which make it different from other organelles within the same cell. If the cell is broken open in a gentle manner, each of its organelles can be subsequently isolated. The process of breaking open cells is homogenization and the subsequent isolation of organelles is fractionation. Isolating the organelles requires the use of physical chemistry techniques, and those techniques can range from the use of simple sieves, gravity sedimentation or differential centrifugation (Figure 9.8), to ultracentrifugation of fluorescent labeled organelles in computer generated density gradients.

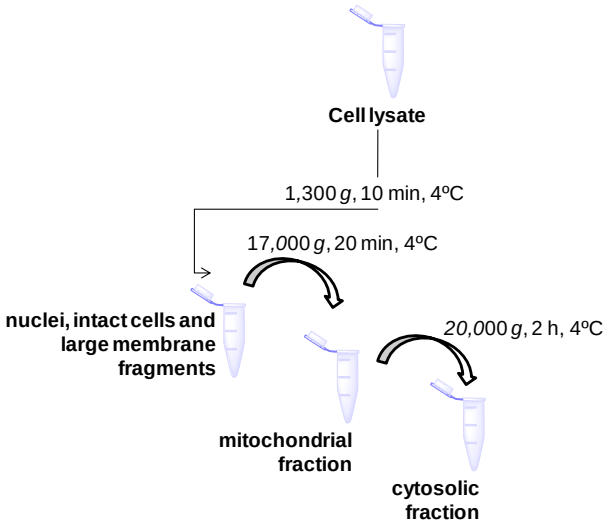

Figure 9.8 Schematic representation of cell fractionation by differential centrifugation.

Protocol

Cellular fractionation was performed as previously described [16]. After PDT, the cells were washed twice with ice-cold PBS and lysed with ice-cold hypotonic buffer (10 mM NaCl, 1.5 mM $MgCl_2$ and 10 mM Tris-HCl at pH 7.5). The cell lysates were transferred to

[25]DTT in Laemmli buffer allows the release of the proteins from beads.

microtubes with the help or a rubber policeman (cell scrapper) and incubated on ice during 10 min. The cell suspension was then transferred into a Dounce homogenizer. To disrupt the membranes, 40 up-and-down strokes were performed. The pellet containing the nuclei, intact cells and large membrane fragments was obtained after centrifugation at 1,300 *g* for 10 min at 4 ºC. The supernatant was recovered and transferred into clean microtubes which were then centrifuged at 17,000 *g* during 20 min at 4º C to obtain the mitochondrial fraction. The pellet rich in plasma membrane and the supernatant rich in cytosolic fraction were obtained after centrifugation at 20,000 *g* during 2h. After centrifugations, the pellets were resuspended in 100 µL of ice-cold hypotonic buffer. The cellular fractions were used for determination of PS fluorescence and for protein concentration determination as described in Western blot section, followed by denaturation with Laemmli buffer.

9.4 *In vivo* biological assays

9.4.1 Equipment and common materials

A. Equipment for bioluminescent imaging

Bioluminescent imaging was performed using IVIS Lumina XR system (Caliper Life Sciences) in combination with its Living Image Software.

B. Equipment for photodynamic therapy

The illumination system used was the Light Source Model Lc-122 from Lumacare, equipped with a halogen/quartz 250 W lamp coupled with the optic fiber probe (400-800 nm). The fluence rates were determined with the energy meter Coherent FieldMaxII-Top with a Coherent PowerSens PS19Q energy sensor.

C. Materials

Type II polycarbonate cages in individually ventilated caging (IVC) systems were from VentiRack Bioscreen TM.

The SuperFrost Plus glass slides (Menzel-Glaser) were from Thermo Fisher Scientific.

9.4.2 Plasmids, buffers, reagents and chemical products

pGL2 luciferase reporter vector was obtained from Promega. pcDNA6.2GW/Em-GFP, pcDNA-ENTR-BP, pLenti6 and blasticidin were from Invitrogen. STAR-Rdpro cells and polybrene were from Sigma. D-luciferin was from Perkin Elmer.

9.4.3 Photosensitizers

PorGal$_8$ and **ChlGal$_8$** were synthesized as described in synthesis of galactose-conjugates section.

9.4.4 Cells

HT-1376 and UM-UC-3 bladder cancer cells were obtained from ATCC and cultured as described in *in vitro* section.

9.4.5 Softwares

The Living Image software was used to calculate photon flux during bioluminescent imaging acquisition.

GraphPad Prism (v.5.00, GraphPad Software) was used for most of the displayed graphs, as well as for the statistical analysis.

9.4.6 Ethics statement

All procedures involving animals were conducted according to the statements on the directive 2013/113/EU of the European Parliament and of the Council Portuguese law (DL 113/2013) and all relevant legislations. All experiments were approved by the Portuguese Veterinary Direction (ORBEA-IBILI-FMUC-06-2015). The authors have an accreditation for animal research given from Portuguese Veterinary Direction (Ministerial Directive 1005/92). We adhere to the ARRIVE guidelines for reporting animal research [17]and to the guidelines for the welfare and use of animals and cancer research [18].

The mice were purchased from Charles River (National Cancer Institute Frederick) and maintained under specific-pathogen-free conditions in the animal care facility of IBILI, Faculty of Medicine, University of Coimbra (Coimbra, Portugal).

The mice were housed in type II polycarbonate cages in individually ventilated caging (IVC) systems enriched with sterelized cardboard tubes and shelters. The mice were fed with sterilized standard laboratory diet and received sterile water *ad libitum*. The animals were housed at approximately 22 ºC, 60% relative humidity, and a 12 h light, 12 h dark cycle was maintained. All mice were quarantined and acclimated to laboratory conditions for 1 week before experimentation.

PDT treatments were performed with mice under a heat pad to maintain body heat and only the tumor areas were irradiated. As the PDT experiments were performed with mice outside of microbiological safety cabinets; simple measures (use of latex gloves and face masks, disinfection of the working bench with 90% alcohol for 3 min) were taken to prevent infections.

Early endpoints were applied during the experiments to increase the precision of the results and to decrease non-specific systemic effects [18]. The mice were euthanized (cervical dislocation) and subjected to necropsy examination when the tumor volume of the control and single PDT groups reached approximately 500 mm^3 (normally at days 9 and 11 after treatment, respectively), when ulcerating lesions occurred, when an animal had lost > 10% of its body weight, or when a mouse appeared seriously ill. At the end of the experiments (13 and 15 days after PDT with **PorGal$_8$** and **ChlGal$_8$**, respectively), all remaining animals were sacrificed and subjected to a gross necropsy examination.

9.4.7 Statistical analysis

Statistical analyses were carried out using a statistics program (GraphPad Prism; GraphPad Software). Student's t-test was used to compare the treatment effects with that of control. P-value was considered at the 5% level of significance to deduce inference of the significance of the data. All graphs and statistics were prepared using the GraphPad Prism 5.0 software.

9.4.8 Protocols

A. In vivo studies with PorGal$_8$

Principle

The most common *in vivo* approach used in PDT experiments is based on subcutaneous tumors in laboratory mice. Human xenograft tumors can be obtained by engraftment of human tumor cells into athymic nude mice or into severe combined immunodeficient mice that are T-

and B-cell deficient. Mouse xenograft models bearing luciferase-expressing cancer cells have been established to monitor PDT efficacy with non-invasive bioluminescence imaging.

Bioluminescence imaging relies on the detection of light produced from cells tagged with luciferase. The firefly luciferase gene is most commonly used in animal tumor models. Luciferase expression is imaged following an intraperitoneal injection of the substrate D-luciferin [19]. Luciferase oxidizes luciferin in the presence of ATP and molecular oxygen to form an electronically excited oxy-luciferin species. Visible yellow-green to yellow-orange light is emitted following the relaxation of excited oxy-luciferin to its ground state.

Protocol: Lentivirus production and transduction in UM-UC-3 bladder cancer cells

The lentiviral vector was generated by Doctor José Ramalho at Laboratório de Biologia Celular e Molecular FCM/CEDOC - Universidade Nova de Lisboa. The coding sequence for firefly (*Photinus pyralis*) luciferase was amplified from pGL2 luciferase reporter vector by polymerase chain reaction PCR (forward primer- ctgttgctagcatggaagacgccaaaaacataaagaaa, reverse primer- gctgaggatccttacattttacaatttggactttccgc), digested with NheI/BamHI and cloned into pcDNA-ENTR-BP with the same restriction enzymes. pcDNA-ENTR-BP, a Gateway® mammalian expression vector was generated based on pcDNA6.2GW/Em-GFP. In order to generate a polylinker containing a multi-cloning site, two DNA sequences (aaagctagcgatctcgagctcaagcttcgaattctgcagtcgacggtaccgcgggcccgggatccagcggccgctctagataactgatca and tcgatgatcagttatctagagcggccgctggatcccgggcccgcggtaccgtcgactgcagaattcgaagcttgagctcgagatcgctagcttt) chemically synthesized were annealed and ligated into pcDNA6.2GW/Em-GFP previously digested with DraI/XhoI. In order to generate recombinant lentiviruses, the firefly luciferase was subcloned into pLenti6 using the Gateway system. Recombinant lentiviruses were produced by transient transfection. pMD2.G (envelope-coding plasmid) and psPAX2 (which expresses Gag, Pol and Rev) were gifts from Didier Trono (Addgene plasmid #12259 and #12260 respectively). All plasmids, including pLenti6 Luc transfer vector were transfected into STAR-Rdpro cells by JetPrime protocol (Polyplus). Supernatant was harvested at 48 h later and used to transduce UM-UC-3 bladder cancer cells in the presence of polybrene (6 µg/mL). Transduced cells were selected using blasticidin (8 µg/mL). Isolated

clones were screened for their luciferase activities using an IVIS Lumina XR equipment (Figure 9.9). To isolate single cell clones, cells were subjected to limited dilution. Individual clones were selected for luciferase activity using an IVIS Spectrum.

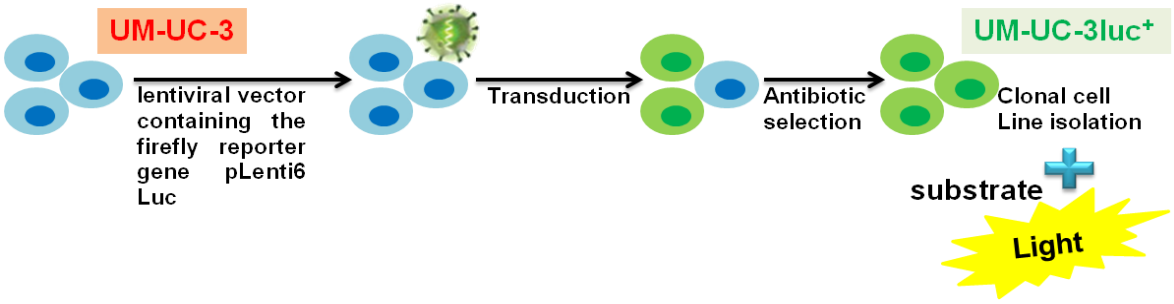

Figure 9.9 Schematic representation of transduction in UM-UC-3 bladder cancer cells.

Protocol: Mice

Male nude Balb/c *nu/nu* mice were used for biodistribution and PDT studies with **PorGal$_8$**. We used a total of 27 animals in the experiments (divided into 5 experimental groups, n = 3 mice for biodistribution studies and n = 6 mice per group of PDT experiments) which were 5 to 8 weeks of age and weighed 20-25 g at the start of the experiments.

Protocol: Inoculation of tumor cells

A cell suspension of 2 x 10^6 UM-UC-3luc$^+$ cells in PBS (cooled on ice in a tube) was inoculated subcutaneously (0.1 mL) under the skin in the dorsal flank regions by using a sterile syringe with a 21-gauge needle. The mice were monitored daily, tumor growth was followed by bioluminescent imaging and tumor volume was measured using an external caliper.

Protocol: Assessment of tumor volume

All measurements of tumor volume were carried out by the same investigator (who was blinded to the experimental groups) to maximize the reproducibility of the data. The tumor growth was observed daily, monitored over time by bioluminescent imaging and measured once they become palpable. To calculate tumor volume, the greatest longitudinal diameter (length) and the greatest transverse diameter (width) from each tumor were determined using

an external caliper. Each tumor´s volume was calculated using the following formula: *tumor volume=length x width*^{2} *x 0.5*.One week after the injection of UM-UC-3luc$^+$, tumors whose volume reached approximately 50 mm^3 were selected for the PDT studies.

Protocol: Study design

Based on previous studies, describing UM-UC-3luc$^+$ bladder cancer cells to develop a xenograft tumor model [20], we determined the sample size using G*Power 3.1 for all power calculations. We required groups of at least 6 mice to achieve appropriate power for anticancer analysis (effect size: a 50% decrease in the bioluminescent signal at 5 days after treatment with PDT; significance level: 5%; desired power of the experiment: 80%). When the volume of xenografts reached approximately 50 mm^3 (normally 7 days after cells inoculation), the tumor-bearing mice were randomly divided into the following 5 groups (Figure 9.10):

Group I) 5 µmol/kg of **PorGal$_8$** injected intraperitoneally for biodistribution studies, Group II) no treatment,

Group III) no **PorGal$_8$** injection and PDT at 50.4 J/cm^2 (*i.e.* 28 mW/cm^2 for 30 min, negative control),

Group IV) 5 µmol/kg of **PorGal$_8$** injected intraperitoneally and no PDT (mice treated with **PorGal$_8$** in darkness),

Group V) PDT at 50.4 J/cm^2 performed 24 h after intraperitoneal injection of 5 µmol/kg of **PorGal$_8$** (PDT treatment group; Table 9.5).

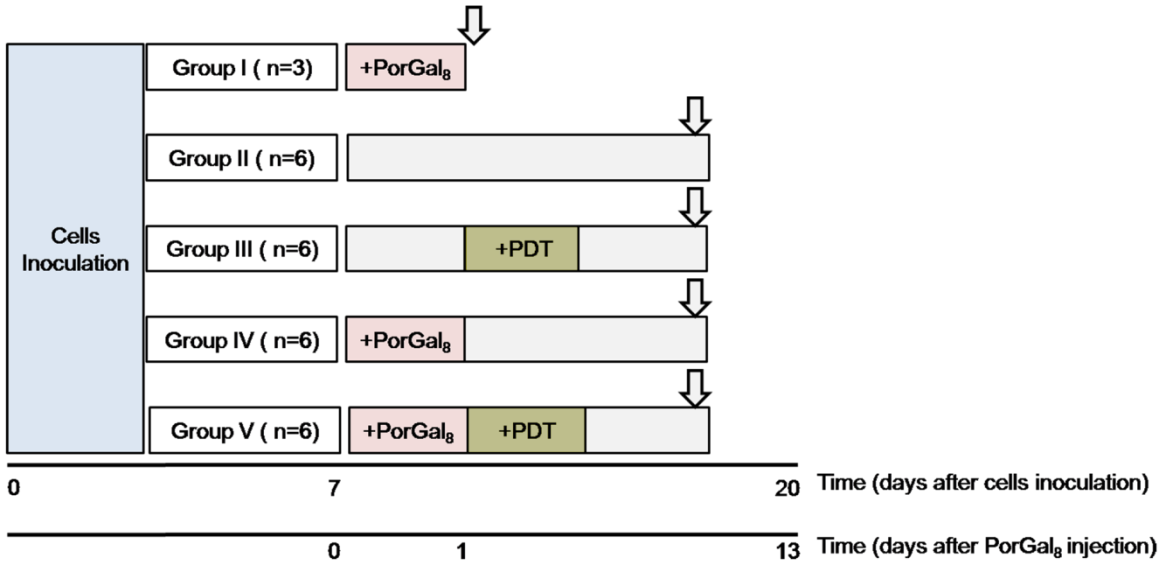

Figure 9.10 Experimental design for *in vivo* studies with **PorGal$_8$** (arrows represent time period after which euthanasia took place).

Table 9.5 Experimental conditions used in *in vivo* studies with **PorGal$_8$**.

Compound	Dose (µmol/kg)	Irradiation system	Potency (mW/cm^2)	Irradiation time (min)	PDT treatment	Model
PorGal$_8$	5 (intraperitoneal)	Lumacare (400-800 nm)	28	30	Single	Xenograft (Male nude Balb/c *nu/nu* mice, UM-UC-3luc$^+$ cells)

Protocol: In vitro and *in vivo* bioluminescent imaging

For *in vitro* luciferase assay, D-luciferin was added to the cell culture medium to obtain a final concentration of 150 µg/mL. The bioluminescent imaging was performed 10 min after adding the substrate into the cells using an IVIS 100 imaging system. Photon flux was calculated using Living Image software and represented as photons/sec/cm^2/sr. Bioluminescence values were then represented as percent photon flux of untreated or vehicle control values.

For *in vivo* imaging, the mice were first anesthetized (2 mg/kgintraperitoneal cocktail of a 2:1 50 mg/mL ketamine in 2.5% chlorpromazine). D-luciferin was then injected intraperitoneally (150 mg/kg) by using a sterile syringe with a 21-gauge needle. The mice were imaged using an IVIS 100 imaging system. Bioluminescence values were calculated by

measuring photons/sec/cm^2/sr in the region of interest surrounding the bioluminescence signal from the tumor.

Protocol: Biodistribution assays

On day 0 (normally 4-5 ppm), the animals of biodistribution study group (n = 3) were injected intraperitoneally with 5 µmol/kg of **PorGal$_8$** (freshly prepared in PBS with a percentage of DMSO of 0.2% v/v) by using a sterile syringe with a 21-gauge needle. At 5 h and 24 h post-injection, the mice were anesthetized (2 mg/kg intraperitoneal cocktail of a 2:1 50 mg/mL ketamine in 2.5% v/v chlorpromazine) and fluorescence images were captured using an IVIS 100 imaging system (excitation at 430 nm and emission 695-770 nm). After final imaging, animals were euthanized (cervical dislocation) and subjected to necropsy examination. Tumor and organs (kidney, heart, liver and lung) were removed for imaging to confirm signal content and assess the tumor-targeting efficacy of **PorGal$_8$**.

Protocol: Photodynamic Therapy study

On day 0 (normally 4-5 ppm), the animals of Groups IV and V were injected intraperitoneally with **PorGal$_8$** as previously described. On day 1 (24 h after injection of **PorGal$_8$**) the tumors of animals, from Groups III and V, were light irradiated. Light irradiation (white light 400-700 nm) was performed with the illumination system LC-122 LumaCare). One day after treatments, the mice were monitored daily, bioluminescent imaging was repeated twice a week after treatment and the tumor volume was measured.

The observations and assessments of the treated group (PDT treatment group) were compared with the negative control groups (negative control groups II, III and IV).

B. In vivo studies with ChlGal$_8$

Protocol: Mice

Male Swiss nude (*nu/nu*) mice were used for PDT studies with **ChlGal$_8$**. We used a total of 24 animals in the experiments (divided into 4 experimental groups, n = 6 mice per group) which were 5 to 8 weeks of age and weighed 20-25 g at the start of the experiments.

Protocol: Inoculation of tumor cells

The xenograft tumor model was developed using HT-1376 human bladder cancer cells. A cell suspension of 2 x 10^6 HT-1376 cells in PBS was inoculated subcutaneously (0.1 mL) under the skin in the dorsal flank regions by using a sterile syringe with a 21-gauge needle.

Protocol: PDTstudy design

Based on previous studies, describing HT-1376 bladder cancer cells to develop a xenograft tumor model [21], we determined the sample size using G*Power 3.1 for all power calculations [22, 23]. We required groups of at least 6 mice to achieve appropriate power for anticancer analysis (effect size: a 50% decrease in tumor volume at 5 days after treatment with PDT; standard deviation: 80; significance level: 5%; desired power of the experiment: 80%).

When the volume (assessment of tumor volume is described in detail in *in vivo* studies with **PorGal$_8$** section) of xenografts reached approximately 50 mm^3 (normally 10 days after cells inoculation), the tumor-bearing mice were randomly divided into the following 4 groups (n = 6 per group, Figure 9.11):

Group I) no **ChlGal$_8$** injection and PDT at 36 J/cm^2 (*i.e.* 30 mW/cm^2 for 20 min, negative control);

Group II) 3.33 µmol/kg of **ChlGal$_8$** injected intratumorally and no PDT (mice treated with **ChlGal$_8$** in darkness);

Group III) PDT at 36 J/cm^2 performed 1.5 h after intratumoral injection of 3.33 µmol/kg of **ChlGal$_8$** (single PDT group);

Group IV) PDT at 36 J/cm^2 performed 40 min after single PDT (repeated PDT group).

On day 0 (4-5 pm), the animals of negative control, single PDT group and repeated PDT group were anesthetized (2 mg/kg intraperitoneal cocktail of a 2:1 50 mg/mL ketamine in 2.5% v/v chlorpromazine) and injected intratumorally with 3.33 µmol/kg **ChlGal$_8$** (freshly prepared in PBS with a percentage of DMSO of 0.3% v/v) by using a sterile syringe with a 21-gauge needle. On the same day, 1.5 h after injection of **ChlGal$_8$** the tumors of animals, from single and repeated PDT groups, were light irradiated. Light irradiation (white light 400-800 nm) was performed with the illumination system LC-122 LumaCare) with light > 500 nm.

The tumors of mice from repeated PDT group were light irradiated for a second time, 40 min after the first irradiation time. One day after treatments, the mice were monitored daily and the tumor volume was measured as described in Supporting Information. The observations and assessments of the treated groups (single and repeated PDT groups) were compared with the negative control groups (negative control groups I and II).

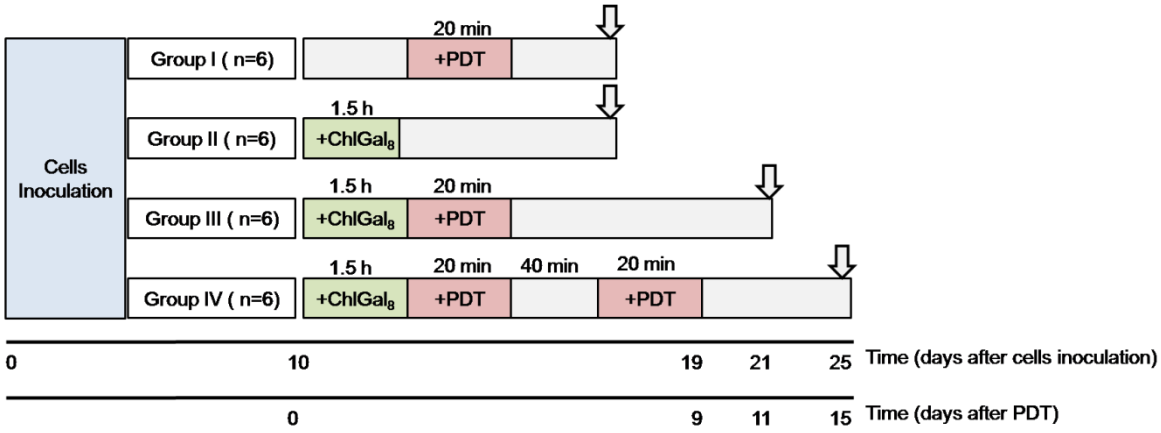

Figure 9.11 Experimental design (arrows represent time period after which euthanasia took place).

Table 9.6 Experimental conditions used in *in vivo* studies with **ChlGal$_8$**.

Compound	Dose (µmol/kg)	Irradiation system	Potency (mW/cm^2)	Irradiation time (min)	PDT treatment	Model
ChlGal$_8$	3.33 (intratumoral)	Lumacare (> 500 nm)	30	20	Single Repeated (40 min dark period interval)	Xenograft (Male Swiss nude *nu/nu*, HT-1376 cells)

C. Immunohistochemistry assays

Principle

Immunohistochemistry (IHC) is a method for demonstrating the distribution and location of proteins in tissue sections. Immunohistochemical staining follows the same basic principles of immunocytochemistry and it is accomplished with antibodies that recognize the target protein. The antibody-antigen interaction is then visualized using either chromogenic detection, in which an enzyme conjugated to the antibody cleaves a substrate to produce a colored precipitate at the location of the protein, or fluorescent detection, in which a

fluorophore is conjugated to the antibody and can be visualized using fluorescence microscopy.

Protocol

Intact tumors were embedded in OCT matrix and snap frozen in dried ice. The samples were stored at -80 ºC until used. Serial cryostat sections (10 μm) of both control and PDT tumors were placed on the same slide to minimize methodological variation during immunostaining. Sections were air dried and fixed in cold acetone for 10 min. The sections were then washed with PBS, permeabilized for 30 min with 0.25% v/v Tx-100 in PBS with 0.02% w/v BSA (PBS/BSA) and blocked with 10% v/v normal goat serum before incubation overnight at 4 ºC with primary antibodies: rabbit anti galectin-1 (1:100 v/v), moue anti E-cadherin (1:100 v/v). Sections were then rinsed with PBS and incubated with DAPI for nuclear staining and the secondary fluorescent antibodies for 1 h at room temperature. The coverslips were mounted using the glycergel mounting medium and sealed with nail polish. The samples were stored in an appropriate box at 4 ºC until acquisition of images by fluorescence microscopy.

9.5 References

1. Silva S, Pereira PMR, Silva P, Paz FAA, Faustino MAF, Cavaleiro JAS, Tomé JPC (2012) Porphyrin and phthalocyanine glycodendritic conjugates: synthesis, photophysical and photochemical properties. Chem Commun 48: 3608-3610.

2. Silva AM, Tomé AC, Neves MGPMS, Cavaleiro JAS (2005) 1,3-dipolar cycloaddition reactions of porphyrins with azomethine ylides. J Org Chem 70: 2306-2314.

3. Silva AMG, Tomé AC, Neves MGPMS, Silva AMS, Cavaleiro JAS (1999) *meso*-Tetraarylporphyrins as dipolarophiles in 1,3-dipolar cycloaddition reactions. Chem Commun 1767-1768.

4. Spiller W, Kliesch H, Wöhrle D, Hackbarth S, Röder B, Schnurpfeil G (1998) Singlet oxygen quantum yields of different photosensitizers in polar solvents and micellar solutions. J Porphyrins Phthalocyanines 2: 145-158.

5. Seybold PG, Gouterman M (1969) Porphyrins. XIII: Fluorescence Spectra and Quantum Yields. J Mol Spectrosc 31: 1-13.

6. Zhang Y-Z, Zhou B, Zhang X-P, Huang P, Li C-H, Liu Y (2009) Interaction of malachite green with bovine serum albumin: Determination of the binding mechanism and binding site by spectroscopic methods. J Hazard Mater 163: 1345-1352.

7. Dam TK, Gabius H-J, André S, Kaltner H, Lensch M, Brewer CF (2005) Galectins bind to the multivalent glycoprotein asialofetuin with enhanced affinities and a gradient of decreasing binding constants. Biochemistry 44: 12564–12571.

8. D'Auria S, Petrova L, John C, Russev G, Varriale A, Bogoeva V (2009) Tumor-specific protein human galectin-1 interacts with anticancer agents. Mol Biosyst 5: 1331-1336.

9. Friedrich J, Seidel C, Ebner R, Kunz-Schughart LA (2009) Spheroid-based drug screen: considerations and practical approach. Nat Protoc 4: 309-324.

10. Liu J, Chen Y, Li G, Zhang P, Jin CZ, Zeng L, Ji L, Chao H (2015) Ruthenium(II) polypyridyl complexes as mitochondria-targeted two-photon photodynamic anticancer agents. Biomaterials 56: 140-153.

11. Khaitan D, Chandna S, Arya MB, Dwarakanath BS (2006) Establishment and characterization of multicellular spheroids from a human glioma cell line; Implications for tumor therapy. J Transl Med 4: 1-13.

12. Yao K, Gietema JA, Shida S, Selvakumaran M, Fonrose X, Haas NB, Testa J, O'Dwyer PJ (2005) *In vitro* hypoxia-conditioned colon cancer cell lines derived from HCT116 and HT29 exhibit altered apoptosis susceptibility and a more angiogenic profile *in vivo*. Brit J Cancer 93: 1356-1363.

13. Vercauteren D, Vandenbroucke RE, Jones AT, Rejman J, Demeester J, De Smedt SC, Sanders NN, Braeckmans K (2010) The use of inhibitors to study endocytic pathways of gene carriers: optimization and pitfalls. Mol Ther 18: 561-569.

14. Kirchhausen T, Macia E, Pelish HE (2008) Use of dynasore, the small molecule inhibitor of dynamin, in the regulation of endocytosis. Method Enzymol 438: 77-93.

15. Ribeiro-Rodrigues TM, Catarino S, Marques C, Ferreira JV, Martins-Marques T, Pereira P, Girão H (2014) AMSH-mediated deubiquitination of Cx43 regulates internalization and degradation of gap junctions. Faseb Journal 28: 4629-4641.

16. Rangel R, Dobroff AS, Guzman-Rojas L, Salmeron CC, Gelovani JG, Sidman RL, Pasqualini R, Arap W (2013) Targeting mammalian organelles with internalizing phage (iPhage) libraries. Nature Protocols 8: 1916-1939.

17. Kilkenny C, Browne WJ, Cuthill IC, Emerson M, Altman DG (2010) Improving bioscience research reporting: the ARRIVE guidelines for reporting animal research. PLoS Biol 8: e1000412.

18. Workman P, Aboagye EO, Balkwill F, Balmain A, Bruder G, Chaplin DJ, Double JA, Everitt J, Farningham DAH, Glennie MJ, Kelland LR, Robinson V, Stratford IJ, Tozer GM, Watson S, Wedge SR, Eccles SA, Navaratnam V, Ryder S, Inst NCR (2010) Guidelines for the welfare and use of animals in cancer research. Brit J Cancer 102: 1555-1577.

19. O'Neill K, Lyons SK, Gallagher WM, Curran KM, Byrne AT (2010) Bioluminescent imaging: a critical tool in pre-clinical oncology research. J Pathol 220: 317-327.

20. van der Horst G, van Asten JJ, Figdor A, van den Hoogen C, Cheung H, Bevers RFM, Pelger RCM, van der Pluijm G (2011) Real-Time Cancer Cell Tracking by Bioluminescence

in a Preclinical Model of Human Bladder Cancer Growth and Metastasis. Eur Urol 60: 337-343.

21. Amit D, Hochberg A (2010) Development of targeted therapy for bladder cancer mediated by a double promoter plasmid expressing diphtheria toxin under the control of H19 and IGF2-P4 regulatory sequences. J Transl Med 8: 1-18.

22. Faul F, Erdfelder E, Buchner A, Lang AG (2009) Statistical power analyses using G*Power 3.1: Tests for correlation and regression analyses. Behav Res Methods 41: 1149-1160.

23. Vatassery GT, Smith WE, Quach HT, Lai JCK (1995) *In vitro* oxidation of vitamin E, vitamin C, thiols and cholesterol in rat brain mitochondria incubated with free radicals. Neurochem Int 26: 527-535.